2-P

CR-128898

REPORT

DRI #2577

COMBUSTION DYNAMICS IN LIQUID ROCKET ENGINES

FINAL REPORT

by

W. H. McLain

NATIONAL AERONAUTICS AND SPACE ADMINISTRATION

Contract NAS9-7566

Technical Management
NASA Manned Spacecraft Center
Houston, Texas 77058
Rocket Propulsion

Denver Research Institute
Denver, Colorado 80210

September 1971

UNIVERSITY OF DENVER • DENVER RESEARCH INSTITUTE

DRI #2577

COMBUSTION DYNAMICS IN LIQUID ROCKET ENGINES

FINAL REPORT

by

W. H. McLain

NATIONAL AERONAUTICS AND SPACE ADMINISTRATION

Contract NAS9-7566

Technical Management
NASA Manned Spacecraft Center
Houston, Texas 77058
Rocket Propulsion Division
Mr. Carl Hohmann

Denver Research Institute
Denver, Colorado 80210

September 1971

FOREWORD

The effort described herein was performed under Contract NAS9-7566. The major objectives of this research program were: (1) to experimentally identify in "real time" the chemical species present in the combustion chamber of a nitrogen tetroxide/aerozine-50 rocket engine during the pre-ignition, ignition and post combustion operating periods, and (2) to determine, if possible, the cause of severe ignition overpressures sporadically observed during the vacuum startup of the Apollo RCS engine.

To achieve these objectives, observation will be made of the emission and absorption spectra associated with specific chemical species present in the rocket chamber during the several phases of operation. Specific emphasis is to be placed on outlining the physical and chemical processes occurring during the preignition and ignition spike periods of operation, and on to the extent to which residual propellants or condensed intermediate reaction products remain after the engine has been operated in a pulse mode duty cycle.

TABLE OF CONTENTS

LIST OF FIGURES

I. INTRODUCTION

1.1 Background

During the development tests of the Apollo vehicle, several hundred thousand test firings were performed using The Marquardt Corp. R4-D nitrogen tetroxide/Aerozine-50 reaction control system rocket engine. One of the problems that occurred during these tests was a sporadic detonation in the thrust chamber. This detonation occurred only during high altitude simulation tests and was not observed during static tests performed at sea level firing conditions. In several well documented occurrences these detonations resulted in extensive structural damage.

Even though the basic mechanism responsible for these detonations was not fully understood, a number of major modifications of the engine were introduced in order to reduce the probability of their occurrence. These modifications were based on the hypothesis that unburned propellant residues were responsible for the observed phenomena. Such residues were observed to form in appreciable quantities during pulse-mode operation under simulated high-altitude-start conditions.

Support of this hypothesis was found in two simple experimental observations. The first was the observation that strong ignition spikes had never occurred on a clean engine test. This was interpreted to mean that the strong ignition spike phenomenon was in some way a result of previous engine tests. The second observation was that the frequency of detonation was dependent on engine attitude; the frequency increased if the engine was tested in a firing attitude such that the propellant residues remained in the engine.

In the final engine configuration, two design changes were incorporated to reduce the problem. The first was the incorporation of an ignition precup in the central portion of the injector plate. The ignition precup consisted of an open ended annulus projecting from the axial center of the injector plate. The propellant manifold was designed in such a manner that the initial propellant flow started through this annulus. The rationale for this design change was that the flow channelization caused by this device increased the local stream pressure in the center of the thrust chamber during the preignition time period. Because of the exponential dependence of burning rate on pressure, it was believed that the increased pressure would reduce the ignition delay time and promote ignition near the injector plate, thus reducing the quantity of propellant residues.

The principal difficulty with this approach was that high-speed motion pictures of the ignition process, taken after the production engine had been developed, indicated that ignition could have occurred either in the precup region or at the nozzle throat. For a throat ignition, it was probable that shock heating was involved and that the mechanism of ignition was different from that on which precup arguments were based.

The second major engineering change was the incorporation of additional electrical heating capacity on the injector of the engine. The heaters provided sufficient heat to maintain the injector at an elevated temperature, apparently removing propellant residuals and engine residues by direct volatilization. The test data available to date indicate that removal of the engine shut-down propellant residual materials eliminates the catastrophic overpressures. However, the use of heaters requires 150 watts of electrical power for each attitude control engine. Since power

is at a premium in a space vehicle, this represents a substantial power drain on the secondary power source units.

1.2 Summary of Recent Research

Although satisfactory engineering solutions were found, the cause of the detonation and the fundamental chemical and physical processes responsible for the phenomenon remained unknown. As a result, a series of research programs were conducted to provide detailed knowledge of the chemical and physical processes responsible.

A number of investigators have provided information about the chemical character of engine residues. Seamans and coworkers[1] have shown that the residues of a MMH/N_2O_4 propellant combination have a chemical composition similar to that outlined in Table I. This elemental composition is interpreted to mean that the overall mixture consists of monomethyl hydrazine admixed with water and an uncertain nitrate adduct, probably HNO_3.

Using standard Trazuzl block tests, Seamans[2] found that the brisance of the residual material was extremely high, and that the explosive force was sufficient to completely destroy the test fixtures in some cases. This was in marked contrast to results obtained with a well behaved explosive such as nitroglycerine. The work of Perlee and coworkers at the Bureau of Mines[3] showed rather conclusively that the infrared spectra of the residue corresponded to that of a hydrazinium nitrate admixed with pure unreacted fuel components. In addition, Perlee[4] studied the required shock overpressures for the pure samples of several hydrazinium nitrates and found that a minimum shock initiation pressure of 22 kilobars were required to initiate the explosion.

TABLE I

MMH/NTO Residues, O/F = 2.0

A. Elemental Analysis

C	16.3%
H	8.6%
N	42.8%
O (By difference)	32.3%

Empirical Formula $C_4H_{24}N_9O_6$

B. Functional Analysis

Total N-N (as MMH)	53.81%
Total ammonic (as CH_2NH_2)	0.44%
Total NO_3^- (as HNO_3)	16.08%
Water	15.3%
CO_2	Trace
NO_2	Trace
Total Analysis	85.6 %

C. Derived Composition of Residue

$CH_3NH_3NO_3$	1.33%
MMH · HNO_3	26.28%
MMH · H_2O	54.8%
MMH	3.22%
% Total	85.63%

There is no evidence from the present work that pressures of this magnitude were present during the starting transients. Perlee[5] has suggested that localized pressures of this magnitude may possibly be reached via multiple reflections in the chamber.

Infrared studies performed by Dauerman and coworkers[6] have suggested that, in addition to the hydrazinium nitrate, there is a possibility that an azide might be present as a major component in the residues. The evidence for this possibility is the observance of a transient peak at a wavelength of 4.8 microns, observed under relatively carefully controlled laboratory conditions. No evidence for the azide peaks in the infrared region was found in the residues examined by either Perlee or Seamans during their early work. However, later work by Perlee[7] indicated that tetrazine derivatives may be present.

A physical characterization of the residues has been reported by the same investigators. The residue material consists of a viscous, yellow liquid. Both under high altitude simulation tests and under ambient pressure conditions, the material is observed to outgas for long periods of time. The most probable cause of the gas formation has been assumed to involve slow liquid phase reactions between unreacted hydrazine and the reaction products.

Recent work of Saad (private communication) has demonstrated increased complexity of the residue mixtures. Chemical analysis of the mixtures under pseudo combustion conditions indicated the presence of dimenthylnitrosamine, monomethyl nitrosamine and the probable transitory existance of nitrosamine for UDMH, MMH, and N_2H_4 reactions with nitrogen

tetroxide respectively. Evidence for these compounds was obtained using a combination of infrared, mass spectrometric, and gas chromatographic analyses. More stable decomposition products of the unstable intermediates were also observed.

Further rocket testing programs have demonstrated that at least two fundamentally different problems are involved in the destructive ignition spiking of pulse-mode rocket engines. The problems are associated with the processes occurring in the preignition and postcombustion phases of operation. Each type of ignition "spike" probably has its origin in a separate physical phenomenon. Engine failures attributed to preignition phenomena have been observed on "first start" tests performed at the Bureau of Mines with a two-dimensional research rocket engine. Because there is no material left from previous runs, a failure on a first start must be explained in terms of the combustion preignition kinetics probably involving both gas and liquid phase reaction mechanisms. Attention has therefore been focused on the gas phase reaction sequences, in part because of the high probability that branched chain reaction sequences in the gas phase could lead to the initiation of detonation via the formation of unstable chemical intermediates. Reactions involving liquid phase components are expected to be relatively slow since they are governed by liquid diffusion velocities and/or mixing of the fuel and oxidizer components and can play no role in the development of high overpressures during the ignition of clean engines.

Engine failures have been observed which can be attributed to a condensed phase detonation of the liquid residues formed during and after engine shutdown. In this case the detonation occurs during the next start up

of the pulse mode engine. Such an event may occur by a pressure or temperature induced initiation of the "primary explosive" which consists of a mixture of hydrazine hydrate and hydrazine nitrates and/or nitrites. It is noted that such mixtures are relatively insensitive explosives. In addition to a direct initiation of the "primary explosive" residues, a second mechanism for explaining the liquid phase detonation may be found by assuming the presence of highly sensitive compounds such as hydrazoic acid, trizene and hyponitrous acid in sufficient quantity in the liquid phase to initiate explosion of the base residues. The present research program indicates that $(HNO)_x$, $(HN)_x$ and HN_3 are present in the volatile gases emitted from the liquid residues. A recent report by the Bureau of Mines indicates the possibility of dimethyl tetrazene as a trace component. If such compounds are present as an entrapped gas phase, the interesting possibility exists that the liquid phase detonation may involve the development of a localized hot spot during an adiabatic compression caused by engine pressurization.

There are at least three ways in which hot spots can be developed. One involves the adiabatic compression of a gas bubble in a liquid explosive; a second involves the heat generated by viscous flow; and a third involves a mechanical abrasion between crystals. Because only a limited acceleration of the fluid can occur during the time period associated with the ignition spike, it is probable that this is not the initiation mechanism in this case. Since in most of the recent work the residues are present only in a liquid form, mechanical abrasions between crystals is ruled out. Because the residues are characterized as frothy liquids the adiabatic compression mechanism is operative and therefore a detailed analysis of this initiation mechanism has been performed.

In this analysis it is demonstrated that liquid phase reactions produce metastable gaseous compounds such as hydrogen azide and triazene and create chemically metastable bubbles. The thermal energy increase caused by the compression of these bubbles then produces localized "hot spots" throughout the liquid. If the temperature of these localized hot spots exceeds the minimum activation energy requirements for chemical decomposition, then the hot spot undergoes a highly exothermic chemical reaction which results in a high energy flux into the relatively inert propellant residues. This energy flux can initiate the residues and cause catastrophic detonations. Because initiation can be started at several locations simultaneously, multiple detonation waves are probably developed which can result in a shaped charge effect which would account for the characteristically high brisance found in the propellant residues. The adiabatic hot spot mechanism is capable of explaining all the phenomena observed both under carefully controlled laboratory experiments and during hot engine tests.

II. THERMODYNAMIC ANALYSIS

2.1 Thermodynamics of Engine Performance

Propellant oxidant/fuel (O/F) mixture ratios were optimized with respect to selected propulsion parameters such as chamber pressure, area ratio, and specific impulse. The theoretically calculated values for these system parameters were correlated with actual engine performance factors through an empirical correction which accounts for propulsion inefficiences and experience on previous engine development programs.

Two sets of calculations were made using the NASA Thermodynamic Analysis Program. The first type of analysis assumed shifting equilibrium during an isentropic expansion from engine thrust chamber conditions through a DeLaval nozzle. A shifting equilibrium analysis provides a theoretical limit to the maximum performance of the system. The two types of analysis, shifting equilibrium and frozen equilibrium, comprise a design envelope that can be used to estimate the performance and chemical characteristics of the propellant system. The method of calculation employed in the present work was developed by Gordon and coworkers[8], and adapted for use on the DRI Burroughs 5500 computer system. The reported calculations are based on 1967 JANAF Thermochemical Data.[9]

2.2 Calculation of Relative Mole Fractions

Propellant combinations with nitrogen tetroxide as an oxidizer and hydrazine, UDMH, or MMH as fuel can be classified as either H-N-O or C-H-N-O atomic systems. Either classification implies that all combinations of compounds may be present that include these atoms and for which thermochemical data are available in the program. For the H-N-O system the list of

possible reaction products is relatively simple, since the major products for this system include water, H_2, OH, NO_2 and NO.

For the C-H-N-O system the list of possible products is much more extensive. Typical calculational results for the propellant combinations involving hydrazine, UDMH, MMH and corresponding to the H-N-O and C-H-N-O systems respectively are presented in Figures 1 to 14. For the propellant combinations considered, about 30 individual species are possible. Of this number, only 23 are present within the defined minimum relative mole limit of 0.000005 moles. Calculations have been performed using a range of O/F mixture ratios from 0.10 to 10.0 over a range of pressures from 10,000 down to 0.3 psia.

The pressure limits were chosen so that they would encompass the pressure regime between the initial start pressure and the high pressure transients caused by rapid shock heating during a gas phase detonation. The large variation in O/F was necessary in order to allow the estimation of the effect of variations of mixture ratio caused by flash vaporization or freezing lag effects.

Although the major species could be estimated from the available literature, because of higher spectroscopic transition probabilities for some of the intermediate chemical species spectroscopic observations of the minor species was anticipated. The thermodynamic calculations outlined in Figures 1 to 14 indicate that a large number of intermediate species may be present under fuel-rich conditions. Such conditions would be expected to exist in the vicinity of the fuel droplet. For an oxidizer-rich combustion system the calculated distribution of combustion products is much less complex. Significant amounts of NO_2 would be predicted in the vicinity of an oxidizer droplet.

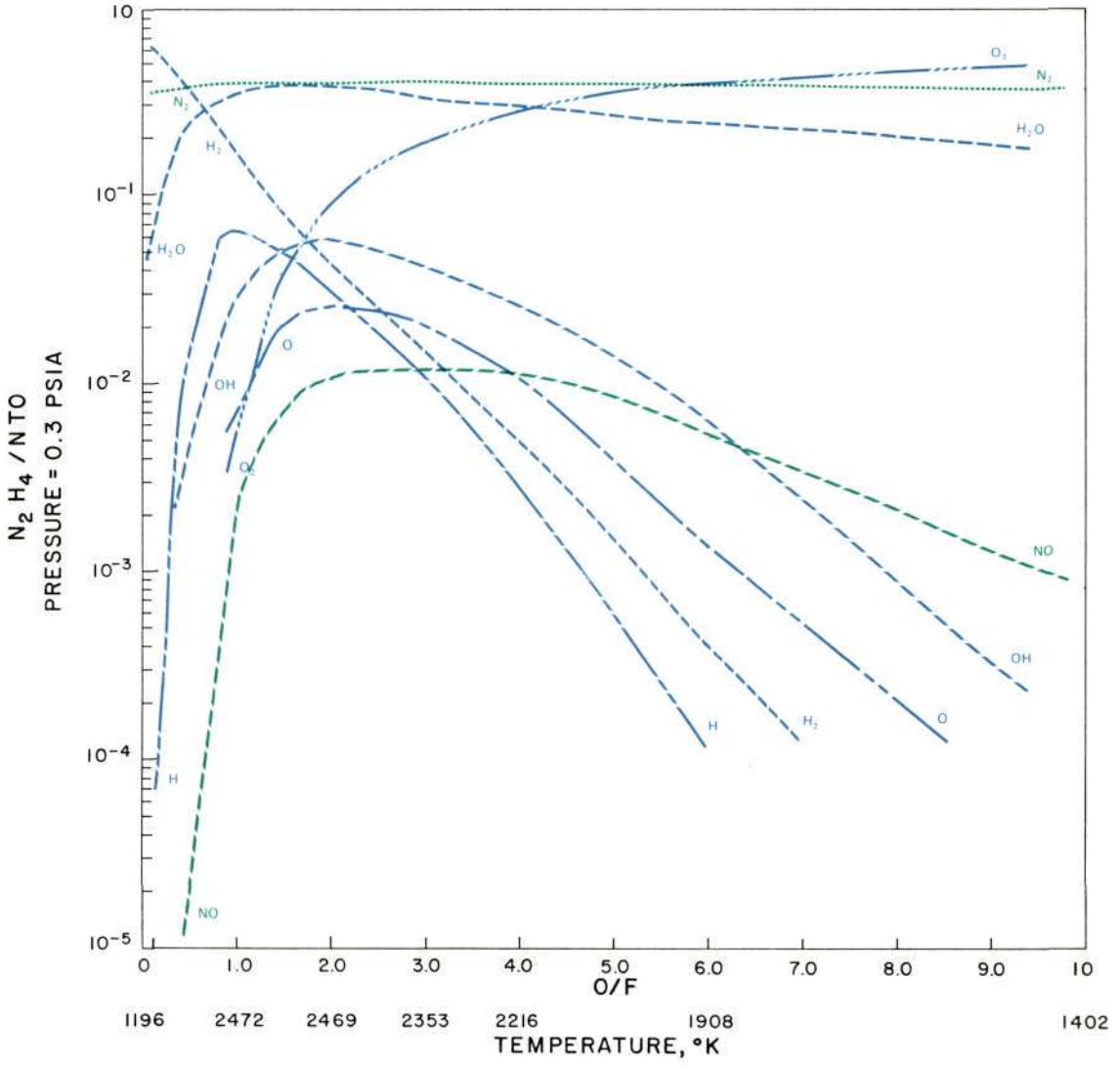
10
10^{-1}
10^{-2}
10^{-3}
10^{-4}
10^{-5}
N_2H_4 / NTO
PRESSURE = 0.3 PSIA
O_2
N_2
H_2O
H_2
OH
O
H
NO
0
1.0
2.0
3.0
4.0
5.0
6.0
7.0
8.0
9.0
10
O/F
1196
2472
2469
2353
2216
1908
1402
TEMPERATURE, °K

Figure 1

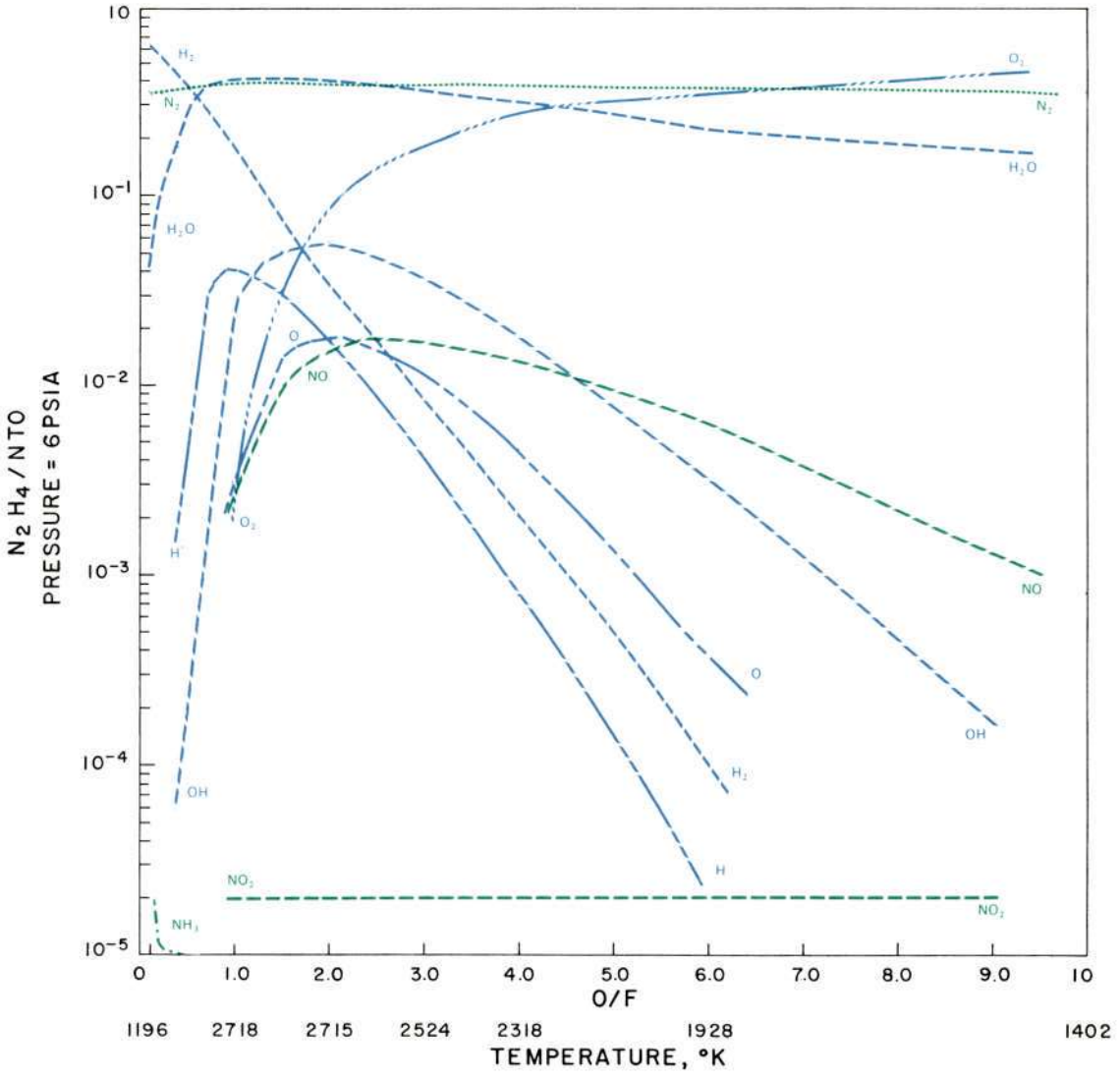
10
10^{-1}
10^{-2}
10^{-3}
10^{-4}
10^{-5}
N_2H_4 / NTO
PRESSURE = 6 PSIA
H_2
N_2
O_2
H_2O
OH
O
NO
H
NO_2
NH_3
0
1.0
2.0
3.0
4.0
5.0
6.0
7.0
8.0
9.0
10
O/F
1196
2718
2715
2524
2318
1928
1402
TEMPERATURE, °K

Figure 2

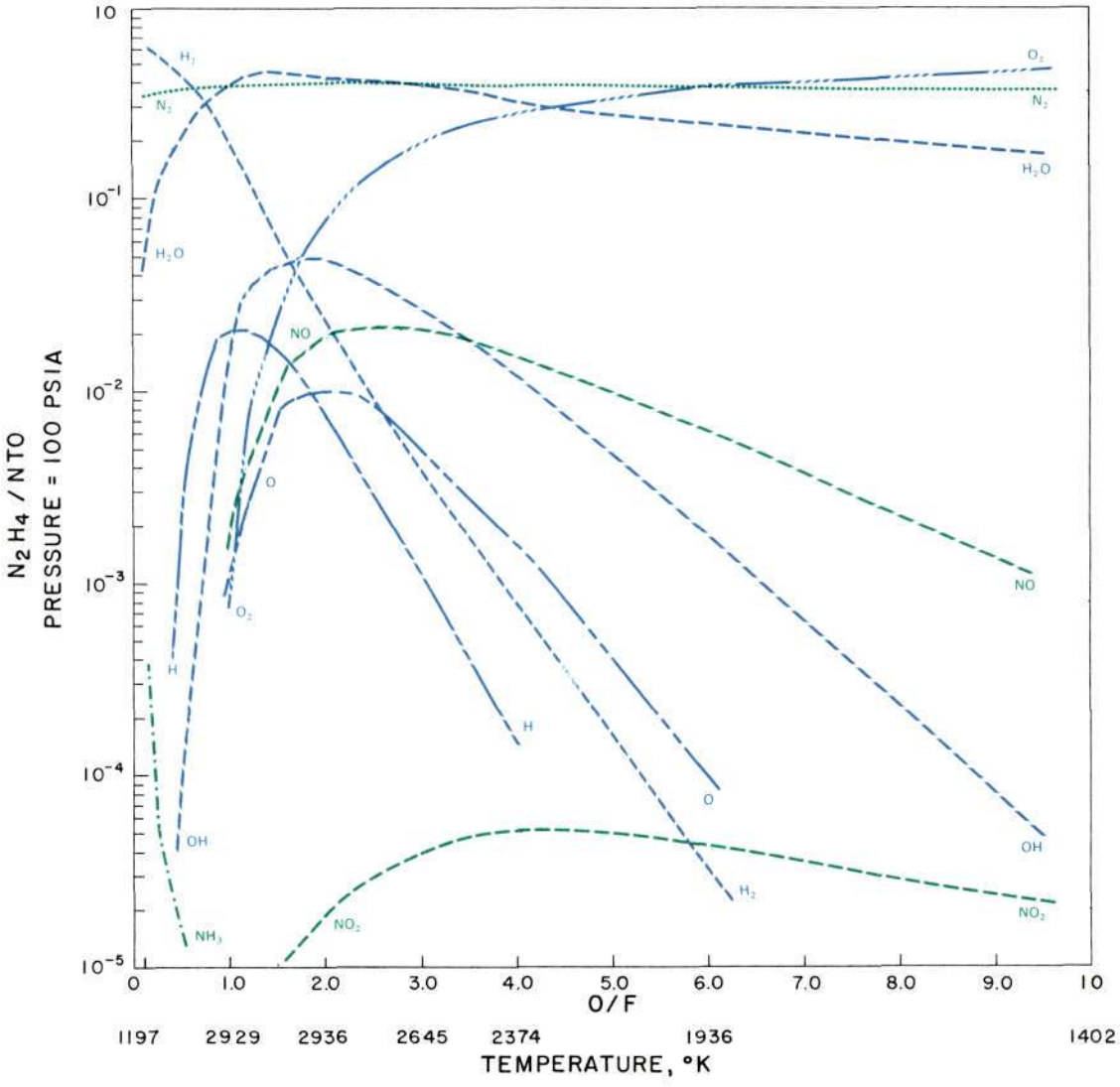
10
10^{-1}
10^{-2}
10^{-3}
10^{-4}
10^{-5}
N_2H_4 / NTO
PRESSURE = 100 PSIA
H_2
N_2
O_2
H_2O
NO
O
H
OH
NH_3
NO_2
0
1.0
2.0
3.0
4.0
5.0
6.0
7.0
8.0
9.0
10
O/F
1197
2929
2936
2645
2374
1936
1402
TEMPERATURE, °K

Figure 3

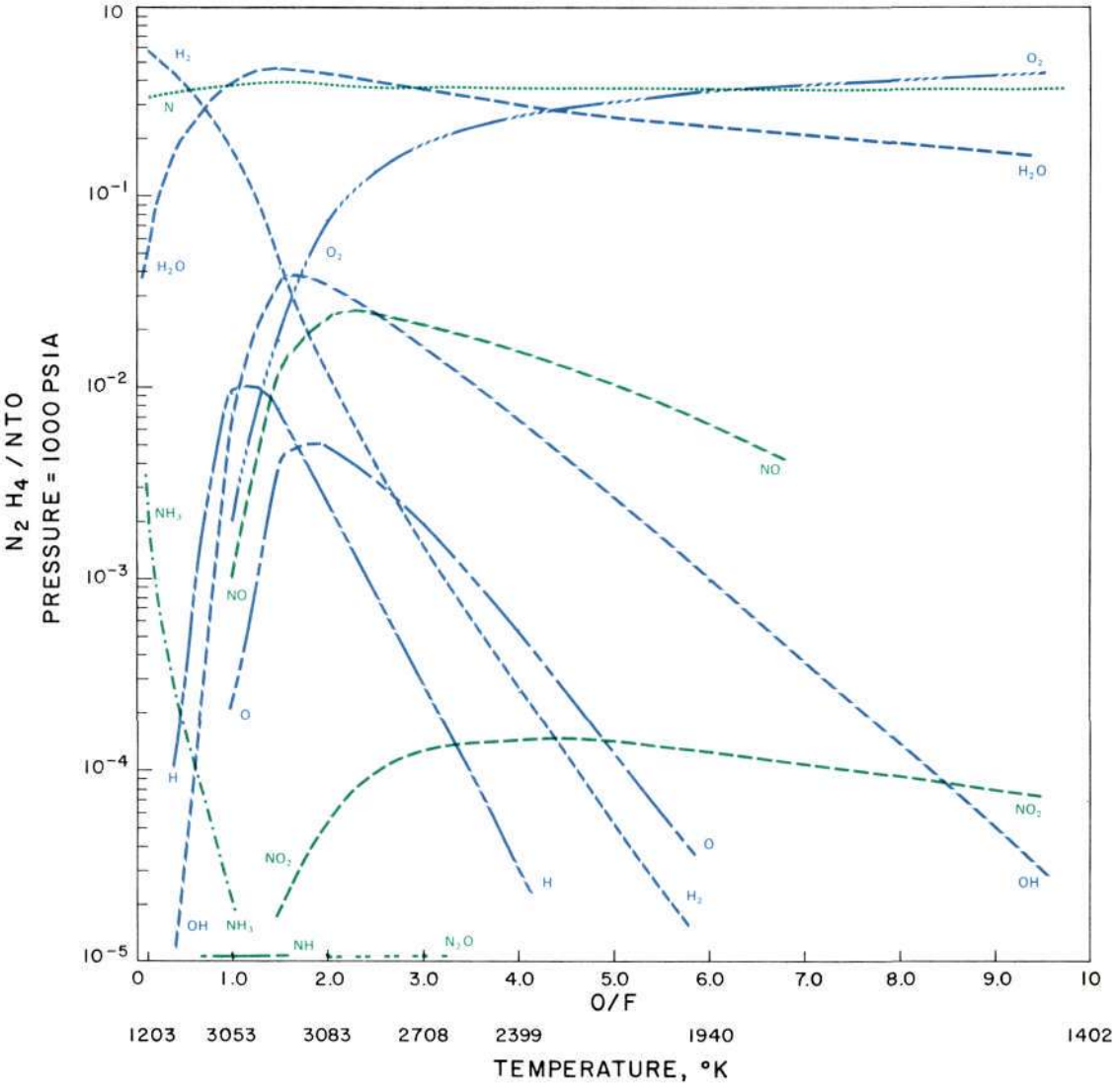
10
10^{-1}
10^{-2}
10^{-3}
10^{-4}
10^{-5}
N_2H_4 / NTO
PRESSURE = 1000 PSIA
H_2
N
H_2O
O_2
NO
NH_3
O
H
NO_2
OH
NH
N_2O
0
1.0
2.0
3.0
4.0
5.0
6.0
7.0
8.0
9.0
10
O/F
1203
3053
3083
2708
2399
1940
1402
TEMPERATURE, °K

Figure 4

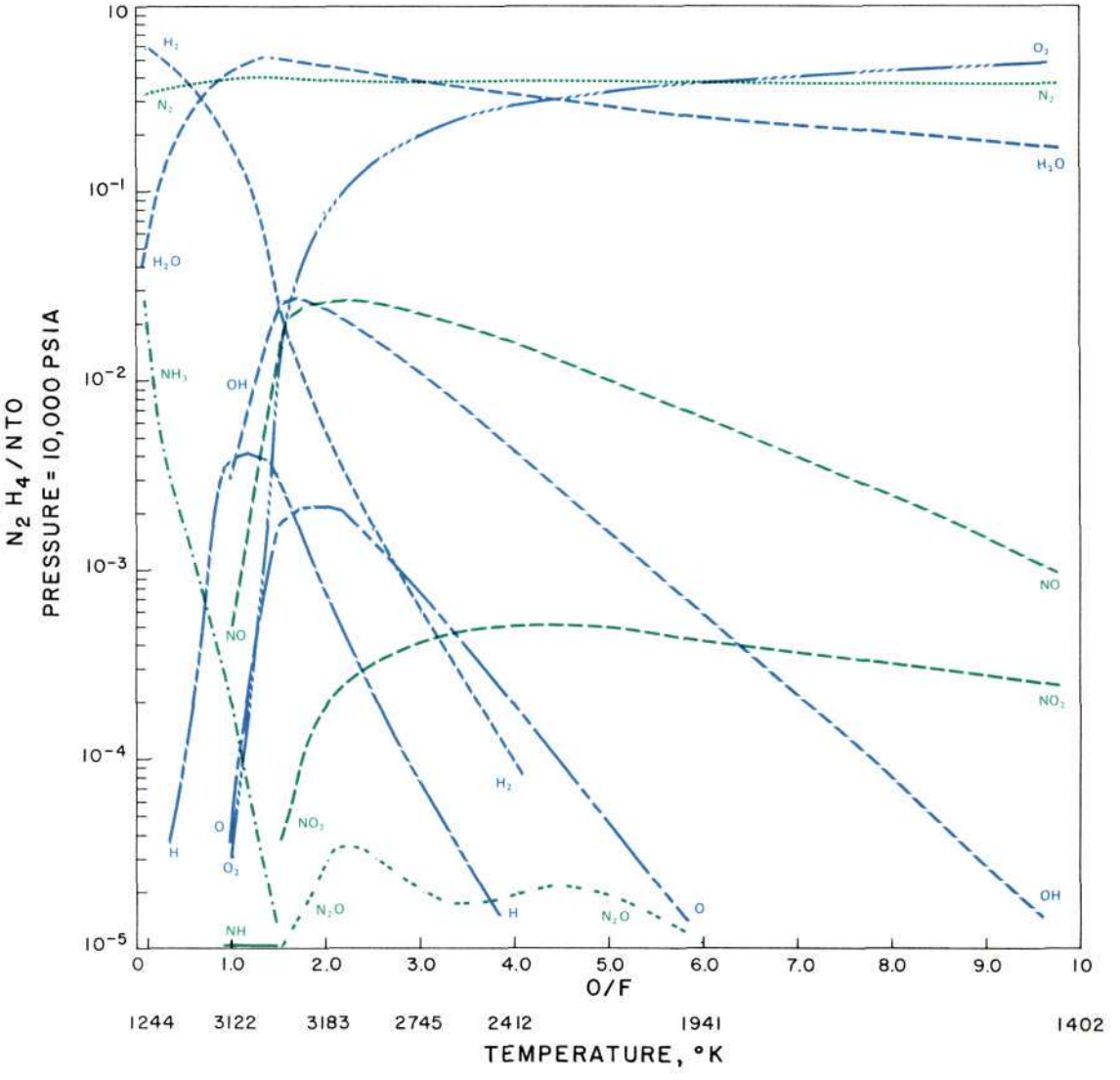
N_2H_4 / NTO
PRESSURE = 10,000 PSIA
10
10^{-1}
10^{-2}
10^{-3}
10^{-4}
10^{-5}
H_2
N_2
O_2
H_2O
NH_3
OH
NO
NO_2
H
O
O_2
NH
N_2O
H_2
H
O
N_2O
NO
NO_2
OH
0
1.0
2.0
3.0
4.0
5.0
6.0
7.0
8.0
9.0
10
O/F
1244
3122
3183
2745
2412
1941
1402
TEMPERATURE, °K

Figure 5

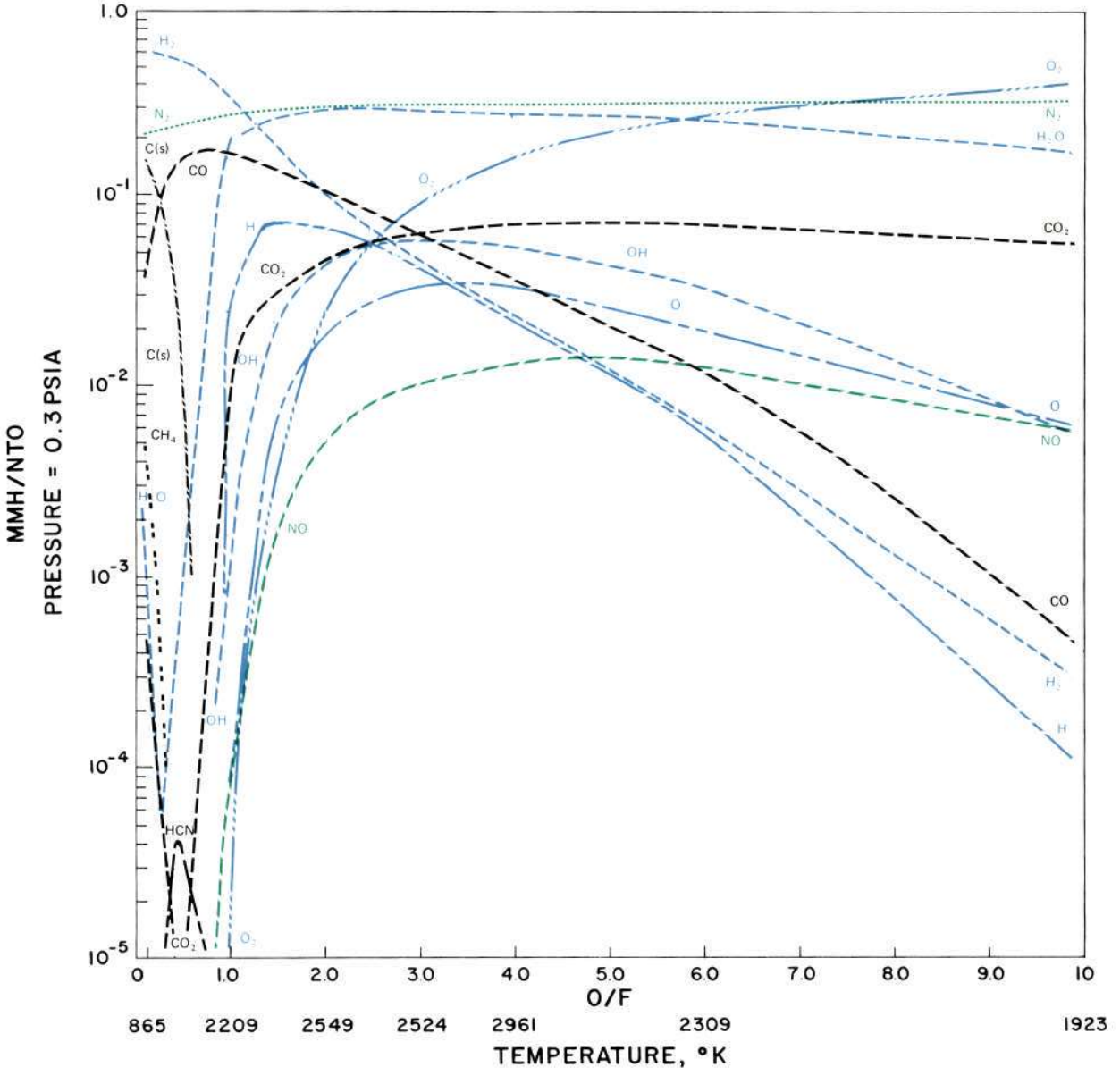
MMH/NTO
PRESSURE = 0.3 PSIA
1.0
10^{-1}
10^{-2}
10^{-3}
10^{-4}
10^{-5}
H_2
N_2
C(s)
CO
O_2
H
CO_2
OH
O
C(s)
CH_4
H_2O
NO
OH
HCN
CO_2
O_2
O_2
N_2
H_2O
CO_2
O
NO
CO
H_2
H
0
1.0
2.0
3.0
4.0
5.0
6.0
7.0
8.0
9.0
10
O/F
865
2209
2549
2524
2961
2309
1923
TEMPERATURE, °K

Figure 6

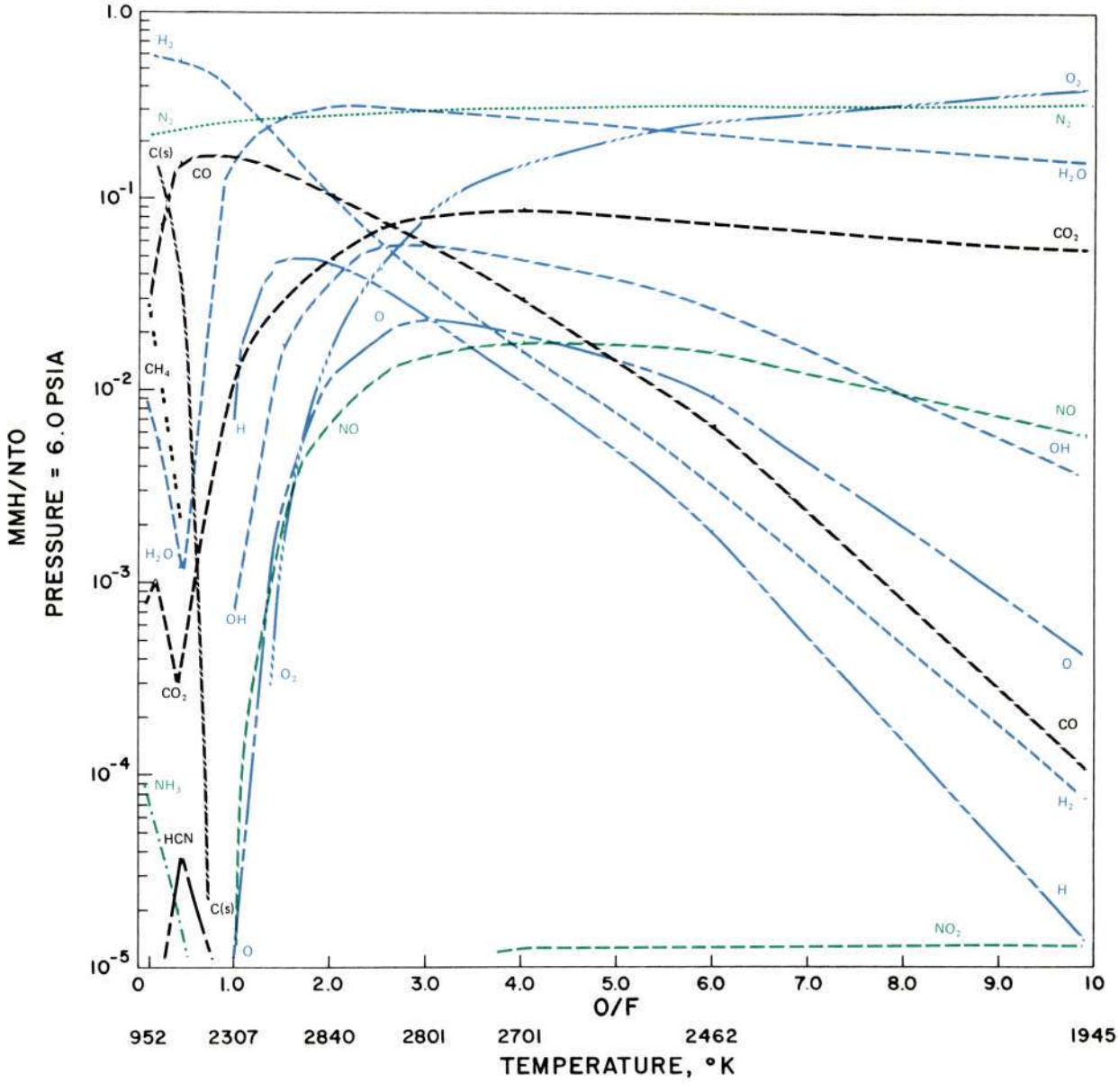
MMH/NTO
PRESSURE = 6.0 PSIA
1.0
10^{-1}
10^{-2}
10^{-3}
10^{-4}
10^{-5}
H_2
N_2
C(s)
CO
CH_4
H_2O
CO_2
NH_3
HCN
C(s)
OH
H
O
NO
O_2
O
O_2
N_2
H_2O
CO_2
NO
OH
O
CO
H_2
H
NO_2
0
1.0
2.0
3.0
4.0
5.0
6.0
7.0
8.0
9.0
10
O/F
952
2307
2840
2801
2701
2462
1945
TEMPERATURE, °K

Figure 7

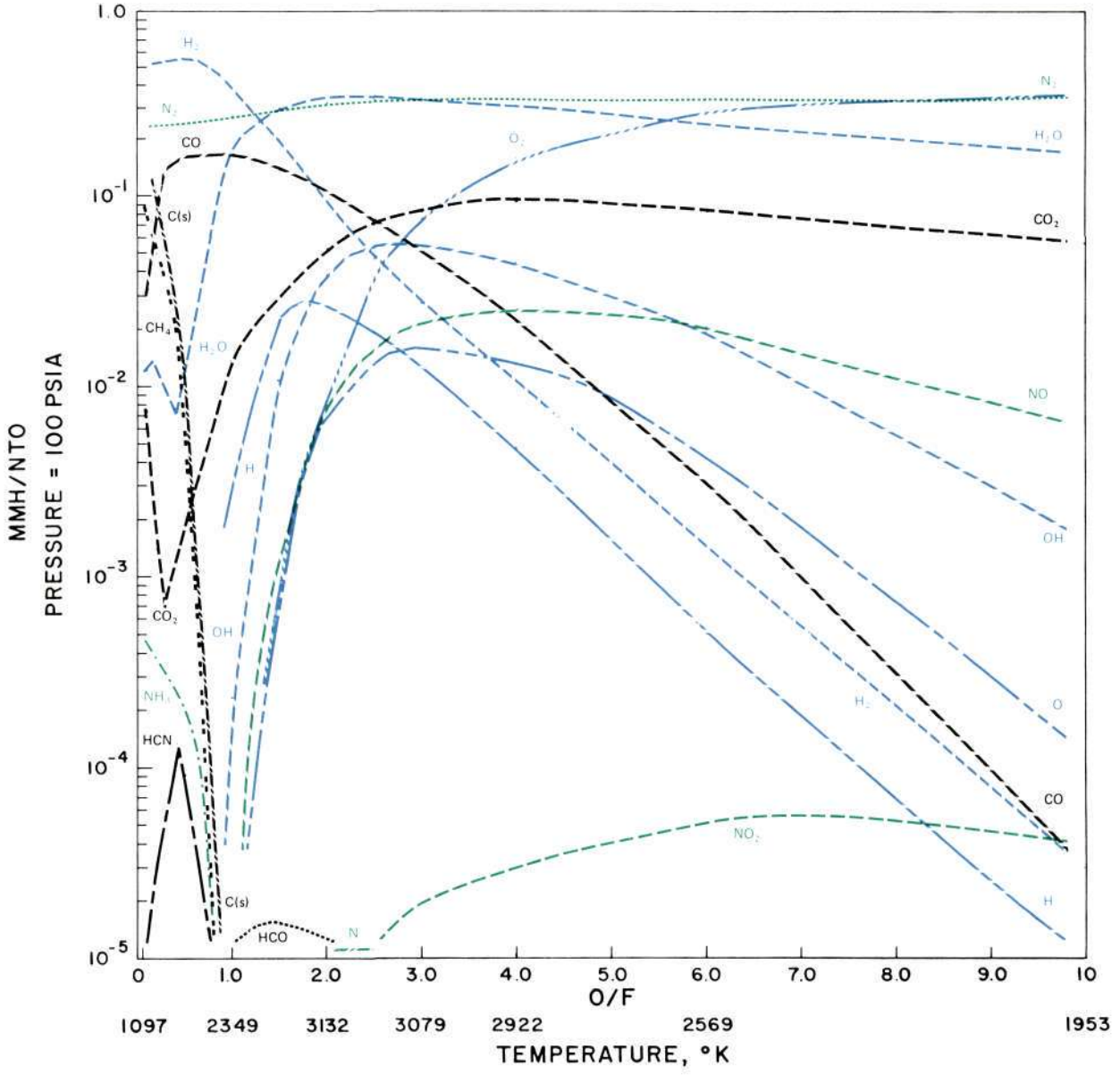
MMH/NTO
PRESSURE = 100 PSIA
1.0
10^{-1}
10^{-2}
10^{-3}
10^{-4}
10^{-5}
H_2
N_2
CO
C(s)
CH_4
H_2O
CO_2
OH
NH_3
HCN
C(s)
HCO
N
H
O_2
NO
NO_2
O
H_2
0
1.0
2.0
3.0
4.0
5.0
6.0
7.0
8.0
9.0
10
O/F
1097
2349
3132
3079
2922
2569
1953
TEMPERATURE, °K

Figure 8

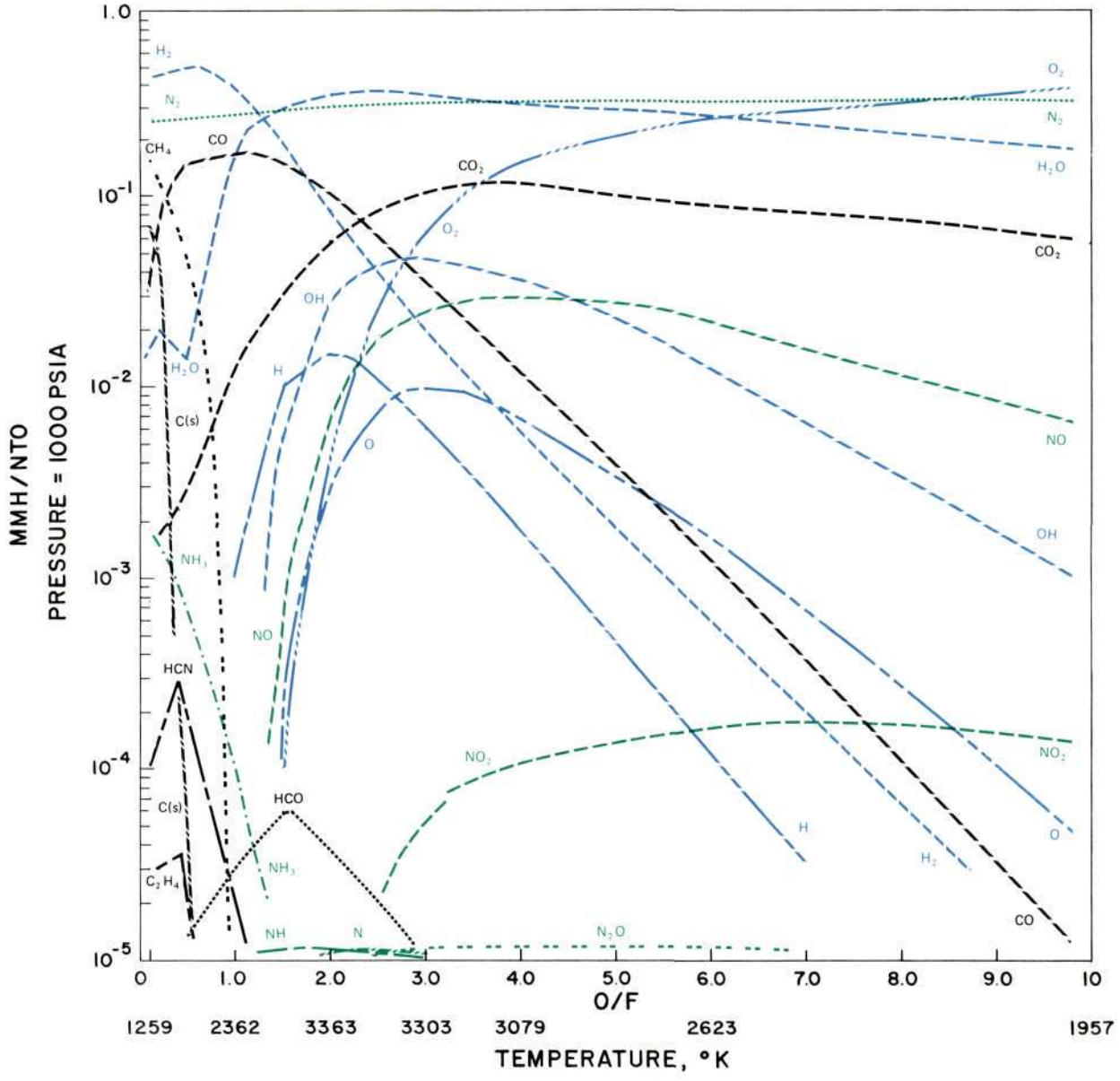
MMH / NTO
PRESSURE = 1000 PSIA
1.0
10^{-1}
10^{-2}
10^{-3}
10^{-4}
10^{-5}
H_2
N_2
CH_4
CO
CO_2
O_2
H_2O
C(s)
OH
H
O
NO
NH_3
HCN
HCO
C_2H_4
NH
N
N_2O
NO_2
0
1.0
2.0
3.0
4.0
5.0
6.0
7.0
8.0
9.0
10
O/F
1259
2362
3363
3303
3079
2623
1957
TEMPERATURE, °K

Figure 9

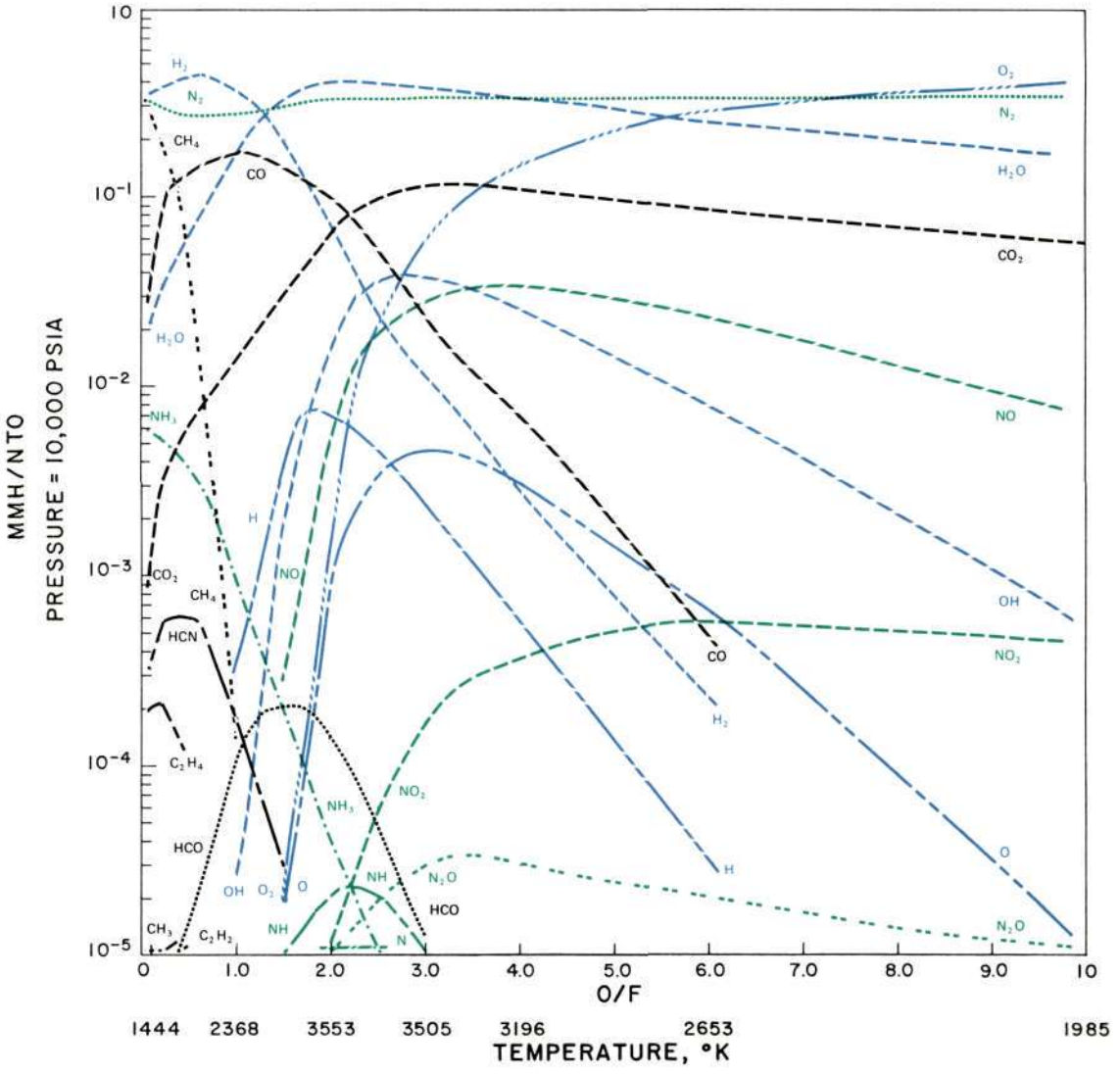
MMH/NTO
PRESSURE = 10,000 PSIA
10
10^{-1}
10^{-2}
10^{-3}
10^{-4}
10^{-5}
H_2
N_2
CH_4
CO
O_2
H_2O
CO_2
NO
OH
NO_2
H
HCN
C_2H_4
HCO
NH
NH_3
N_2O
N
O
CH_3
C_2H_2
0
1.0
2.0
3.0
4.0
5.0
6.0
7.0
8.0
9.0
10
O/F
1444
2368
3553
3505
3196
2653
1985
TEMPERATURE, °K

Figure 10

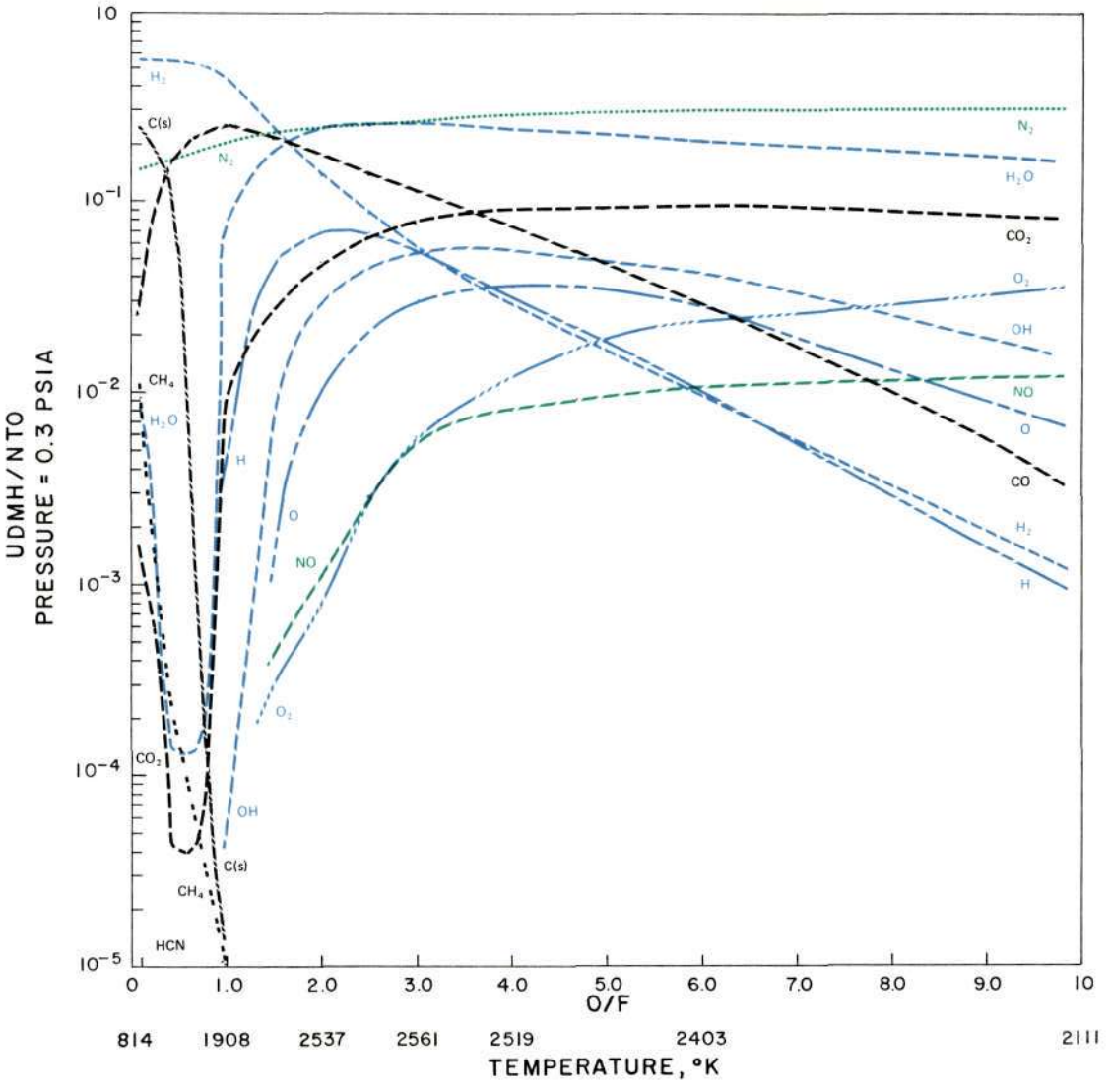
UDMH / NTO
PRESSURE = 0.3 PSIA
10
10^{-1}
10^{-2}
10^{-3}
10^{-4}
10^{-5}
H_2
C(s)
N_2
CH_4
H_2O
CO_2
HCN
H
O
NO
OH
O_2
N_2
H_2O
CO_2
O_2
OH
NO
O
CO
H_2
H
0
1.0
2.0
3.0
4.0
5.0
6.0
7.0
8.0
9.0
10
O/F
814
1908
2537
2561
2519
2403
2111
TEMPERATURE, °K

Figure 11

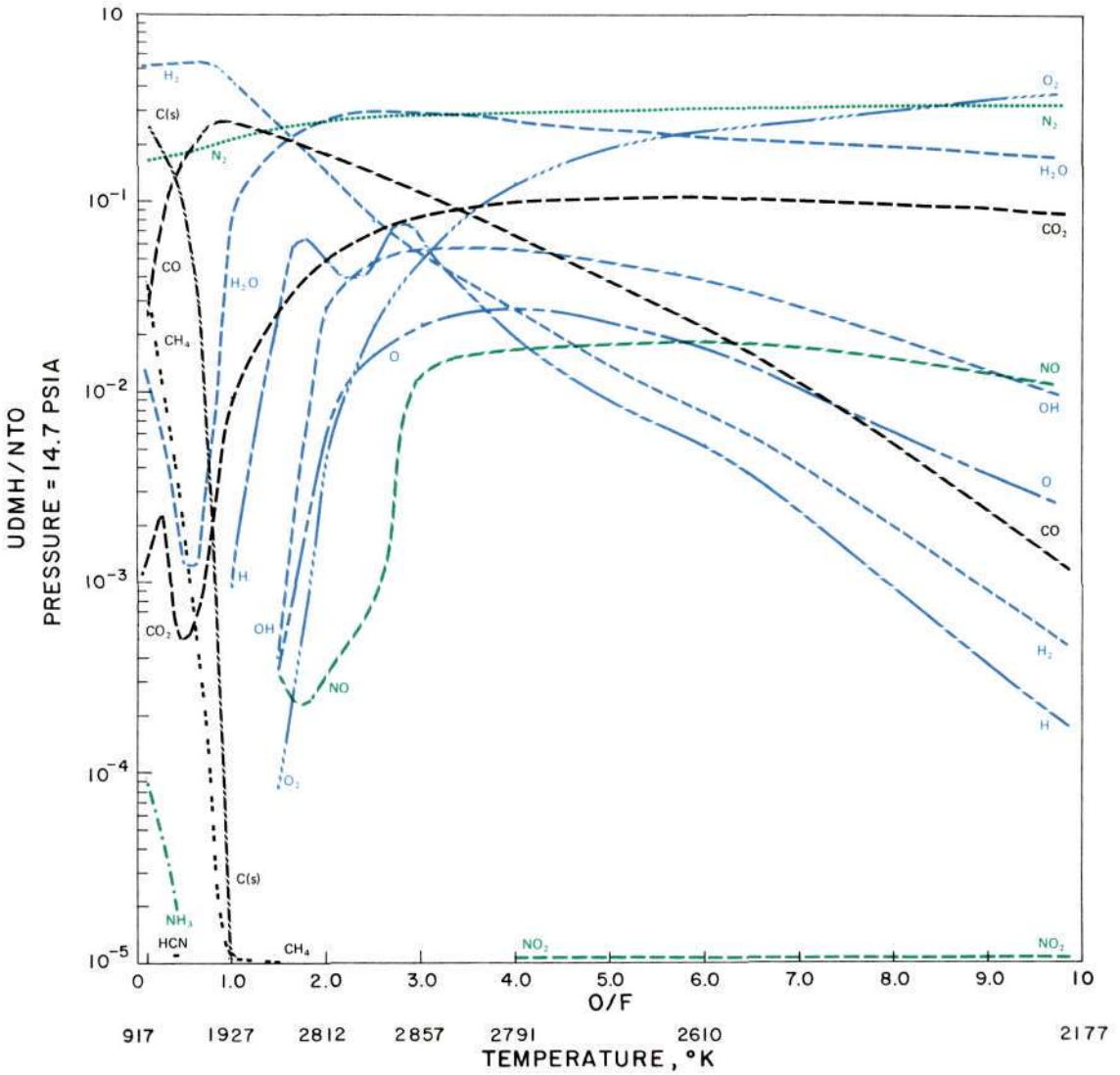
UDMH / NTO
PRESSURE = 14.7 PSIA
10
10^{-1}
10^{-2}
10^{-3}
10^{-4}
10^{-5}
H_2
C(s)
N_2
CO
H_2O
CH_4
CO_2
H
OH
NO
O
O_2
NH_3
HCN
CH_4
NO_2
O_2
N_2
H_2O
CO_2
NO
OH
O
CO
H_2
H
NO_2
0
1.0
2.0
3.0
4.0
5.0
6.0
7.0
8.0
9.0
10
O/F
917
1927
2812
2857
2791
2610
2177
TEMPERATURE, °K

Figure 12

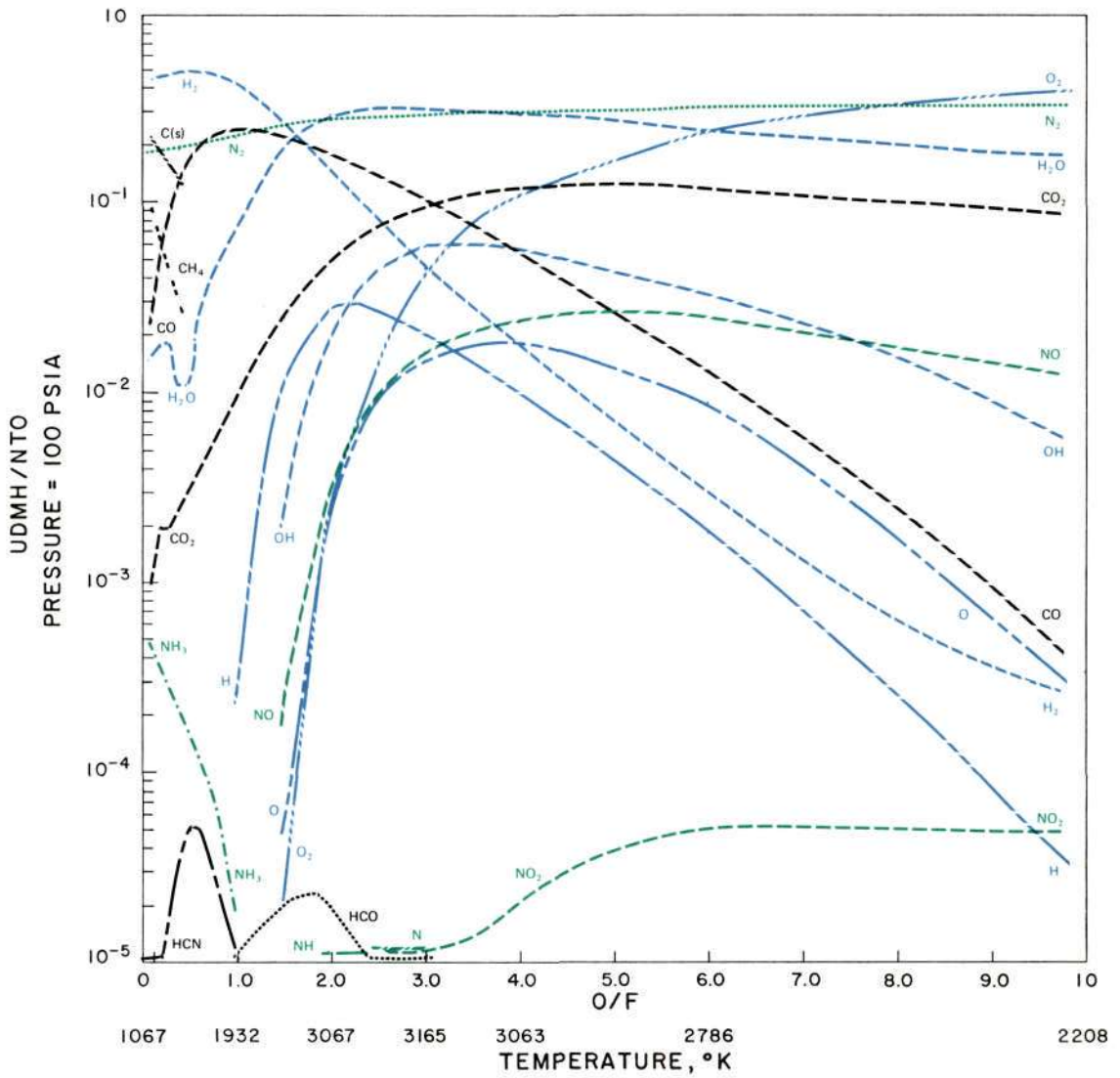
UDMH/NTO
PRESSURE = 100 PSIA
10
10^{-1}
10^{-2}
10^{-3}
10^{-4}
10^{-5}
H_2
C(s)
N_2
CH_4
CO
H_2O
CO_2
OH
H
NO
NH_3
O
O_2
HCN
HCO
NH
N
NO_2
O_2
N_2
H_2O
CO_2
NO
OH
O
CO
H_2
NO_2
H
0
1.0
2.0
3.0
4.0
5.0
6.0
7.0
8.0
9.0
10
O/F
1067
1932
3067
3165
3063
2786
2208
TEMPERATURE, °K

Figure 13

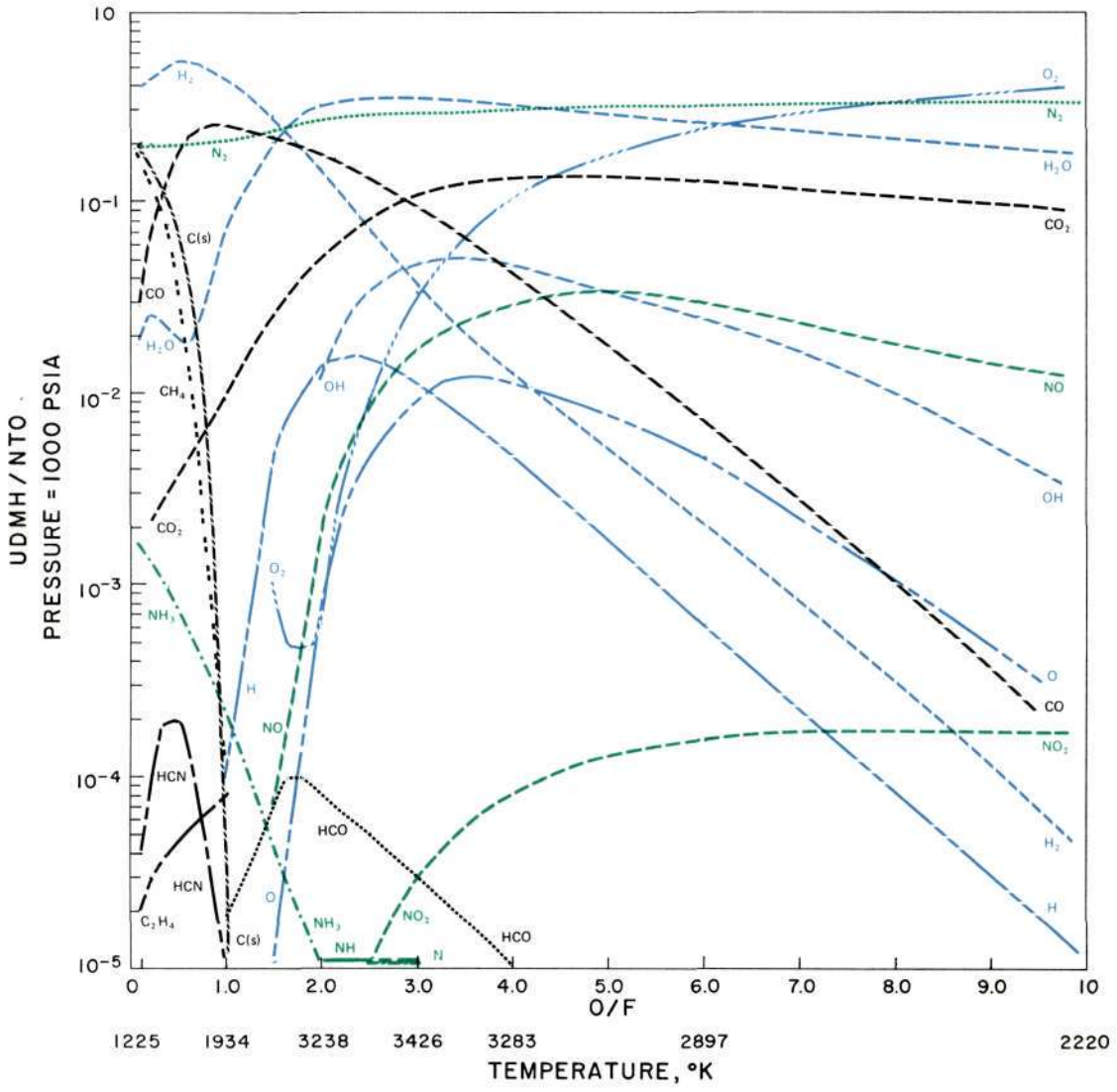
UDMH / NTO
PRESSURE = 1000 PSIA
10
10^{-1}
10^{-2}
10^{-3}
10^{-4}
10^{-5}
H_2
N_2
C(s)
CO
H_2O
CH_4
CO_2
NH_3
H
HCN
HCN
C_2H_4
C(s)
O_2
OH
NO
O
HCO
NH_3
NH
N
NO_2
HCO
O_2
N_2
H_2O
CO_2
NO
OH
O
CO
NO_2
H_2
H
0
1.0
2.0
3.0
4.0
5.0
6.0
7.0
8.0
9.0
10
O/F
1225
1934
3238
3426
3283
2897
2220
TEMPERATURE, °K

Figure 14

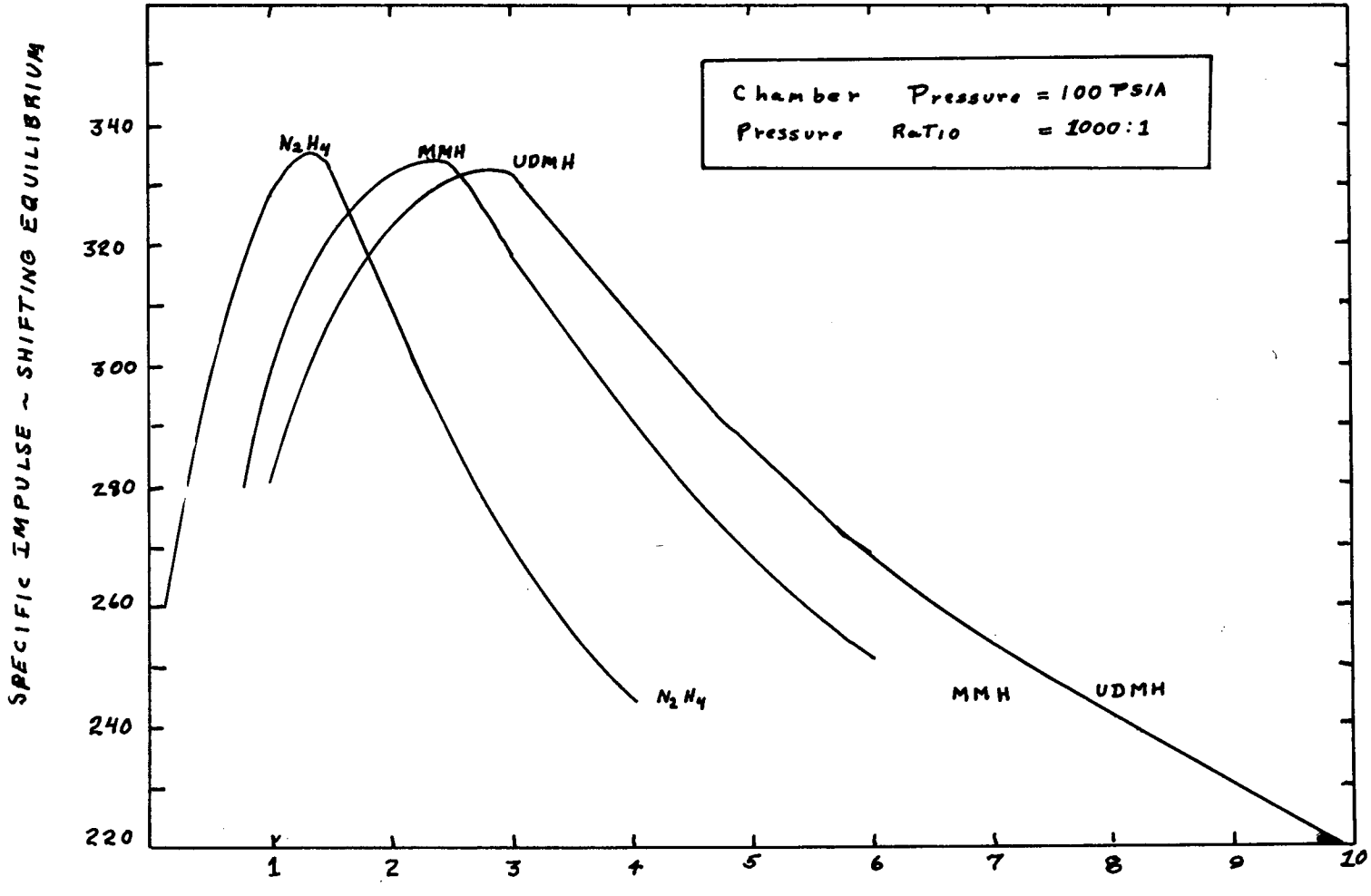

Figure 15. Calculated Specific Impulses Assuming Shifting Equilibrium

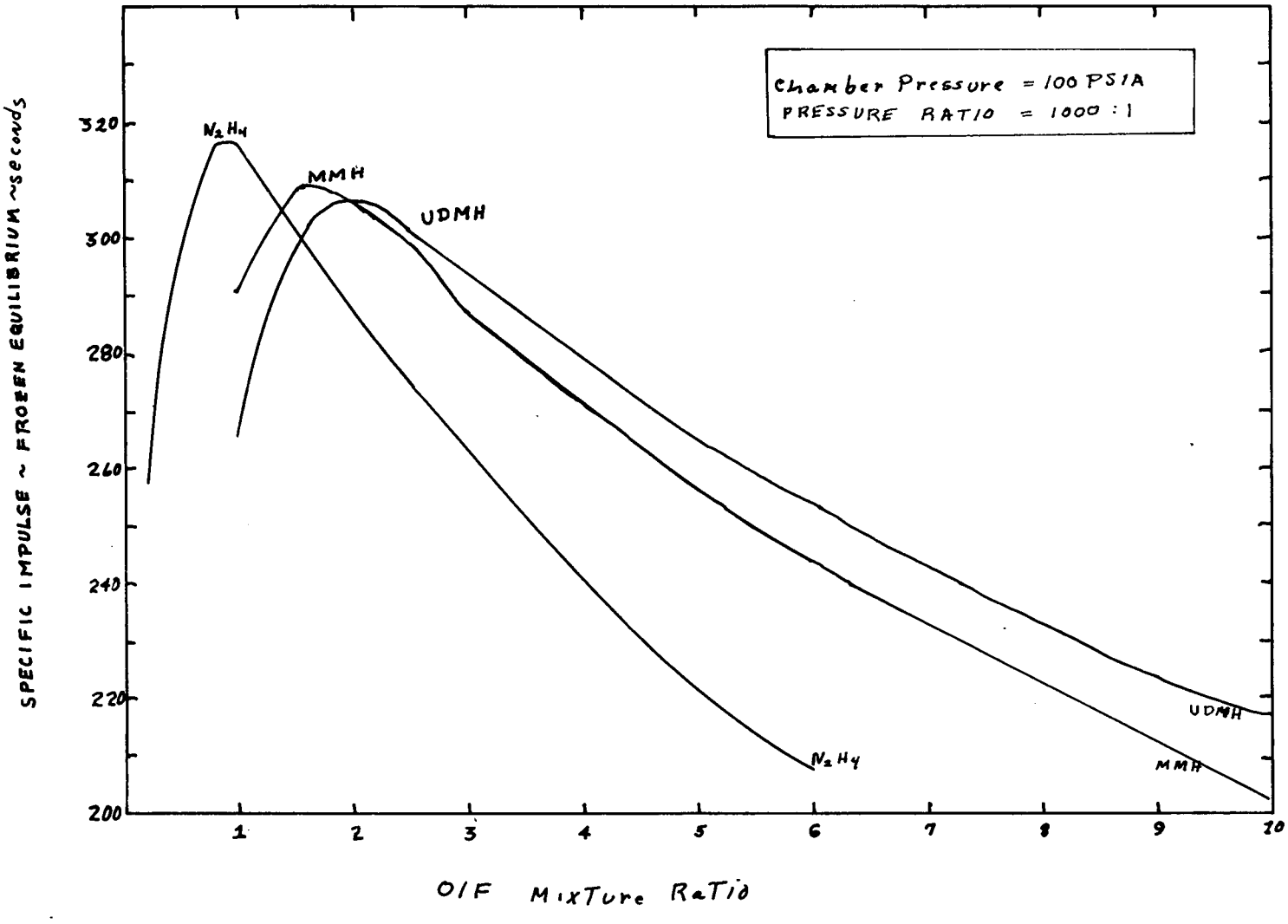

Figure 16. Calculated Specific Impulse from Equilibrium vs. O/F Mixture Ratio

III. MECHANISMS AND RATES OF CHEMICAL REACTIONS IN THE LIQUID AND GASEOUS PHASES.

3.1 Introduction

The thermodynamic analysis outlined in Section II provides a powerful tool for predicting the products formed during the ignition and combustion processes under equilibrium conditions. In the ignition of a pulse mode engine, kinetic factors such as the rate of injection, flash vaporization, mixing and chemical reaction rates strongly modify such thermodynamic analyses.

It is useful to review the reported chemical reaction mechanisms involving the decomposition of nitrogen tetroxide and hydrazine, since many of the expected phenomena are attributable to the formation of metastable chemical intermediates which would not be formed if equilibrium conditions were present. These reaction mechanisms have been studied by a number of individual investigators [10 - 13]. One of the more comprehensive summaries of the rates of individual reactions associated with the oxidation of N_2H_4 by NO_2 is given by Sawyer[11]. In this summary, previous work in the field is reviewed, as well as data from a stirred flow reactor developed at Princeton [12]. The Princeton work can be interpreted that the reduction of NO_2 occurs as a two-step process in which the first step is a reduction of NO_2 to NO. The overall reaction mechanism suggested by Sawyer, based on experimental results from the stirred flow reactor, indicated a first order dependence with respect to the concentrations of both N_2H_4 and NO_2 for the formation of NO. NO remains as a stable product for a relatively long period of time and subsequently reacts further to form N_2 and H_2O.

Since the reaction delay for this second step is of the same order as the entire pulse-mode engine firing period, emphasis in the present review is placed on the first stage reduction step of this reaction sequence.

3.2 Liquid Phase Reactions

Liquid phase reactions between N_2O_4 and N_2H_4 have also been investigated [14]. Because of the extreme reactivity of this chemical system, the development of liquid phase study methods has been exceedingly difficult. Therefore, most of the recent investigators in the field of propulsion have assumed (rather than identified) the reaction products and have emphasized the effects of heat addition on rates of evaporation of liquid droplets. Because the currently assumed reaction mechanisms used to describe the thermal effects are somewhat doubtful, emphasis in this section is placed on a review of important liquid phase chemical reactions. Of significance is the Curtius reaction

$$N_2H_5^+ + HNO_2 \longrightarrow HN_3 + H^+ + H_2O$$

which suggests that hydrogen azide would be produced. Also, it is noted that the oxidation of hydrazine by an oxidizing agent containing nitrogen usually produces HN_3. Therefore, this review indicates that HN_3, $N_2H_5H_3$ and $H_2H_5^+ \cdot NO_3^-$ would be expected products of reaction for liquid phase reactions occurring either in very dilute reaction mixtures, or at low reaction temperatures.

Perlee and coworkers [3], have identified hydazinium nitrate as the primary explosive present in engine residues using infrared spectroscopy.

A verbal report from an in-house program at the Aerospace Corporation suggests that hydrazinium nitrite may also be present. From the point of view of gas phase reaction kinetics, hydrazinium nitrite would be expected to form in a direct bimolecular reaction between a collisionally stabilized HONO and a hydrazine molecule. This reaction would be expected to be reasonably efficient and to produce the $N_2H_5^+NO_2^-$ intermediate. The formation of the hydrazinium nitrate in the gas phase is more difficult to explain since it would require the production of HNO_3 at some point in the kinetic reaction chain. A possible mechanism for the formation of HNO_3 in the gas phase would be the reaction

$$HONO + NO_2 \rightarrow HONO_2 + NO$$

Although intermediate compounds of this type could form via a gas phase reaction mechanism and would subsequently condense, an alternative possibility is that hydrazinium nitrate forms in the liquid phase reaction between a major combustion product such as water, and condensed N_2O_4. Since an azide similar to hydrazoic acid was also found as a volatile reaction by Dauermann, et al, during a study of liquid phase reactions, it is necessary to develop a kinetic mechanism which can allow this formation to occur as a natural consequence of other reactions. A reaction scheme suggested as being reasonable involves the following sequence of reactions:

$$H_2O + N_2O_4 \rightarrow HNO_3 + HNO_3 \qquad (3.2\text{-}1)$$

$$H_2H_4 + HNO_3 \rightarrow N_2H_5^+ \cdot NO_3^- \qquad (3.2\text{-}2)$$

$$H_2H_5NO_3 + HNO_2 \rightarrow HN_3 + HNO_3 + 2H_2O \qquad (3.2\text{-}3)$$

$$HN_3 + N_2H_4 \rightarrow N_2H_5N_3 \qquad (3.2\text{-}4)$$

In this reaction sequence, (3.2-3) is the Curtius reaction. It is noted that two highly unstable compounds, HN_3 and $N_2H_5N_3$, are predicted. Direct chemical evidence for these two intermediate species is described in detail in a later section. One interesting feature of this mechanism is that two moles of hydrazinium nitrate would be formed for each mole of water or N_2O_4 consumed, which would suggest the formation of relatively large amounts of this intermediate product.

An alternative direct reaction between hydrazine and nitrogen tetroxide,

$$N_2H_4 + N_2O_4 \rightarrow NH_4NO_3 + N_2O + N_2 + H_2O \qquad (3.2\text{-}5)$$

may also occur. Support for this latter reaction is from a wet chemical analysis performed by Dauerman and infrared data obtained recently at the DFVRL in Germany. Since the NH_4^+ infrared peak is masked by other reaction products there is some doubt as to the product identification.

Hydrogen azide could disappear via Thiele's reaction:

$$N_3H + HNO_2 \rightarrow N_2 + N_2O + H_2O \qquad (3.2\text{-}6)$$

However, this requires a relatively high hydrogen ion concentration which is unlikely in this case because of the high percentage of unreacted hydrazine in the residue materials.

3.3 Mechanisms and Rates of Gas Phase Chemical Reactions

The kinetic mechanism proposed by Glassman and Sawyer[15] for the reaction between N_2H_4 and NO_2 involves a two-stage reduction of NO_2. The first step of this reduction is a reduction of NO_2 to NO which occurs at a fast rate. This is then followed by the subsequent further reduction of NO

to form N_2 and water. The stage II reduction occurs at a slow rate and in the flow reactor at Princeton was well separated from the stage I reduction. Since the ignition and combustion of a pulse-mode rocket engine will typically use a total hot firing cycle between 10 to 20 milliseconds the emphasis in this analysis will be placed on reaction involving stage I. It is assumed for this analysis that, both because of the short duration and because of the rapid quenching which occurs under space simulated rocket testing, the stage II reaction does not have time to proceed to completion.

The Glassman-Sawyer mechanism depends primarily upon the stripping of hydrogen atoms from N_2H_4 and N_2H_3 molecules. Studies by Gray and Thyne[16] of H-atom abstraction from N-H bond by CH_3 radicals demonstrate the susceptibility of hydrazine to attack. They found hydrazine to be 300 times more reactive than ammonia in this regard. Therefore, Glassman and Sawyer assumed that the initial step involved the abstraction of hydrogen from hydrazine to form HONO which subsequently decomposes to form OH and NO. A series of further abstraction was then followed, as outlined in the following reaction sequence:

$$N_2H_4 + NO_2 \xrightarrow{k1} N_2H_3 + HONO \qquad (3.3\text{-}1)$$

$$HONO \xrightarrow{k2} OH + NO \qquad (3.3\text{-}2)$$

$$N_2H_3 + NO_2 \xrightarrow{k3} N_2H_2 + HONO \qquad (3.3\text{-}3)$$

$$N_2H_4 + OH \xrightarrow{k4} N_2H_3 + H_2O \qquad (3.3\text{-}4)$$

$$N_2H_3 + OH \xrightarrow{k5} N_2H_2 + H_2O \qquad (3.3\text{-}5)$$

Additional hydrogen abstraction reaction by atomic hydrogen

$$N_2H_4 + H \rightarrow N_2H_3 + H_2 \qquad (3.3\text{-}6)$$

$$N_2H_3 + H \rightarrow N_2H_2 + H_2 \qquad (3.3\text{-}7)$$

and termination reactions

$$N_2H_2 \longrightarrow N_2 + H_2 \qquad (3.3\text{-}8)$$

$$H_2 + OH \longrightarrow H_2O + H_2 \qquad (3.3\text{-}9)$$

$$NO_2 + H \longrightarrow OH + NO \qquad (3.3\text{-}10)$$

were other reactions also postulated by these authors.

Taking a simplified model based on the reactions (3.3-1) - (3.3-5) are assumed to be rate controlling, and then making the usual steady state assumption which is required by the principle of detailed balancing, the concentrations of the intermediates are found to be given by the following expressions:

$$[OH] = \left(\frac{k_1 k_3}{k_4 k_5}\right)^{\frac{1}{2}} [NO_2] \qquad (3.3\text{-}11)$$

$$[N_2H_3] = \left(\frac{k_1 k_4}{k_3 k_5}\right)^{\frac{1}{2}} [N_2H_4] \qquad (3.3\text{-}12)$$

$$[HONO] = \left\{\frac{k_1 + \left(\frac{k_1 k_3 k_4}{k_5}\right)^{\frac{1}{2}}}{k_2}\right\} [NO_2] \quad [N_2H_4] \qquad (3.3\text{-}13)$$

The reaction rate for hydrazine is then

$$\frac{d\,[N_2H_4]}{dt} = -\left\{k_1 + \left(\frac{k_1 k_3}{k_4 k_5}\right)^{\frac{1}{2}}\right\} [NO_2] \quad [N_2H_4] \qquad (3.3\text{-}14)$$

which has a first order dependence on both hydrazine and nitrogen dioxide. This first order dependence was observed in the stirred flow reactor at Princeton, which confirmed the proposed mechanism.

A rate expression for NO_2 comsumption can be developed

$$\frac{d\,[NO_2]}{dt} = \left\{\frac{k_1 + \left(k_1 k_3 k_4\right)^{\frac{1}{2}}}{k_5}\right\} [NO_2] \quad [N_2H_4] \qquad (3.3\text{-}15)$$

which exhibts a first order dependence with respect to the initial reactants. Again the type of dependence was observed experimentally in the stirred flow reactor and tended to confirm the mechanisms. Similarly the rate expression for nitric oxide buildup is given by

$$\frac{d\,[NO]}{dt} = k_2\,[HONO] = \left\{ k_1 + \left\{ \frac{k_1 k_3 k_4}{k_5} \right\}^{\frac{1}{2}} \right\} [NO_2]\,[N_2H_4] \qquad (3.3\text{-}16)$$

which is again first order with respect to both reactants. From available rate data this formulation appears to hold for high temperature, high pressure reaction systems.

In the above scheme it is interesting to note that no account is taken of the termination reaction $N_2H_2 \longrightarrow N_2 + H_2$ which Glassman and Sawyer suggest. If we assume that this dissociation reaction does not proceed to completion but that rather a condensation occurs

$$x N_2H_2 \longrightarrow (N_2H_2)_x \qquad (3.3\text{-}17)$$

then $(N_2H_2)_x$ would appear in the condensed phase as a stable product. The kinetic expression for its formation is

$$\frac{d\,[N_2H_2]}{dt} = k_3\,[N_2H_3]\,[NO_2] + k_5\,[N_2H_3]\,[OH] \qquad (3.3\text{-}18)$$

$$\frac{d\,[N_2H_2]}{dt} = \left\{ \frac{(k_3 k_1 k_4)^{\frac{1}{2}}}{k_5} + k_1 \right\} [N_2H_4]\,[NO_2] \qquad (3.3\text{-}19)$$

which is also first order with respect to NO_2 and N_2H_4. This expression is identical to that for the consumption of NO_2, indicating that the rate of formation of an explosive intermediate can also be correlated with the first order consumption of either of the reactants. This buildup would be expected

to occur more readily at low temperatures, since the termination reaction (3.3-8) must involve either a four-center decomposition or a hydrogen transfer followed by a three-center reaction. Data from the stirred flow reactor cannot discriminate between a termination and condensation reaction by following the reactant decay rates unless a plot of temperature vs. energy released is also available.

Low temperature conditions exist during the vacuum ignition of a rocket motor, and therefore it is predicted that substantial N_2H_2 could be formed during the preignition phase. Polymerization of N_2H_2 to form $(NH)_x$, (where $x > 2$), produces triazene and tetrazene derivatives. Therefore, it is predicted that such compounds could be formed by gas phase preignition reactions. Evidence for such intermediates has been found in the liquid residue from rocket engines during this program. Data from the stirred flow reactor cannot discriminate as to whether this polymerization is occurring.

At low pressure, reaction (3.3-2) is favored. However, in the reactions where local pressures may be high, collisional stabilization to form nitrous acid would be expected.

$$HONO^* \longrightarrow HONO \qquad (3.3\text{-}20)$$

If we assume that nitrous acid is collisionally stabilized, a simplified Glassman-Sawyer reaction mechanism results.

$$N_2H_4 + NO_2 \longrightarrow N_2H_3 + HONO \qquad (3.3\text{-}1)$$

$$N_2H_3 + NO_2 \longrightarrow N_2H_2 + HONO \qquad (3.3\text{-}3)$$

$$N_2H_4 + OH \longrightarrow N_2H_3 + H_2O \qquad (3.3\text{-}4)$$

$$N_2H_3 + OH \longrightarrow N_2H_2 + H_2O \qquad (3.3\text{-}5)$$

In this simplified mechanism HONO and N_2H_2 are considered as stable end products formed during the preignition period of operation. Using the steady state assumption

$$\frac{d\left[N_2H_3\right]}{dt} = 0 = k_1\left[N_2H_4\right]\left[NO_2\right] - k_2\left[N_2H_3\right]\left[NO_2\right] \qquad (3.3\text{-}21)$$

the rate of reactant consumption becomes

$$\frac{d\left[N_2H_4\right]}{dt} = -k_1\left[N_2H_4\right]\left[NO_2\right] \qquad (3.3\text{-}22)$$

$$\frac{d\left[NO_2\right]}{dt} = -2k_1\left[N_2H_4\right]\left[NO_2\right] \qquad (3.3\text{-}23)$$

for the fuel and the oxidizer respectively. This simplified mechanism can be extended to provide a basis for the formation of NO and H_2O by two consecutive hydrogen abstractions by NO_2 involving either (3.3-1) or (3.3-3) followed by

$$HONO + N_2H_4 \xrightarrow{k_6} H_2ONO + N_2H_3 \qquad (3.3\text{-}24)$$

$$HONO + N_2H_4 \xrightarrow{k_7} H_2ONO + N_2H_2 \qquad (3.3\text{-}25)$$

$$H_2ONO \xrightarrow{k_8} H_2O + NO. \qquad (3.3\text{-}26)$$

An analysis of this scheme shows the same first order dependence that was present in the G-S mechanism.

A third mechanism involves the stabilization of HNO intermediates by the following series of reactions

$$N_2H_4 + NO_2 \longrightarrow HONO + N_2H_3 \qquad (3.3\text{-}1)$$

$$HONO \longrightarrow NO + OH \qquad (3.3\text{-}2)$$

$$NO + N_2H_4 \longrightarrow HNO^* + N_2H_3 \qquad (3.3\text{-}27)$$

with the HNO* becoming stabilized. Evidence for this type of stabilization is the observation of (HNO) emission spectra and the presence of $(HNO)_x$ infrared absorption bands in the condensed residues. Although this radical is unstable it has an upper state electronic "lifetime" of about 0.1 second which is an order of magnitude longer than the pulse-mode combustion process. For this reason it would be possible to form substantial quantities of $(HNO)_x$ under the reaction conditions present in the pulsed rocket engine.

As described later, during the high altitude simulation tests the nitrogen tetroxide forms a fine mist whereas the fuel stream remains as an integral liquid jet. This process results in a high concentration of $NO_2(g)$ surrounding the fuel droplets. As the fuel droplets evaporate, a stepwise hydrogen abstraction can occur resulting in the possibility of completely stripping hydrogen from the hydrazine.

$$N_2H_2 + NO_2 \xrightarrow{k_8} HONO + N_2H \qquad (3.3\text{-}28)$$

$$N_2H + NO_2 \xrightarrow{k_9} N_2 + HONO \qquad (3.3\text{-}29)$$

$$N_2H + N_2H_2 \xrightarrow{k_{10}} N_4H_3 \qquad (3.3\text{-}30)$$

This suggests that an oxidizer lead could lead to the production of complex gas phase azide compounds. Experimental evidence for such compounds was found in chemical analyses of residues in this program.

3.4 Survey of Specific Rate Constants Available from Literature

A literature search was performed in order to document the range of specific rate constants that have been investigated for the gas phase reactions involving nitrogen tetroxide and hydrazine. Because of increased complexity and limitations in time a similar search was not performed for MDH and UDMH decomposition reaction. The results of this effort are contained in Appendix A for nitrogen tetroxide and hydrazine and their decomposition products.

The data is summarized by plotting the specific reaction rate constant vs. temperature for the forward reaction.* The units of the specific rate constant are: sec^{-1} for unimolecular reactions, $cm^3\text{-}mole^{-1}\text{-}sec^{-1}$ for bimolecular reactions, and $cm^6\text{-}mole^{-2}\text{-}sec^{-1}$ for termolecular reactions. In many cases, experimental variations of several orders of magnitude are reported. Since it was beyond the scope of this program to critically evaluate each of the reported references, the variations are reported without comment. It is perhaps instructive to note the wide variations as an example of the lack of precision and accuracy in the field of gas phase kinetic studies. In the case of gas phase reactions occurring during the combustion of a hypergolic liquid bipropellant rocket engine, further uncertainties are caused by lack of detailed knowledge of the development of spray size distribution and heterogeneous reaction kinetics.

*See Appendix (A)

NO_2 REDUCTION (1st Stage)

$$N_2H_4 + NO_2 \longrightarrow N_2H_3 + HONO$$

$$HONO \xrightarrow{M} OH + NO$$

$$N_2H_3 + NO_2 \longrightarrow N_2H_2 + HONO$$

$$N_2H_4 + OH \longrightarrow N_2H_3 + H_2O$$

$$N_2H_3 + OH \longrightarrow N_2H_2 + H_2O$$

Postulate

$$NO + N_2H_4 \longrightarrow HNO + N_2H_3$$

$$HNO \longrightarrow (HNO)_x$$

$$NO + N_2H_4 \longrightarrow NOH + N_2H_3$$

$$NOH \longrightarrow H_2N_2O_2$$

Figure 17. NO_2 Reduction Sequence.

HYDRAZINE DECOMPOSITION

$$N_2H_4 \xrightarrow{M} NH_2 + NH_2$$

$$N_2H_4 + NH_2 \longrightarrow N_2H_3 + NH_3$$

$$N_2H_3 \xrightarrow{M} NH_2 + NH$$

$$N_2H_3 + NH_2 \longrightarrow N_2H_2 + NH_3$$

$$N_2H_2 \longrightarrow N_2 + H_2$$

Postulate

$$N_2H_2 \longrightarrow (NH)_x \quad (x > 2)$$

Figure 18. Hydrazine Decomposition Sequence.

HYDRAZINE/NITROGEN TETROXIDE
(Stage I)

$$N_2H_4 + NO_2 \xrightarrow{k_1} N_2H_3 + HONO$$

$$HONO \xrightarrow{k_2} HO + NO$$

$$NO_2 + N_2H_3 \xrightarrow{k_3} HONO + N_2H_2$$

$$NO_2 + N_2H_2 \xrightarrow{k_4} N_2H + HONO$$

$$NO_2 + N_2H \xrightarrow{k_5} \underline{N_2} + HONO$$

$$N_2H_3 \xrightarrow{k_6} NH + NH_2$$

$$NH + N_2H_4 \xrightarrow{k_7} NH_2 + N_2H_3$$

$$NH + NO_2 \xrightarrow{k_8} HONO + N$$

$$N + NO_2 \xrightarrow{k_9} NO + NO$$

$$NO + NO_2 \xrightarrow{k_{10}} N_2O_3 \longrightarrow NO + NO_2$$

$$NO + N_2H_4 \xrightarrow{k_{11}} \underline{HNO} + N_2H_3$$

$$NO + N_2H_3 \xrightarrow{k_{12}} \underline{HNO} + N_2H_2$$

$$NO + NH_2 \xrightarrow{k_{13}} \underline{HNO} + NH$$

$$NO + NH \xrightarrow{k_{14}} \underline{HNO} + N$$

$$NH_2 + N_2H_4 \xrightarrow{k_{15}} N_2H_3 + NH_3$$

$$NH_2 + NO_2 \xrightarrow{k_{16}} HONO + NH$$

$$OH + N_2H_4 \xrightarrow{k_{17}} N_2H_3 + \underline{HOH}$$

Overall

$$N_2H_4 + NO_2 \longrightarrow HNO + H_2O + N_2$$

Figure 19. Overall Hydrazine/Nitrogen Tetroxide Reaction Sequence.

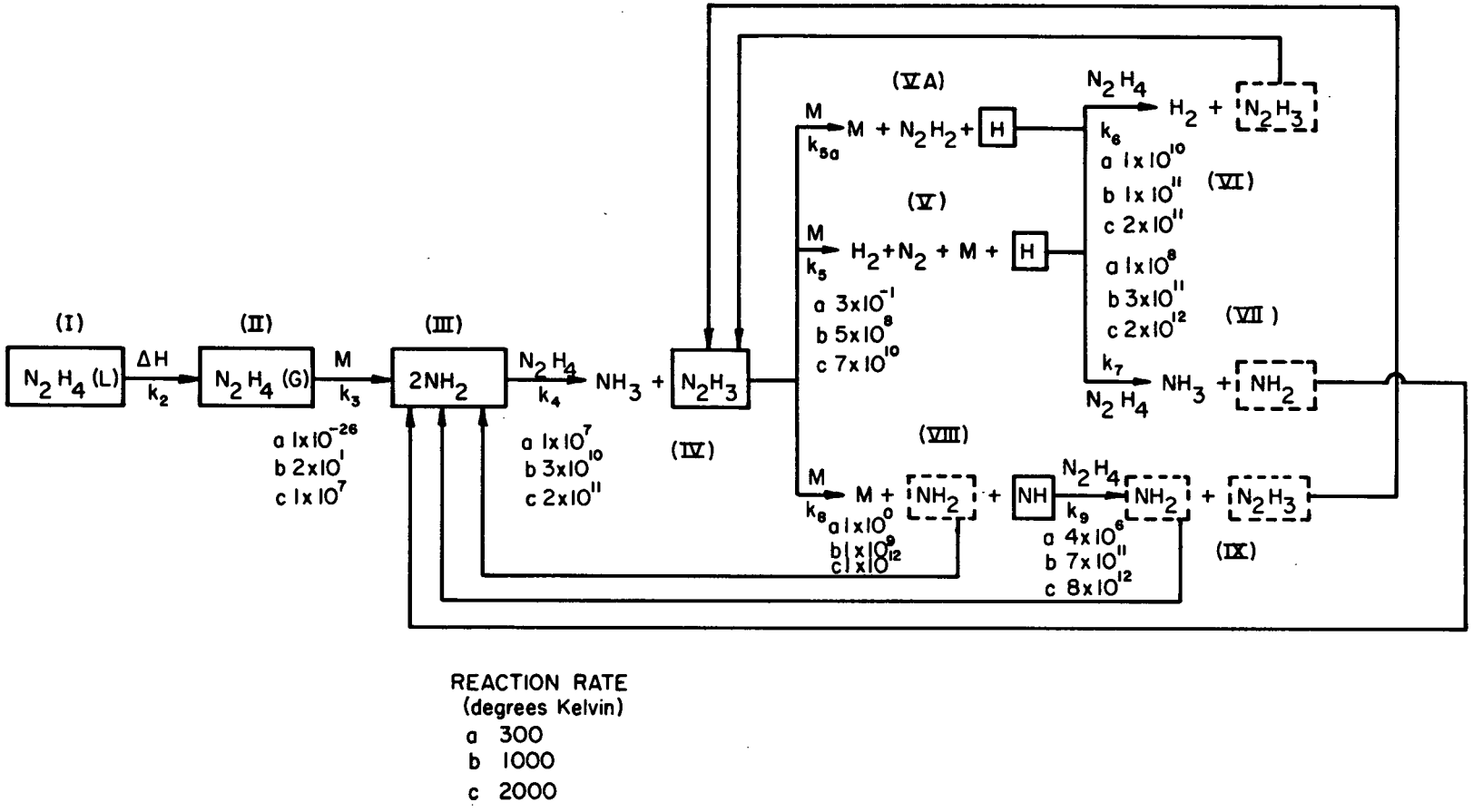

Figure 20. Morphological Kinetic Rate Diagram for the Decomposition of Hydrazine

IV. EXPERIMENTAL PROCEDURES

4.1 Introduction

An experimental test program was developed in order to investigate the physical and chemical processes responsible for the observed detonations in pulse mode engines. The purpose of the test program was to study the buildup of residue material in rockets under laboratory conditions. The major design criterion for this work was an operational thrust chamber pressure of 100 psia and short pulse capability in order to simulate high altitude operation of the Marquardt RL-10 reaction control system rocket engine.

To perform these tests, a highly instrumented 2 dimensional rocket engine and a high altitude simulation test facility were designed and built. The experimental test chamber had a volume of about 550 cubic feet and an altitude simulation capability of 200,000 ft. (0.15 Torr).

In order to allow a direct comparison of data obtained in this program with data reported by a concurrent test program at the Bureau of Mines, the thrust chamber and injector configurations were similar to those used at the Bureau of Mines test facility. Therefore, the pulse mode rocket developed for use on this program was a two-dimensional thrust chamber utilizing a one-on-one injector. Development of the thrust chamber also involved the design and construction of relatively complex propellant handling and propellant flow control systems. Instrumentation for this test facility required a very high response tape recording system in order to record high frequency transducer data and to monitor fast response spectrophotometric output.

4.2 Test Facilities

4.2.1 Two Dimensional Rocket Engine

A configuration similar to the Bureau of Mines' engine was used for these studies. Thrust chamber geometry, injector impingement angles, impingement distances, and inlet orifice dimensions were identical, in order to allow comparison of data generated between the two concurrent programs. However, a number of differences exist in the configuration of this engine and the Marquardt R4-D. The major difference involves placement of a single one-on-one doublet injector along the center axis rather than a set of eight doublets arranged on a concentric circle normal to this axis. This arrangement reduces the effective mixing and allows the propellants to impinge on the aft chamber walls. A second difference is that fuel weepers used for thrust chamber cooling in the Marquardt engine were not incorporated in the design and impingement of the fuel onto cold chamber surfaces near the injector plate did not occur. The Reynolds number of the propellant flows is calculated to be about 2.8 times greater than that of the operational engine although, since both should be in a stable turbulent flow regime, no significant effect is expected from this factor.

The main elements of the design departure from the Bureau of Mines engine can be summarized as follows:

1. A 6061 aluminum thrust chamber fitted with viewing ports replaced an all plexiglass engine.
2. Direct electronic monitoring of reactant flow rates replaced photographic flow monitoring system.

3. A valve system which enable recycling under vacuum conditions in addition to precisely controlled reactant injection replaced a burst diaphragm flow controller.
4. Thrust chamber structures capable of withstanding internal detonations were employed.

The aluminum housing was chosen because the number of firings required a rugged, nonreactive, easily machinable, construction material. The window orientation was chosen to maximize the optical depth of the reaction chamber in order to increase the emission and absorption signals. Flow rates were monitored using a linearized electronic readout on a high-speed tape system. To allow this readout, the piston in each reactant reservoir was fitted with a core of permeable material that affected the inductance of a nonuniform coil wound along the wall of the reservoir. The inductance of the coil was then a function of the core position and could be related to the instantaneous flow rate of the reactants.

Design drawings of some of the major components are presented in Figures 21 through 25 . Figure 21 shows the thrust chamber. This is a two-piece sandwich construction in which the individual components are bolted together. Window ports are located to view the impingement point of the fuel and oxidizer streams. The materials of construction which were used are a 6061 aluminum alloy for the thrust chamber and quartz optical windows. Figure 22 shows the injector block. Impingement angles of 30° and 40° are used for fuel and oxidizer propellant streams. Figure 23 shows the valve assembly and fuel inlet system. Valve action is performed by a rapid acceleration of the Teflon piston via a rapid pressure release on one

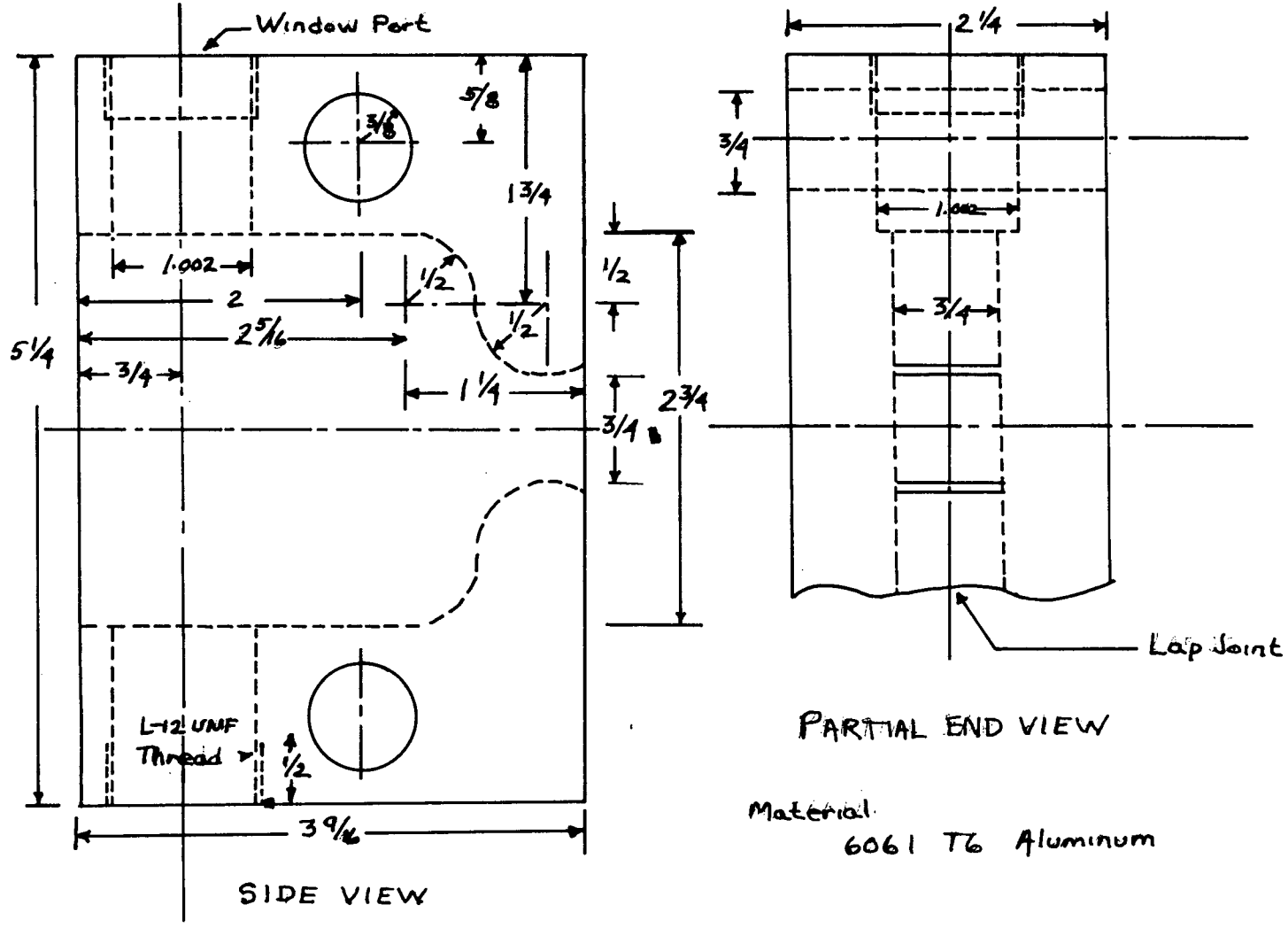

Figure 21. Rocket Thrust Chamber

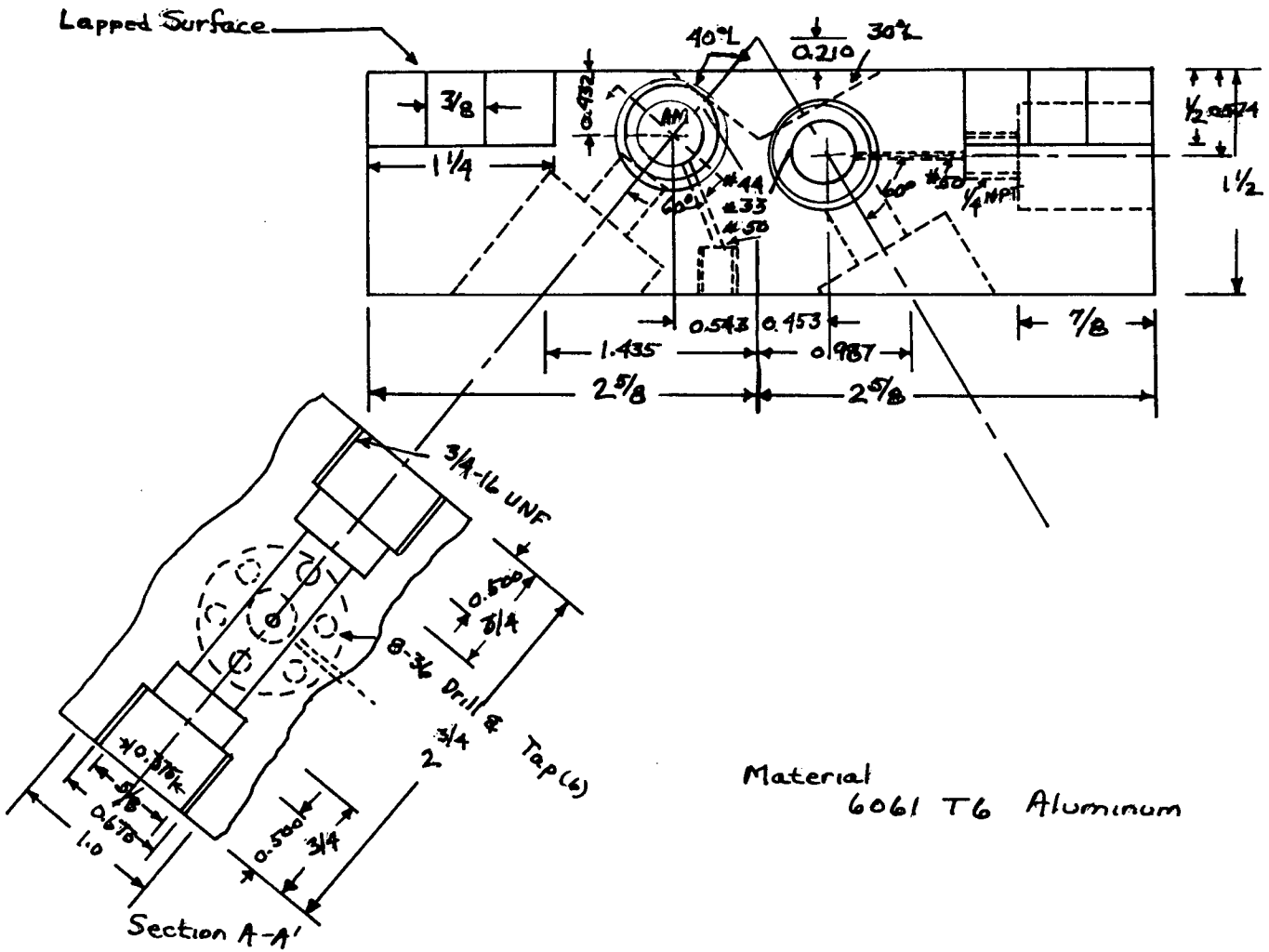

Figure 22. Injector, Side View

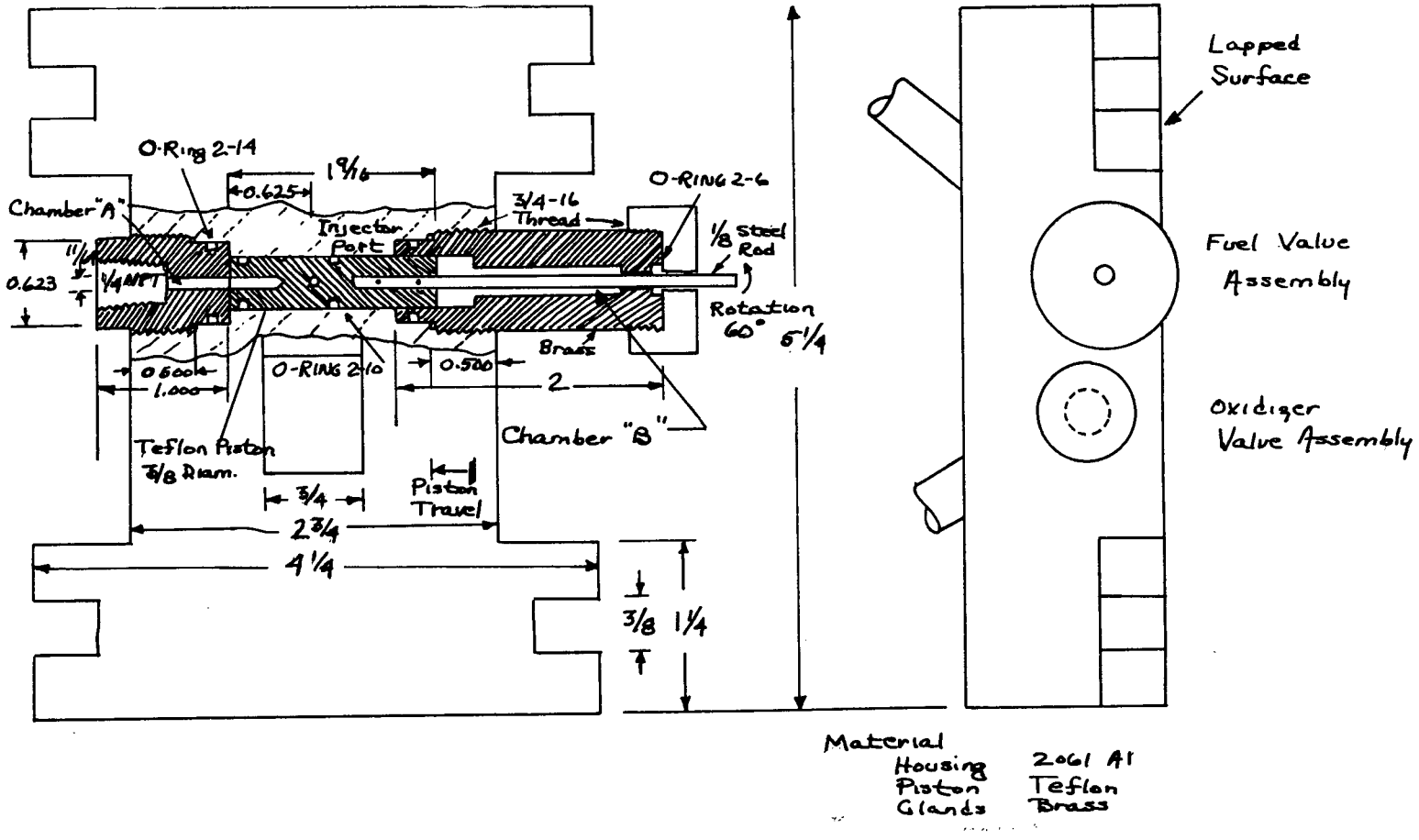

Figure 23. Valve Assembly, Piston in Discharge Position

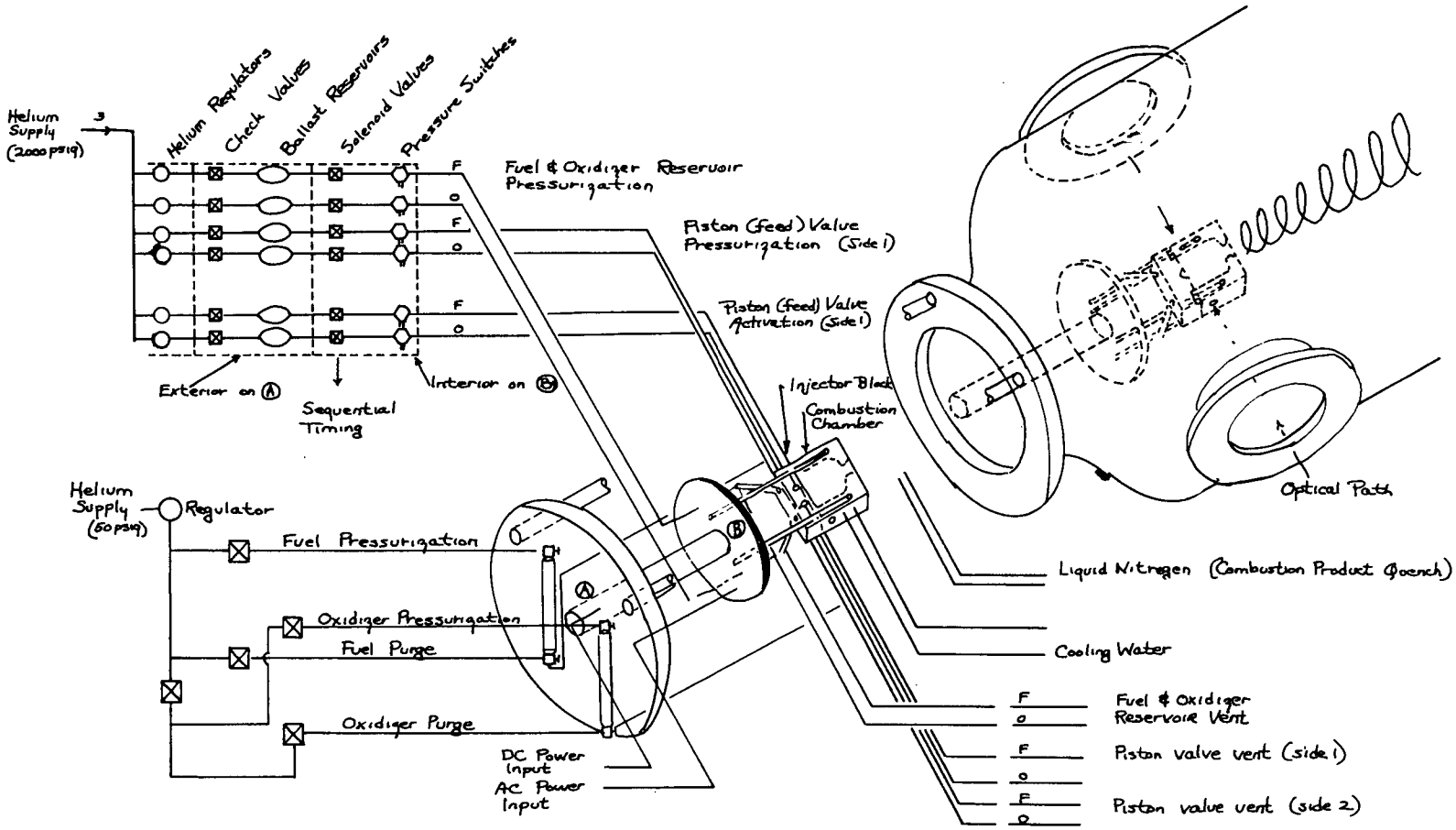

Figure 24. Schematic Diagram of Propellant Handling System and Experimental Test Chamber

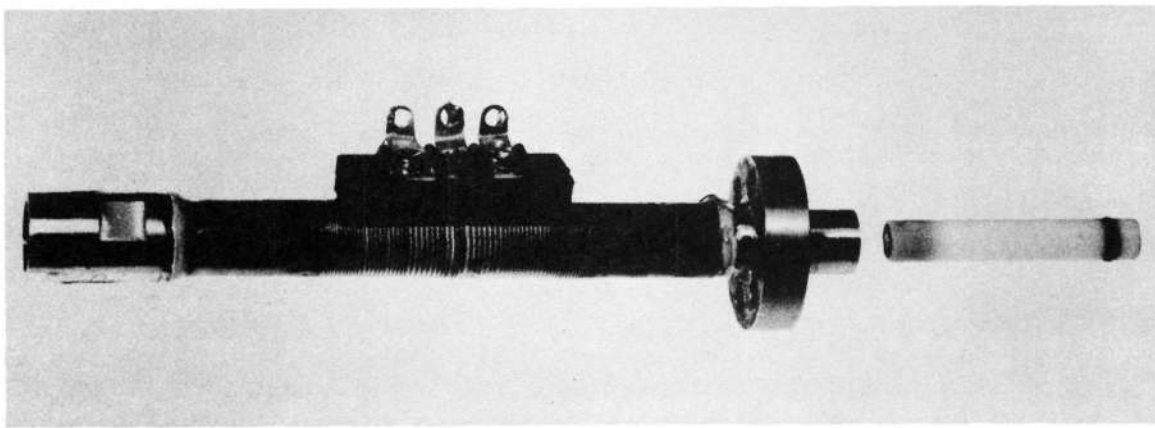

Detail of the Construction of the Reservoir Monitor (Nonlinear Inductor) and Piston Design

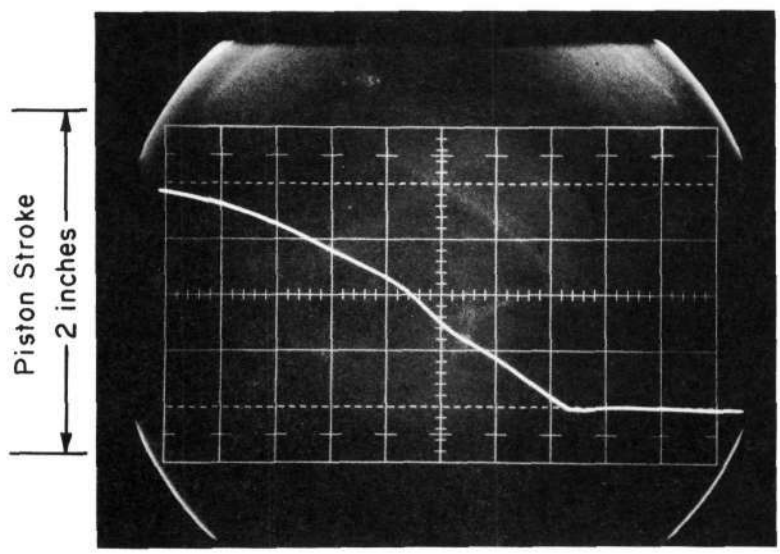

Example of Transient Response Obtained From Reservoir Volume Monitor

Figure 25. Reservoir Monitor and Piston

end of the piston. The valve is essentially a piston that contains a mating passage that matches the injector passage when the piston is translated into position. The Teflon piston is actuated pneumatically in order to minimize piston mass and to obtain an adjustment actuating force. The system features ppositive sealing which allows prepressurization of the reactant reservoirs, and the filling method prevents the formation of a vapor pocket within the reservoir. The design also isolates the reactant supplies from the chamber during the filling cycle and from both the chamber and reservoir during firing. This approach allows the motor to be recycled while under vacuum conditions together with the advantage of the fixed-volume injection scheme. The reactant reservoirs are shown in Figure 25.

4.2.2. Vacuum Test Facility

A vacuum test facility was assembled and evacuated to a pressure corresponding to an altitude of 200,000 feet. A schematic diagram of this facility is given in Figure 26. A stokes 212G (130 cfm) and a Kinney KMB-230-130 pumping system was used. A detailed view of the optical port for this facility is given in Figure 27. This facility consisted of a large vacuum chamber (490 cubic feet) and a thick-walled test section (20 cubic feet) connected by a 16-in. flange. The test chamber has $\frac{1}{2}$ in. steel walls which are capable of sustaining moderate blast waves. This chamber was fitted with three 8-in. observation ports. The large chamber is of riveted steel construction and is used to provide a ballast volume for the test chamber.

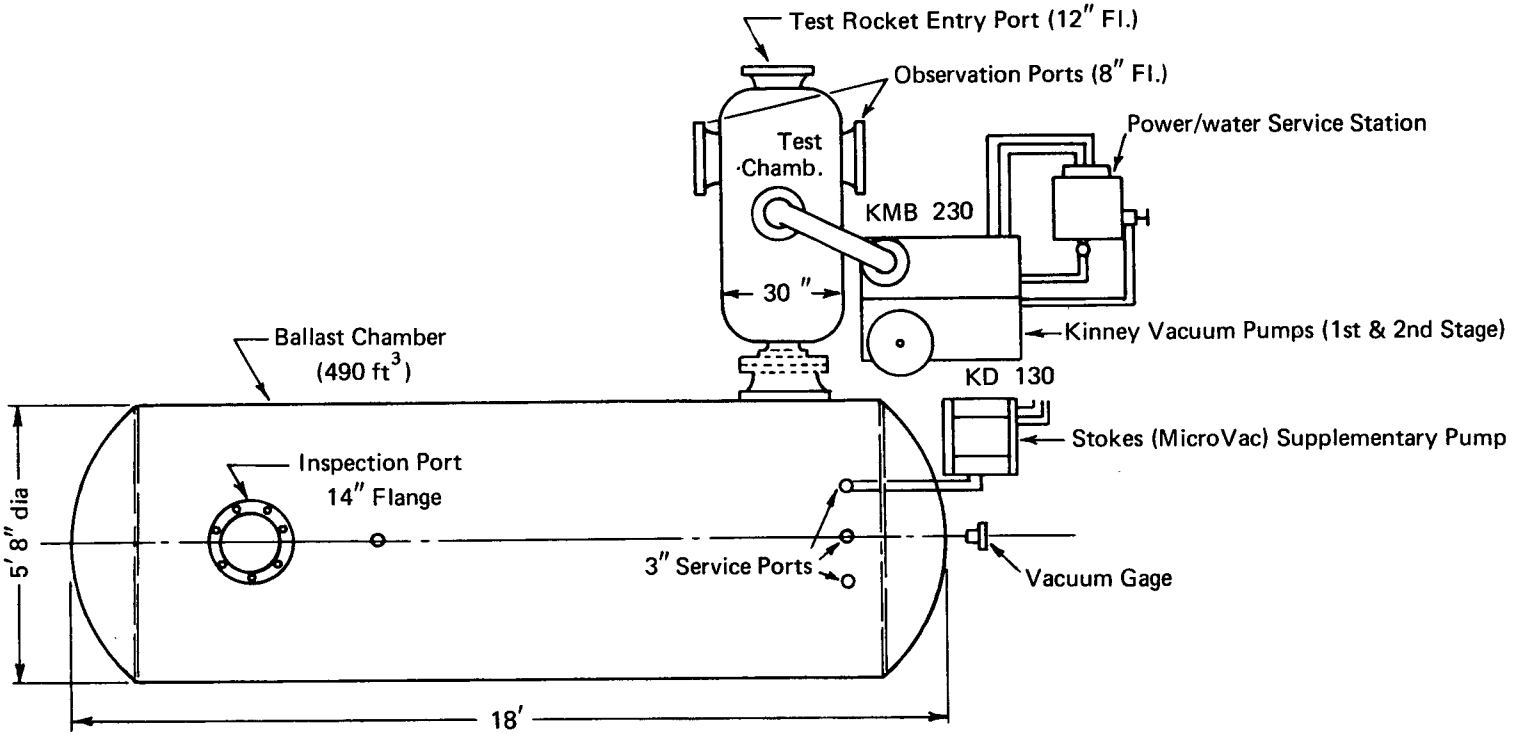

Figure 26. Sketch of Rocket Test Chambers and Vacuum System

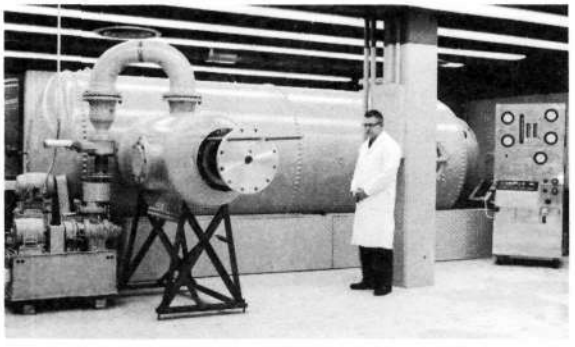

a. Side View

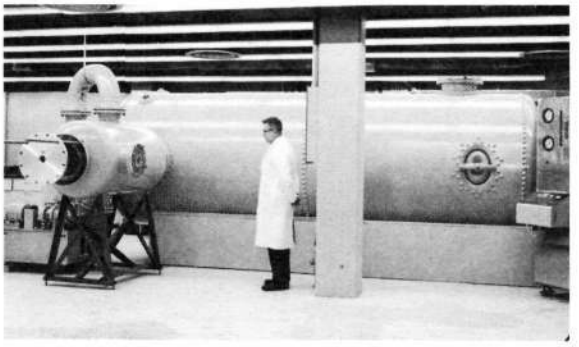

b. Side View

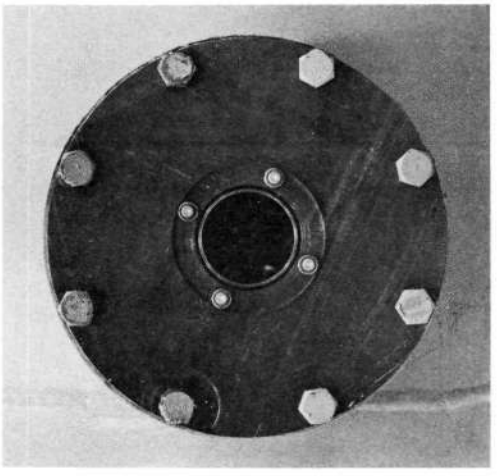

c. Optical Point

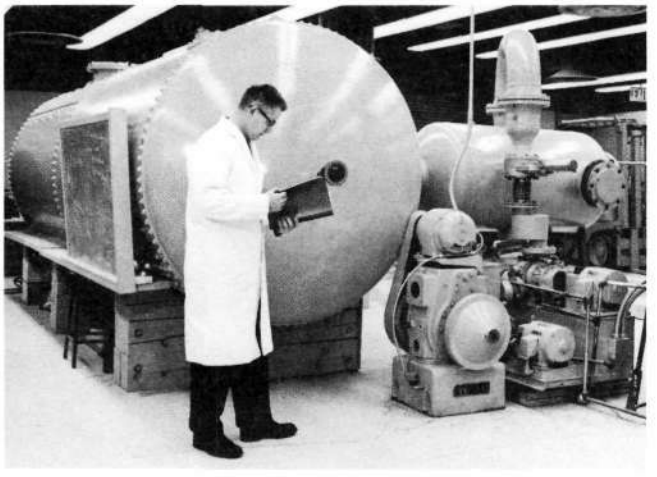

d. End View

Figure 27. Vacuum Test Facilities for Rocket Research Studies

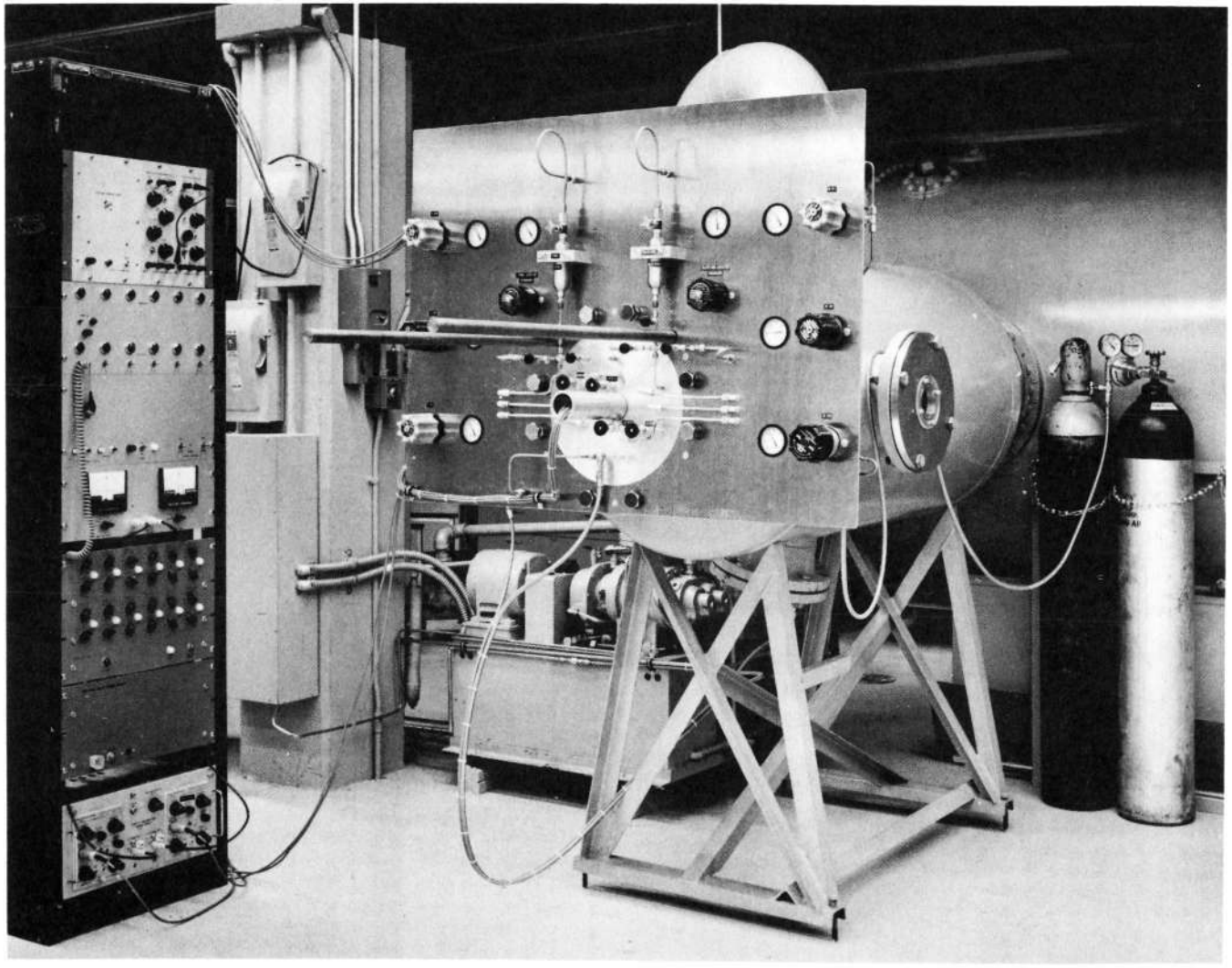

Figure 28. Overall View of Control Panel and Operational Instrumentations

4.2.3 Propellant Handling System

Schematic diagrams of the propellant handling system are shown in Figures 29 through 31 . Figure 31 also shows the relative placement of engine hardware within the test chamber. To achieve fast dynamic response for valve actuation, helium gas is used as a pressurant. The main fuel and oxidizer handling systems are mounted directly on a demountable vacuum test chamber face plate.

4.3 Instrumentation

A variety of techniques were used to monitor the chemical and physical processes that occurred during the pulse-mode operation of the 2-D rocket engine. Pressure measurements were made using two Kisler 601A pressure transducers. These transducers were located in the upper wall of the thrust chamber. One transducer was emplaced near the point of propellant impingement; the second transducer was located in the aft end of the chamber just before the converging throat section. The output of these transducers was simultaneously displayed on a Tektronic 547 or 555 oscilloscope and recorded on a 14 channel Mincom M34 high-speed tape recorder. To amplify the transducer signal two charge amplifiers were used. The frequency response of the tape recorder was dependent on whether direct or FM mode of operation was used with a frequency response of 80 kilohertz and 600 kilohertz being the maximum available from the FM and Direct mode respectively. In order to reduce a zero point drift of the transducers caused by thermal shock, a very thin film of grease was applied to the face of each transistor prior to hot testing.

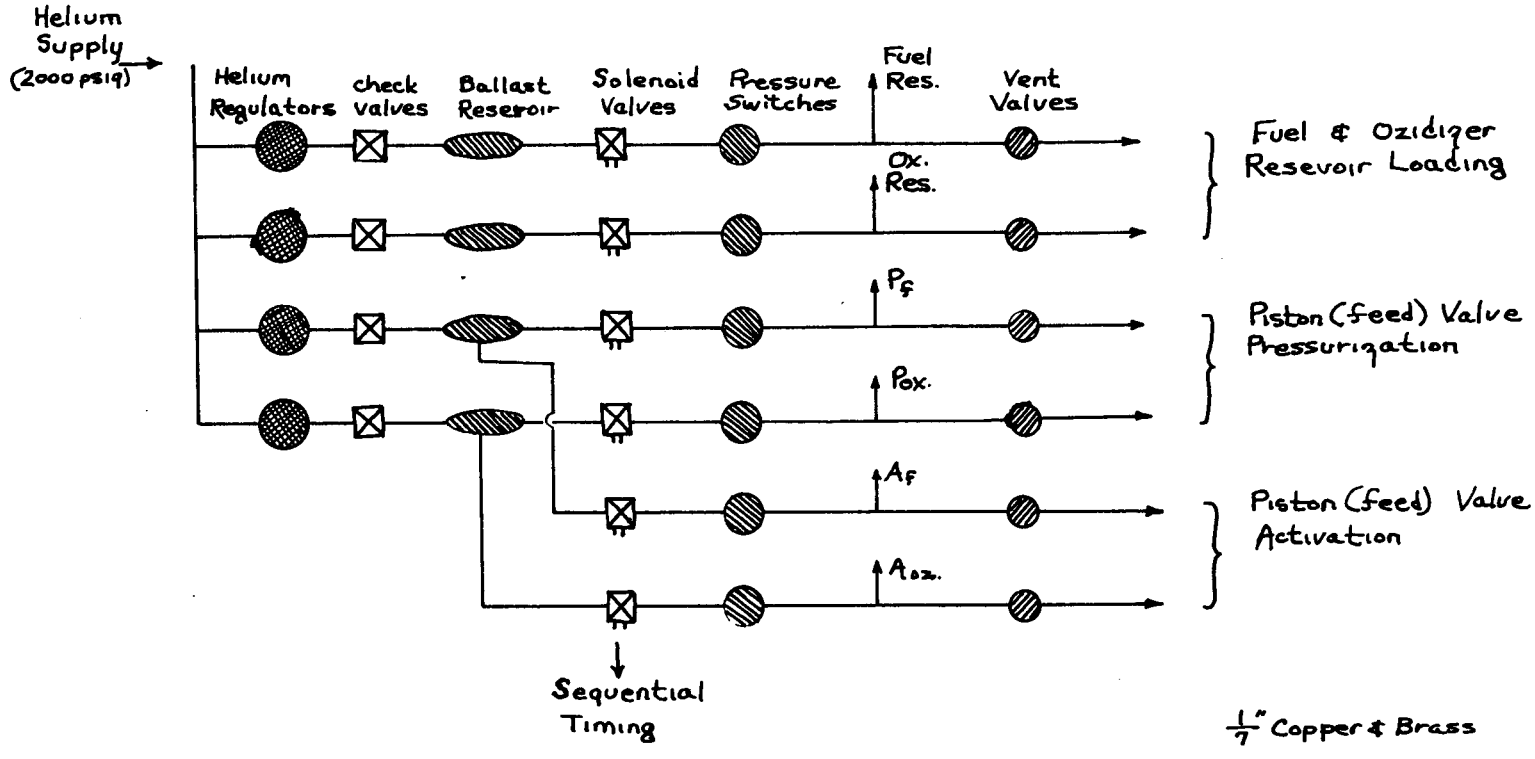

Figure 29. Schematic Diagram of Propellant Handling System

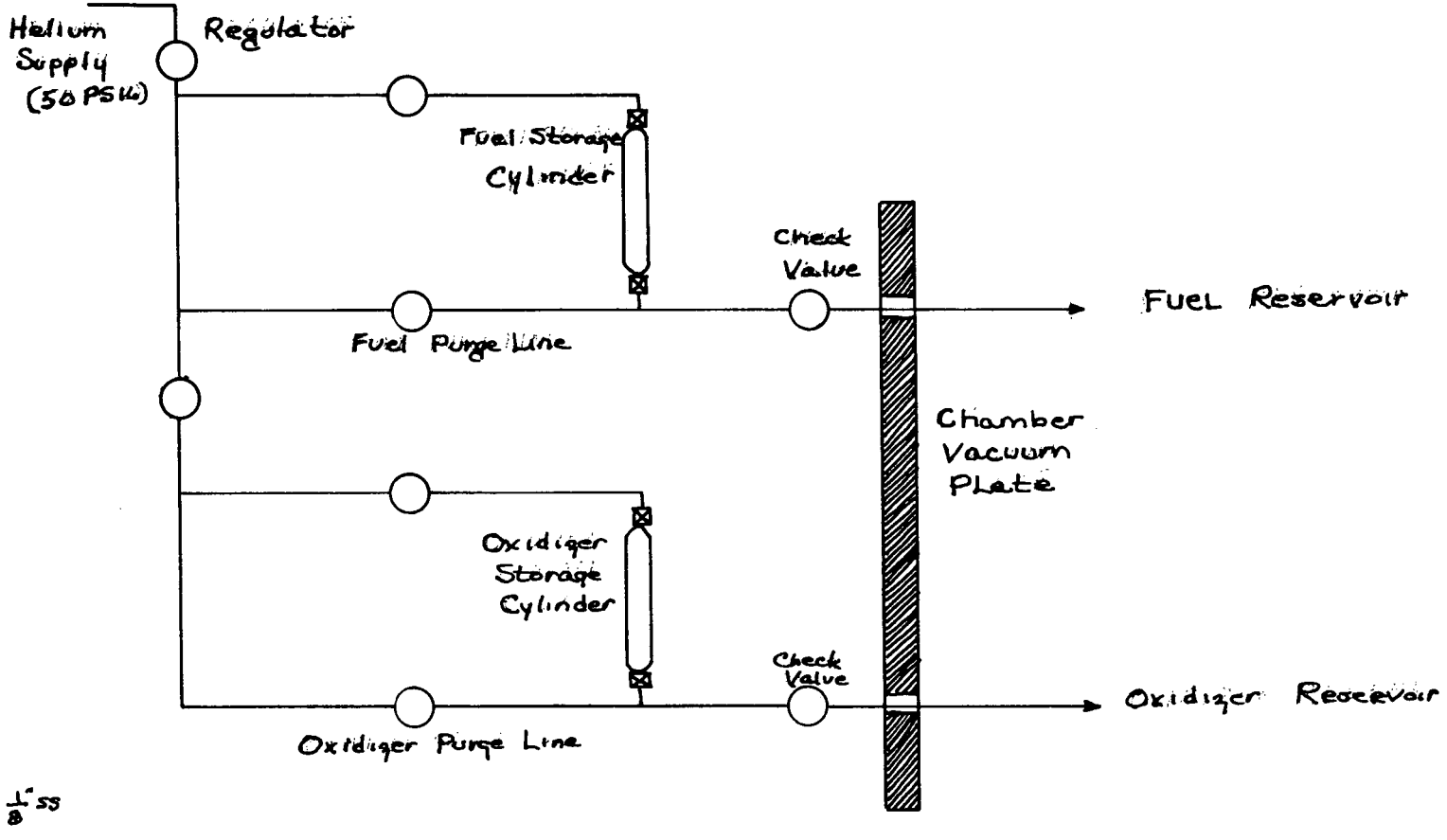

Figure 30. Schematic Diagram of Fuel and Oxidizer Pressurization Systems

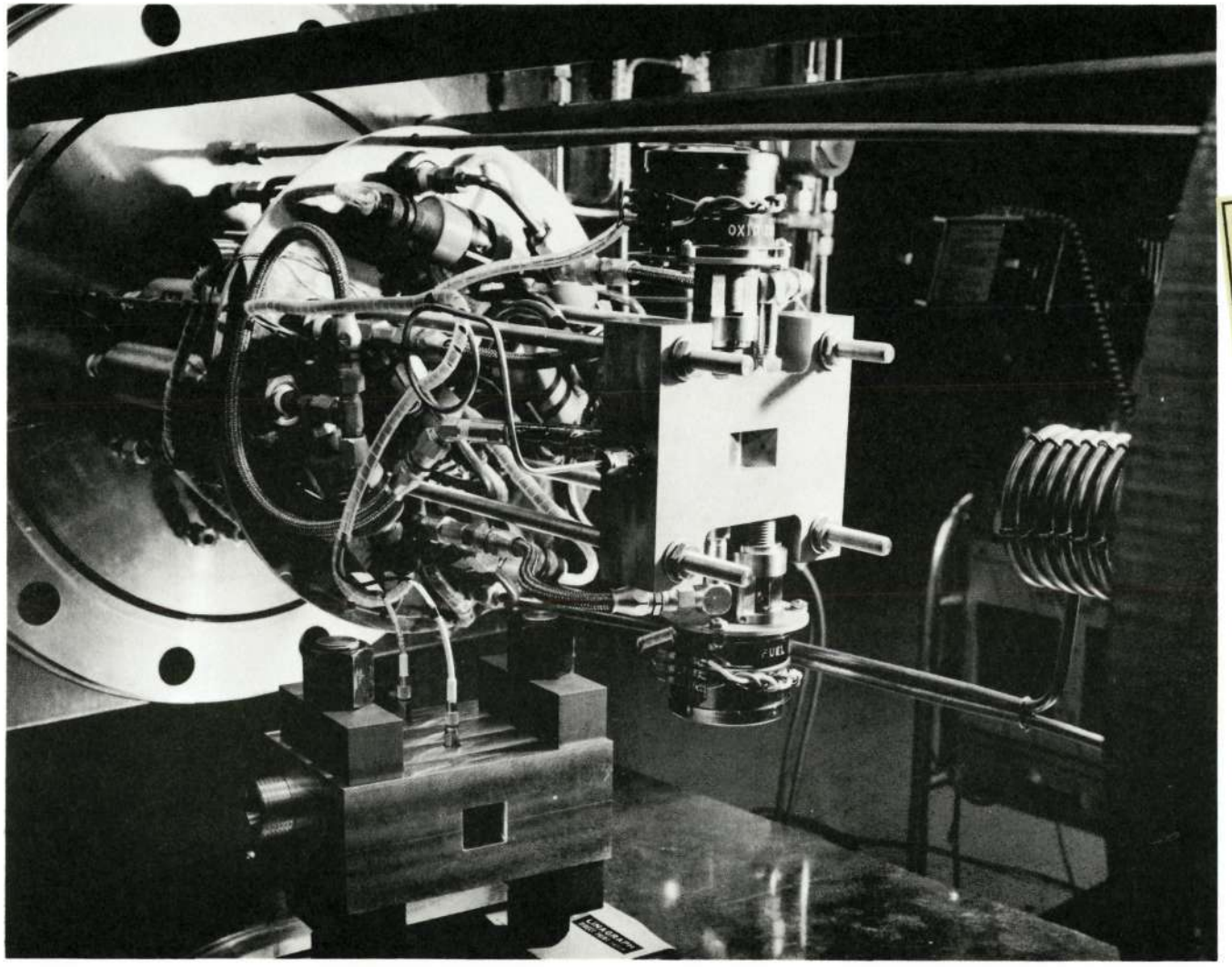

Figure 31. Injector Block with Chamber Detached

Propellant flow measurements are made using the specified nonlinear inductor described in the previous section. The frequency response of the inductor was limited by the frequency response of a set of preamplifiers to 6 kilohertz.

Spectral data were recorded using a number of different spectrographs and spectrophotometers. Time integrated spectra in the visible region between 2600Å and 7500Å are taken using a Bausch and Lomb 1.5 meter grating spectrograph. This spectrograph has a resolution of 14.763Å/mm. Time resolved spectrographic data were obtained using a CINE quartz prism spectrograph. This spectrograph is a specialized spectrograph that had been developed to record time resolved spectral data emanating from large scale detonations, and has a spectral response between 2200Å and 6500Å, covering the ultraviolet and visible regions. However, because of its inherent low resolution only a limited amount of work could be performed with this spectrograph. A one meter Jarrell-Ash spectrograph was modified for use on a polychrometer. This instrument uses a grating of 1158 lines/mm with useful band width of about 800Å. This instrument was modified to obtain time resolved short-band pass spectral records by incorporating a rotating quartz refraction prism in the optical path. A Warner Swasy Model 501 high-speed scanning spectrophotometer was used in the visible and infrared spectral region.

A combination of emission and absorption spectra was used to follow the reaction processes occurring during the operation of the rocket thrust chamber. A controllable pulsed backlight source lamp was developed to aid in this analysis. A Hewlett Packard 213 pulse generator with a Xenon Arc Lamp which was collimated into a probing beam approximately 3/8 inch in

diameter was also designed and fabricated. In order to avoid overdriving the lamp for other than brief time periods a short duration, repetitive pulse was imposed on a continuously operated lamp.

A typical oscilloscope output of the light system is shown in Figure 32a, together with a plot of the relative radiant output characteristics of the lamp as a function of wavelength. Typically, light pulses with a 15 microsecond half-width at a repetition rate of 5 kH were obtained. This repetition rate could be substantially increased. The light was run continuously at a low level and is pulsed to a transient intensity of approximately four times the steady state output. The intensity shift is shown in the oscilloscope output tracing. A line spectrographic record of this lamp in operation is shown in Figure 32b.

High-speed photographic studies were performed using either a HyCam or an Eastman 16mm camera. Both cameras were used to obtain data at about 3000 frames-per-second although the HyCam had a much higher framing rate capability.

4.4 Cold Flow Testing

Cold flow tests were performed to test the design of the overall system. These tests had three objectives: (1) to test the integrated control and propellant handling systems; (2) to aid in the development of operational test procedures; and (3) to test the operating characteristics and reliability of the propellant valving and control systems. As outlined previously, specialized valves were designed and constructed in order to allow recycling of the engine system without breaking vacuum, and to retain the concept of using fixed-volume piston-driven propellant reservoirs.

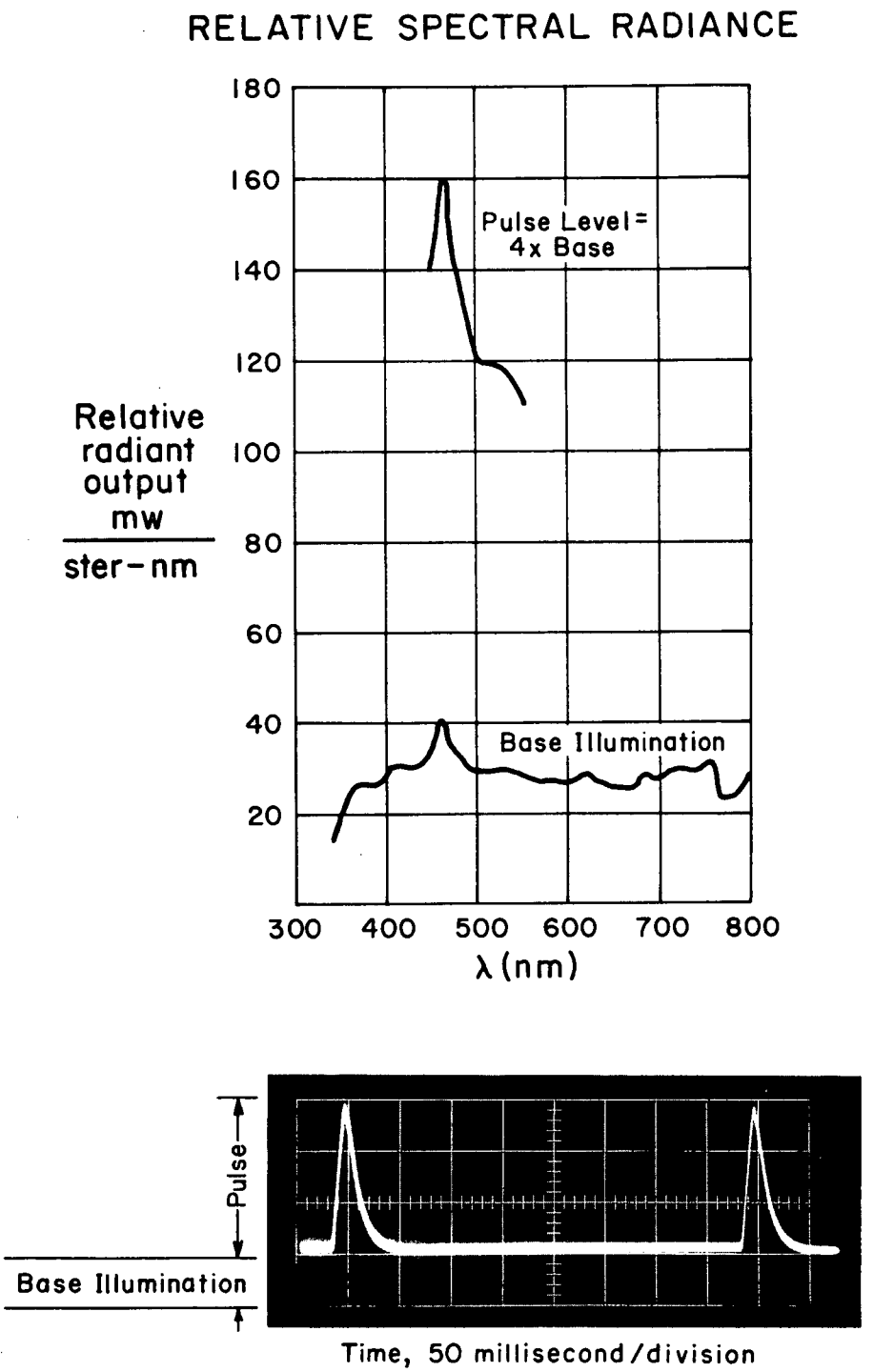

Figure 32. Performance of Pulsed Xenon Lamp Measured at 500 nm

Precise and accurate propellant control in terms of lead, lag, and rate of flow were achieved with this valve system using water as a propellant simulant. No leakage of propellant around the moving seals was observed under either ambient or high altitude pressure conditions. Figure 33 shows a stroboscopic view of a typical cold flow test. Total propellant flow for this test is 2.5 cc. and total firing duration is 20 milliseconds with a 5 millisecond fuel lead.

A relatively large number of cold flow tests (approximately fifty) were performed in order to determine the reproducibility of propellant handling systems and to outline necessary operational pressures required for specific flow rates. Based on these tests, it was determined that the fuel (or oxidizer) leads could be sequenced with high relative precision. Since the unique flow monitoring methods developed could be directly correlated with actual propellant flow a relatively precise knowledge of the exact propellant flow was provided. These tests indicated that the test design concepts, as developed, in fact provided a highly flexible and precisely controlled propellant handling system.

4.5 Single Propellant Tests

Tests using single streams of individual propellants were performed in order to obtain background data concerned with the spray patterns and spray droplet size distribution functions. Results of these tests indicated that the initial spray patterns were strongly dependent on propellant physical properties.

During cold flow testing two problems developed with the recommended grease used to seal the moving "o" ring on the propellant reservoir. The

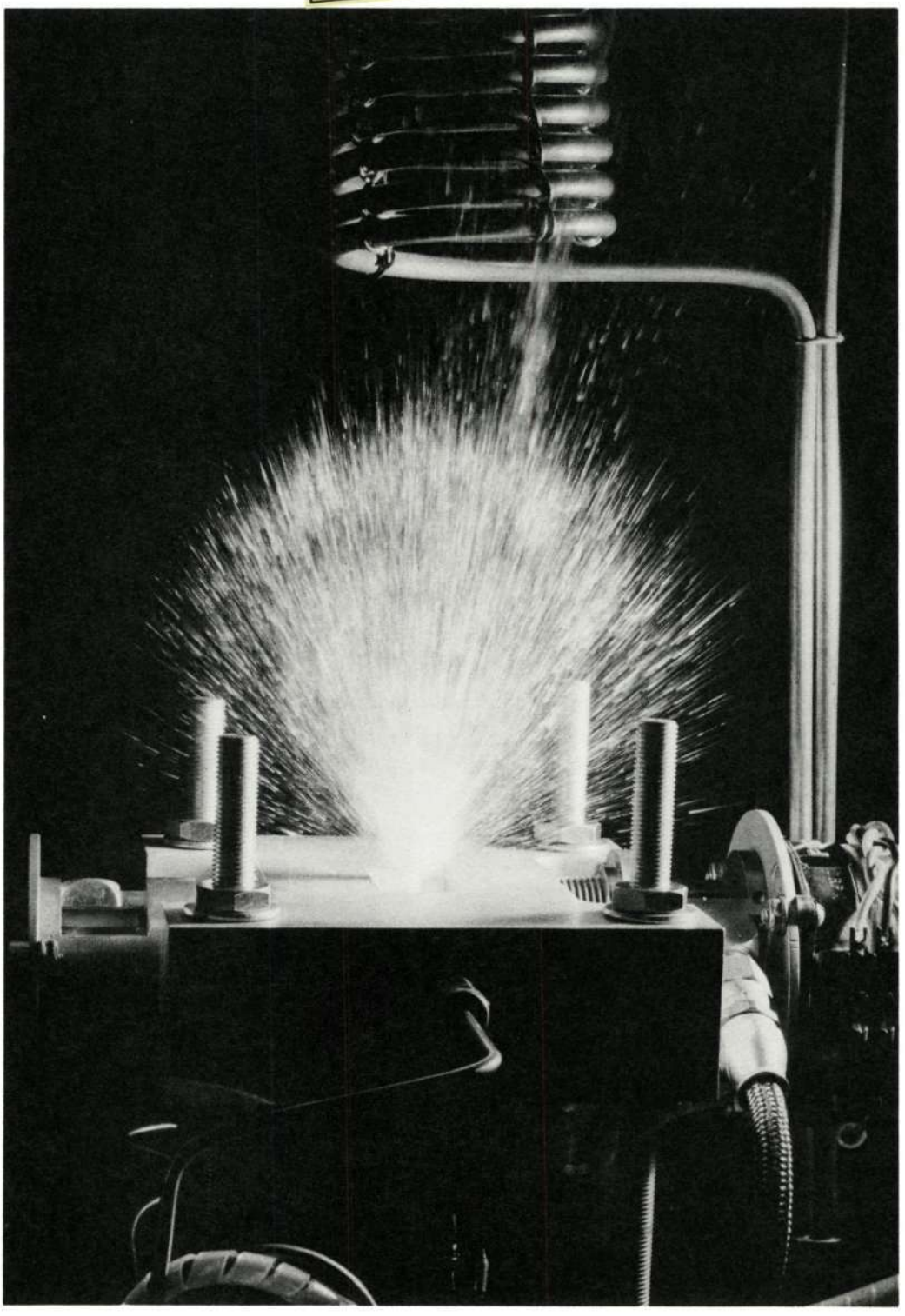

Figure 33. Strobe View of Water on Water Injector

first problem involved the lack of adherence of the grease to the piston wall surfaces, caused by an apparent setting of the grease in a semi-regular microcrystalline structure. The second problem involved the chemical attack of the liquid oxidizer on the grease. A series of compatibility tests was therefore initiated and a change of lubricant was implemented. The Dri-Lube* grease which undergoes only limited chemical degradation upon contact with liquid NTO appears to be a satisfactory lubricant.

*Dri-Lube; Type 822; MMSN 306A, Lox, NTO, Hydrazine Compatible.

V. EXPERIMENTAL RESULTS

5.1 Introduction

Using the test facilities and instrumentation described above, three series of rocket tests were performed. The first series involved cold flow tests in which simulated propellants were used in order to verify the design and operation of the rocket engine and propellant handling systems. During these tests calibration of the fuel flow rates and verification of electronic sybsystems were performed.

A second series of tests involved studies of the effects of high altitude simulation on propellant injection hydraulics. For this purpose a large number of tests were performed using single propellants. In addition, a few selective hot firings were performed in order to demonstrate the combined effects for typical propellant systems. These tests were used to provide information on spray distribution patterns and to investigate the effect of changes in propellant physical properties on droplet vaporization rates.

The third series was a hot firing test program. During this series of tests, flow, pressure and spectral data were recorded. In some cases a chemical analysis of the residues formed during pulse mode operation was also made in order to verify and extend the results of other investigators.

A more detailed description of these tests together with a documentation of typical results is presented in this section.

5.2 Cold Flow Tests

An extensive series of approximately 150 "cold flow" tests were carried out in order to verify the design and operation of the 2-D rocket

engine and the propellant handling systems. A relatively large effort was directed toward the dynamic calibration of the propellant flow monitoring system.

Calibration curves were prepared in order to correlate the propellant flow output signals with actual propellant injection rates. The calibrations indicated a high degree of repeatability ($\pm 2\%$) between consecutive tests. Figure 34b shows a signal obtained from a typical test run. In this oscilloscope record, the piston travel displacement is displayed in the ordinate with time on the abscissa. As indicated, the time base is 1 millisecond per major division. The slightly curved shape of the flow response curve in the central region is a result of variations in induction coil spacing which were hand wound, and does not indicate a fluctuation in propellant flows. In reducing the data it is necessary to subtract this variation in order to obtain a true flow response curve.

Figure 34a shows a typical spray pattern obtained from these tests. On this test the thrust chamber had been removed in order to allow better observation of the development of the spray pattern. As can be seen, there is a relatively even distribution of material throughout in the spray area. The slight asymmetry of this pattern is caused by a difference in momentum vector of the two propellant streams which results from the difference in density between water and nitrogen tetroxide. A crude calculation of this momentum imbalance effect was made and it was concluded that the resultant spray distribution for an actual "hot" test would be uniformly distributed. Considering the one-on-one type of injector used, this experimental result was considered to be within the range of variation of design parameters.

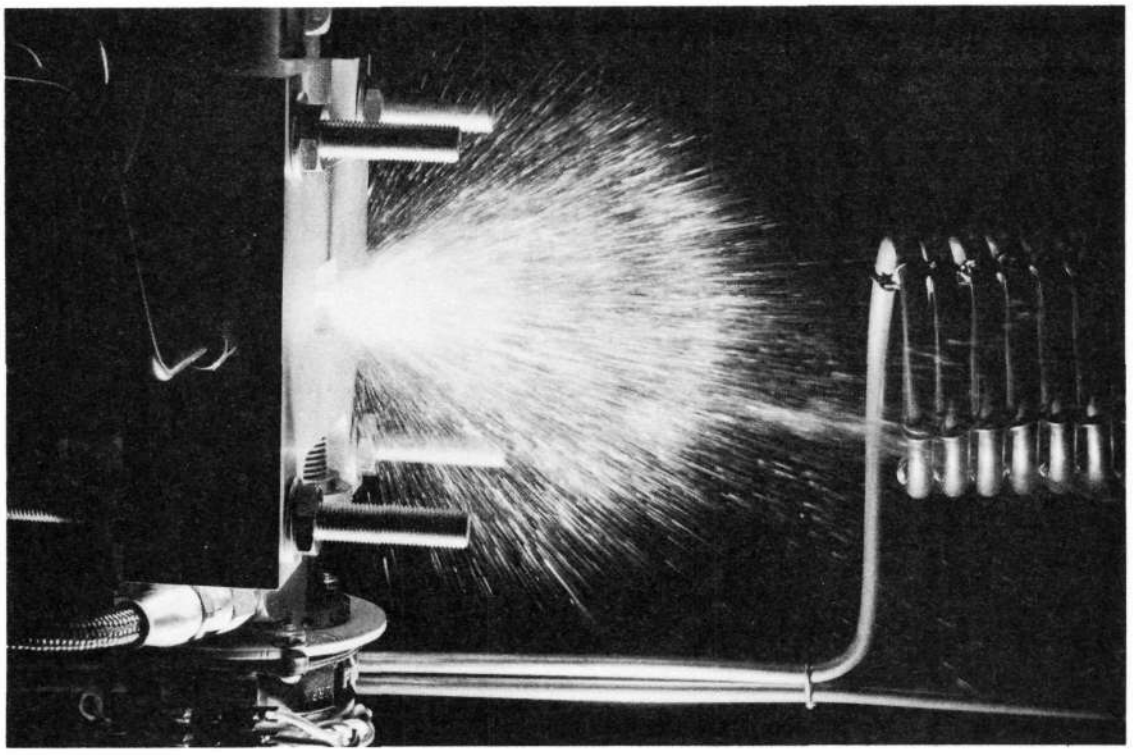

a

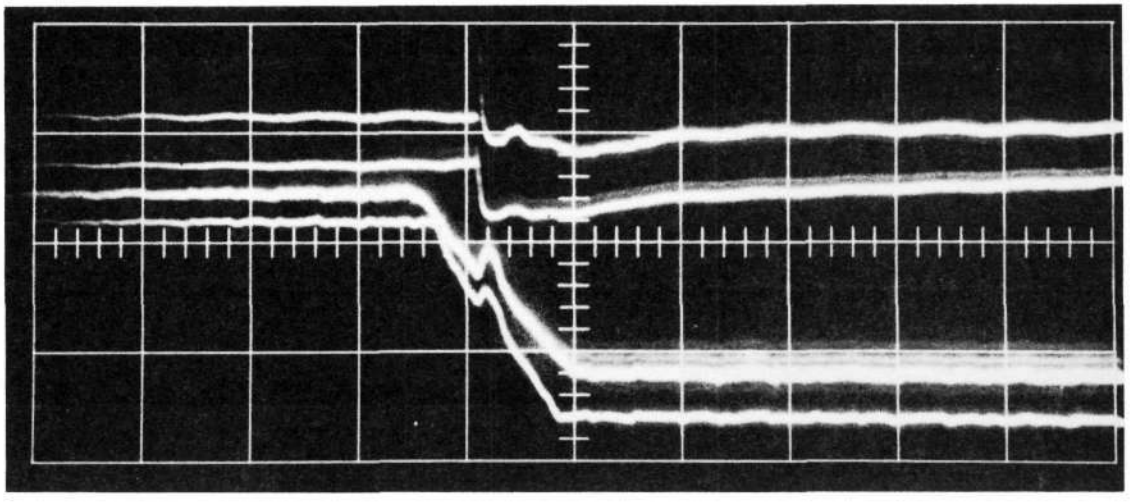

b

Figure 34. Spray Pattern and Oscilloscope Trace of the Dynamic Response for Propellant Flow and Pressure Transducers

To provide detailed information with regard to the injection hydraulics and the propellant sequencing parameters, the development of sprays during cold flow tests was monitored using high speed motion pictures. These photographs showed in considerable detail the physical phenomena which occurred during propellant sequencing. A relatively complete series of tests was conducted using water to simulate both fuel and oxidizer. A portion of a typical sequence showing some of the details involved in the injection hydraulics is given in Figure 35 .

At the onset of propellant flow, a small filament corresponding to leading edge of the lead propellant is observed. In most cases this edge has either an upward or downward momentum vector corresponding to the opening of the oxidizer or fuel valve respectively. Under high vacuum conditions the leading edge is developed into a "blossom" in which the propellant stream is effectively broken up. The reason for this transient blossom effect is not presently understood, but it may involve either a pre-nucleation of the propellant by the dissolution of pressurant gases or a breakup caused by the increased turbulence when injectors having large L/D ratios are used since during valve opening the orifice has a rapidly changing cross section. In the latter case, it is probable that the L/D as well as the injector characteristics are substantially changed by the valve actuation. The propellant stream assumes the form of a highly turbulent column immediately after the onset of main propellant flow.

Upon termination of propellant flow these photographs demonstrate an extremely sharp fuel or oxidizer flow cut-off. This is in contrast to most propellant engine systems in which manifold effects are present with

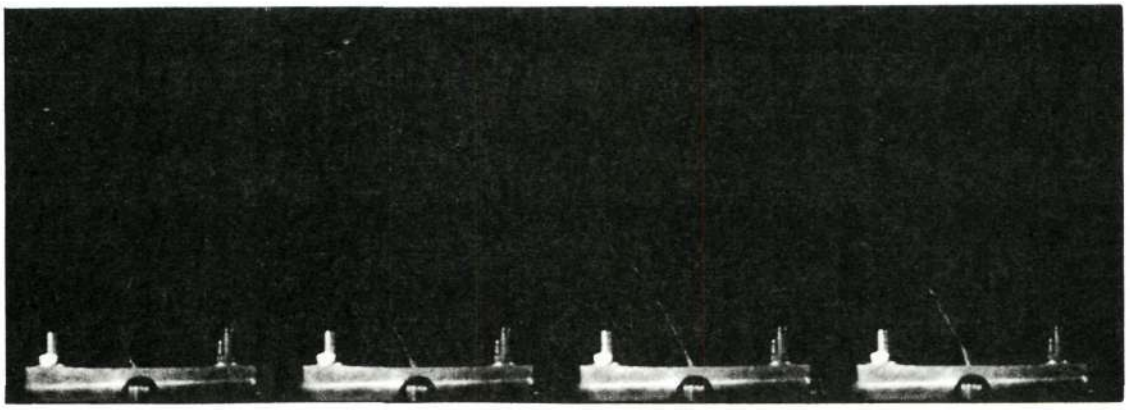

a

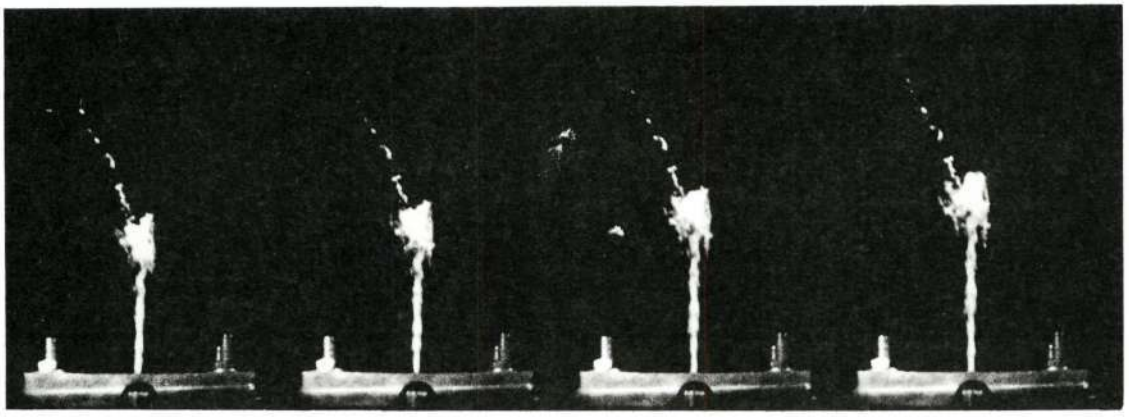

b

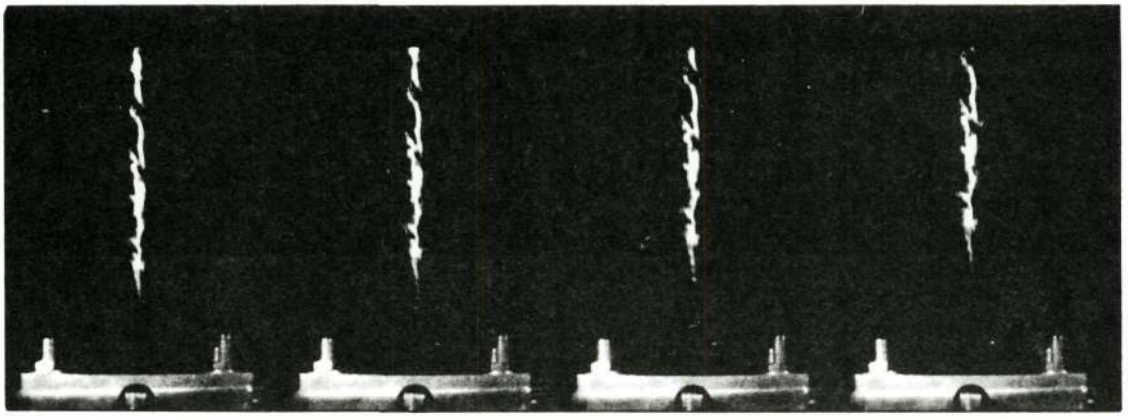

c

Figure 35. Vacuum Injection Behavior for N_2H_4 at 100,000 Feet ~ 3,000 fps

The concommittant dribble volume. The propellant injector developed on this program is essentially a zero dribble volume system which eliminates the formation of hydrazinium nitrate residues formed from the residual propellant emptying from injector manifolds and propellant lines.

5.3 High Altitude Propellant Injection Studies

A series of tests was performed in order to outline the characteristic behavior of hydrazine/NTO propellants under simulated high altitude startup tests. Forty-three tests were run using both single propellant flows and hot firings. For a given injection momentum there was a strong altitude effect on propellant stream disintegration. In order to permit better observation of the behavior during the preignition phase under vacuum start-up conditions, the thrust chamber was removed. Characteristically, under high altitude simulation the fuel stream remained integral throughout the flow region observed. This was in marked contrast to the behavior of the oxidizer, which underwent rapid disintegration to form a very fine aerosol at the face of the injector.

Three typical spray patterns are shown in Figure 36 . As can be observed, the oxidizer fans out in a wide spray, whereas, the fuel (N_2H_4) retains its jet integrity even at very low pressures. This behavior can be predicted on the basis of vaporization theory providing essentially empirical correlation parameters are used. For a hot firing the effect of the large differences in vaporization is graphically shown by the last photograph. The hydrazine consists of a liquid column immersed in a fine aerosol of NTO. This characteristic behavior does not occur during ambient pressure testing. All photographs were taken on a HyCam camera operated at

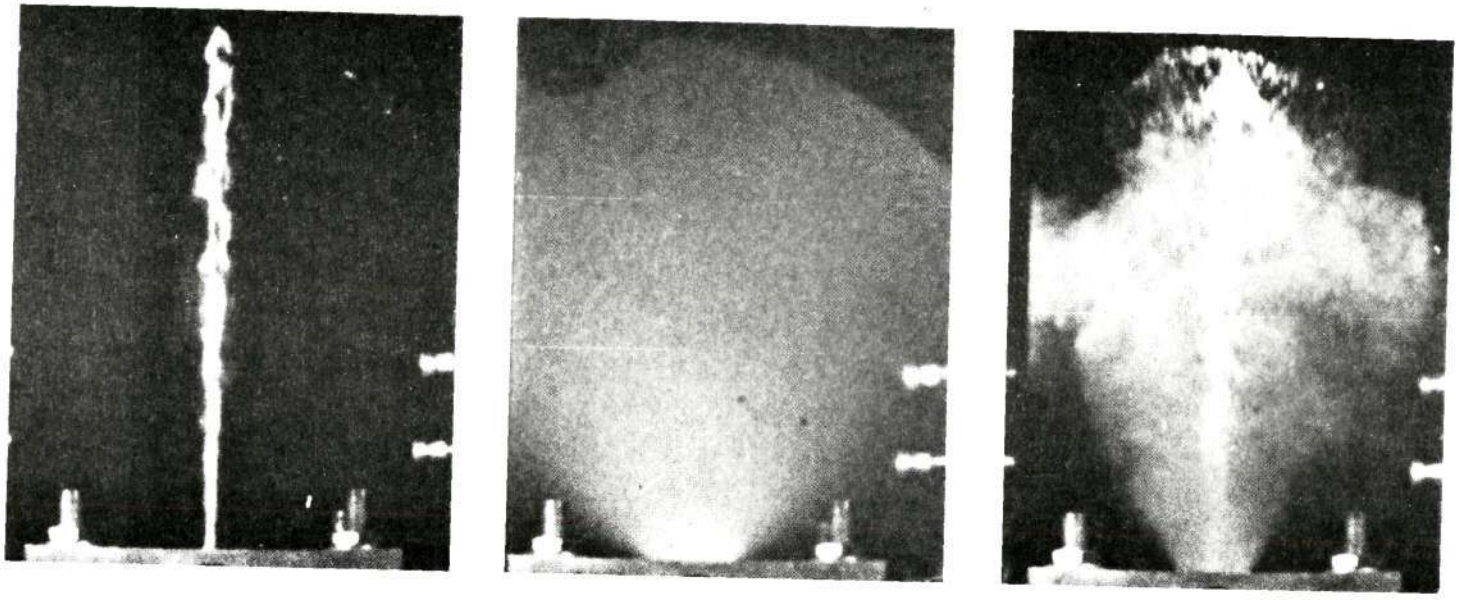

N_2H_4 3mm N_2O_4 10mm N_2H_4/N_2O_4 100mm

Figure 36. High Altitude Spray Pattern

300 PPS using 2484 Eastman Kodak Film (ASA 2000). The event is frontlighted using a bank of three high intensity lights.

5.4 Hot Firing Tests

A large number of hot firing tests using hydrazine/NTO propellant was performed. The major objective of these tests was to obtain spectral data which would provide information regarding the chemical processes responsible for the catastrophic overpressures. Approximately 90 tests were run at low ambient pressures. A number of detonations were observed during the course of testing. In most cases those detonations were nondestructive in that the engine hardware remained intact, but the force of the detonation was occasionally sufficient to completely shatter the $\frac{1}{4}$ inch quartz viewing ports.

5.4.1 Pressure and Flow Response Data

Using the instrumentation described previously, data on pressure, flow, and spectra were recorded. An oscilloscope trace of the dynamic response for propellant flow and pressure transducers is shown in Figure 37. The time base for this test is 20 milliseconds per major division with the time axis running from left to right. Because this record is typical of most of those taken, a detailed explanation of the trace is given below.

Pressure data were recorded on the upper two traces of the oscilloscope and measured at two locations. No significant time variation between the two locations were observed during any of the testing performed. In Figure 37 a deflection on the vertical scale (upwards) indicates an increase in pressure and a standardized vertical scale deflection of 500 psia/cm was used throughout these studies. In this record a pressure spike of about 1100 psia was recorded although pressure levels well above 2000 psia were

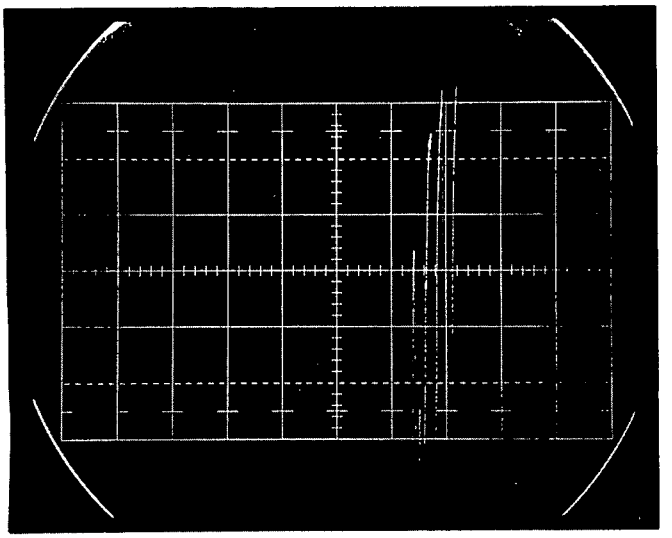

a

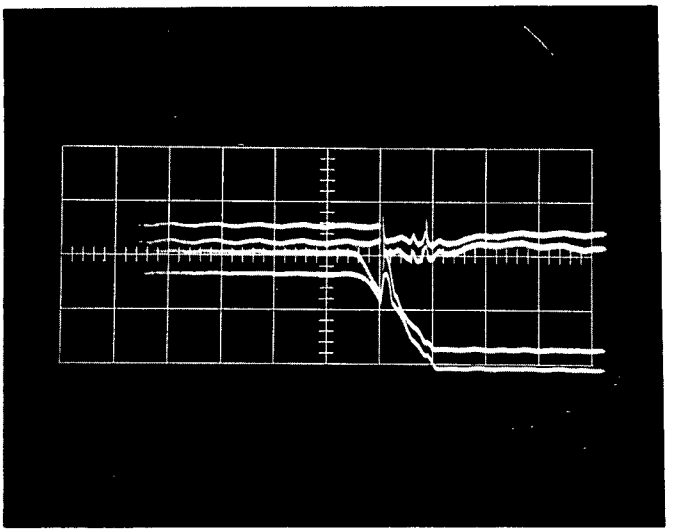

b

Figure 37. Dynamic Responses for Propellant Flow and Pressure Transducer

observed during these tests. There is a zero point shift which occurs immediately after the start of the pressure signal. This shift limits the accuracy of measurement to about 15 percent with a greater uncertainty in measurement at the higher pressure levels. The cause of this shift is not known, although it may be attributed either to a thermal shock or to a contact resistance effect. A thin layer of grease applied to the surface of the transducer in order to reduce thermal shock was only partially effective. A series of tests in which a photoflash bulb was placed approximately $\frac{1}{2}$ inch from the transducer surface verified the hypothesis that the baseline shift is in some way related to a thermal shock caused by the impingement of radiant energy onto the transducer surface. Conditions were adjusted so that there could be no pressure fluctuation during this test. The larger shift in the second trace possibly may be attributed to increased thermal shock since it is located in the aft end of the thrust chamber where local temperatures are somewhat higher. This zero point shift causes a large uncertainty in the absolute value of the recorded pressure level. As can be seen by inspection, the baseline returns asymtotically to the original value after about 200 milliseconds.

Propellant flow rates are recorded on the lower two traces. Fuel flows are recorded on the upper trace and oxidizer flows on the lower trace. For precise analysis it was necessary to take into account a slight fluctuation in signal in the central portion of the propellant reservoir caused by the inductor coil windings. A careful analysis of these records shows a fuel lead of 3.5 milliseconds. Seven milliseconds later a sharp reversal in the flow of both the fuel and oxidizer occurs. This fluctuation in flow corresponds exactly with the pressure transducer records indicating a high

pressure ignition spike. The fine structure of this record also indicates a series of three flow perturbations, each of which is directly correlated with a pressure fluctuation in the thrust chamber. These results demonstrate that the instrumentation, as developed, can monitor direct interactions between the ignition process and the injection hydraulics. These fluctuations occur at a frequency of about 200 cycles per second and could therefore be described as a low frequency chugging.

An insight into the transient flow characteristics at the onset and shutoff of propellant flow can be obtained by close examination of the shape of the flow response curve. At the onset of propellant flow the flow curve has a round shoulder which indicates a constantly increasing flow rate during valve actuation. At the termination of flow a very sharp discontinuity is observed, indicating an almost instantaneous cutoff of flow. This correlates with visual studies obtained using high speed photographic techniques.

5.4.2 Infrared Analysis of Engine Residues

The severe ignition overpressures sporadically observed during the vacuum ignition of NTO/A-50 propellants are believed to result from a detonation of the residue material formed in the chamber. Therefore, a careful chemical analysis was performed on residue samples obtained from hot engine firings. Figure 38 shows the infrared absorption pattern obtained from a typical MMH/NTO residue.

In addition to hydrazinium nitrates several other species were detected. These included triazene (H_3N_3), hydrazoic acid (HN_3), hyponitrous acid ($N_2H_2O_2$), and monomethyl triazene ($CH_3N_3H_2$). These species were present in

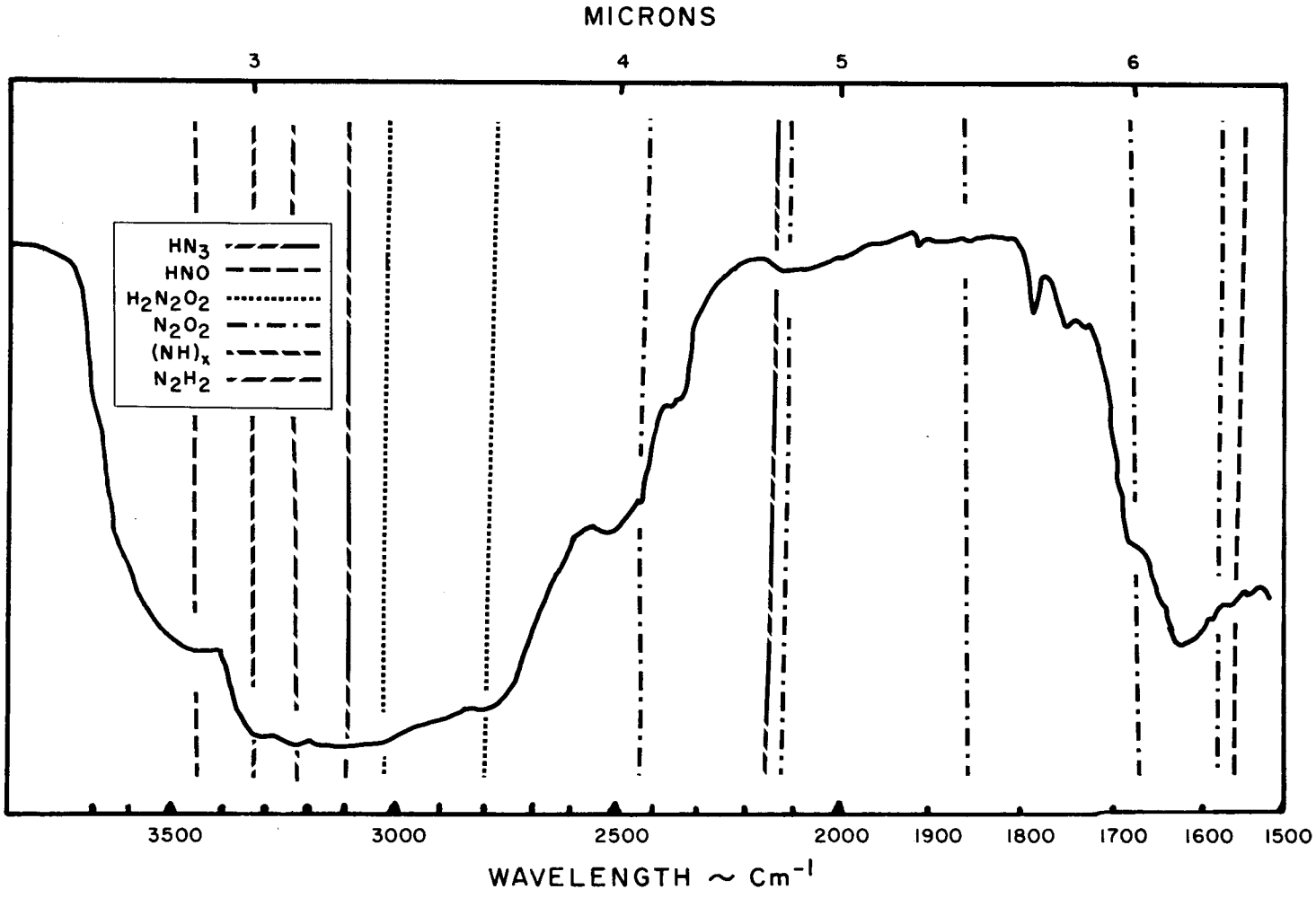

Figure 38 . Typical Infrared Absorption Pattern for NTO/MMH Residue

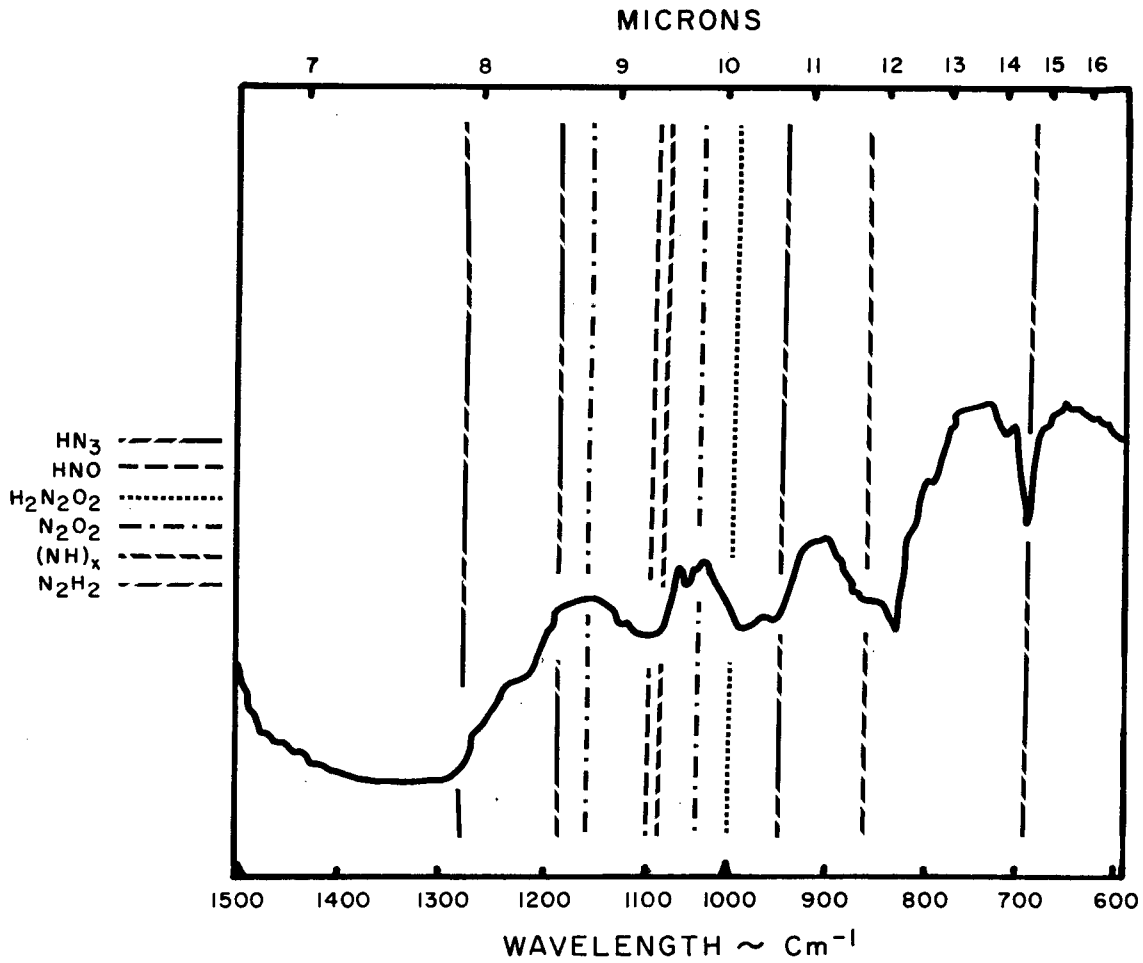

Figure 38 (cont.) Typical Infrared Absorption Pattern for NTO/MMH Residue

small amounts and their significance is believed to be associated with their possible role in increasing the explosive sensitivity of the base material. Triazene, monomethyltriazene and hydrazoic acid were identified in both mass spectrometric and infrared analysis. Hyponitrous acid was identified in the infrared analysis only. For these compounds all reported bands between 2.5 and 15 microns were either specifically present or, alternatively, were positioned at a frequency corresponding to a major absorption band of hydrazinium nitrate and/or one of its derivatives. The single exception to these patterns was a weak combination band $\nu_3 + \nu_5$ for $N_2O_2^-$ which was not observed.

Mass spectrometric data (outlined in the following section) indicated sizable M/e ratios at 43, 45, and 59 which are correlated with HN_3, H_3N_3 and $CH_3N_3H_2$ respectively. Secondary breakdown peaks could not be used because of a lack of compound reference breakdown data for the mass spectrometer used. These data were obtained from the volatile material evolved from a sample of the residue which had been frozen using liquid nitrogen and then evacuated to pull off dissolved gases. Therefore, the mass spectral data provides information about the character of the gaseous species which are formed by reactions taking place in the liquid phase of the residues. In general the mass spectral patterns were well correlated with infrared absorption data.

The relevance of the presence of the observed metastable compounds to the problem of ignition overpressures and detonation is that they can be expected to act as sensitizing agents. It is probable that these compounds are formed in different stages of the reaction. For example, it is hypothesized that HNO is formed as a stable intermediate during the gas phase

reaction of NO_2 with hydrazine. Subsequently, this dimerizes to form hyponitrous acid. Since a well known synthetic route for the formation of HN_3 is the reaction of $H_2H_2O_2$ and N_2H_4 in the cold, it is probable that HN_3 is formed in liquid phase reactions between the unburned propellant and quenched intermediate combustion products during the shutdown phase of engine operation.

5.4.3 Mass Spectral Analysis of Engine Residues

Additional information regarding the chemical composition of the engine residues was obtained by a mass spectral analysis of the volatile components emanating from the residue formed after a MMN/NTO engine firing. Sample material was obtained from the thrust chamber wall after a firing in which a severe detonation had occurred at the observation window port. Because of the mode of fracture at the window it is believed that the material collected represented a sensitized but undetonated liquid explosive.

As shown by Perlee, an overpressure of the order of 22 kilobars is required to detonate hydrazinium nitrate in an "unconfined" space. No evidence was found from transducer data that pressure levels of this order were present in the chamber. The sample was held at low pressures for several hours at room temperature conditions. Although the sample was held under an inert atmosphere there is a possibility that air oxidation in addition to slow liquid phase reactions occurred.

A typical mass spectral record is given in Figure 39 . This record plots the observed peak height vs. the mass-to-charge ratio. Corrections have been made for the background. Two scale sensitivities are given at the

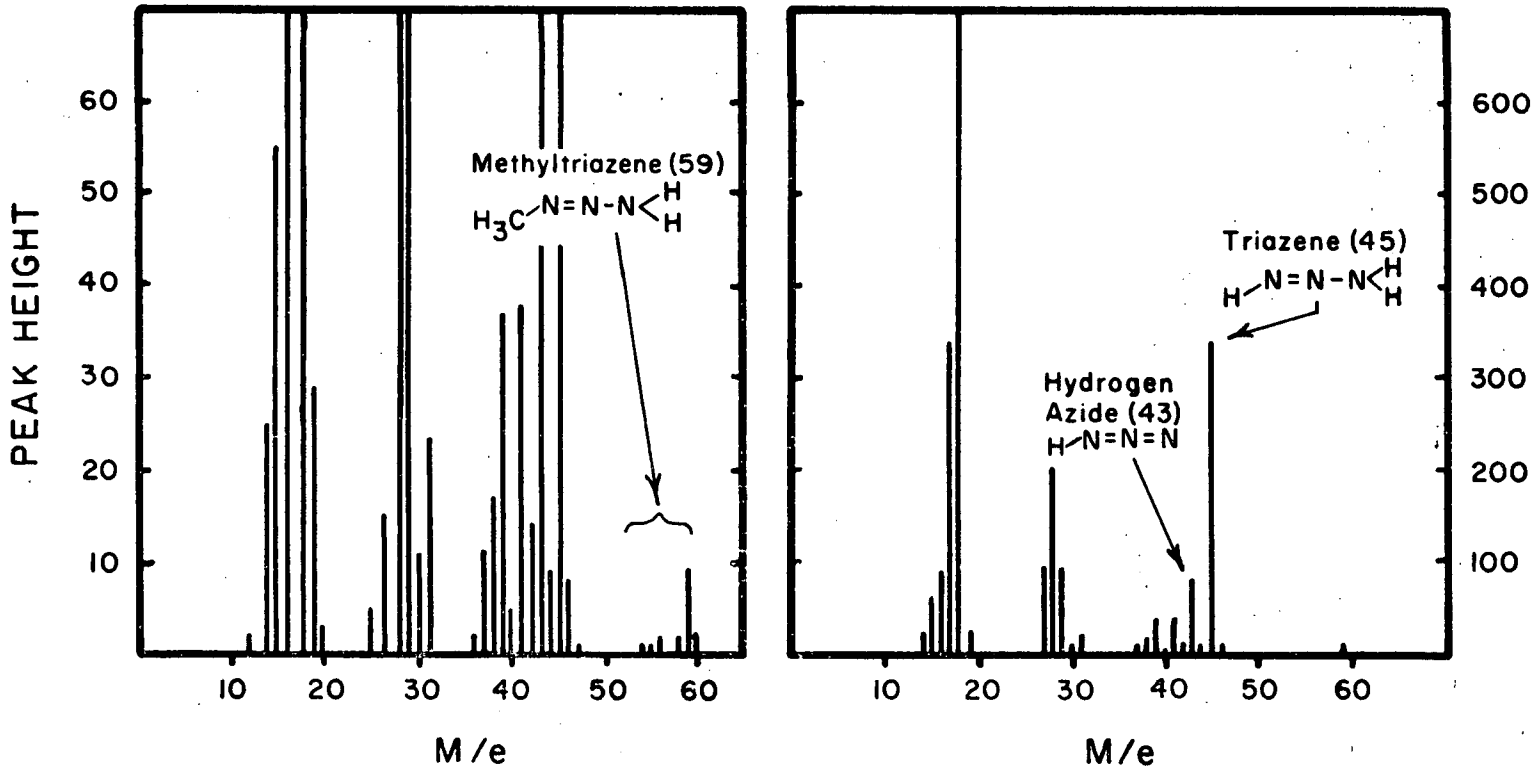

Figure 39. Mass Spectral Analysis

abscissa. Of specific interest to this research are the peaks observed at M/e values of 43, 45, and 59 which are correlated with hydrazoic acid, triazene and monomethyltriazene respectively. The ratio of the 43/42 peak for pure HN_3 reported by Ray et al,[17] is 10:1 which is within the experimental range observed during these studies. No information was found for the spectral breakdown pattern of triazene and monomethyltriazene. A detailed analysis of the breakdown pattern at lower M/e values was not performed since the mixture has a complex breakdown pattern in the lower M/e region. Because the mass spectrometer used a magnetic scanning principle there are substantial differences in M/e peak sensitivities, compared to values given in the American Petroleum Institute Tables.

From these analyses it is concluded that there is evidence for the presence of hydrogen azide, triazene, and monomethyltriazene in the liquid residues. These compounds are known to be relatively shock sensitive and may act as sensitizing agents, i.e., as explosive initiators. Because of the delay in sampling and analysis it is not known whether these are formed on a time scale similar to the engine pulse width or at relatively slow rates. It would be desirable to monitor the gases evolved from the residues using a time-of-flight mass spectrometer directly attached to the thrust chamber.

5.4.4 Emission Spectra Obtained from Hot Firings

Figure 40 shows a typical time integrated spectrum from an MMH/NTO pulse mode engine firing. The spectrum was obtained using a grating Bausch and Lomb spectrograph having a resolution of 14.753Å/mm. Because of the brief duration of combustion, it was necessary to develop a high performance

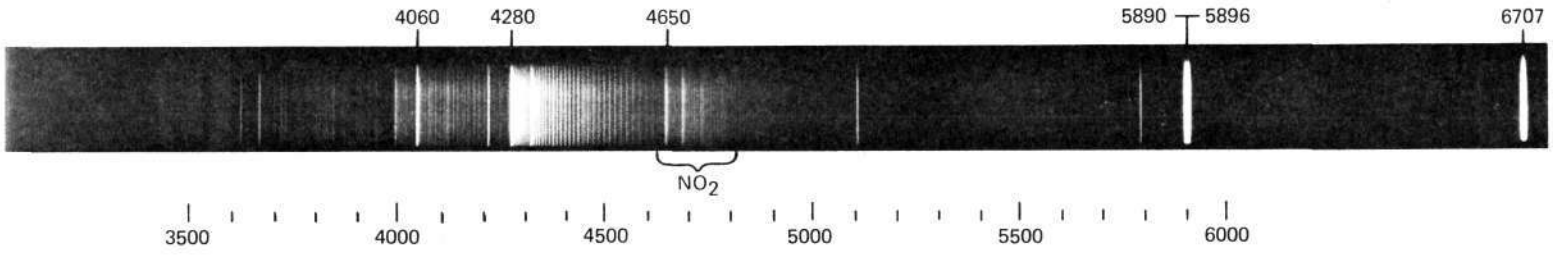

Figure 40. Time Integrated Emission Spectra NTO/MMH Engine Test Firing

film-developer combination. The best compromise between grain size and speed was found to be Eastman Kodak 2485 film using an M62 developer. This combination provided an estimated ASA rating of about 1200. Figure 41 shows a densitometer tracing of the same spectrum. As can be determined from these figures, there is a relatively complex spectral emission pattern exhibited by the reaction. Atomic Na and Li are prominent and serve as a calibration check. The gross structure consists of a series of bands degrading to the red with band heads at approximately 4060, 4280, and 4650Å, together with a series of weaker emission bands extending from about 3200 to the upper end of the red cutoff limit of the film.

The analysis of the spectrum is divided into two parts. The first part is concerned with the identification of the principal emission bands, while the second part is concerned with the identification of the weaker fine structures. This analysis indicates that the species responsible for the three main band structures is an electronically excited metastable state of NO_2. The fine structure or the weaker bands, which can be detected by using a densitometer, consists of a large number of individual species and for the most part represents transient metastable compounds.

The principal emission structure in the region between 4000 and 5000Å can be correlated with an NO_2 fluorescence between a metastable upper electronic state and the ground state. One major problem in making this assignment is the unusual clarity of the band structure. This unusual clarity is difficult to explain unless it is assumed that the usual absorption bands are limited to a specific transition associated with a chemiluminescence reaction. Previous studies in this wavelength region have

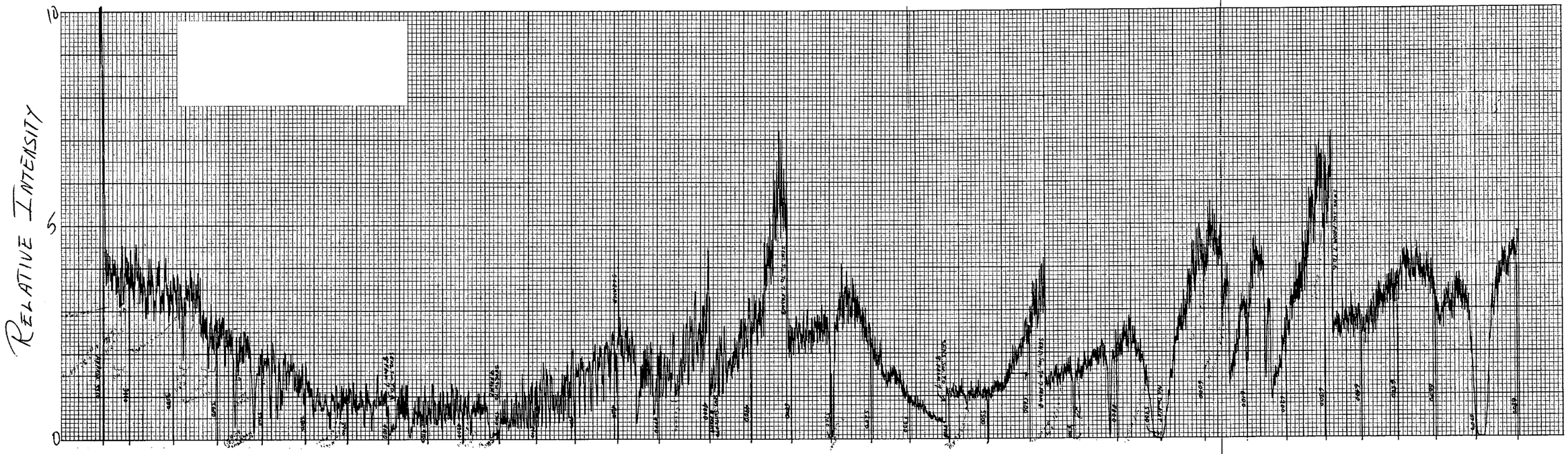

Figure 41. Densitometer Tracing of VISIBLE Spectra from NTO/MMH Residue

FOLDOUT FRAME-1

FOLDOUT FRAME-2

assigned the broad continuum in the region derived from the same fluorescence, and commonly referred to as the afterglow, to a reaction product formed by the reaction $O+NO \longrightarrow NO_2^*$. More recent studies indicate that this continuum is in reality a series of closely spaced lines which extend to the near infrared up to about 1.3 microns.

A number of investigators have examined these structures using both absorption and emission studies. The absorption of NO_2 at low temperatures (liquid helium) was studied by Robinson[18]. The structure at this temperature remains complex, indicating extensive band structures. The visible NO_2 bands have been observed as chemiluminescence in the reaction between NO and atomic oxygen and it is probable that the air afterglow is a pseudocontinuum produced by the many overlapping bands in this reaction. For NO_2 produced by exciting lines photochemically, the lifetime of the excited state is found to be about 44 microseconds. As noted by Hertzberg[19], this lifetime is two orders of magnitude longer than the value calculated using integrated absorption coefficient data. Douglas[20,21] suggests that this difference is connected with strong perturbations of the excited state by the numerous vibrational levels of the ground state. More recently, Douglas and Huber[22] have analyzed a progression of bands among the visible absorption bands with a spacing of 880 cm^{-1}. These bands consist of simple P, Q, and R branches and are assigned to the $K' = 0 \longleftrightarrow K'' = 1$ sub-bands of a $^2B_1 \longleftrightarrow {}^2A_1$ electronic transition.

The assignment of the experimental spectra obtained in this program to a fluorescence of NO_2 was made by a comparison of the spectral flates with absorption and fluorescent emission studies reported in the literature.

Such a comparison shows that many of the bands present are the same as those reported by Douglas and by Douglas and Huber*. In the region between 4100 and 4800Å a progression involving an 880 cm^{-1} interval is seen. Band heads at 4020 and at 4260 correspond to those reported above.

A difficulty in these assignments in the relatively sharp features of the spectra. Instead of a relatively diffuse continuum a series of rather well defined lines is recorded. One explanation for this effect may be the production of an excited metastable NO_2 state directly in a one-step reaction. As reported by Broida[23], the spectra obtained using an emission produced when atomic oxygen and nitric oxide are mixed has a definite structure, and therefore direct reaction

$$NO + O \longrightarrow NO_2 + h\nu$$

In order to explain these results it was necessary to develop a kinetic reaction sequence involving the following sequence of reactions in which the energized NO_2 formed via the reaction of NO and O is collisionally stabilized to form a metastable NO_2* molecule in an excited electronic state. The NO_2* can then either radiate or be collisionally stabilized to form NO_2 in the ground state. The fluorescence then is exhibited as a discrete spectrum in the bands observed. This process can be shown by reference to a potential energy diagram taken from Broida and shown in Figure 42 .

The reaction between NO ($^2\Pi$) and O (^3P) results in a

*ibid

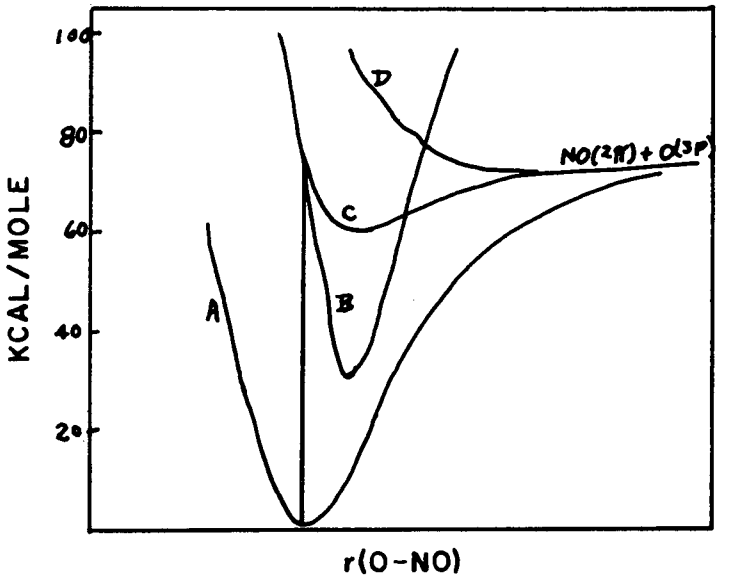

Figure 42. Potential Energy Curves for NO_2 Dissociation

repulsive state D or a bound state C. Radiation from C to A directly would be expected to result in a relatively ill-defined spectrum because of the shallow potential minimum exhibited by the state C. However, the transition of C to B can occur by a resonance transfer process. Molecules formed in B can radiate to the ground state A and because the potential minimum is deep, a complex structure can result. The spectra thus observed corresponds to the experimental spectra obtained in this program. The major difference is an increased definition of major structure.

Under the present experimental tests it is unlikely that a direct reaction between NO and O occurs. There is no evidence for the presence of appreciable quantities of atomic oxygen in the spectra, although further work should be performed in the ultraviolet regions to verify this point. Under the present reaction conditions a direct formation of the upper electronic state of NO_2 (B) in a bimolecualr collision between NO and NO_2 is much more likely. In this case, reactions (1) and (2) are combined in one step, resulting in an oxygen transfer reaction. The subsequent reaction sequence remains unchanged and involves either a radiation or collisional deactivation. Because the NO_2 (B) is formed directly, the reaction NO_2 (B) $\longrightarrow$ NO_2 (C) must be relatively slow compared to the probability of radiation to the ground state, thus accounting for the clarity of the spectra.

An estimate of the spectroscopic value for the heat of reaction of $NO_2 \longrightarrow NO + O$ (all ground electronic states) can be obtained from the observed short wavelength cutoff at 4060 $\pm$20Å. Examination of

the weaker emission bands indicate the presence of a number of individual band or atomic lines. In addition to the presence of Na and Li in the spectra, other components which have been tentatively identified are CH, OH, the further positive bands of N_2, CN, NO, weak NH_2, and others. These species would all be expected to result in gas phase reactions at high temperatures, and therefore their presence is predicted.

Under most circumstances these bands would be much greater in intensity and thus their relatively weak intensity must be explained. Because of the relative weak intensities observed, it is quite likely that these molecular species are present in relatively low concentrations. Based on calculated integrated emission probability functions the resultant spectra should be much stronger. The most probable explanation for the lack of intensity is that the concentration levels are low, corresponding to a nonequilibrium distribution of propellants. Therefore, it is inferred that kinetic processes involving the vaporization of the fuel component may be important. This inference is supported by other lines of evidence including direct photographic documentation of the startup of the chemical reactor.

Perhaps as important to the above argument as the species observed is the absence of major expected emission bands. There is little evidence that the NH_2 alpha emission bands are present or that hydroxyl radical is present in the reaction mixture. Although the strongest emission band for hydroxyl emission is the 3064Å band which

is interfered with by the fore optics of the spectrograph, in the tests using a Cini quartz prism spectrograph no OH was found. This also tends to confirm the possibility that there is a high degree of nonequilibrim.

5.4.5 HNO in Emission

A typical "real time" emission spectrum from MMH/NTO engine firing is presented in Figure 43 . Analysis of this spectrum indicates that the HNO (100 - 000) transition at 6170Å may be present in emission. The assignment of this band is based on the work of Cashion and Polanyi[24] . Unfortunately, because of a dropoff in the film recording sensitivity above the 6500Å region, confirmation of the $(0,1,0)' \rightarrow (0,0,0)''$ and $(0,0,0)' \rightarrow (0,0,0)''$ bands at 6930Å and 7680Å respectively, could not be made. Additional data is necessary in the near infrared region in order to remove possible ambiguities in the band assignment. The presence of this band correlates with infrared absorption data obtained from engine residues and may indicate that metastable intermediate products condense on the engine walls. The lifetime of HNO in the excited state is long relative to the pulse firing duration and has been estimated to be 0.1 second by several investigators. This is much longer than the total firing duration of our present engine.

5.4.6 Physical Characterization of the Residues

The liquid residues formed in a pulse mode engine had a consistency corresponding to a medium to high viscosity liquid. The material was yellowish-brown, which after a period of several days

C 2

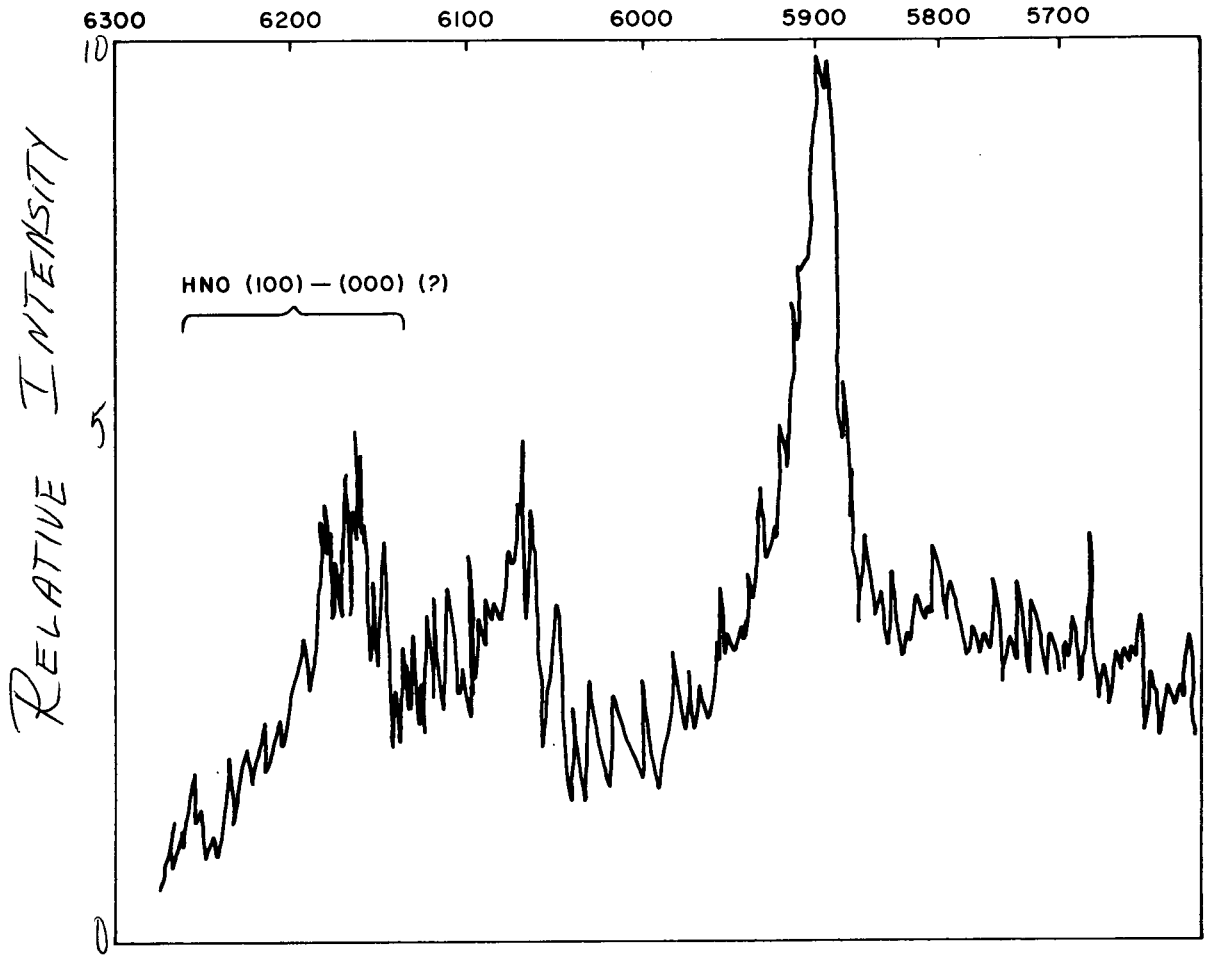

Figure 43. Hydrazine-Nitrogen Tetroxide Spectra

turned into a dark aquamarine. The specific gravity was 1.2 for a residue formed from an MMH/NTO test. The residues under vacuum had a frothy characteristic and were observed to outgas or bubble at a relatively fast rate. A photomicrograph of a typical residue is shown in Figure 44 . As can be observed, a large number of gas bubbles is present. The largest bubble diameter (at ambient pressure) was 1.2 mm. A plot of the distribution of sizes in a typical area is given in Figure 45. It can be seen from this plot there is a relatively large number of smaller bubbles in the mixture, but frequency of occurrence is relatively constant in the range 0.2 to 0.5 mm. The fact that the bubbles coalesce into each other accounts for the smaller number at the larger diameter. The maximum bubble diameter is limited by the depth of the film thickness.

5.4.7 Pressurization Studies for N_2O_4

A series of time/pressurization curves were developed for NTO injected into air at various start pressures. The experimental results are shown in Figures 46 through 47 . As expected the rate of pressurization is dependent on the initial start pressure and is much more rapid at low initial pressures, decreasing with increasing ambient pressure. A comparison of the rate of pressurization for a N_2O_4 pressurization calculated by the CSC program[2] was made and a typical run presented below.

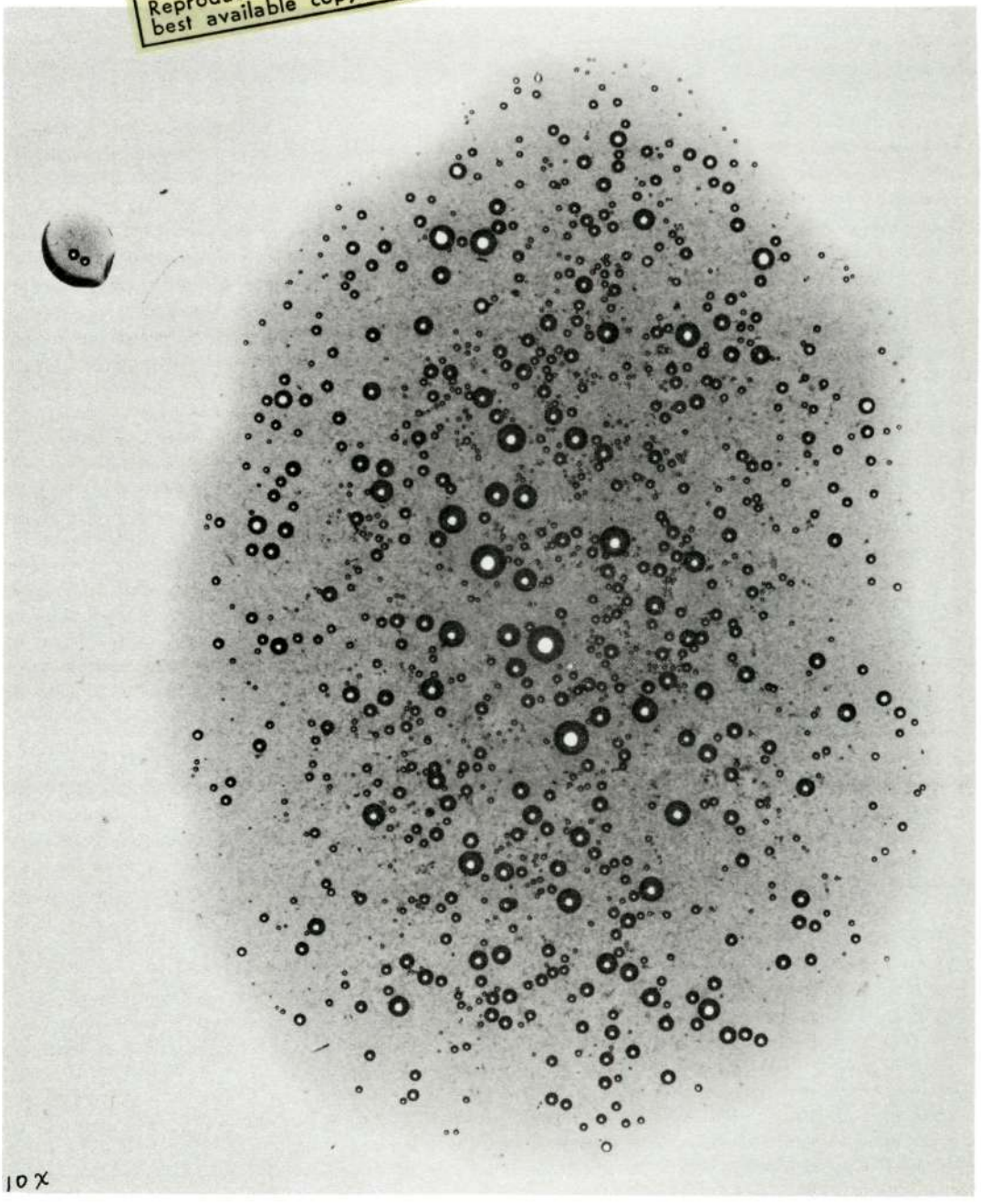

Figure 44. Photomicrograph of Propellant Residue

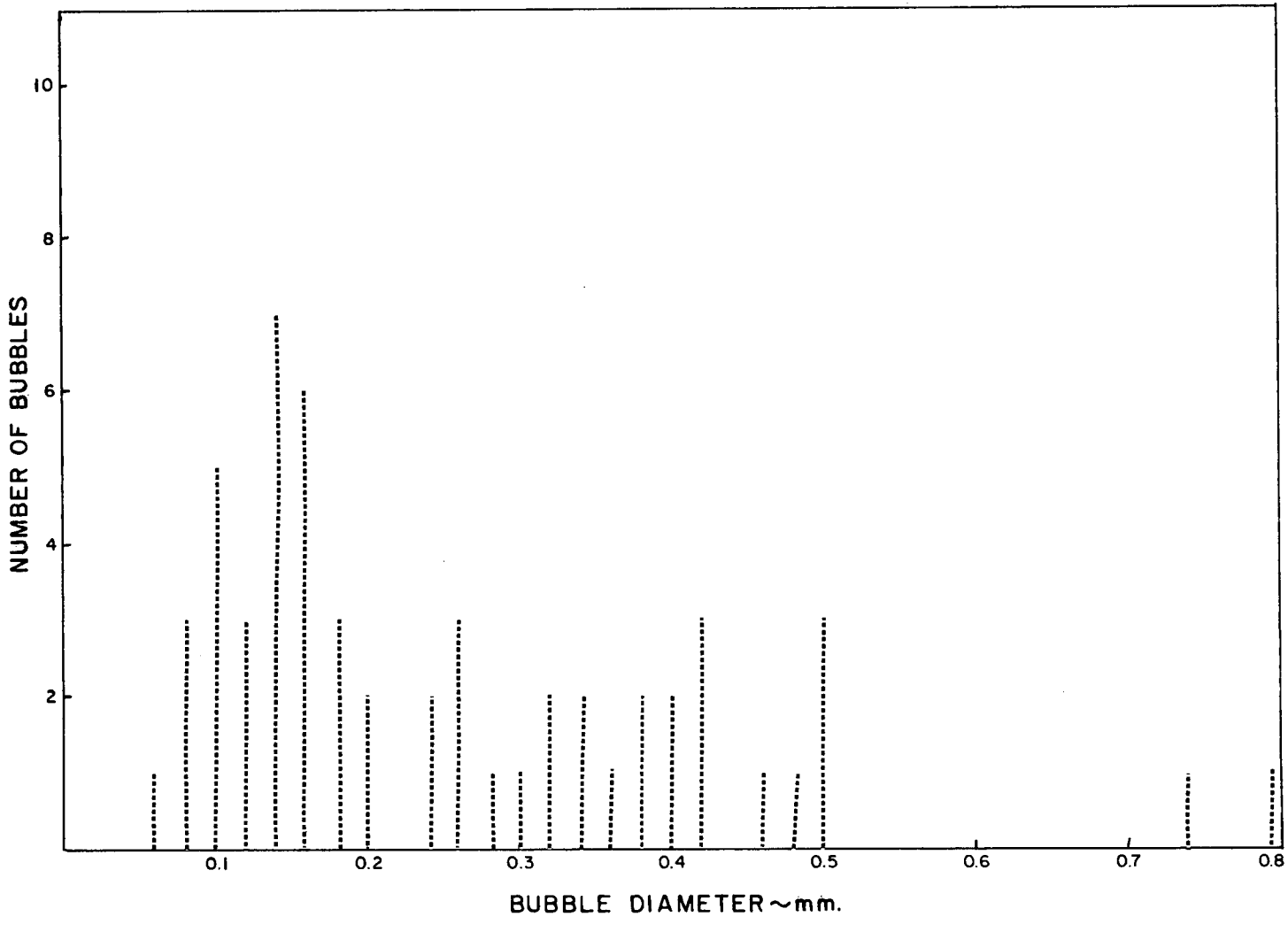

Figure 45. Size Distribution of Bubbles at 1 Atmosphere for NTO/MMH Residue

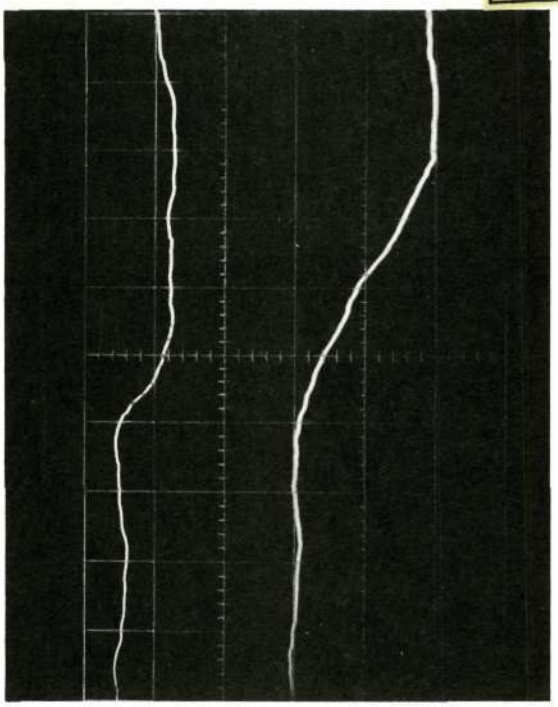

Run 25. Start pressure: 6.0 psia

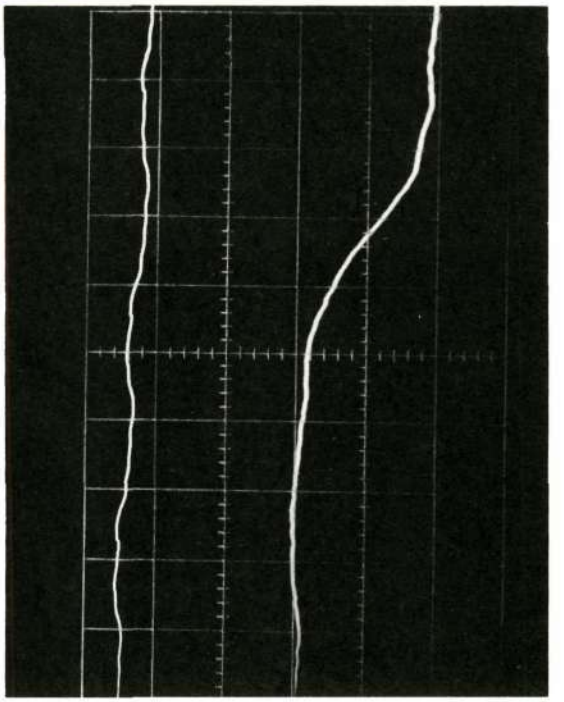

Run 27. Start pressure: 12.0 psia

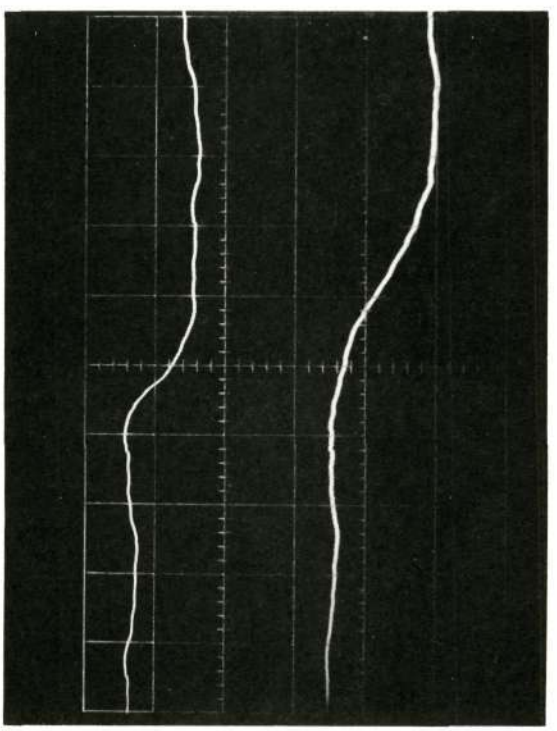

Run 24. Start pressure: 2.75 psia

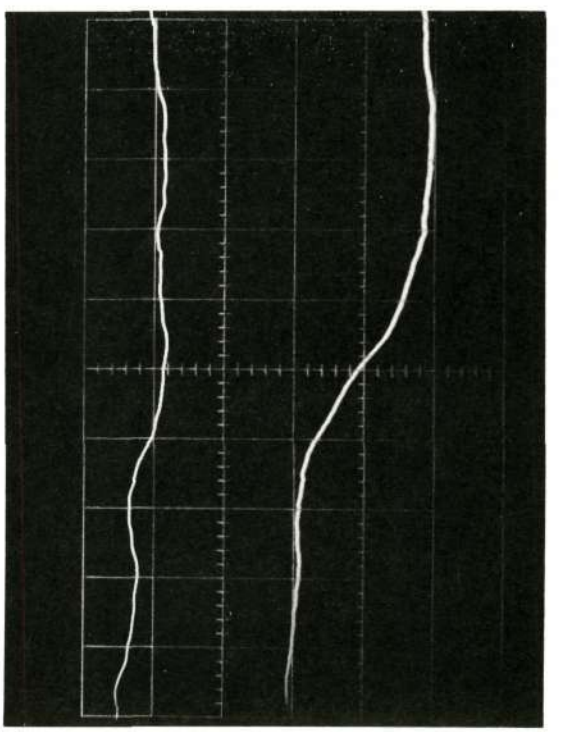

Run 26. Start pressure: 9.0 psia

Fig. 46 Pressurization Rate Histories for a N_2O_4 (1) Jet Stream Under Simulated Space Start Condition.
(Top trace: Pressure, Bottom trace: Flow, Time base: 5 ms/cm, N_2O_4 flow volume: 1.5 cc, Transducer pressure: 50 lb/cm)

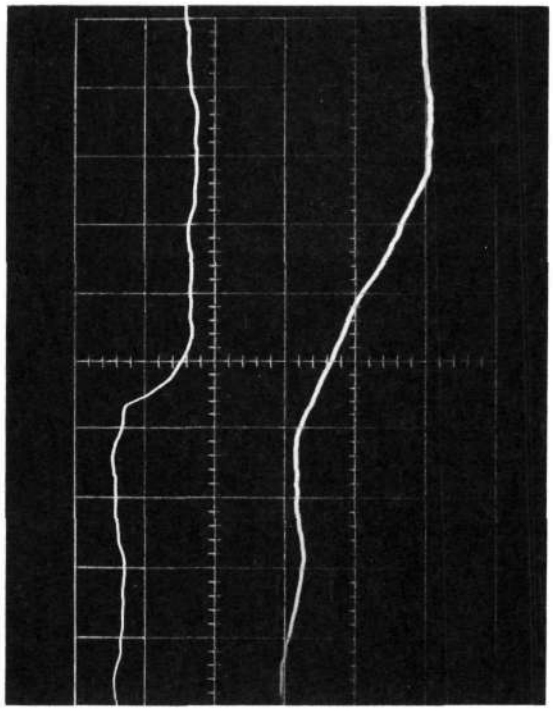

Run 16. Start pressure: 15 mm Hg.

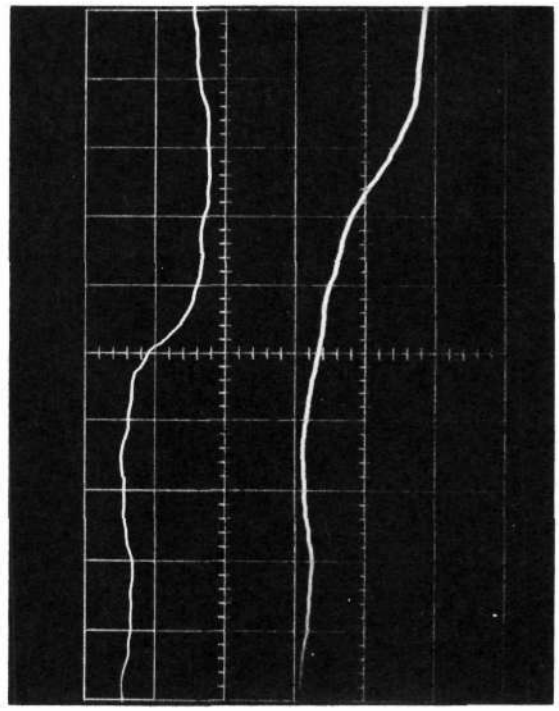

Run 22. Start pressure: 20 mm Hg.

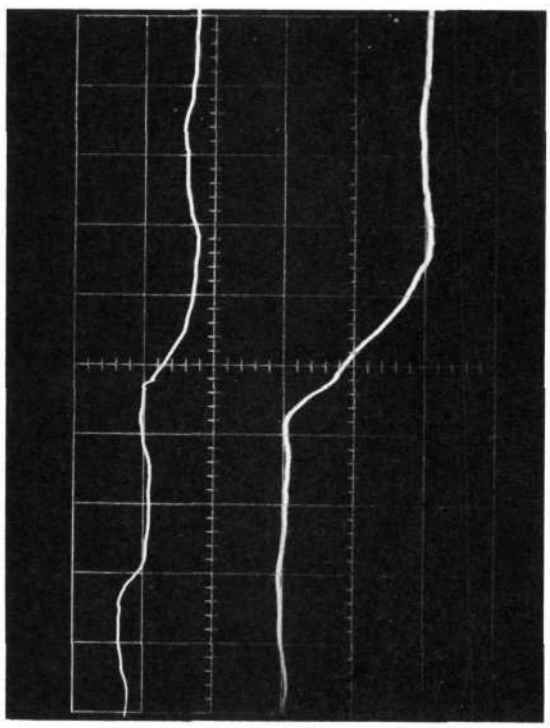

Run 15. Start pressure: 10 mm Hg.

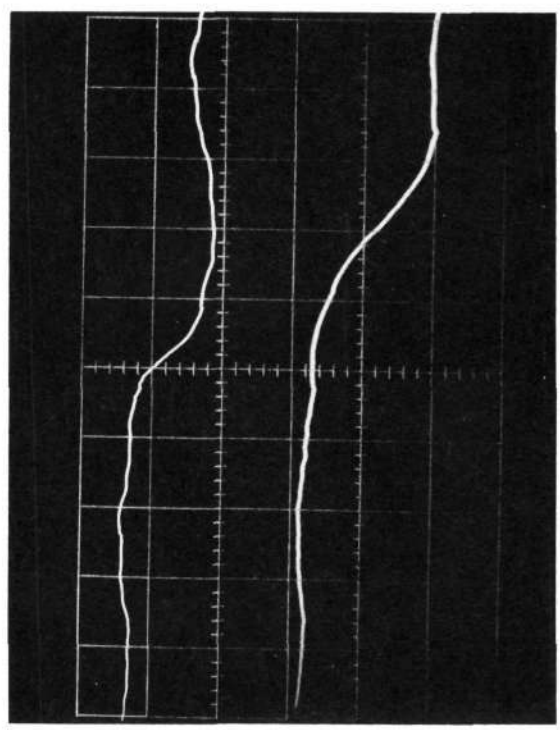

Run 21. Start pressure: 20 mm Hg.

Fig. 47 Pressurization Rate Histories for a N_2O_4 (1) Jet Stream Under Simulated Space Start Condition.
(Top trace: Pressure, Bottom trace: Flow, Time base: 5 ms/cm, N_2O_4 flow volume: 1.5 cc, Transducer pressure: 50 lb/cm)

	Pressure	
Time	Experimental	Calculated
0 ms	0 psia	0 psia
1 ms	10 psia	3 psia
2 ms	17 psia	10 psia

As can be readily observed there is a difference of a factor of two or three between the rate of pressurization experimentally determined and the rate as calculated in the preignition time regime using the Seamans program. This study was conducted in order partly to provide a better understanding of the vaporization rates as they affect the ignition and partly to document the phenomena using the unique flow time analytical capability of the rocket engine developed on this program.

5.5 Ammonia/Hydrazine Mixtures

One of the obvious problems was that the one-on-one injector used in this study did not produce the same droplet size distribution for the hydrazine fuels and the nitrogen tetroxide oxidizer. This fact makes any interpretation using analytical models involving uniform droplet sizes (e.g., Seamans[2] program) extremely questionable. Two solutions to this problem of increasing the breakup of fuel sprays were investigated. One solution involved the use of a chemical additive and the second involved the use of heated fuels in which the fuels were heated up to a temperature at which the vapor pressure of the hot hydrazine was equal to the vapor pressure of nitrogen tetroxide at normal temperature

injection conditions. Because the use of chemical additives imply a reduction of performance it was desirable to illustrate the principle by using an "additive" which would in itself be a high performance propellant fuel. Ammonia (NH_3)was chosen for this purpose and mixtures of ammonia/hydrazine were injected into the space chamber using the injector block assembly previously described. Typical results of this test are shown in Figures 48 a,b,c. Figure 48a shows N_2O_4 injected at about 15 mm Hg, Figure 48b shows N_2H_4 injected at about 10 mm Hg,and Figure 48c shows a 52/48 percent by weight mixture of $NH_3(l)/N_2H_4(l)$ injected at 10 mm Hg. As can be readily observed, there is little breakup of the N_2H_4, a very rapid breakup of N_2O_4 with a characteristic fan at the injector face and a reasonably good dispersion of the NH_3/N_2H_4 propellant under these conditions. It was concluded that if it became necessary to increase the dispersion of liquid hydrazine fuels it could be accomplished by changing to a NH_3/N_2H_4 mixture. It is also noted that theoretically it should be possible to make substantial changes in the rate of propellant stream breakup by modifying the surface tension and that the use of surfactants (surface active agents) used in the stabilization of gels, etc., should be investigated. There is a problem of the transport of the surfactant molecules to the droplet surface under the very short times associated with the injection process.

5.6 Heated Propellant Dispersion Studies

The above argument is based on the concept of changing the vapor pressure of the fuel to enable a sure rapid volatilization and breakup

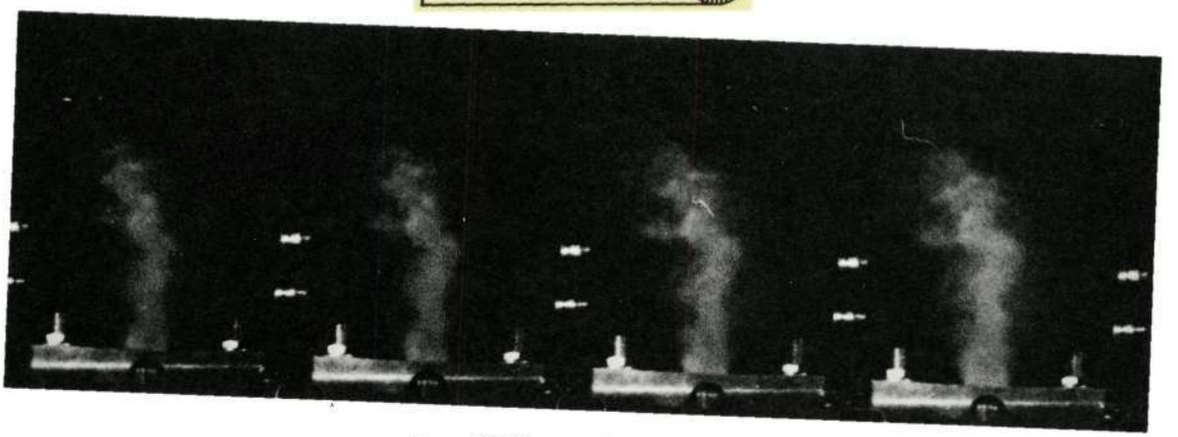

a. N_2O_4 at 15mm Hg

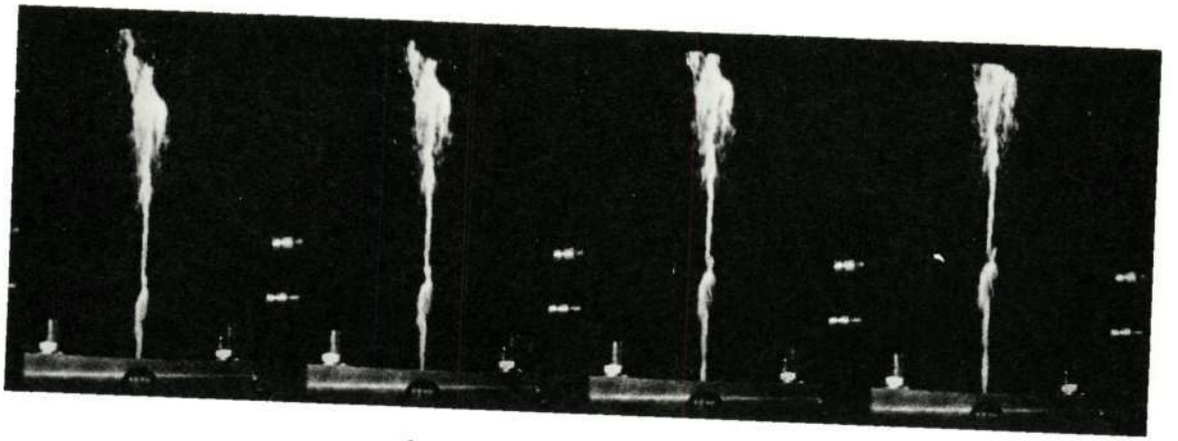

b. N_2H_4 at 10mm Hg

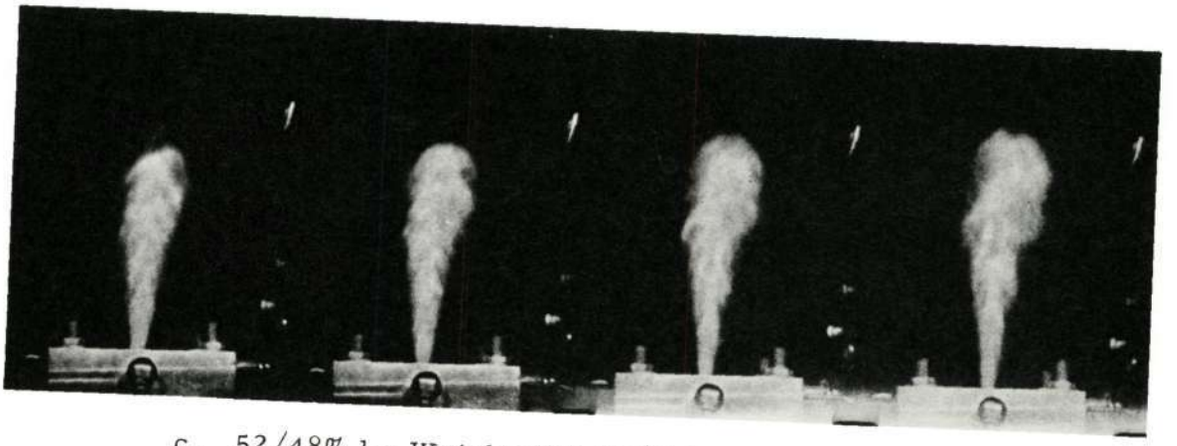

c. 52/48% by Weight NH_3 (ℓ)/N_2H_4 (ℓ) at 10mm Hg

Figure 48. Comparison of Spray Patterns for N_2O_4, N_2H_4, and a 52/48 Mixture of NH_3 (ℓ)/N_2H_4 (ℓ)

of the jet stream. Theoretically, it should be possible to accomplish the same effect by heating the propellant fuel to a temperature corresponding to the temperature at which the vapor pressure of the fuel jet is approximately equal to the vapor pressure of the oxidizer at ambient temperature. A series of hot fuel tests were conducted to verify this hypothesis. The results of this series of tests are shown in Figure 49. As can be readily observed there is only a very small change in the dispersion of the jet of hydrazine at 165°F. Therefore, although it may be beneficial to heat the propellant in order, for example, to increase the reaction rates, the heating apparently does not make a substantial change in the rate of jet disintegration under these experimental circumstances.

5.7 Real Time Pressure and Visible Emission Tests for a N_2H_4/N_2O_4 Propellant

5.7.1 Pressure Studies

Experimental pressure data were obtained for a N_2H_4/N_2O_4 rocket test firing. The test conditions included startup using a clean engine at a simulated altitude greater than 90,000 feet. During this test one of the two 1/4 in. quartz viewing ports was blown out. The fracture pattern indicated destruction probably occurred via a high overpressure rather than a detonation at the window site. Propellant flow was characterized by a 2 msec fuel lead and total flow time was approximately 20 msec. The pressure-time trace indicated a series of three pressure spikes each in excess of 700 psi. The individual pressure spikes are separated by 3 to 4 msec indicating a low frequency chugging at 250-300 cps. There was a one-to-one correspondence

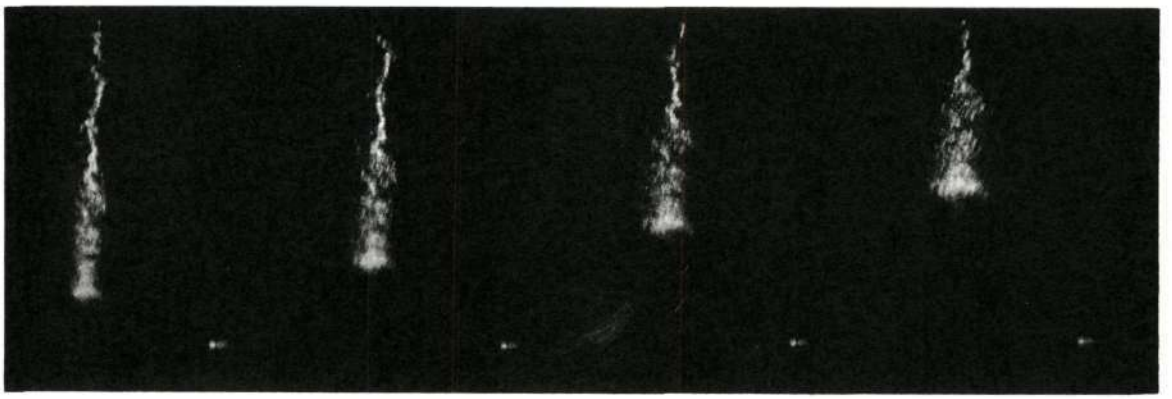

a. N_2H_4 Dispersion at 125° F

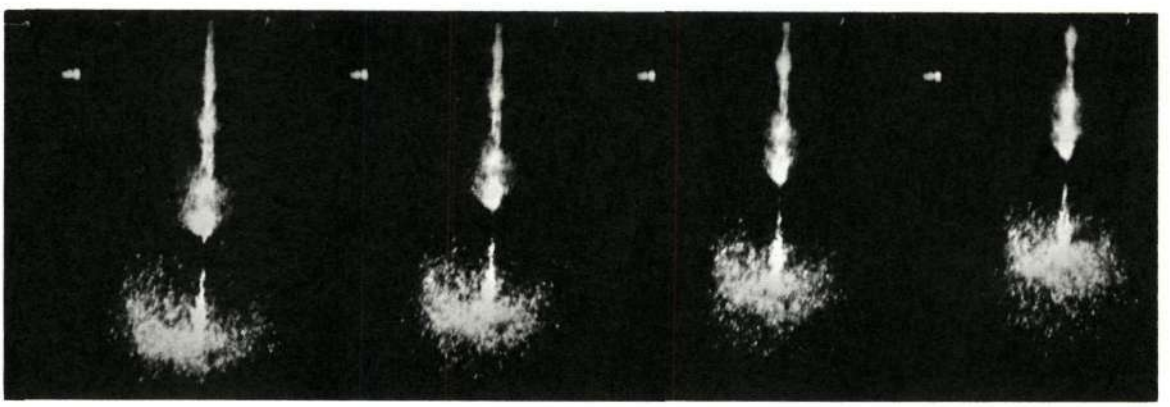

b. N_2H_4 Dispersion at 165° F

Figure 49. Effect of Fuel Temperature on Hydrazine Jet Spray Pattern

between these low frequency pressure fluctuations and observed variations in the fuel and oxidizer flow rates.

A composite pressure-time history of the test is given in Figure 50 through 52. This history covers the time immediately prior to ignition to the onset of the post combustion time period. In this case the time scale was expanded to 100 μsec - cm^{-1} in order to be able to correlate pressure fluctuations with emission spectra obtained from the W/S scanning spectrophotometer operated at a 1.25 msec sweep rate.

Immediately after ignition a base line shift occurs for the pressure transducer output. This shift requires a correction of 300 psi to be applied to the data. It was believed that this shift was caused by the thermal shock of the piezoelectric crystal. In order to verify this hypothesis a series of tests were performed in which radiant energy emanating from an A-1 flashbulb was directed onto the surface. A direct correlation was made between the flash duration and the base line deflection of the transducer under conditions involving no change in pressure. Although the rise time of the flashbulb is slower than the observed rise time of the spectral radiation and pressure in the 2-dimensional rocket engine, the grey body emissivity of the bulb is about the same as that expected from the rocket combustion. From this evidence it was concluded that the base line shift is caused by the influx of radiant energy onto the surface of the transducer and not to other possible sources of instrumental error such as point-contact inductances.

Although the physical and chemical processes occuring in the thrust chamber are very complex, the form of the correction curve to

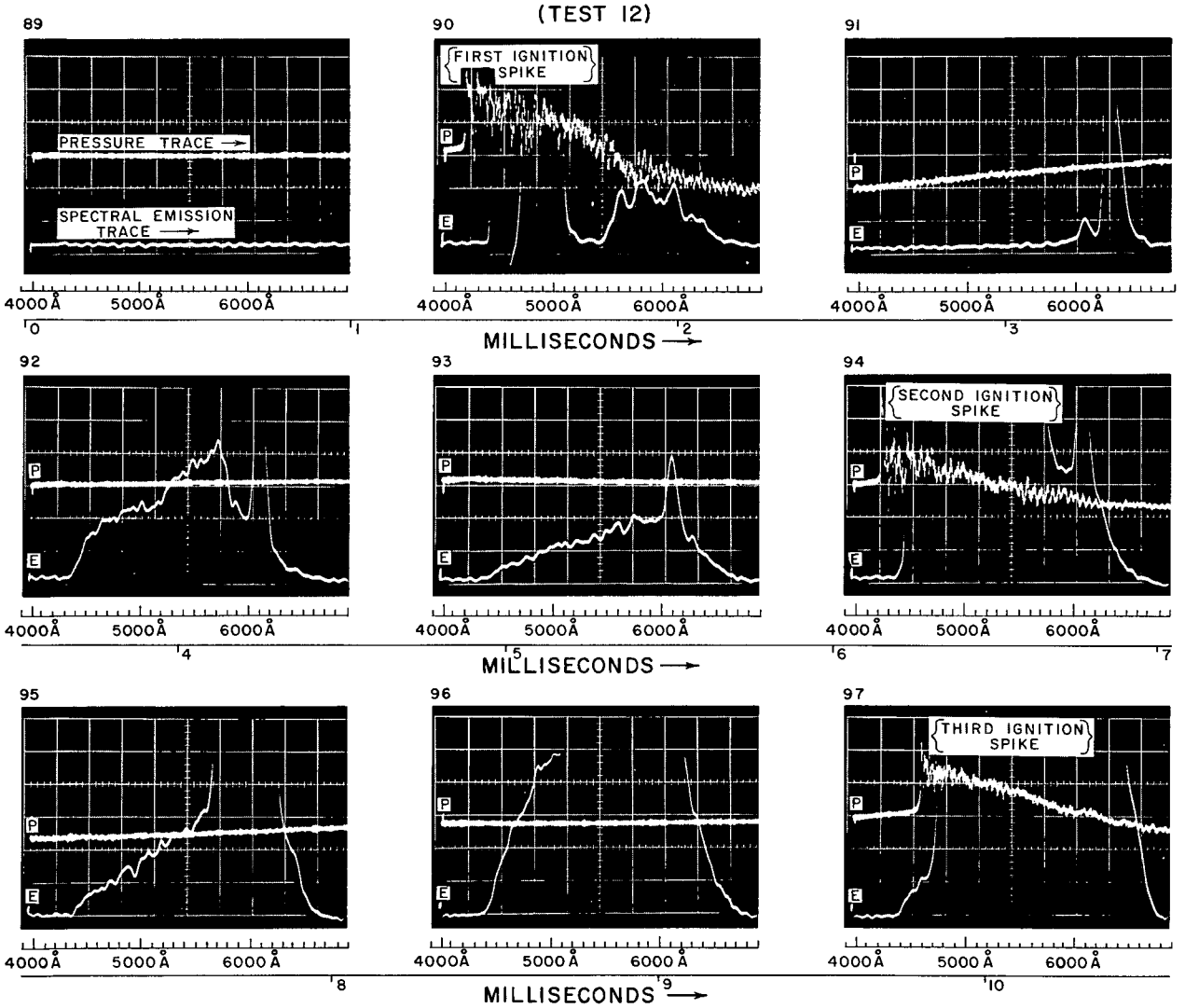

Figure 50

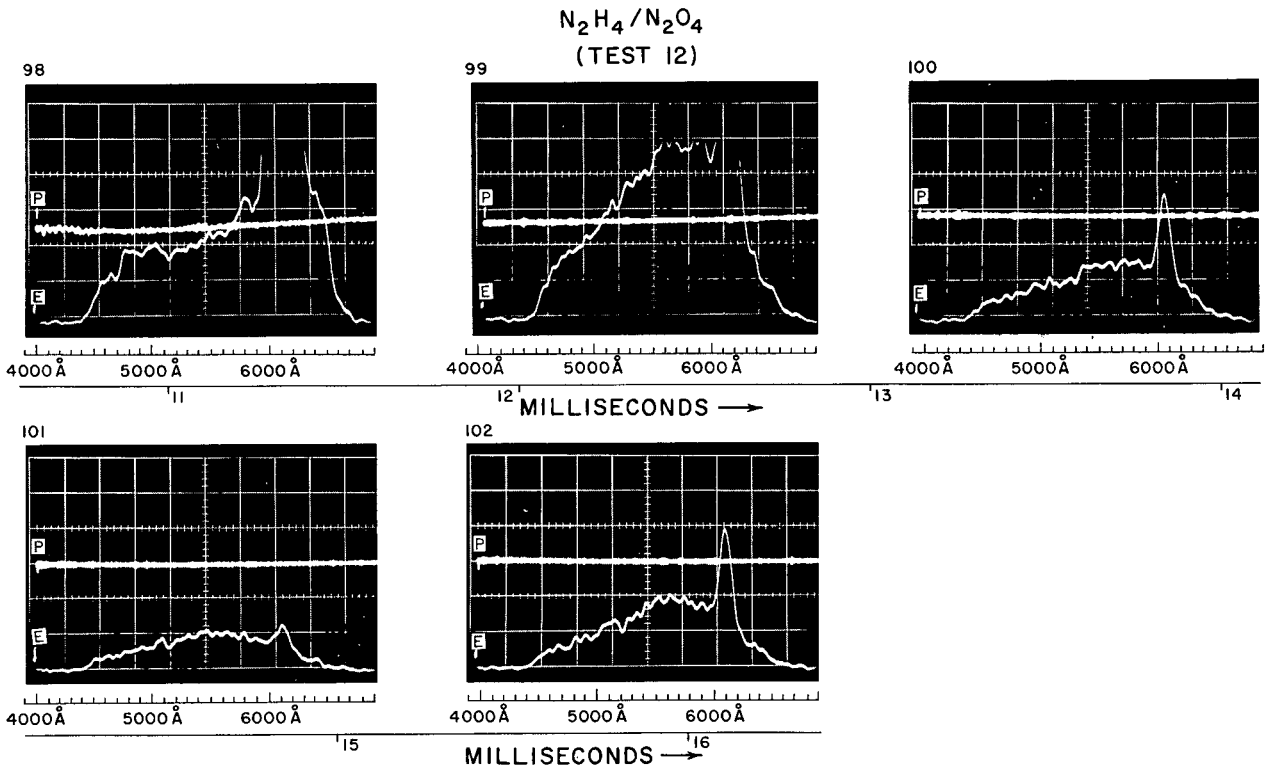

Figure 50 (cont.)

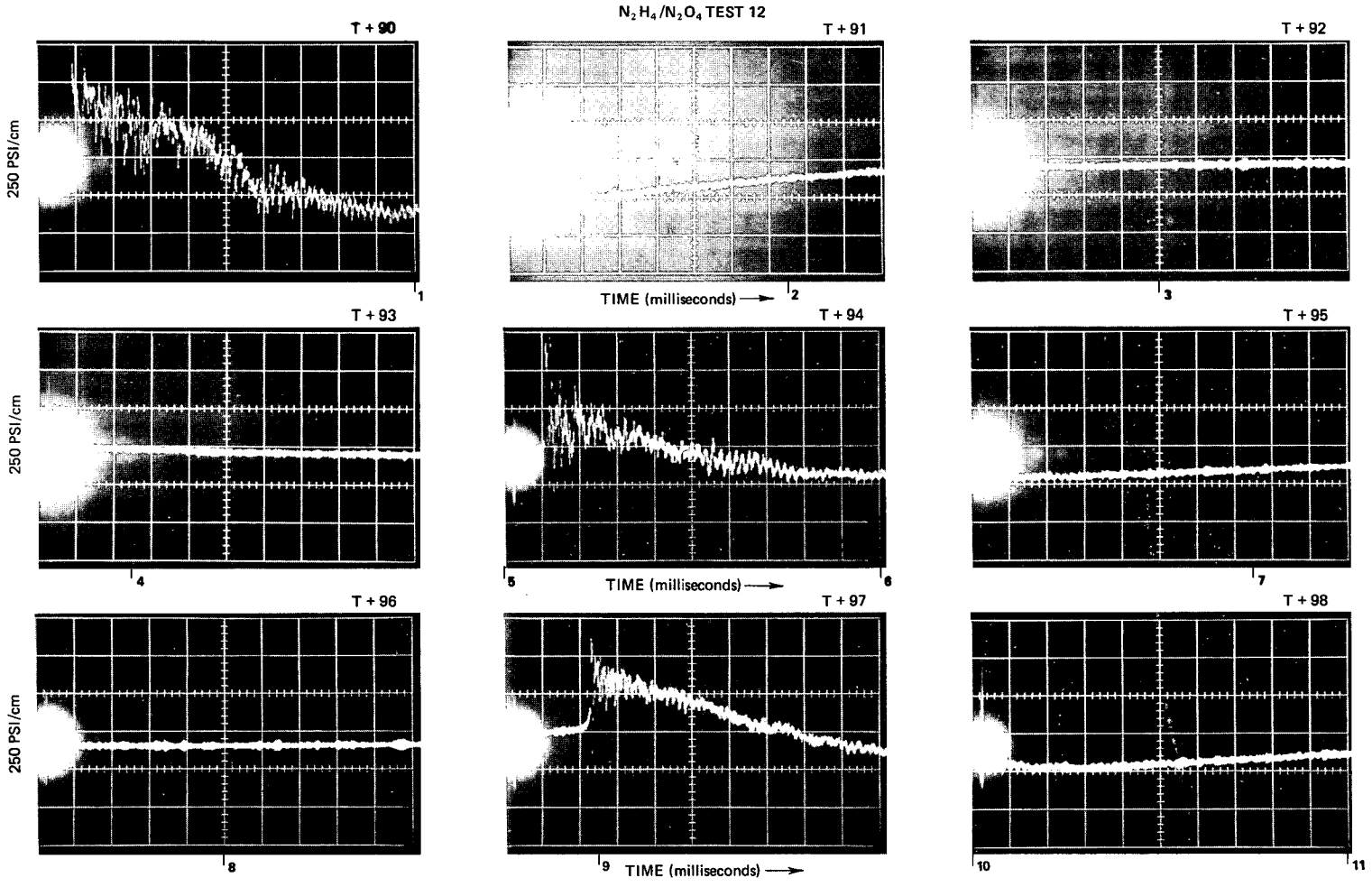
N_2H_4/N_2O_4 TEST 12
T + 90
T + 91
T + 92
T + 93
T + 94
T + 95
T + 96
T + 97
T + 98
250 PSI/cm
250 PSI/cm
250 PSI/cm
TIME (milliseconds) →
TIME (milliseconds) →
TIME (milliseconds) →
1
2
3
4
5
6
7
8
9
10
11

Figure 51

N_2H_4/N_2O_4

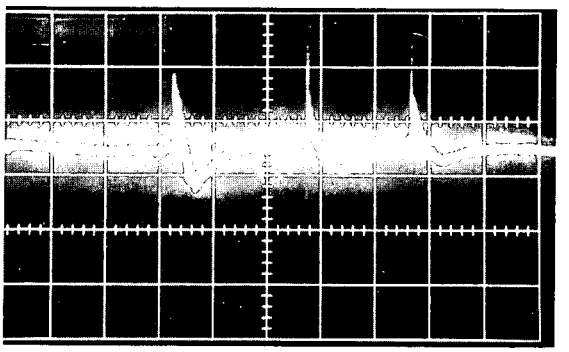

Test 12 (T + 85) 2 msec/cm → 500 PSI/cm ↑

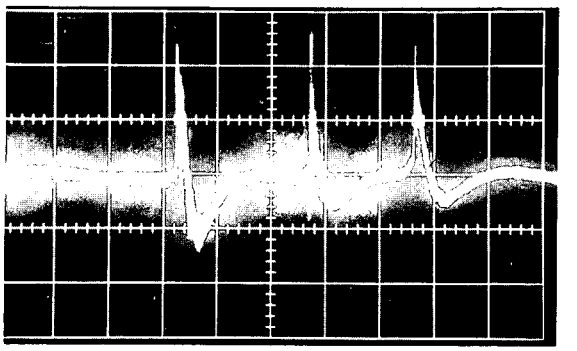

Test 12 (T + 85) 2 msec/cm → 250 PSI/cm ↑

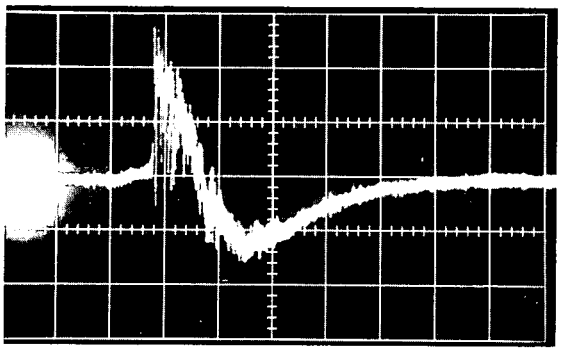

Test 12 (T + 89) 500 μsec/cm → 250 PSI/cm ↑

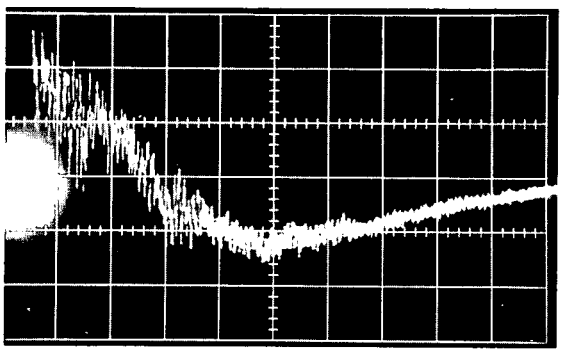

Test 12 (T + 90) 200 μsec/cm → 250 PSI/cm ↑

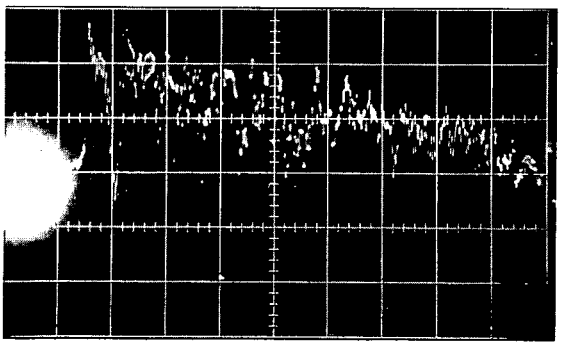

Test 12 (T + 90) 50 μsec/cm → 250 PSI/cm ↑

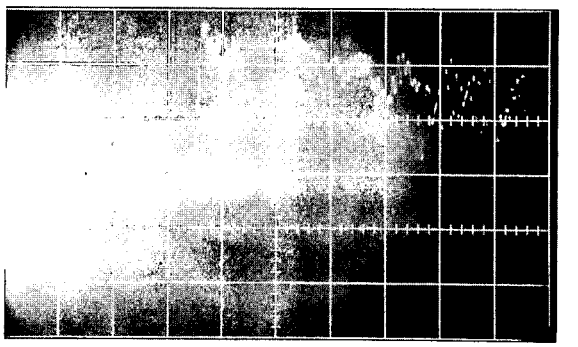

Test 12 (T + 90) 20 μsec/cm → 250 PSI/cm ↑

Figure 52: Pressure-Time History of N_2H_4 /N_2O_4 Firing

be applied to the transducer output can be obtained by observing that immediately following the high pressure transient a series of rarefaction waves occur. Evidence for this effect is indicated by the voltage output falling below the original base line. This envelope of points provide a minimum value to the rate of shift of the base line caused by thermal shock, since it can be shown that the value of the pressure during this rarefaction cannot be less than zero. Using this envelope of points the actual chamber pressure can be estimated.

The gross pressure-time history indicates a series of three high pressure transients. It is probable that each of these three transients represent a separate ignition event since direct propellant flow measurements indicate that the chamber pressures are high enough to reverse the flow in the injector manifold and propellant tanks. The result of flow reversal caused by a preceding pressure spike is that the next overpressure spike results from propellant flow conditions with zero fuel lead or lag. Therefore a number of similarities should exist in the detailed pressure-time history of each overpressure spike.

The structure of each "ignition spike" appears to be similar. A gross description indicates that there are four regions of interest. The first region consists of the preignition time period in which no increase in pressure is observed (within experimental error). The second region is the initial buildup of pressure in the engine. This occurs in time period of 30-50 μ sec during which time the chamber pressure rises from a very low value to a pressure level between 75 and 150 psi. The shape of the pressure curve is expotential in form indicating the onset of a "runaway" temperature excursion. This is

typical of combustion processes accelerating from a normal deflagration to a detonation. The third region occurs over a time period of about 20 μ sec. During this time period a closely spaced series of high pressure transients are observed. The pressure levels reached during this time period are in excess of 1000 psi with rise times on the order of between 1 to 2 μ sec Because the response of the 603Å transducer is limited to 1 μ sec it is possible that the actual pressure rise times may be considerably shorter. The fourth time region probably involves a "more or less steady state" deflagration of the propellants which results in a pressure decay from about 700-800 psi to a low steady state chamber pressure.

A preliminary analysis associated with the third region of interest indicates that there are at least three superimposed wave forms with individual frequencies of 4×10^5, 4×10^4 and 2×10^4 cps respectively. The high frequency component corresponds to the crystal ring frequency of the 603Å transducer. The low frequency component can be interpreted as a standing wave in either the longitudinal or lateral resonance modes of the thrust chamber. The component undergoes a rapid attenuation. If this assignment is correct then an average chamber temperature in the neighborhood of 3000°K can be derived implicitly from sonic velocity considerations. Two alternate assignments can be made to account for the intermediate frequency wave form. The first alternative involves the excitation of a standing wave oscillating in the vertical mode (short path length) of the thrust chamber. This assignment then implies a localized temperature

between 5000-6000°K. A second alternative is to assign the intermediate oscillation to the excitation of a standing wave in the thrust chamber walls. The implied sonic velocity of 20,000 fps is similar to that expected for an aluminum thrust chamber. This latter assignment requires a relatively close coupling of the thrust chamber with the transverse oscillation mode of the piezioelectric crystal. Experiments in which an explosive actuation of the normal resonance frequencies of the thrust chamber are planned for the future in order to aid in the interpretation of the transducer output signals in this intermediate range.

5.7.2. Spectral Emission Studies in the Visible Region

5.7.2.1 Analytical - The Effect of Pressure on High Temperature Gaseous Emissivities

As described previously, strong pressure fluctuations are observed during the ignition and combustion of the N_2H_4/N_2O_4 pulse mode rocket engines. In order to interpret the spectral emission obtained during engine test firing it is necessary to understand the relation between molecular emissivities and pressure. A preliminary analysis of the dependence of emissivity on pressure is outlined in this section. The treatment presented herein closely follows that of Penner.

The effective emissivity $\epsilon_{eff,i}$ of an individual species in a high temperature gas is given by the expression

$$\epsilon_{eff,i} = \frac{4.76 \times 10^{7}}{26.4}\left(\frac{hc}{kT}\right)^{5} \omega_o^{4} \exp\left(\frac{-hc\,\omega_o}{kT}\right)\left(2\delta\psi f\frac{\rho}{\rho_o}\right) \quad (1)$$

where h = Plancks constant

k = Boltzmann constant

T = absolute temperature

c = the velocity of light

ω_o = the fundamental vibrational frequency

δ = path length

f = the absorption oscillator strength

ψ = the ratio of the number of species i molecules to the total number contained in the system

ρ/ρ_o = the density of the system relative to its density at STP conditions.

The spectral distribution of radiant energy for each species is given by

$$\frac{d\epsilon_{eff,i}}{d\omega} = \epsilon_{eff,i} \frac{4\omega^2 d\omega}{\omega_o^4} \qquad (2)$$

For each molecular species (e.g., NO) it is necessary to sum over each band that can contribute to the radiant energy.

For NO, the G and γ bands are of major importance in the visible region. These bands correspond to the

$$B^2\Pi \rightarrow X^2\Pi \text{ and } A^2\Sigma^+ \rightarrow X^2\Pi \qquad (3)$$

transitions respectively and

$$\epsilon_{tot} = \sum_j \sum_i \epsilon_{eff,i} \qquad (4)$$

From this sum it is possible to determine both the shape of the emissivity curve as well as the absolute magnitude of the total energy flux in any specific interval of wavelength.

Pressure effects on emissivity occur from interactions of the last four parameters of equation(1). As a first approximation it can be assumed that the major effect will result from variations in ρ/ρ_o. This assumption results in a linear dependence of effective emissivity on pressure.

The effect of ignoring the ψ parameter is to legislate that the pressure fluctuation frequencies are much faster than the characteristic kinetic relaxation time of the system. It is probable that this parameter can be neglected for the intermediate frequency pressure oscillations but that substantial errors may exist in correlating emissivity data for the low frequency pressure spikes. The effects of pressure on the δ and f components of emissivity can be estimated via considerations of optical depth and Doppler line shifts.

5.7.2.2. Direct Determination of Temperature from Experimental Spectral Data

5.7.2.2.1 Theory

The two-color technique for the determination of temperatures from spectroscopic data requires an experimental determination of the radiant intensities emitted from a given flame in two well-defined wavelength regions. The measured radiant intensities define two brightness temperatures and a color temperature. The brightness temperature T_{br} at the wavelength λ is defined as the temperature at which the emitter under study emits the same spectral intensity of radiation as a blackbody. The color temperature T_c of an emitter is defined as the temperature at which a blackbody emits radiation having the same ratio of radiances at the wavelength λ_1, and λ_2 as the emitter under study.

$$\frac{R^o(\lambda_1,T_c)}{R^o(\lambda_2,T_c)} = \frac{\epsilon_1(\lambda_1,T)}{\epsilon_2(\lambda_2,T)} \frac{R^o(\lambda_1,T)}{R^o(\lambda_1,T)}$$

This expression assumes that the two brightness temperatures are the same and the emissivities of the species in the flame zone are invariant over two chosen wavelength regions. If the emissivities are not the same,

then independently determined emissivity data must be used in order to calculate the true flame temperature from the observed consideration of the individual emitting species providing the relative concentrations are know, but the procedures are relatively complex.

As a first approximation the assumption of constant emissivity will be utilized in this treatment. The rate of emission of radiant energy from a blackbody, i.e., the emitted radiant flux, is then given by Planck's equation. For sufficiently small values of the product of wavelength and temperature, Wien's equation is applicable.

$$R^{o}(\lambda,T)d\lambda = \frac{C_1}{\lambda^5} \exp(-\frac{C_2}{\lambda T})d\lambda$$

Combining equations (1) and (2) the relation between the color temperature and the true temperature can be derived.

$$\frac{1}{T} - \frac{1}{T_c} = \frac{\ell n(\epsilon_1/\epsilon_2)}{C_2[(1/\lambda_1) - (1/\lambda_2)]}$$

This relation indicates that the color temperature will be equal to the true temperature, independently of the choice of λ_1, and λ_2 if the emitting source is either a blackbody ($\epsilon_1 = \epsilon_2 = 1$) or a greybody ($\epsilon_1 = \epsilon_2 < 1$). A direct test can be made for the presence of a black or greybody by determining whether the observed color temperatures are independent of wavelength.

5.7.2.2.2 Experimental

A direct determination of temperature using a two-color spectrographic technique was made for a N_2H_4/N_2O_4 propellant combination. Since each scan required 1.25 msec, the time resolution of the temperature measurement corresponded to this interval. A series of trial calculations were made to establish which spectral region exhibited greybody emission characteristics. Based on these trial calculations, a color temperature derived

from the relative radiant emissivities at 5400Å and 5000Å was selected, based on the observation that the emissivity in this region was found to be relatively independent of wavelength. The derived temperatures for Test 12 are given in Table II. As indicated on several scans, there is an undefined temperature corresponding to large ignition spike over-pressures which occurred during the time interval.

Based on this data it is interesting to note that temperature rises between 400 to 1000°K-msec^{-1} are observed immediately prior to an ignition spike. Also, it is noted that after complete propellant shutdown there is continued burning and that the rate of temperature decrease is roughly linear at about 100°K-msec^{-1}. A summary of the flow conditions for the burn include a short fuel lead (3 msec) with a nominal O/F mixture ratio of 1.8. The termination of the oxidizer flow occurred during the third ignition spike and the fuel flow terminated approximately 1.0 msec later. The induction time required for the first ignition spike was approximately 7 msec respectively. A space simulation altitude in excess of 100,000 ft was used for this test.

TABLE II

Spectroscopic Temperature for N_2H_4/N_2O_4 Test 12

Time (Milliseconds)	Temperature (°K)		Comment
0	Undefined		First Igniton Spike
1.25	Undefined		
2.50	2380		
		520	
3.75	2900		
5.00	Undefined		Second Ignition Spike
6.25	2460		
		1300	
7.50	3750		
8.75	Undefined		Third Ignition Spike
10.00	3100		Termination of Propellant Flow
		100	
11.25	3000		
12.50	2800		
		125	
13.85	2675		
		225	
15.00	2450		

VI. DISCUSSION

6.1 Introduction

Based on an extensive hot firing program, several engineering correlations had been developed with regard to pressure spiking in pulse-mode NTO/N_2H_4 rocket engines. These correlations had been established by the following: (1) the catastrophic overpressures were a function of previous engine test history; (2) the probability of the overpressures was increased for engines which were fired in an upward attitude; (3) the probability of large ignition overpressures was increased as the ambient temperature of the rocket engine decreased; and (4) the overpressure severity increased as the ambient pressure in the thrust chamber decreased. These correlations indicated the existence of a causal relationship between engine residues and the high pressure spiking phenomena.

Additional evidence for such relationships was available from high speed photographic studies of the rocket plume performed at NASA-Houston. In this study it was observed that a liquid residue was formed in the engine during actual test firing and that residue was observed to drop from the lip of the exhaust nozzle. This observation was unexpected since thermodynamic calculations for the engine indicated a chamber temperature well above the boiling point for any of the considered products of reaction. The fact that this material was a liquid under these extreme environmental conditions indicated that the material was neither the raw propellant nor products of reaction such as water produced in the process of combustion.

Preliminary tests at Marquardt indicated that this material might consist of a combination of fuel and fuel nitrate. These chemical tests at Marquardt [25] were performed by showing that a liquid phase reaction between N_2H_4 and HNO_3 resulted in an "energy rich" product which underwent an explosion when confined in a sealed capsule. A direct chemical analysis of the residue for nitrate ion was positive.

In a subsequent research program at the Bureau of Mines, Perlee[3,4,5] demonstrated that the compounds were, in fact, hydrazinium nitrates. This demonstration was made by synthesizing hydrazinium nitrate, unsymmetrical dimethyl hydrazinium nitrate, and monomethyl hydrazinium nitrate by means of standard chemical synthesis, and then comparing the infrared spectra of these compounds with the infrared spectra of actual engine residues.

This analysis was correlated by results obtained by Seamans[1,2] who also performed an elemental chemical composition analysis that indicated a mixture of hydrazinium nitrate admixed with raw fuel. Based on this evidence it was generally agreed: (1) that hydrazinium nitrate was formed; and (2) that it acted as a primary explosive and was responsible for the detonation.

In addition to the hydrazinium nitrate, Dauerman[6] reported the presence of a short lived azide peak at 4.9μ. This transient peak occurred in the condensate formed from the direct reaction between nitrogen dioxide and hydrazine under closely controlled laboratory conditions. Support for this possibility was also found

from data obtained by B. Clark* at Bell Aerosystems and by H. O. Weiss[26] at Dynamic Science. In this work it was necessary to freeze the residues at LN_2 temperature in order to obtain the 4.9μ absorption peak. Infrared studies at 4.9μ conducted by Perlee, Seamans, , and at Edwards Air Force Base (unreported) were negative for azide. Therefore, there was a difference in experimental results with regard to the existence of an azide in the propellant residues.

A major reason for being interested in identifying azide derivatives as components in propellant residues was that studies by Perlee indicated that shock overpressures greater than 22 kbar were required for the initiation of hydrazinium nitrate. Such pressures had not been observed during hot firings and therefore it was believed that a shock sensitive chemical initiator had to be present in the residues. Because of their inherent instability and their relative ease of chemical formation the most obvious candidates would be the azides.

A difficulty with the identification of azide intermediates was the nature of the azide peak, which as observed by Dauerman had a "lifetime" of about 8.5 sec. In a pulse-mode operation a typical firing cycle will involve a series of short bursts 13 msec on, 87 msec off. The lifetime of the azide peak then was long relative to the "off time." However, in a number of instances high overpressures occurred upon engine starts which were initiated long after a previous test. The longest documented occurrence of this type was about 1.5 hours after a previous test. Partly because of this test and partly because of the

*Personal Communication.

lack of agreement between several investigators as to the presence of hydrogen azide in the residue material, an alternate mechanism was invoked by Perlee to explain the initiation. This alternative was the hypothesis that the initiation was caused by a rapid cavitational collapse of a void in the residue created by a shock reflection at the chamber wall. The shock was assumed to have been generated during a relatively "low pressure" ignition overpressure. This possibility has not been disproven as yet and may, in fact, be a source of initiation for certain engine geometrical configurations.

Seamans[1,2] observed another characteristic effect associated with the residue. In a series of Trauzl block tests he observed that about fifty percent of the time the lead test block was completely destroyed. A similar occurrence took place during hot firing programs at NASA-Houston in a test engine. This high brisance of the residue was difficult to explain for two reasons. First, the residue consisted principally of a mixture of water, hydrazine, and hydrazinium nitrate. Thermochemically this mixture was a very poor explosive which would be expected to have a brisance very much less than nitroglycerin which was used as a comparative standard. Secondly, the more sensitive materials in these residues, which could conceivably cause this high brisance, were present only for relatively short periods of time. Also, there was not direct evidence that these intermediate compounds were present in the residues analyzed by Seamans.

Based on the above survey, three major questions arose. The first question was concerned with the chemical composition of the

residues, i.e., to what extent were chemical intermediates formed and what was their chemical characterization. The second question was concerned with the extent of chemical disequilibrium in the preignition and combustion phases of operation. Generally it was assumed that pseudoequilibrium conditions prevailed throughout the actual engine firing cycle and that the bulk of the residues were formed by the condensation of raw propellants on the chamber walls after engine shutdown. The source of these propellants was the residual material which remained in either the injector manifold or the fill lines after the engine valves were closed. The third question which had to be answered was how to explain the high brisance characteristic of the detonation and a corollary question of why the phenomena had occurred only during high altitude simulation tests and had not been observed for the sea level testing incurred during previous engine development programs. The following discussion outlines test results obtained during the course of this research program and suggests a physical mechanism based on these results which can explain all of the major phenomena observed.

6.2 Chemical Characterization of the Engine Residues

The chemical analysis of propellant residues has been described in sections IV and V. Infrared absorption studies of these residues confirm the results of Perlee[3,4,5]. These studies indicate that the primary composition of the residue consists of a mixture of the hydrazine and hydrazine nitrate. A direct correlation can be made with the infrared spectra of the hydrazinium nitrate derivatives

synthesized by Perlee and the infrared spectra obtained from actual residue material. There is little doubt that the residues formed consist primarily of these compounds together with combustion products (e.g. water).

There is also direct infrared evidence for the presence of hydrogen azide, which tends to support the experimental results of Dauerman. The spectrum obtained in this program shows a much weaker absorption pattern, indicating only a small quantity of material. This is in contrast to the strong absorption peak observed by Dauerman. The most probable reason for this discrepancy is that under the experimental conditions used by Dauerman the early liquid - liquid phase reaction was observed and the volatility of HN_3 was sufficiently high to result in the loss of a large percentage of the material after a substantial period of time.

The presence of HN_3 and/or other azides was also confirmed by mass spectral analysis. For the mass spectral analysis the sampling procedure involved an "in vacuo" degasification of the residue. Samples of the effluent gas produced by bubble formation were then obtained by allowing the sample to froth for several hours. This procedure thus allows an analysis of the gases contained in the bubbles produced by the slow liquid - liquid reaction. By this method these bubbles were found to contain HN_3, triazene, and methyl triazene for residues obtained from an MMH/NTO propellant combination. Other components such as hydrogen and nitrogen were probably also present. Quantitative analyses of the relative mole fraction of individual

species were not possible without an extensive study of individual breakdown patterns in the mass spectrograph ionization chamber. Except for the hydrazinium nitrates, the compounds were present in very small quantities. Assuming that these materials are distributed more or less evenly throughout the liquid it is doubtful that they would participate as a liquid phase initiator for the primary hydrazinium nitrate explosive.

From these results we conclude that the residues contain a relatively large number of explosion-sensitive compounds. However, these compounds are present only in trace quantities.

6.3 Mechanism and Theory of Explosive Initiation in Rocket Engine Residues

6.3.1 Mechanism

The residue formed from an NTO/N_2H_4 propellant consists of a mixture of fuel and fuel nitrate together with small amounts of detonation-sensitive compounds. These residues are also characterized as high brisance explosives, because extensive damage results when they are initiated. In rocket tests this initiation has occurred only during high altitude simulation testing. It is necessary, therefore, to explain why a thermochemically unbalanced and relatively poor explosive can exhibit high brisance detonation behavior, and why this behavior occurs only during the simulated high altitude testing.

The theoretical approach used to describe these processes assumes that the engine pressurization processes cause an adiabatic compression of small bubbles that are formed in the liquid residues by slow "liquid phase" reactions. The pressurization process then

results in the development of a localized "hot spot." This "hot spot" may be inert or chemically reactive. If it is chemically reactive then its temperature involves a balance between the rate of heat dissipation caused by convective and conductive heat fluxes. The critical condition for explosion occurs when the self-heating within the spot exceeds the rate at which heat can be dissipated.

Based on the experimental evidence obtained during the course of this program, it is assumed that the bubbles consist either of pure hydrogen azide or hydrogen azide diluted by other components. Since the concentrations of these components is not known it is assumed that the dilutent may be described as an inert substance, e.g., nitrogen.

6.3.2 Hot Spot Theory

A number of theoretical formulations have been developed to describe the critical conditions for the occurrence of an exponential temperature rise resulting from a chemically reactive hot spot contained in an explosive material. These formulations are based on a solution to the general differential equation.

$$\rho C \frac{\partial T}{\partial t} = K\left(\frac{\partial^2 T}{\partial x^2} + \frac{P}{x}\frac{\partial T}{\partial x}\right) + Q f e^{-E/RT}$$

where K, ρ, and C are the thermal conductivity, density, and specific heat respectively and are assumed to be temperature independent. P is a steric factor which assumes the values 0, 1, or 2 for a slab, cylinder or sphere, and Q, E, and f are the heat released per unit volume, the activation energy, and the Arrhenius pre-exponential factor, respectively.

The initial boundary conditions are assumed to be :

$$T = T_1 \qquad x < A$$

$$T = T_0 \qquad x > A$$

where A is the half width or radius of the hot spot.

With these boundary conditions, the dimensionless variables Θ and δ can be formulated:

$$\Theta = \left[E / RT_1^2 \right] \left[T_1 - T_0 \right] \tag{6.3-2}$$

$$\delta = \frac{Q f E A^2 e^{-E/RT}}{RT_1^2 K} \tag{6.3-3}$$

This mathematical formulation neglects loss of reactant, change of thermal properties with temperature, differences in the thermal properties of the hot spot and the material outside of it, changes in phase caused by thermal heating and reactions other than single step reactions controlled by temperature. For a given Θ these variables assume critical values Θ_c and δ_c as a condition of explosion.

The relations for the critical condition have been examined by previous investigators and a summary of the correlations between δ_c and Θ_c for hot spot spheres are listed in Table III. From these correlations the critical radius can be evaluated at any specified temperature by

$$A = \left[RT_1^2 K \right] \left[Q f E e^{-E/RT_1} \right]^{-1} \left[f(\Theta_0) \right] \tag{6.3-4}$$

where $f(\Theta_0)$ is defined from Table III values.

TABLE III

CRITICAL COMPARISON OF CRITERIA
FOR SPHERICAL HOT SPOTS

Boddington	$\delta_c = \left(\frac{9}{2\pi}\right) \left(\theta_0\right)^2$
Friedman	$\delta_c = 4.7\ \delta_0$
Zinn	$\delta_c = 25$
Merzhanov	$\delta_c = 12.1\ \ell n\ \theta_0^{0.6}$
Rideal and Robinson	$\delta_c = 2\ \theta_0$
Thomas	$\delta_c = \frac{25}{1 + \frac{10\pi^{\frac{1}{2}}}{\theta_0 (1 + P)} + \frac{50\pi}{\theta_0^2 (1 + P)^2}}$

The critical induction time, τ_c , can be evaluated using

$$\tau = \frac{\rho C A_c^2}{\delta_c K} \qquad (6.3\text{-}5)$$

where A_c corresponds to the critical radius and C, K, and ρ are evaluated at the hot spot temperature, T_1, attained after an adiabatic compression. The thermal conductivity K was calculated using the Eucken approximation for polyatomic molecules

$$K = \left(C_p + \frac{5}{4}\frac{R}{M}\right)\mu \qquad (6.3\text{-}6)$$

In the viscosity equation σ represents a Lennard-Jones characteristic cross section and Ω is a temperature-dependent Stockmayer potential function. C_p is calculated using the sum of the translational, rotational, and vibrational partition functions and the viscosity μ is approximated using

$$\mu = 2{,}669 \times 10^{-5}\frac{\sqrt{MT}}{\sigma^2 \Omega \mu} \qquad (6.3\text{-}7)$$

In order to apply these theories it is necessary to estimate the values to be assigned to the activation energy E and pre-exponential factor f. For a unimolecular hydrazoic acid decomposition a value of 10^{13} was assigned to the pre-exponential factor. The activation energy was estimated at a value of 40 kcals/mole. This value for activation energy was based on the enthalpy change for the reaction

$$HN_3\ (^1A') \rightarrow NH\ (^1\Delta) + N_2\ (^1\Sigma_g^+) \qquad (6.3\text{-}8a)$$

In this reaction it is noted that dissociation into the NH ($^1\Delta$)

state is assumed rather than dissociation via either of two other possible routes:

$$HN_3\ (^1A') \longrightarrow NH\ (^3\Sigma^-) + N_2\ (^1\Sigma g^+) \qquad (6.3\text{-}8b)$$

$$HN_3\ (^1A') \longrightarrow N_3\ (^2\Pi g) + H\ (^2S_g) \qquad (6.3\text{-}8c)$$

Reaction (6.3-8c) requires an activation energy of at least 85 kcals/mole and is therefore ruled out. Reaction (6.3-8b) although energetically most favorable, violates the Wigner spin correlation rules and is quantum mechanically "forbidden."

The energy of the $^1\Delta$ potential curve above that for $^3\Sigma$ was taken as 1.3 electron volts although it should be noted that uncertainties in the correlation energy would imply only a value less than 2.0 ev. Values for the enthalpy of NH were taken from the JANAF Thermochemical Tables and the heat of formation of HN_3 was taken to be +73 kcals/mole. Using the above values as minimum, actuation energy of 40 kcals/mole was estimated for reaction (6.3-8a). Together with the correlations outlined in Table II for the several hot spot theories, values of δ_c, A_c and t_c were calculated.

A graphical analysis using these theories is given in Figures 53 - 57 for pure HN_3/N_2 compositions. Of particular interest to this study is the variation of critical radius and critical induction time with initial temperature. The initial radius corresponds to the radius of the collapsed bubble following an adiabatic compression. The initial compression process results in the heating of the bubble to an elevated

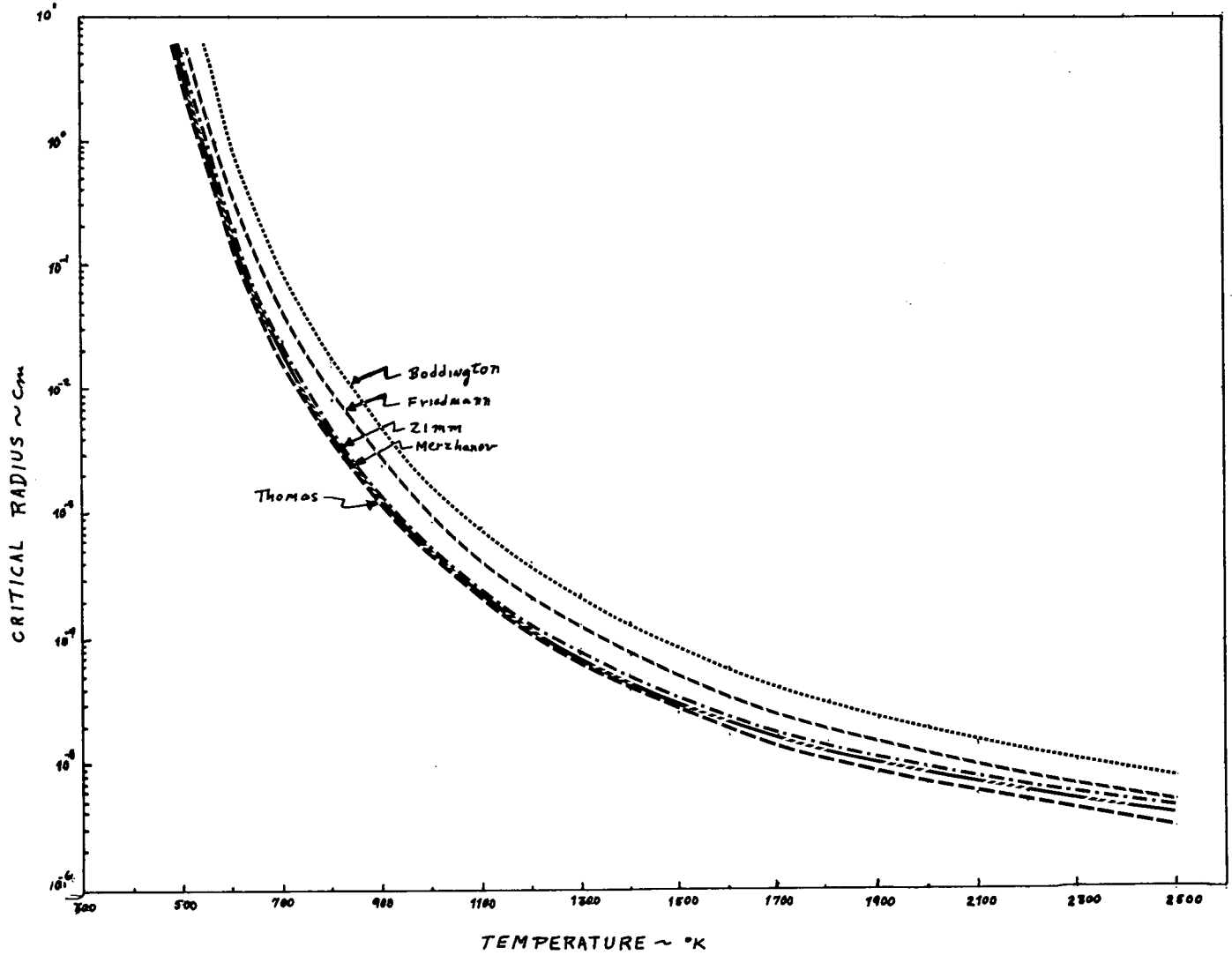

Figure 53 Comparison of Theoretical Predictions for Hydrogen Azide Critical Radius

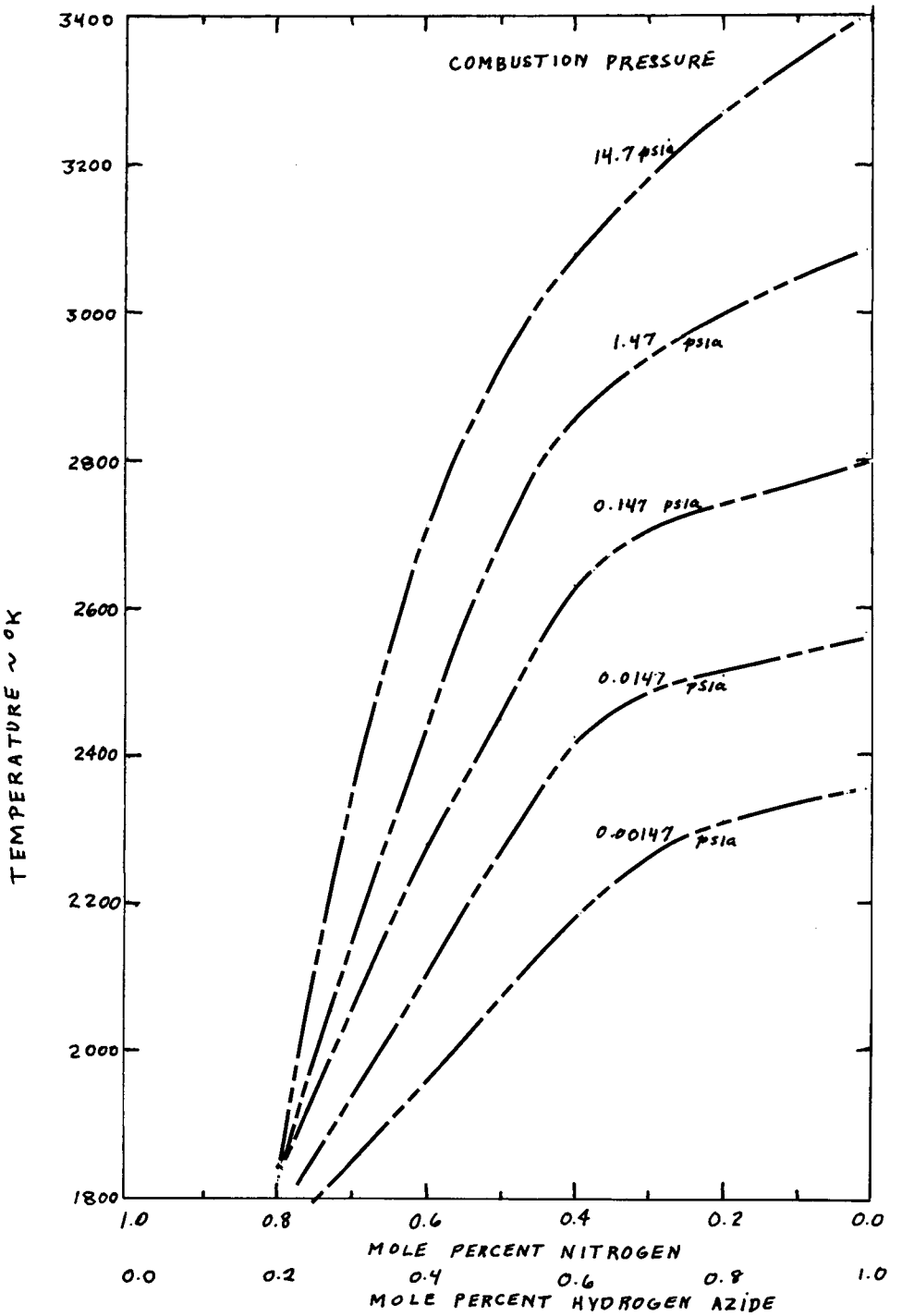

Figure 54. Temperature Increase Caused by the Adiabatic Combustion of Hydrogen Azide/Nitrogen Mixtures

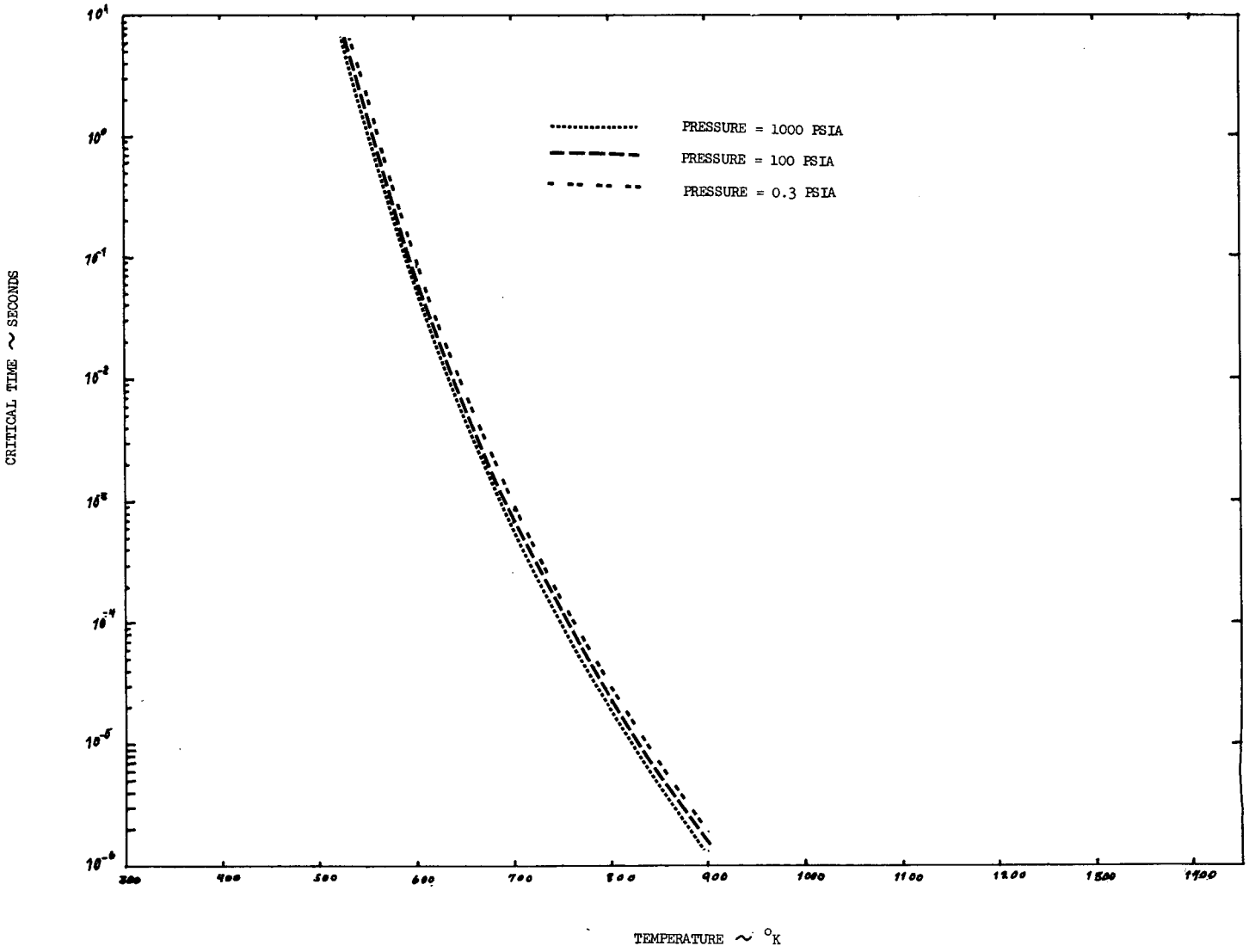

Figure 55. Critical Initiation Times for Pure Hydrazoic Acid Gaseous Hot Spots

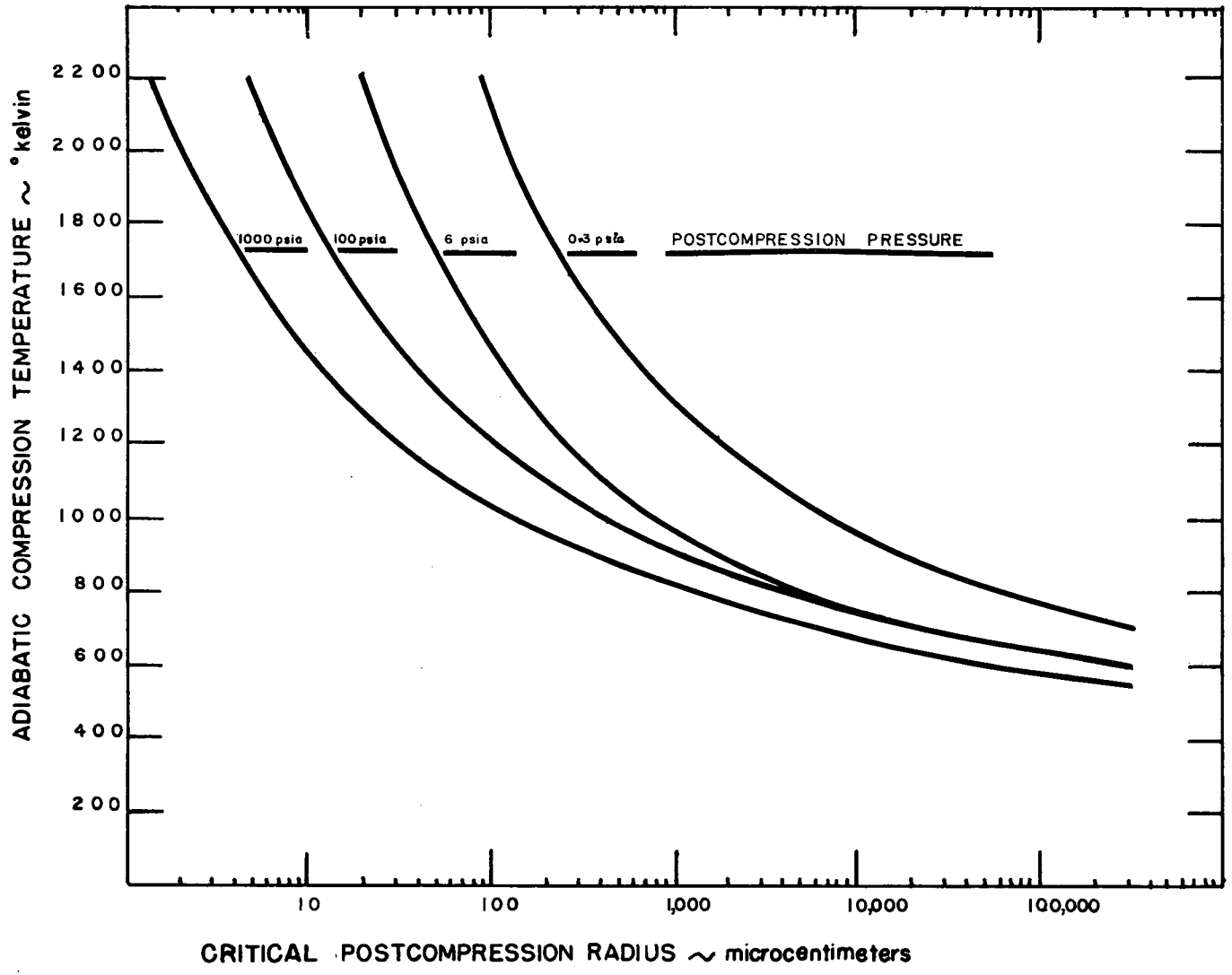

Figure 56. Adiabatic Compression Temperature Vs. Critical Postcompression Radius

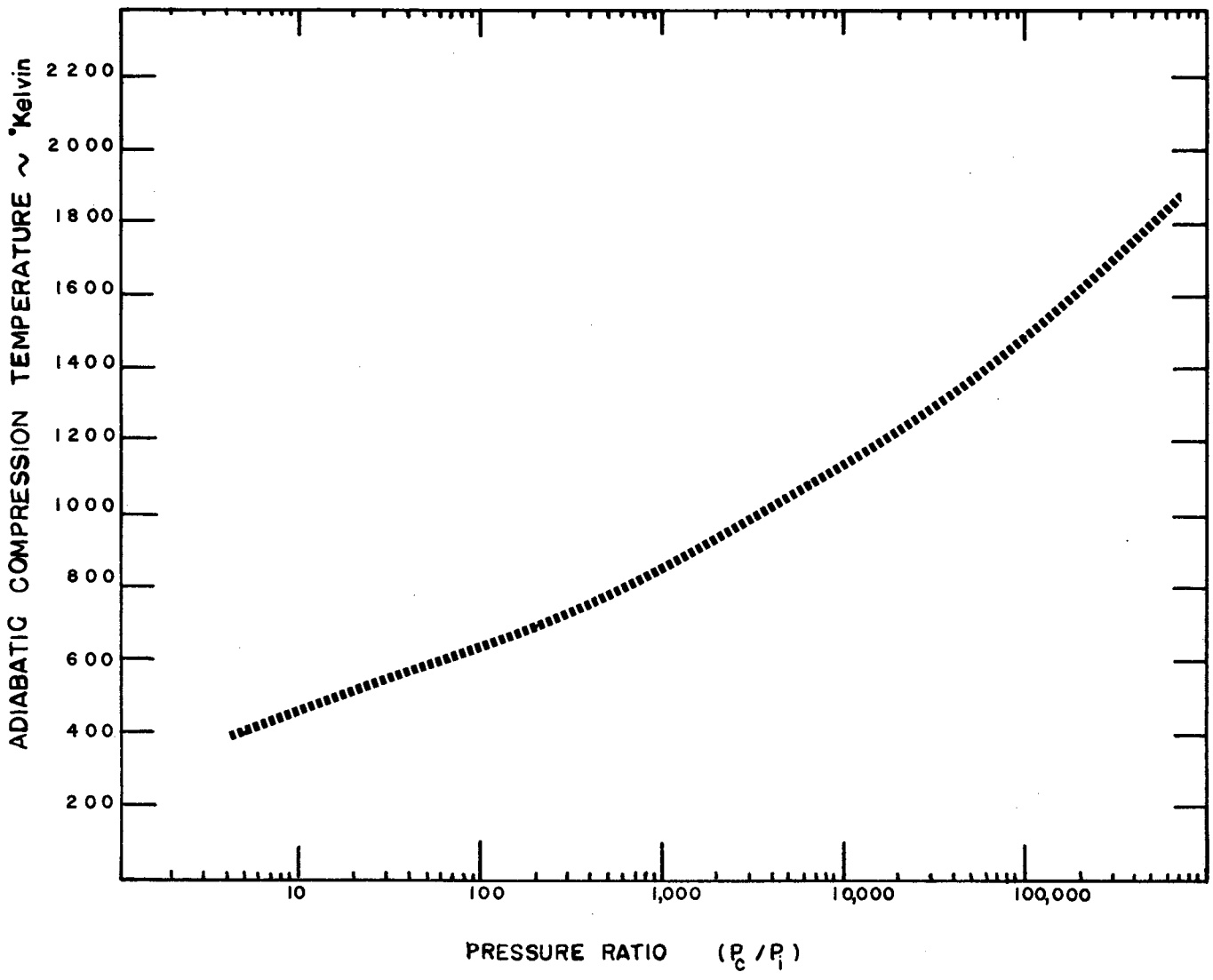

Figure 57. Adiabatic Compression Temperature Vs. Pressure Ratio

temperature T_2, calculated using the expression

$$T_2 = T_1\left[\frac{P_2}{P_1}\right]^{\frac{\gamma(T)-1}{\gamma(T)}} \qquad (6.3\text{-}9)$$

in which $\gamma(T)$ is the temperature-dependent ratio of specific heats. The value of C_p was calculated using statistical mechnical partition functions in which the translational and rotational degrees of freedom were considered fully active and the vibrational partition function was calculated using the Einstein functions and spectroscopic fundamental frequencies. For HN_3 the frequencies were taken as 3336, 2140, 1275, 1150, 522, and 672 cm^{-1}.

In this model the residue material during a vacuum ignition event is subjected to a pressure pulse corresponding to either a steady state combustion pressure or an ignition transient overpressure. For the present study the steady state combustion pressure is about 100 psia although transducer data overpressures up to 1500 psia have been recorded experimentally. Assuming that steady state thrust chamber conditions are achieved, the pressure ratios causing an adiabatic temperature increase will vary between 50:1 and 4000:1. This corresponds to vehicle operations between 50,000 and 150,000 feet altitude. For pure HN_3 the resultant compression temperatures were calculated to lie between 750 and 950° K.

Using the theories previously developed for hot spot initiation in homogeneous explosives, calculations were made of the critical radius and critical time required for pure hydrazoic acid. These calculations used temperature as a variable and the results are listed in Figure 56 for operating pressures of 1000, 100, 6.0 and 0.3 psia

respectively. For operations at 50,000 feet in which ignition transients of 1,000 psia occur, the critical induction time is about 100 milliseconds and the critical postcompression radius is about 0.1 mm. For this condition the required precompression radius is estimated to be about 1.2 mm. Since the liquid residues in the thrust chamber are between 0 - 1 mm in thickness we conclude that it would not be possible to initiate the explosion at 50,000 feet. Also, since the gaseous components are complex mixtures and not pure HN_3, it is doubtful whether heat release per unit volume is sufficiently high to allow initiation. This conclusion is supported by all the rocket test data available at the present time.

For operations at 150,000 feet the pressure ratio is about 5000:1. Corresponding to this pressure ratio, the adiabatic temperature rise is about 950° K. Again assuming steady state conditions at the operating chamber pressure of 100 psia the critical time is 0.6 microseconds and the critical radius is 8×10^{-3} mm with an associated precompression critical bubble diameter of 0.2 mm. Since bubble diameters of this size are observed throughout the residue it is much more probable that initiation will take place. It is concluded that at 150,000 feet the probability of initiation is high for residues having thicknesses greater than 0.5 mm.

The effect of high pressure ignition transients can be estimated by assuming that near-equilibrium conditions are achieved during the initial adiabatic compression. Transducer data taken at Marquardt[25] indicate that pressure transients well over 2,000 psia may be reached during ignition. These spikes are about 50 microseconds in duration

and have extensive fine structure with high pressure regions on the order of 5 microseconds. For operations above 50,000 feet, pressure ratios having a minimum value of 5000:1 are reached with compression temperatures estimated above 900° K. Since these are essentially the same conditions as those found at 150,000 feet, it would be predicted that pressure spiking could induce initiation either by a hot spot mechanism during "steady state" ignition at high altitudes or during engine spiking at higher ambient pressure.

The temperature rise within the reactive hot spot after initiation can be calculated by assuming an adiabatic temperature increase caused by the chemical decomposition. A series of thermochemical equilibrium calculations has been carried out for pure hydrogen azide and mixtures of hydrogen azide and nitrogen. The results of these calculations at 14.8 psia are presented in Figure 54 for temperature increase and relative mole fraction. A precompression temperature of 300° K is taken as an initial temperature for this calculation. As can be seen by inspection, temperatures between 2,000 and 4,000° K are reached following decomposition of HN_3 - N_2 mixtures. In practice these temperature values would be somewhat higher due to the enthalpy increase caused by the initial compression. Because dissociation will limit the temperature increase, a direct estimation of total temperature cannot be performed. Therefore it is assumed that these temperatures are sufficiently high to cause initiation of the primary explosive contained in the engine residues and that the major time delays are associated with the development of the reaction front in the compressed gaseous hot spot.

Example Case

For an engine designed to operate at 100 psia chamber pressure, determine the critical time and critical precompression bubble radius for start operations of 60, 80, 100, and 120 thousand feet. For this case, using this theory, the following values are obtained.

Start Altitude	60	80	100	120
Critical Postcompression Radius (mm)	0.5	0.12	0.03	0.003
Pressure Ratio	90	120	600	1200
Temperature Ratio	620/300	720/300	800/300	900/300

Using these values as input parameters the critical operating envelop can be established and the results are summarized in Figure 58. Depending upon the initial operating conditions, a critical time between 0.1 μsec and 10 msec is required.

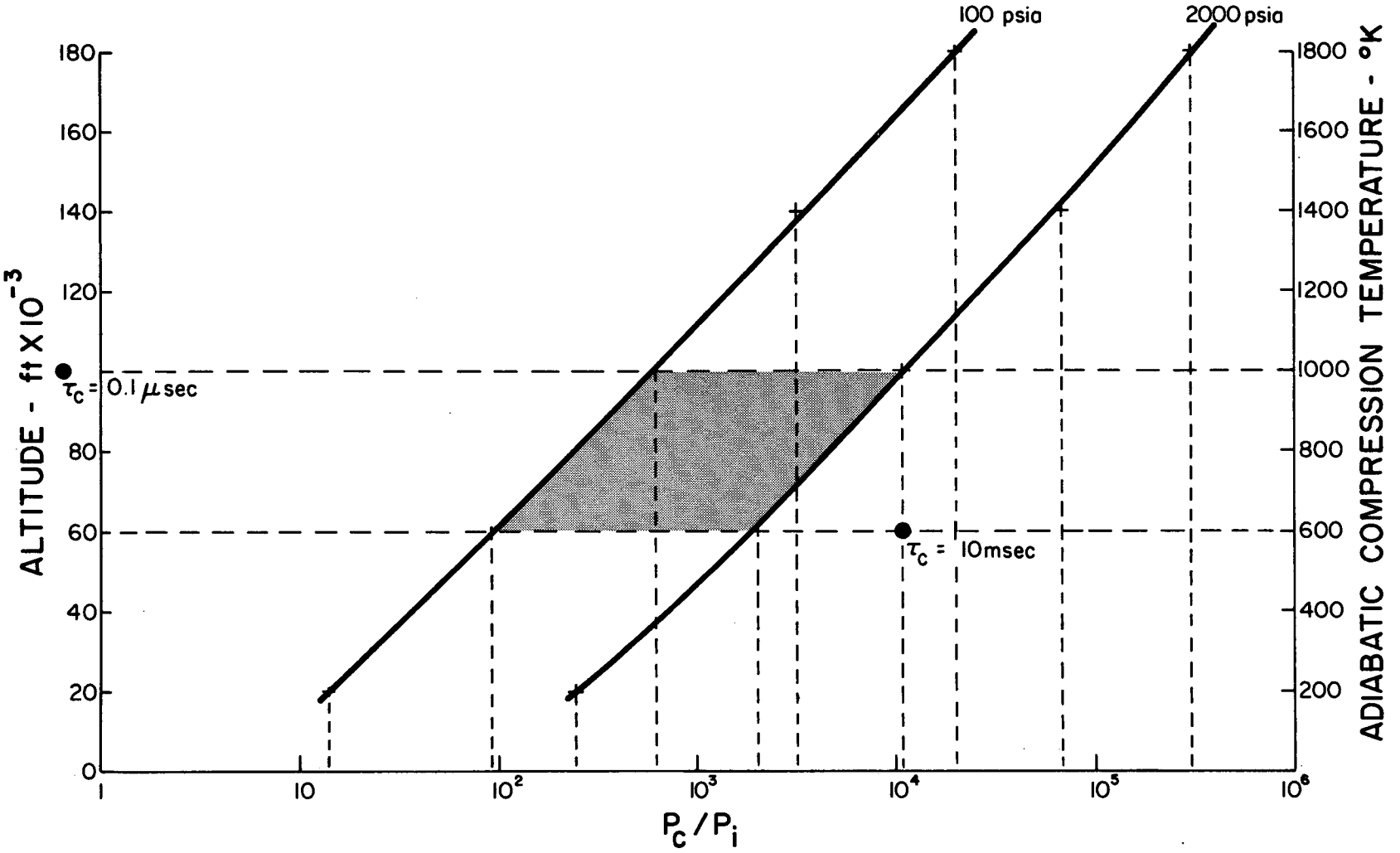

Figure 58. Critical Operating Envelope for Example Case

In summary, the hot spot mechanism outlined above is capable of providing an explanation for all the major phenomena observed in the test programs. The pressure dependence (i.e., high altitude effect) is attributed to the requirement of a high pressure ratio in order to exceed the minimum activation energy necessary for the decomposition of HN_3 or other similar compounds. The characteristically high brisance of a relatively poor explosive is a result of the simultaneous initiation of a number of localized "hot spots" contained throughout the residue. These "hot spots" may be created either through a normal engine pressurization process during which the temperatures reached are low but the time available for coupling the energy to the primary explosive is long, or alternatively through a gas phase detonation which results in a higher temperature for a much shorter time period. Additional experimental shock tube studies to further define which of these two possibilities is most important should be performed.

6.4 Nonequilibrium Processes Associated with Rocket Ignition at Low Pressure

6.4.1 Chemical Disequilibrium

The experimental results described in SectionsIV-V indicate that the assumption of equilibrium conditions is probably not valid for pulse-mode rocket engines operated at space ambient conditions.

The calculated high temperature chemical composition for an O/F of 2.0 for an MMH/NTO propellant system show sizable concentrations of OH, H_2O and HCO and only small quantities of NO_2. Time integrated emission spectra, however, show strong band structures which are best

identified with a nitrogen dioxide NO_2^* fluorescence, an HNO emission, and weak band of CH, NH, N_2 and other species. The absence of HCO or HCN bands in the emission is probably significant since for both species, the transition probabilities are high which should cause relatively strong spectral emission characteristics, even though their absolute concentration levels are small. The absence of these bands indicated that the reactions do not proceed to completion and that the system is not in chemical equilibrium.

The conclusion that the system is not in chemical equilibrium is also supported by the discontinuous emission experimentally observed. For example, the emission record of sodium lines shows a series of discrete ignitions which are in fact closely spaced temperature pulses.

6.4.2. Nonequilibrium Effects Caused by Disintegration of Propellant Jets at Low Pressures

Ignition delay models describing the physical processes governing the kinetics of droplet evaporation and chemical processes governing the rates of chemical reaction prior to ignition have been applied to the problems of hypergolic ignition in space ambient engines. Mathematically in one model (Seamans), the propellant spray is represented by a three drop size array. The three drop sizes are obtained by applying a logarithmiconormal distribution to a given mass median drop size and then selecting three radii such that a prescribed weight flow distribution is satisfied. In this model both fuel and oxidizer drop sizes are assumed to follow the same logarithmiconormal distribution function.

The assumptions for this model were experimentally tested by observing the development and growth of propellant sprays under vacuum startup conditions. A photographic record of a typical high altitude bipropellant spray has already been given in Figure 36. The oxidizer (N_2O_4) fans out in a very fine mist, whereas the fuel (N_2H_4) retains its jet integrity even at very low pressure.

Based on this photographic evidence, several conclusions can be drawn. First, mixing in a one-on-one unlike injector used in this program is poor under vacuum startup conditions. In effect, the reactants consist of a liquid column of hydrazine burning in a finely divided nitrogen tetroxide aerosol. Since a typical firing pulse of an attitude control engine is 20 msec in duration, a significant proportion of the fuel is able to strike a cold surface prior to ignition and this may be one of the reasons that large amounts of unreacted hydrazine were found in the residue mixtures. A second conclusion is that current theoretical models predicting the rate of initial pressurization of N_2H_4/NTO rocket engines must use different particle-size distribution functions for the fuel and oxidizer components if they are to be applied to problems involving vacuum startup.

A series of calculations were performed in order to outline the effects of temperature, droplet size, and mass flux on rate of evaporation of rocket propellants. For these calculations it was assumed that the rate of instantaneous evaporation for a spherical liquid drop can be calculated using the relation[27]

$$W_a = \Theta\, k_{xm} \Pi D^2 \frac{x_{a_0} - x_{a_\infty}}{1 - x_{a_0}} \quad (6.4.2\text{-}1)$$

where

D is the diameter in cm

x_{a_0} is the vapor pressure of A at the surface droplet

x_{a_∞} is the pressure of A at a long distance

For forced convection k_{xm} is given by

$$k_{xm} = \frac{c_f D_{ab}}{D}\left[2.0 + 0.6\left(\frac{D v_\infty \rho_f}{\mu_f}\right)^{1/2}\left(\frac{C_p \mu}{K}\right)_f^{1/3}\right] \quad (6.4.2\text{-}2)$$

in which the subscript f denotes the properties of the fluid at the "film temperature" and "film composition" evaluated by

$$T_f = \frac{1}{2}\left(T_0 + T_\infty\right) \quad (6.4.2\text{-}3)$$

$$x_{af} = \frac{1}{2}\left(x_{a_0} + x_{a_\infty}\right) \quad (6.4.2\text{-}4)$$

For high transfer rates, Θ, the correction coefficient is calculated from

$$\Theta = \frac{\ln(R+1)}{R} \quad (6.4.2\text{-}5)$$

where R denotes generalized flux ratio for momentum, energy and molar fluxes.

Limiting the argument to high mass transfer rates becomes

$$\Theta = \frac{\ln(R_{ab}+1)}{R_{ab}} \quad (6.4.2\text{-}6)$$

in which R_{ab} is given by

$$R_{ab} = \frac{X_{ao} - X_{a\infty}}{\frac{N_{ao}}{N_{ao}+N_{bo}} - X_{ao}} \qquad (6.4.2\text{-}7)$$

where

N_{ao} is the molar flux of A at the surface

N_{bo} is the molar flux at B at the surface

Under conditions where there is no mass transfer of B at the surface these equations reduce to

$$W_a^{(m)} = ln(R_{ab}+1)\,\Pi D^2 k_{xm} \qquad (6.4.2\text{-}8)$$

Physical parameters necessary for the evaluation of were either taken from literature values or were calculated for binary system. The value for D_{ab_f} was calculated using the expression:

$$D_{ab} = \frac{2.265 \times 10^5}{C} \frac{\sqrt{T(1/M_a + 1/M_b)}}{\sigma_{ab}^2 \quad \Omega_{D_{ab}}} \qquad (6.4.2\text{-}9)$$

where

σ_{ab} is the Lennard Jones characteristic diameter,

$\Omega_{D_{ab}}$ is the Stockmayer potential taken as a temperature dependent function.

Based on this theoretical formulation a series of calculations were performed.

Typical results of this calculation are given for N_2O_4 and N_2H_4 in Figure 59 for a 10^{-2} mm drop size. These results provide an estimate of the initial mass flux from the spherical drop assuming the

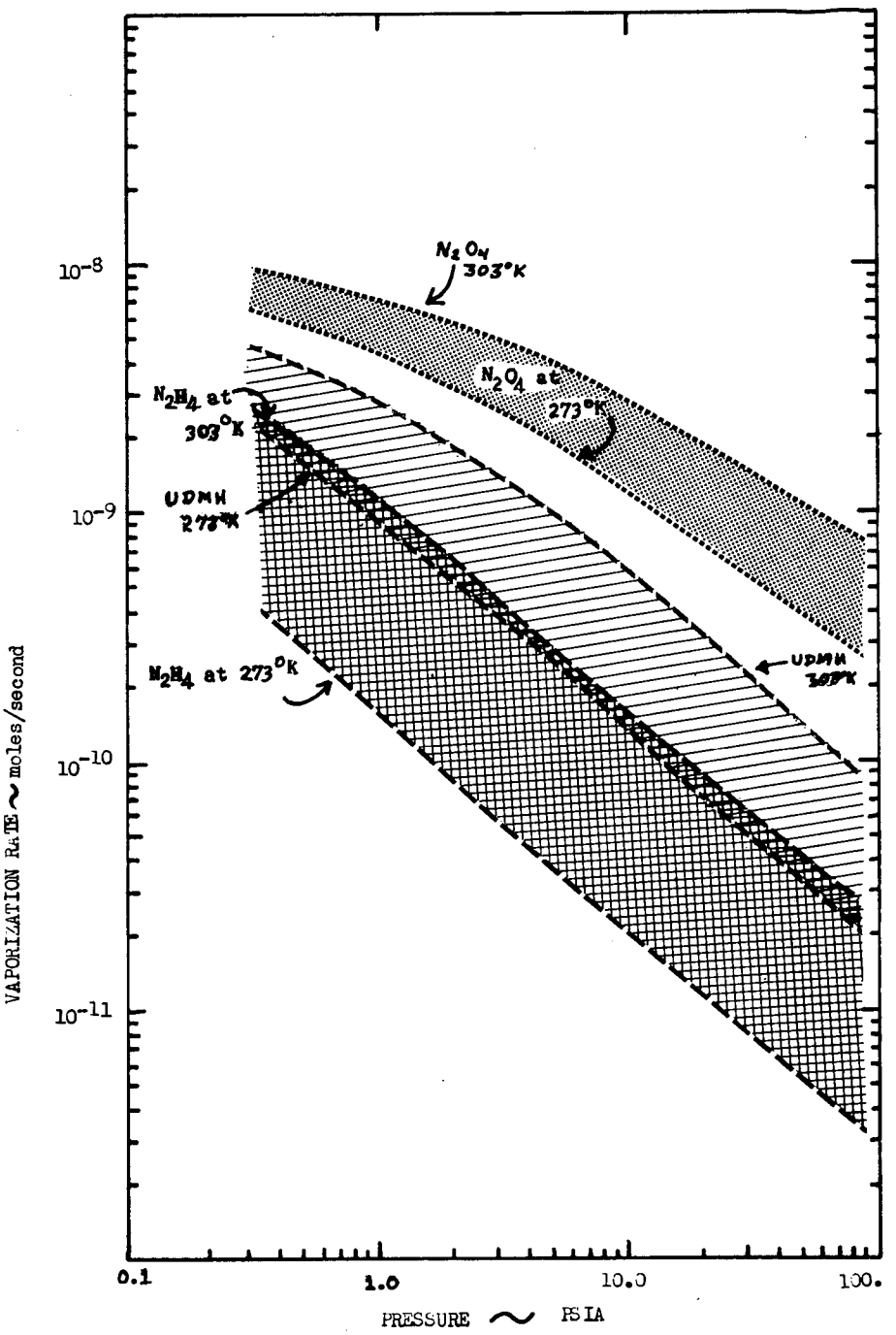

Figure 59. Instantaneous Vaporization Flux from 10^{-4} cm Droplet with Velocity of 100 cm/second

ambient pressure given on the abscissa. The relative rates of evaporation differ by about two orders of magnitude at 100 psia and by about one order of magnitude at the lower start pressure. In addition to the pressure effect the effect of temperature is much stronger for hydrazine than for nitrogen tetroxide.

In order to determine whether an improvement in the rate of dispersion of the hydrazine could be effected by increasing the temperature a series of experimental tests were performed. The temperature of the hydrazine was increased from room temperature to 120°F and 160°F and the hot hydrazine injected into the vacuum chamber.

At 120°F the calculated instantaneous rate of evaporation of a droplet of hydrazine was estimated to be approximately the same as that of nitrogen tetroxide at room temperature and breakup of the fuel into a fuel-spray was followed using high speed photography. There was no observable effect caused by the increased temperature. The conclusion was reached that an increase in the injection temperature of hydrazine to a temperature at which the initial rate of vaporization was calculated to be the same as the rate of vaporization for NTO under normal conditions did not result in an increased dispersion of the liquid stream. The theory used for this purpose is believed to represent a reasonably valid approximation and should be capable of describing qualitative effects. The fact that this treatment, based on equilibrium vapor pressure and gas transport arguments apparently does not describe even qualitatively the experimental observations,

tends to indicate that other factors, e.g., dissolved gases or surface tension effects caused by trace impurities, may be responsible for the spray breakup. It is noted that relatively few studies have been performed outlining these effects at very low pressures.

6.5 Flash Photolytic Effects

An experimental problem in this program was to develop a suitable spectroscopic method which would allow the course of reaction to be followed by observing "simultaneously" time integrated emission-absorption spectra. An attempt was made to solve this problem by the use of a short duration flash technique in which a very intense pulsed light source was used to backlight the rocket test engine at preselected frequency rates. A potential criticism of this approach was the possibility that the light pulse might flash photolyze and/or sensitize the reaction mixture by creating high free radical concentration. For any sensitization process two mechanisms are operative. One is an increase in the temperature of the reaction mixture caused by the thermalization of "hot" reaction products. The second is an increase in the concentration of intermediate species with the resultant change in reaction velocity. In either case, if the system perturbation is sufficiently high, so that the system is brought to a point above the explosion limits, then the measurement methods would not be passive with respect to the reaction system. An estimate of the effects of photochemical activation was required, and an outline of the general theoretical approach necessary to evaluate these effects is presented in the following discussion.

The general approach used was to examine the time dependent behavior of a reaction system subjected to either short-duration or steady-state radiation fluxes. Because of the extreme complexity of this problem for the reaction mixtures present in a rocket chamber, preliminary calculations were restricted to each of the individual components. Fuel components which were considered include hydrazine (N_2H_4), monomethyl hydrazine (MMH), and unsymmetrical dimethyl-hydrazine (UDMH). Oxidizer components consisted of dinitrogen tetroxide (N_2O_4) and NO.

A possible kinetic path for the thermal decomposition of hydrazine is outlined below:

Initiation

$$N_2H_4 \xrightarrow{k_1} 2NH_2 \qquad (6.5\text{-}1)$$

Propagation

$$N_2H_4 + NH_2 \xrightarrow{k_2} NH_3 + N_2H_3 \qquad (6.5\text{-}2)$$

$$N_2H_3 \xrightarrow{k_3} N_2 + H_2 + H \qquad (6.5\text{-}3)$$

$$N_2H_4 + H \xrightarrow{k_4} NH_3 + NH_2 \qquad (6.5\text{-}4)$$

Chain Branching

$$N_2H_3 \xrightarrow{k_5} NH + NH_2 \qquad (6.5\text{-}5)$$

$$N_2H_4 + NH \xrightarrow{k_6} NH_2 + N_2H_3 \qquad (6.5\text{-}6)$$

Termination

$$NH_2 + N_2H_3 \xrightarrow{k_7} NH_3 + N_2 + H_2 \qquad (6.5\text{-}7)$$

$$N_2H_3 + N_2H_3 \xrightarrow{k_8} 2NH_3 + N_2 \qquad (6.5\text{-}8)$$

$$N_2H_3 + H \xrightarrow{k_9} N_2 + 2H_2 \qquad (6.5\text{-}9)$$

$$NH_2 + NH_2 \xrightarrow{k_{10}} N_2H_4 \qquad (6.5\text{-}10)$$

Since this reaction sequence is complex, it is useful to adopt a simplified sequence similar to that proposed by Berlad[28]. This includes an additional initiation step associated with a photochemical activation mechanism.

Initiation

$$N_2H_4 \xrightarrow{k_\nu} 2NH_2 \qquad (6.5\text{-}11)$$

$$N_2H_4 \longrightarrow 2NH_2 \qquad (6.5\text{-}12)$$

Propagation

$$N_2H_4 + NH_2 \longrightarrow NH_3 + N_2H_3 \qquad (6.5\text{-}13)$$

Chain Branching

$$N_2H_3 \longrightarrow NH + NH_2 \qquad (6.5\text{-}14)$$

$$N_2H_4 + NH \longrightarrow NH_2 + N_2H_3 \qquad (6.5\text{-}15)$$

Termination

$$N_2H_3 + NH_2 \longrightarrow NH_3 + N_2 + H_2 \qquad (6.5\text{-}16)$$

$$NH_2 + NH_2 \longrightarrow N_2H_4 \qquad (6.5\text{-}17)$$

A similar scheme was used for the decomposition of UDMH and MMH with appropriate modification of specific rate constants and energy factors.

The equations can be further simplified to a general form for the general series of hydrazine-based fuels.

Photochemical Initiation $F \longrightarrow A + NH_2$ (6.5-18)

Collisional Initiation $F \longrightarrow A + NH_2$ (6.5-19)

Propagation $F + A \longrightarrow P_1 + B$ (6.5-20)

Propagation $F + NH_2 \longrightarrow NH_3 + B$ (6.5-21)

Termination $B + NH_2 \longrightarrow P_1 + N_2 + H_2$ (6.5-22)

In this simplified format the tabulation of species F, A, B and P_1 for these fuels is given by:

Species	Hydrazine	MMH	UDMH
F	N_2H_4	CH_3HNNH_2	$(CH_3)_2NNH_2$
A	NH_2	CH_3HN	$(CH_3)_2N$
B	N_2H_3	$CH_3HN - NH_2$	$CH_3CH_2 - NH_2$
P_1	NH_3	CH_3H_2N	$(CH_3)_2HN$

For hydrazine, the sequence of reactions can be written:

$$N_2H_4 \longrightarrow 2NH_2 \qquad (6.5\text{-}23)$$

$$N_2H_4 + NH_2 \longrightarrow NH_3 + N_2H_3 \qquad (6.5\text{-}24)$$

$$N_2H_4 + NH \longrightarrow NH_2 + N_2H_3 \qquad (6.5\text{-}25)$$

$$N_2H_3 + NH_2 \longrightarrow NH_3 + N_2 + H_2 \qquad (6.5\text{-}26)$$

Using a steady state treatment for the intermediate radical species NH_2, N_2H_3 and NH, we solve to find the steady state concentration of NH_2 formed by thermal activation processes:

$$[NH_2]_{ss} = \frac{k_1}{k_2} + \frac{k_5}{k_7} \qquad (6.5\text{-}27)$$

If we include a photochemical activation mechanism given by

$$N_2H_4 \longrightarrow 2NH_2 \qquad (6.5\text{-}28)$$

then the photochemical steady state concentration for NH_2 is given by

$$[NH_2] = \frac{k_\nu}{k_2} + \frac{k_5}{k_7} \qquad (6.5\text{-}29)$$

A combined thermal and photochemical activation mechanism then yields for NH_2

$$[NH_2] = \frac{k_\nu}{k_2} + \frac{k_1}{k_2} + \frac{k_5}{k_7} \qquad (6.5\text{-}30)$$

A further modification for collisional activation was developed to yield

$$[NH_2] = \frac{k_y}{k_2} + \frac{k_1}{k_2}[M] + \frac{k_5}{k_7}[M] \qquad (6.5\text{-}31)$$

where M represents the activating third body. The explicit use of this latter formulation aids in the formulation of pressure dependencies for the reaction sequence. Since the vacuum ignition involves a reaction which occurs throughout a wide pressure regime the rate constants have to be examined to determine whether they are themselves functions of pressure over the range of the ignition process.

The effect of flash photolysis was determined by comparing the rate of decomposition for individual components, which is associated with the energy density flux of the light source, to that which is expected for the normal thermal decomposition. This was evaluated by examination of the extinction coefficients for specific components and intermediate species for selected flash intensities.

Calculations were performed to assess the effects of possible photochemical activation on a change in reaction mechanism. Results of this calculation are similar to those of Berlad, corresponding to a gas density for N_2H_4 at 60 psia and 300°K. Four plots are presented: (1) the reaction rate vs. time (Figure 60); (2) relative hydrazine concentration vs. time (Figure 61); (3) NH vs. time (Figure 62); and (4) NH_2 vs. time (Figure 63). As can be determined from the plot of reaction rate vs. time, an induction time is observed

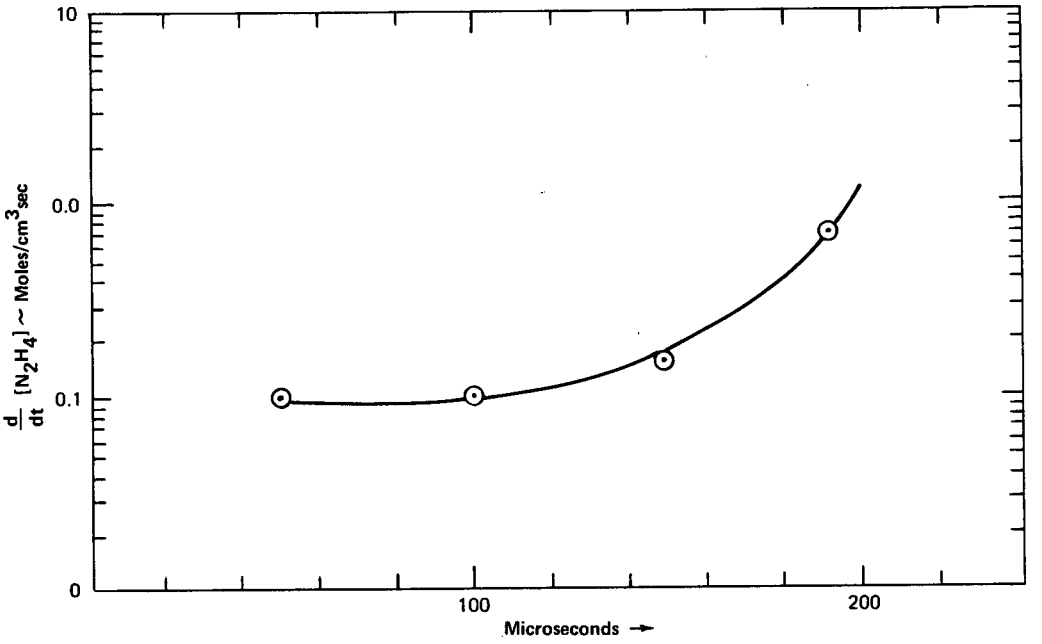

Figure 60. Reaction Rate vs. Time

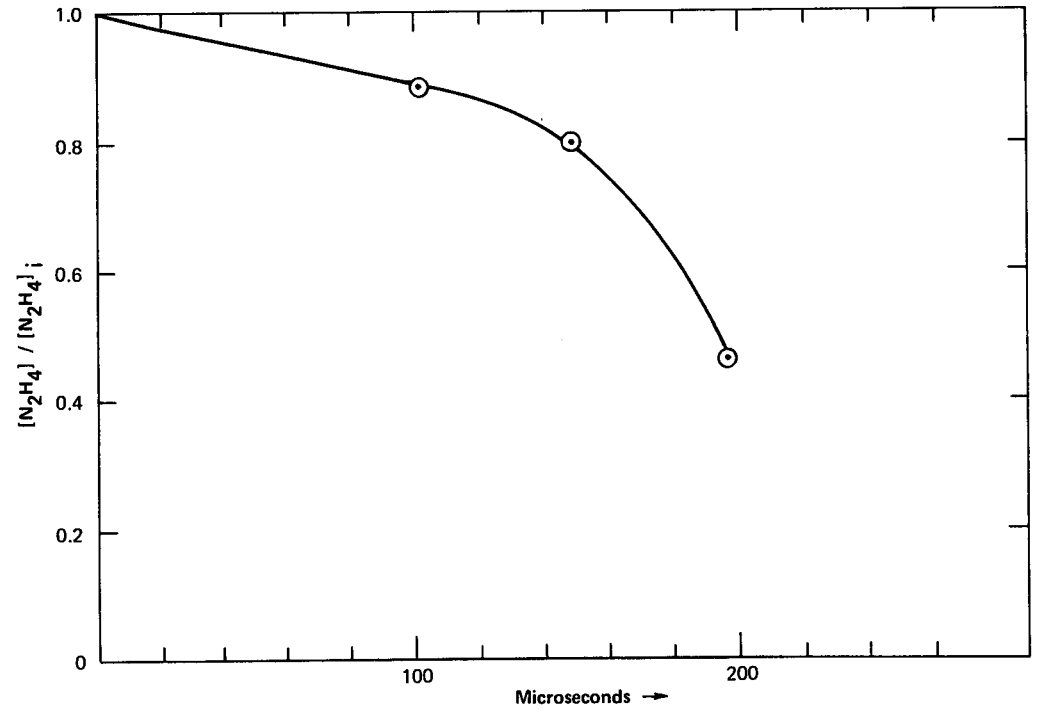

Figure 61. Hydrazine Concentration vs. Time for Steady Irradiation

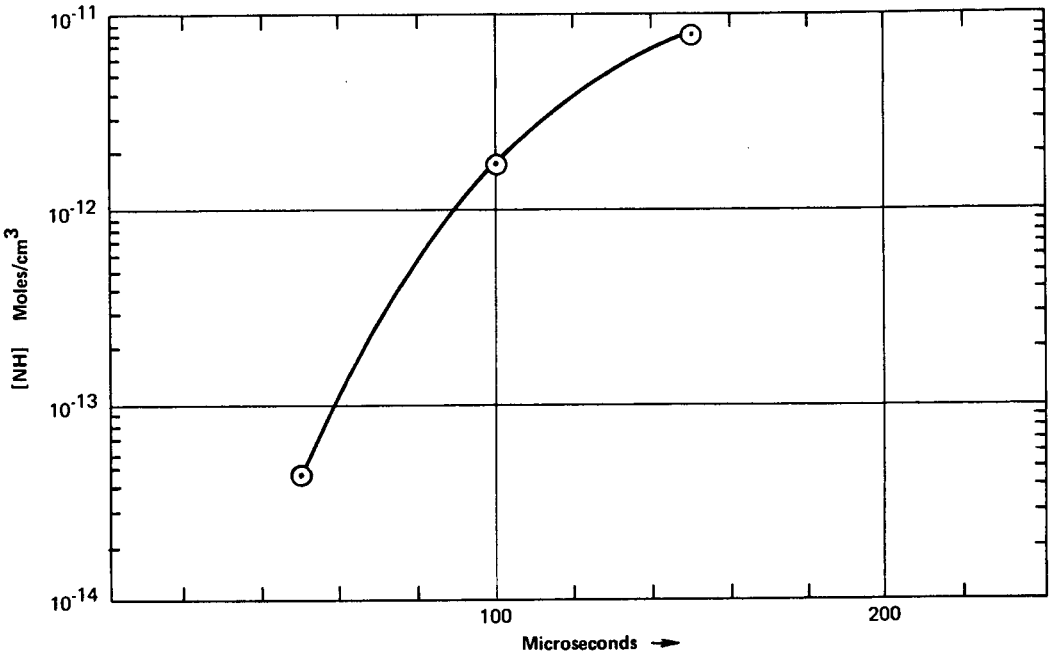

Figure 62. [NH] vs. Time

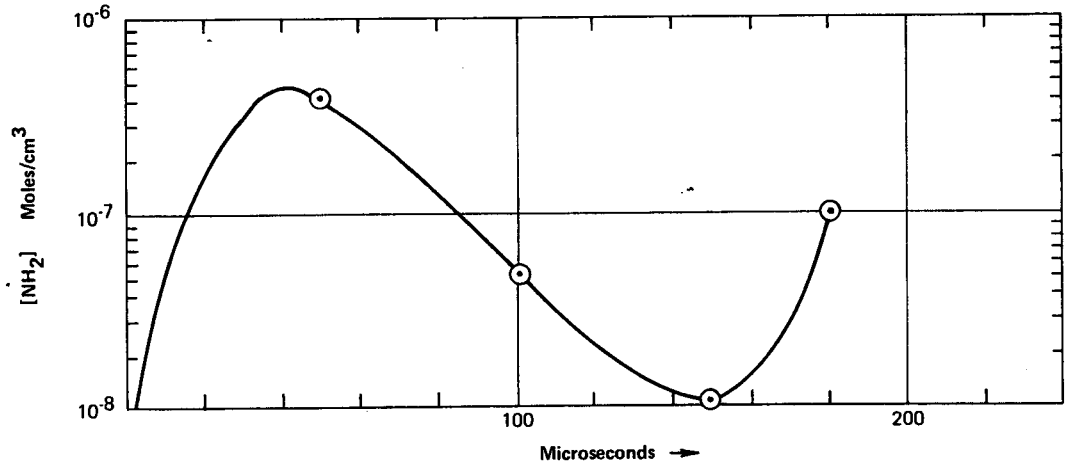

Figure 63. [NH_2] vs. Time

corresponding to a time delay of about 150 microseconds. During this interval, the hydrazine concentration is reduced by about 15 percent and a corresponding buildup of reactive intermediates occurs.

The major conclusion of this analysis was that there should be no appreciable perturbation of the ignition process caused by the absorption of radiant energy by hydrazine. However, it should be noted that it may be possible to alter the reaction mechanism by using somewhat higher energy levels over a broader geometric cross section. Such a technique could provide a way of significantly reducing ignition delay times and thereby reduce the amount of residues formed during pulse-mode operation.

6.5.1 Comparison of Gas Parameters and Ignition Time for N_2H_4 and MMH

The Seamans program[2] was used to calculate gas temperature, and fuel and oxidizer vapor pressure in the reaction chamber. Results for N_2H_4/NTO and MMH/NTO are presented in Figure 64. The calculations indicate that the ignition time for N_2H_4 is about 35% of that for MMH.

Variation of several program parameters produced no appreciable change in the program results. The parameters varied were: fuel droplet temperature, fuel evaporation coefficient, activation energy for ignition (this affects ignition delay time only), activation energy for intermediate, and maximum and minimum values of drop wall heat transfer factor.

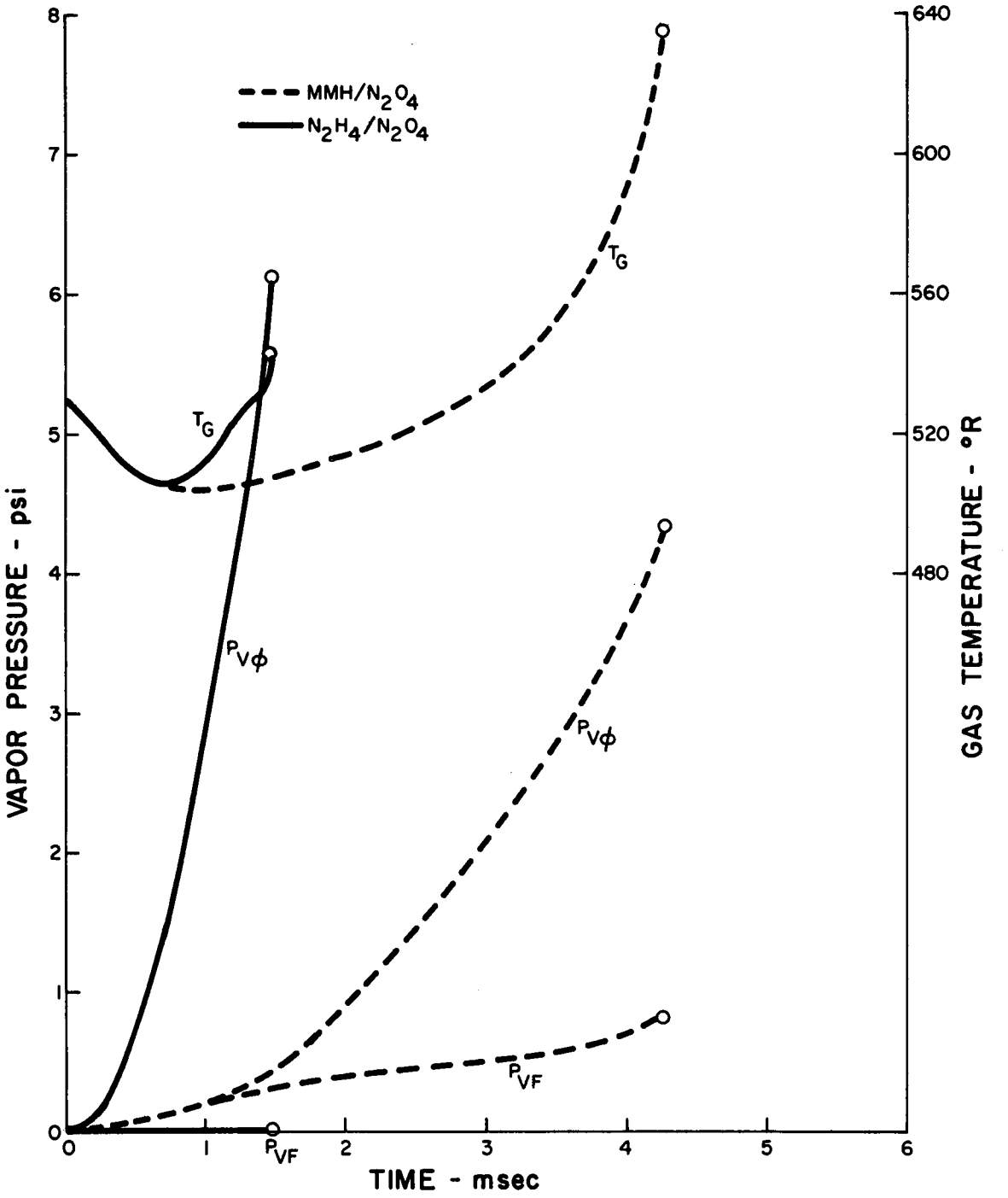

Figure 64. Calculated Gas Temperature and Fuel and Oxidizer Vapor Pressure for N_2H_4/NTO and MMH/NTO

6.6 Relative Activation Energies for N_2H_4, MMH and UDMH

The "hard start" pressure transients associated with the ignition of hydrazine based fuels decrease in the order N_2H_4 > MMH> UDMH. This can be correlated to the decrease in rate of decomposition found by Eberstein and Glassman[12] in temperature ranges between 800 and 1220°K where the first order rate of reaction took the ordering UDMH >MMH> N_2H_4. Extrapolation of their data shows that there is a crossover between the rate of reaction of N_2H_4 and MMH at about 750°K and a crossover for MMH and UDMH at about 1100°K. Presumably the hard start problem is related in some way to these rates of decomposition and where the rate of decomposition is fast the ignition proceeds more smoothly. Experimental results of Eberstein and Glassman show that the activation energy required for decomposition had the order MMH> N_2H_4>UDMH. Assuming that the rate limiting step corresponds to the initial N-N bond dissociation then the predicted ordering of the relative activation energies would be UDMH> MMH > N_2H_4.

Electron impact studies by Dibeler et al[29], show that the N-N bond is strengthened by the addition of methyl radicals and that the (N-N) bond strength of N_2H_4, MMH, and UDMH are 60, 67, and 72 Kcals/mole respectively. Pyrolytic of hydrazine using a toluene carrier (Kerr et al[30]) showed the opposite ordering for the N-N bond of 57.1, 51.9 and 49.6 Kcals/mole respectively. Kerr's data is in agreement with the kinetic results of Eberstein and Glassman and with the observation in the rocket propulsion field. Dibeler's data would predict the opposite trend unless a chain branching mechanism involving a methyl radical would cause a change in kinetic mechanism through this homologous series. Ebersten and Glassman

and most of the subsequent workers in the propulsion field have developed a model for the decomposition of hydrazine fuels in attempts to explain the rough start in terms of a branching model in part because it is then possible to reconcile the results of Kerr and Dibeler.

However, it is not necessary to resort to a branching chain mechanism. The problem arises by the use of the simple Arrhenius model describing reaction rates in which

$$k = A \exp(-E/RT)$$

In this relation the reaction velocity, k, is proportional to an Arrhenius preexpotential factor A and a quantity exp (-E/RT) where E is the activation energy and R and T are the gas constant and absolute temperature respectively. Using the Arrhenius form of kinetic behavior and correlating experimental results with theory experimental results are interpreted in terms of an energy of activation and a preexpotential factor, A. Both of these are usually assumed constant for engineering calculations. Using more detailed theories of kinetics, as derived by methods of either classical or quantum statistical mechanics, it can be shown that the experimental activation energy E is related to the probability that the molecule contains a total energy E' distributed among y-square terms. Since each effective mode of vibration contributed two square terms the maximum number possible for a nonlinear x-atom molecule y has the value

$$3n - 6/2$$

In practice, the number of effective square terms are chosen relative to experimental data and y becomes a somewhat arbitrary parameter related to the complexity of the molecule. The implication of this is that the experimentally observed activation energy is not only a function of bond

strength but also is dependent on the ability of the molecule to exchange stored energy into the bond. This means that all other things being equal a more complicated molecule will exhibit a lower activation energy and that the experimental rates should follow the order UDMH> MMH> N_2H_4 which is, in fact, observed. This type of argument can be used and kinetic models developed which do not necessarily have to resort to chain branching mechanisms.

The reaction velocities for decomposition also exhibit a crossover at about 750°K for MMH and N_2H_4 and at about 1250°K for MMH and UDMH. A possible explanation for this crossover is that the number of effective oscillators which exchange energy with the breaking bond increase with increasing temperature and that the number of possible interacting cross terms increase with increasing molecular complexity. The detailed contributions of interacting nonorthogonal cross terms are not predicted by any present theory. Therefore, it would be expected that the rate of decomposition of more complex molecules would increase more rapidly than less complex molecules. Thus, it would be expected that MMH reacts less rapidly at lower temperatures than N_2H_4 and that a crossover at 750°K would occur. In such a detailed analysis it would be expected that at low temperatures corresponding to the fuel rich region surrounding a fuel droplet the rate of reaction of N_2H_4 would exceed that of UDMH and produce substantial quantities of an unstable chemical intermediate. These effects would be greatly magnified for pulse mode operations.

One result of the above argument is that it demonstrates how difficult it is to develop a kinetic model for the decomposition of hydrazine propellants without a much greater understanding of the fundamental chemical

reaction rates. The use of the reaction mechanism which may be valid at 1000°K may not necessarily describe the expected rates of reaction at low temperatures surrounding the fuel droplet, and the use of the kinetic mechanisms describing the combustion processes at higher temperatures may or may not be valid. The use of global kinetics where a constant activation energy is assumed or experimentally evaluated may not allow extrapolation to more or less complicated molecules. Since with very few exceptions most engineering approaches use either a first or second order kinetics scheme to simplify mathematical solution, the results from these engineering calculations are a priori extremely questionable. At the present time, there is no conclusive evidence that the kinetic mechanism usually assumed for the decomposition of hydrazine fuels correctly describes the process since it is possible to explain the observed chemical stoichiometry and reaction orders using an alternative mechanism involving the unimolecular decomposition of N_2H_4. Such a decomposition would result in the production of metastable azide derivatives in both the gas and liquid phases.

VII. CONCLUSIONS

Based on the results of this program, several conclusions can be formulated.

1. The catastrophic overpressures observed in space simulated, pulse-mode, rocket engines using nitrogen tetroxide/hydrazine propellants are a result of a liquid phase detonation in the unburned propellant residues formed during previous firing. The mechanism of detonation involves one or more "hot spots" generated by an adiabatic compression of gas bubbles contained within the residues. These "hot spots" undergo an exothermic chemical reaction forming a localized high energy region in the propellant residues and then transfer sufficient heat to cause explosive initiation in the residues.

2. A chemical characterization of the propellant residues indicates that they consist principally of a mixture of fuel and fuel nitrates. In addition, a number of other chemical species are also present. In the liquid phase these include hydrogen azide, triazene, hyponitrous acid and tetrazene. In the gas phase, hydrogen azide, triazene together with other unidentified species are present.

3. The usual assumptions of chemical and physical equilibrium used in engineering design calculations do not apply during the ignition of space ambient rocket engines using NTO-Hydrazine propellants. Physical disequilibrium is caused by a flash vaporization of the

nitrogen tetroxide resulting in the formation of a finely divided aerosol whereas, the fuel stream remains as an integral highly turbulent jet. These effects result in strong chemical disequilibrium which allows the formation of sensitive explosive intermediates probably via a heterogeneous reaction between NO_2 and liquid fuel.

4. The use of time resolved spectrophometric techniques can provide information concerning intermediate chemical species after ignition has occurred.

5. The use of time resolved spectrochemical techniques could not provide information concerning intermediate chemical species in the pre-ignition time regime.

In summary, the major work effort of this research program has been devoted to finding a general mechanism which can cause the initiation of a propellant residue. The mechanism suggested is capable of explaining all the phenomena thus far observed. In particular it provides a unique explanation for observed high brisance of the explosive material and predicts the observed high altitude dependency.

REFERENCES

1. Seamans, T. F., and Dawson, B., "Hypergolic Ignition at Reduced Pressures", AFRPL-TR-67-129, June 1967.

2. Seamans, T. F. and Waser, P. C., "Effects of Additives on Ignition Delay and Chamber Pressurization of Space-Ambient Engines", AFRPL-TR-69-68, July 1969.

3. Perlee, H. E. et al., "Preignition Phenomena in Small A-50/NTO Pulsed Rocket Engines", Journal of Spacecraft & Rockets, Vol. 5, No. 2, Feb. 1968, pp. 233-235.

4. Perlee, H. E., Miron, Yael, and James, Harvey, "Hypergolic Ignition and Combustion Phenomena in the Propellant System Aerozine-50/N_2O_4", Report No. 4071, Nov. 30, 1968, Explosives Research Center, Bureau of Mines, Pittsburgh, Pennsylvania.

5. Perlee, H. E., "2nd Hypergolic Ignition Conference", NASA Houston (1967).

6. Dauerman, AIAA Journal, 6, (11), 1968, 2186.

7. Perlee, H. E., Private Communication.

8. Huff, V. M., Gordon, S., and Morrell, V. E., "General Method and Thermodynamic Tables for Computation of Equilibrium Composition and Temperature of Chemical Reactions", NACA Report 1037, (1951).

9. JANAF, "Thermochemical Data", The Dow Chemical Company (1965).

10. Michel, K. W., and Wagner, H. Gg., "The Pyrolysis and Oxidation of Hydrazine Behind Shock Waves", Tenth Symposium (International) on Combustion, The Combustion Institute, Pittsburgh (1965).

11. Sawyer, R. F., "The Homogeneous Gas Phase Kinetics of Reaction in the Hydrazine-Nitrogen Tetroxide Propellant System", AFOSR Report No. 66-0855, Contract AF 49 (638)-1268 (1965). AD 634 277.

12. Eberstein, I., Glassman, I., "The Gas-Phase Decomposition of Hydrazine and its Methyl Derivatives", Tenth Symposium (International) on Combustion, The Combustion Institute, Pittsburgh, 1965, pp. 365-374.

13. Eberstein, I., "The Gas-Phase Decomposition of Hydrazine Propellants", Princeton University, Technical Report 708 (1964), Department of Aerospace and Mechanical Science.

14. Audrieth, L. F., and Ogg, B. A., "The Chemistry of Hydrazine", Wiley, New York, 1951, p. 118.

15. Sawyer, R. F., and Glassman, I., "Eleventh Symposium (International) on Combustion", The Combustion Institute, Pittsburgh (1967), pp. 861-868.

16. Grey, P., and Thyne, J. C. J., "Arrhenius Parameters for Elementary Combustion Reactions: H-atom Abstraction from N H Bonds." Tenth Symposium (International) on Combustion, 435-443, (The Combustion Institute, Pittsburgh, 1965).

17. Ray, A. B., Koehler, G., Salser, G. E., and Dauermann, L., "Evidence of the Formation of Azides in the N_2H_4/N_2O_4 Reaction." pp. 2186-2187, AIAA Journal (1968).

18. Robinson, G. W., McCarty, M., and Keelty, M. C., J. Chem. Phys., Vol. 27 (1957), pp. 588.

19. Hertzburg, G., "Electronic Spectra of Polyatomic Molecules", D. Van Nostrand Co., New York, 1966, pp. 508.

20. Douglas, A. E., reference not available.

21. Douglas, A. E., and Huber, K. P., Can. J. Phys., Vol. 43, (1965), pp. 74.

22. Douglas, A. E., and Huber, K. P., Can. J. Phys., 43, 74 (1965).

23. Broida, H. P., Schiff, H. I., and Snyder, G. S., Trans. Fara. Soc., Vol. 57 (1961), pp. 259.

24. Cashion, J. K., and Polanyi, J. C., "Infrared Chemiluminescence from the Gaseous Reaction Atomic H Plus NO; HNO in Emission", J. Chem. Phys., Vol. 31 (1959), pp. 317-318.

25. Juran, V., and Stechman, R. C., "Ignition Transients in Small Hypergolic Rockets." Journal of Spacecraft and Rockets, Vol. 5, No. 3, March 1968, pp. 288-292.

26. Weiss, H. G., "A Basic Study of the Nitrogen Tetroxide-Hydrazine Reaction," Rept. SN-4500, July 1965, Dynamic Science Corp., Monrovia, California.

27. Bird, R. B., Stewart, W. E., and Lightfoot, E. N., "Transport Phenomena", John Wiley and Sons, New York (1960), Chapter 21.

28. Berlad, A. L., and Buley, E. R., "Radiative Effects on Explosive Instability", Final Report Contract AF04(611)-10928-4, August 1966.

29. Dibeler, V. H., Franklin, J. L., and Pease, R. M., J. Am. Chem. Soc. 81, 68 (1958).

30. Kerr, J. A., Skehar, R. C., and Trotman-Dikensen, A. F., J. Chem. Soc., 1963, 3217.

ACKNOWLEDGEMENTS

Contributions of the following individuals are gratefully acknowledged: Mr. J. Kottenstette, Mr. Robert Marchese, Mr. Larry Brown and Professor W. Ross. A particular debt of gratitude is expressed for the work of Mr. R. Marchese who was responsible for conducting most of the experimental tests.

DRI #2577

COMBUSTION DYNAMICS IN LIQUID ROCKET ENGINES

FINAL REPORT - APPENDICES

by

W. H. McLain

prepared for

NATIONAL AERONAUTICS AND SPACE ADMINISTRATION

Contract NAS9-7566

Denver Research Institute
Denver, Colorado 80210

September 1971

A-I

TABLE OF CONTENTS

APPENDIX A

Specific Reaction Rate Constants For Nitrogen Tetroxide, Hydrazine, And Their Decomposition Products

A 1-(a)

APPENDIX A

Specific Reaction Rate For Nitrogen Tetroxide, Hydrazine, and Their Decomposition Products

Figures 1 through 25 show the variation of specific reaction rate constant, k, with temperature for selected gas phase reactions involving nitrogen tetroxide and hydrazine. The units of k are: sec^{-1} for unimolecular reaction, $cm^3 - mole^{-1} - sec^{-1}$ for bimolecular reaction, and $cm^6 - mole^{-2} - sec^{-1}$ for termolecular reaction.

In many cases, experimental variations of several orders of magnitude are reported. Since it was beyond the scope of this program to critically evaluate each of the reported references, the variations are reported without comment. It is perhaps instructive to note the wide variations as an example of the lack of precision and accuracy in the field of gas phase kinetics studies.

A list of references from which the reaction rate data were obtained is given on pages A27 - A33. This is followed by a table listing those references that were used for the reactions in each figure.

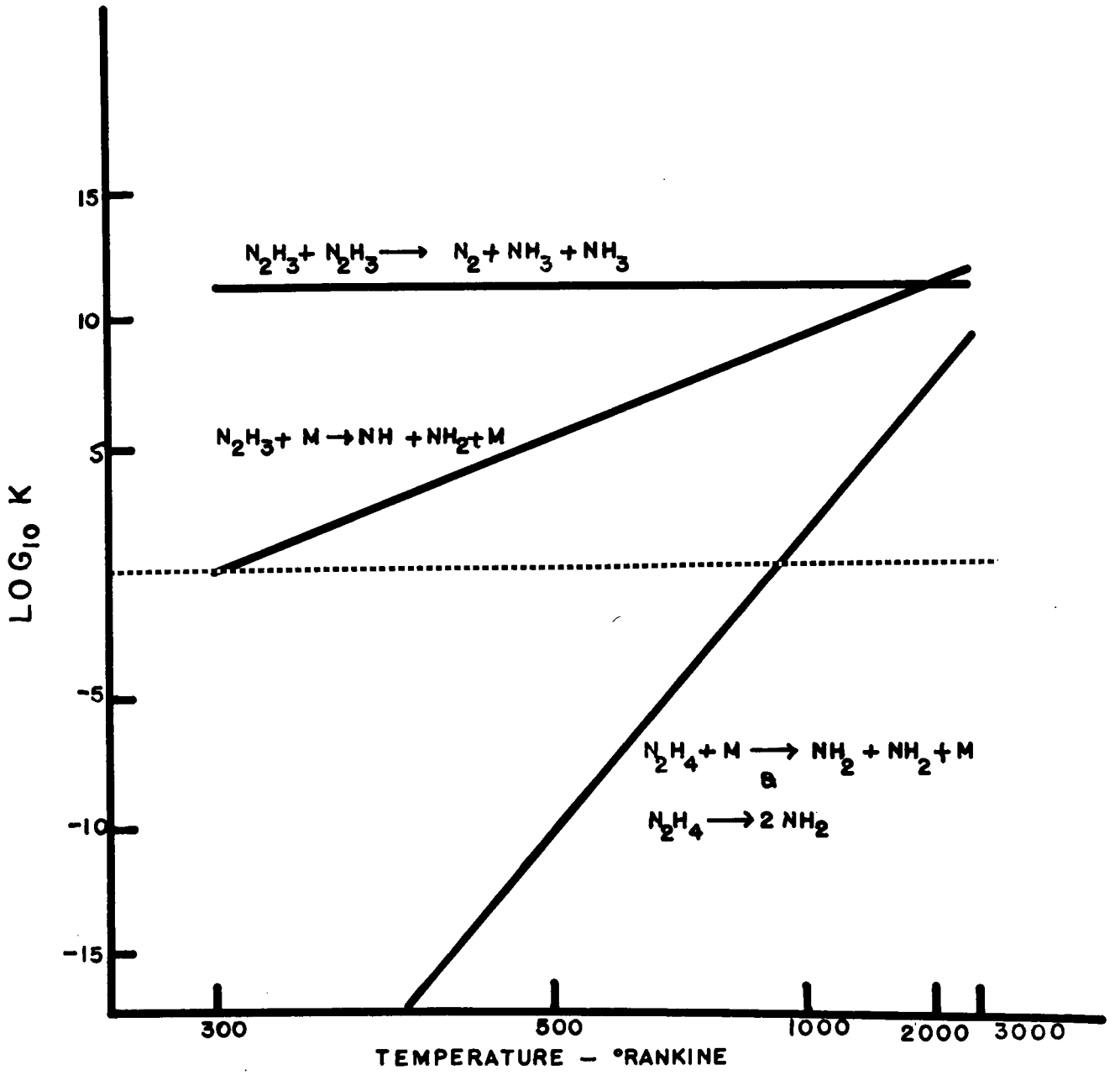

FIGURE 1: SPECIFIC RATE CONSTANT vs TEMPERATURE

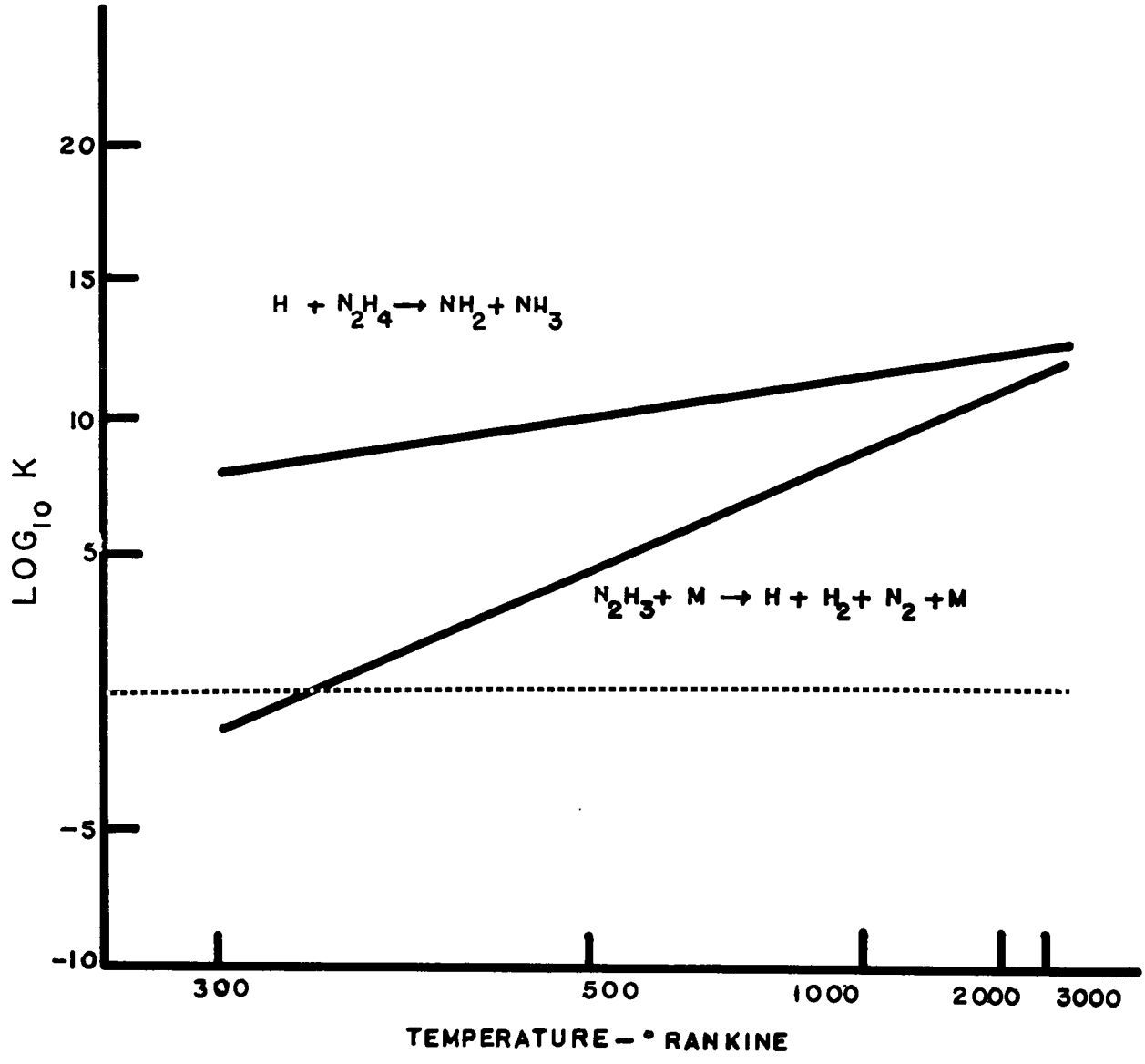

FIGURE 2 SPECIFIC RATE CONSTANT vs TEMPERATURE

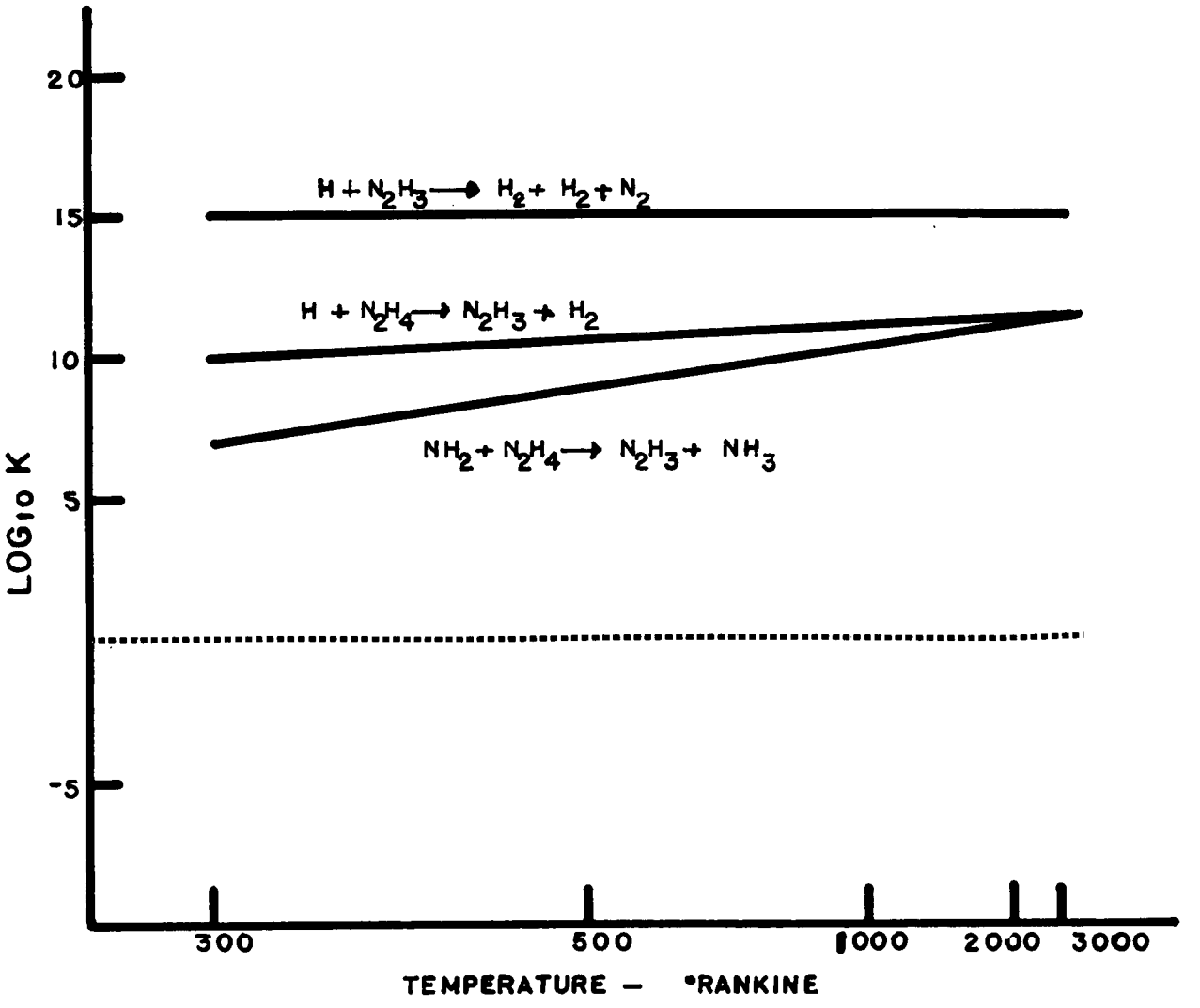

FIGURE 3. SPECIFIC RATE CONSTANT vs TEMPERATURE

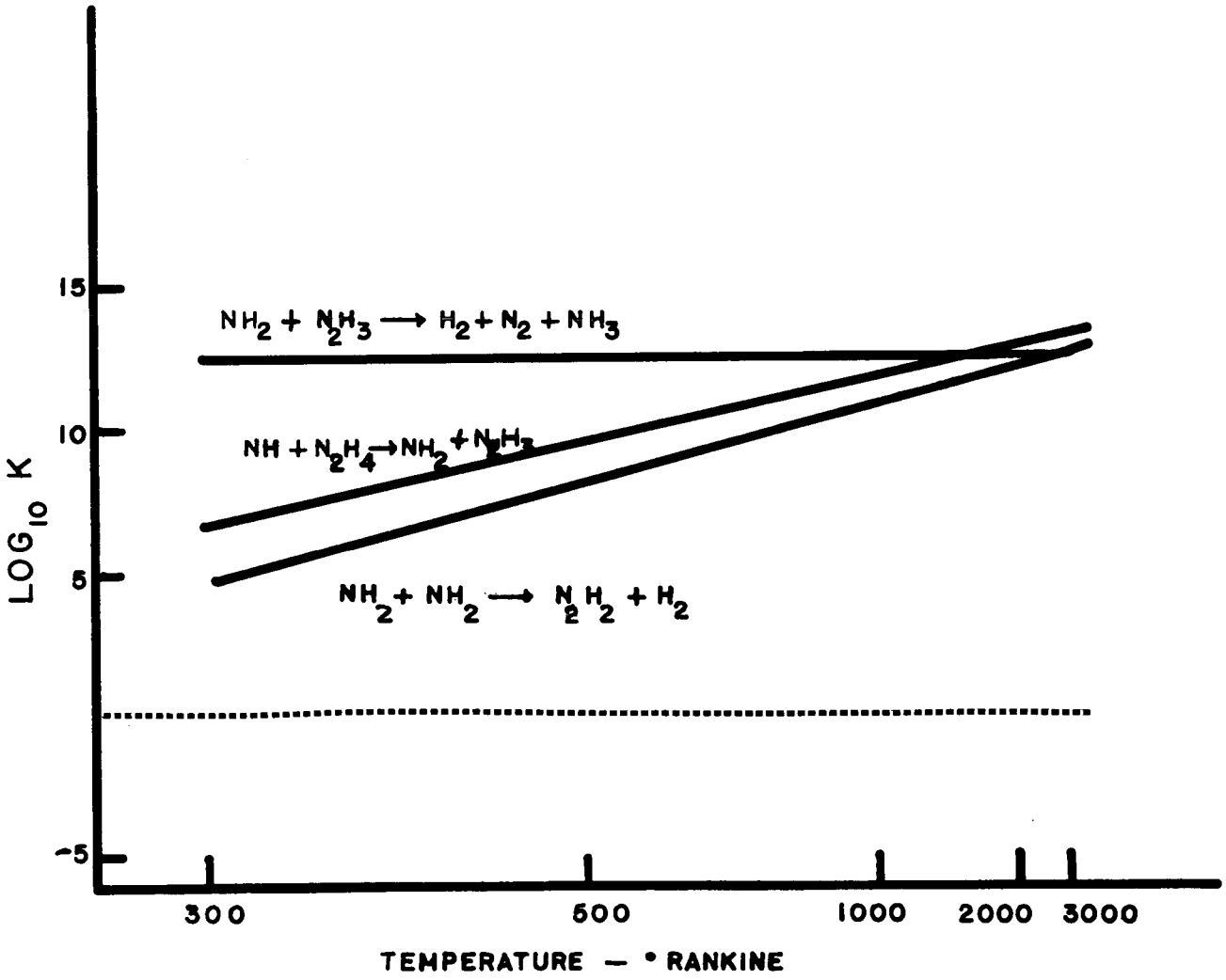

FIGURE 4 SPECIFIC RATE CONSTANT vs TEMPERATURE

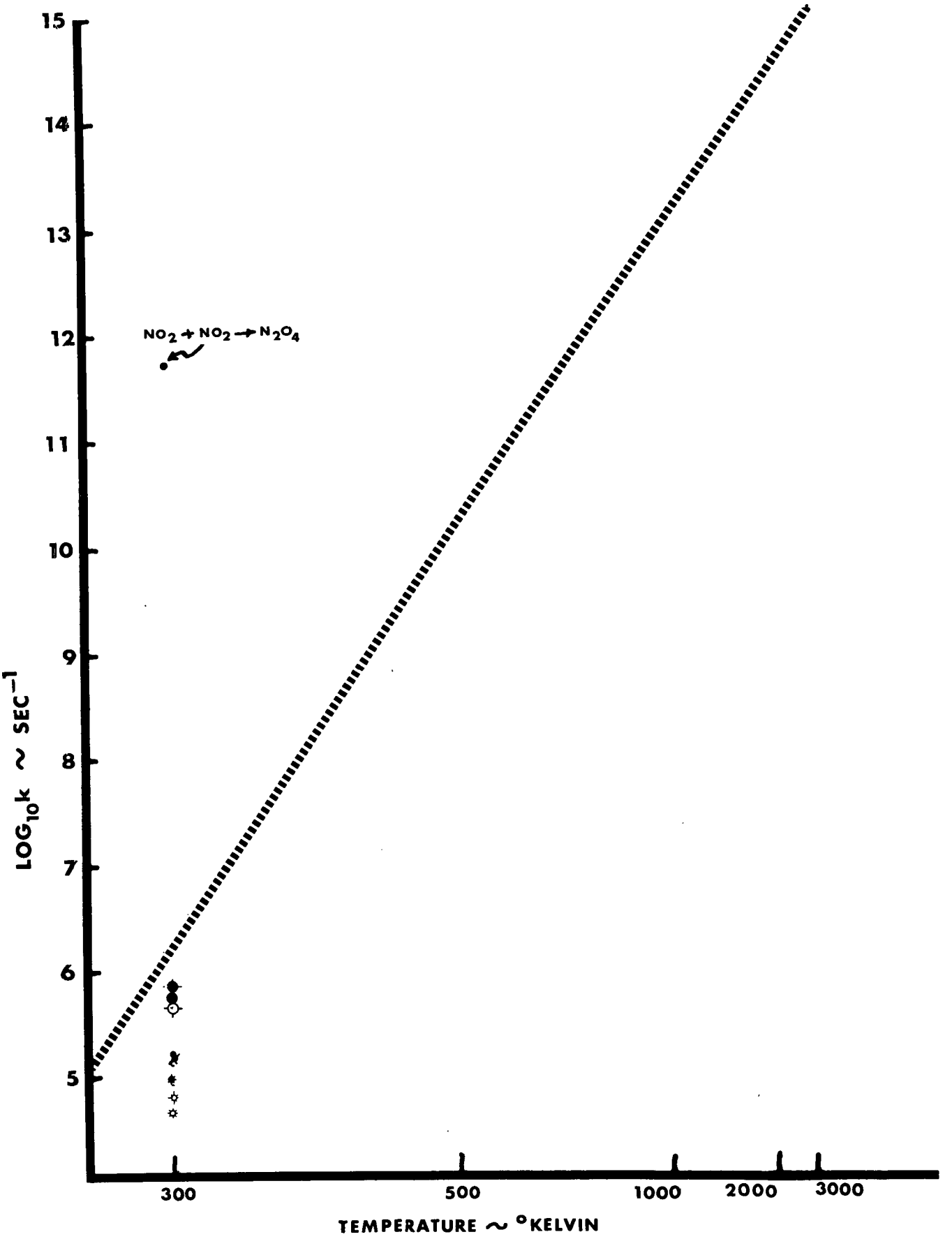

FIGURE 5 SPECIFIC RATE CONSTANT vs TEMPERATURE
$N_2O_4 \rightarrow NO_2 + NO_2$

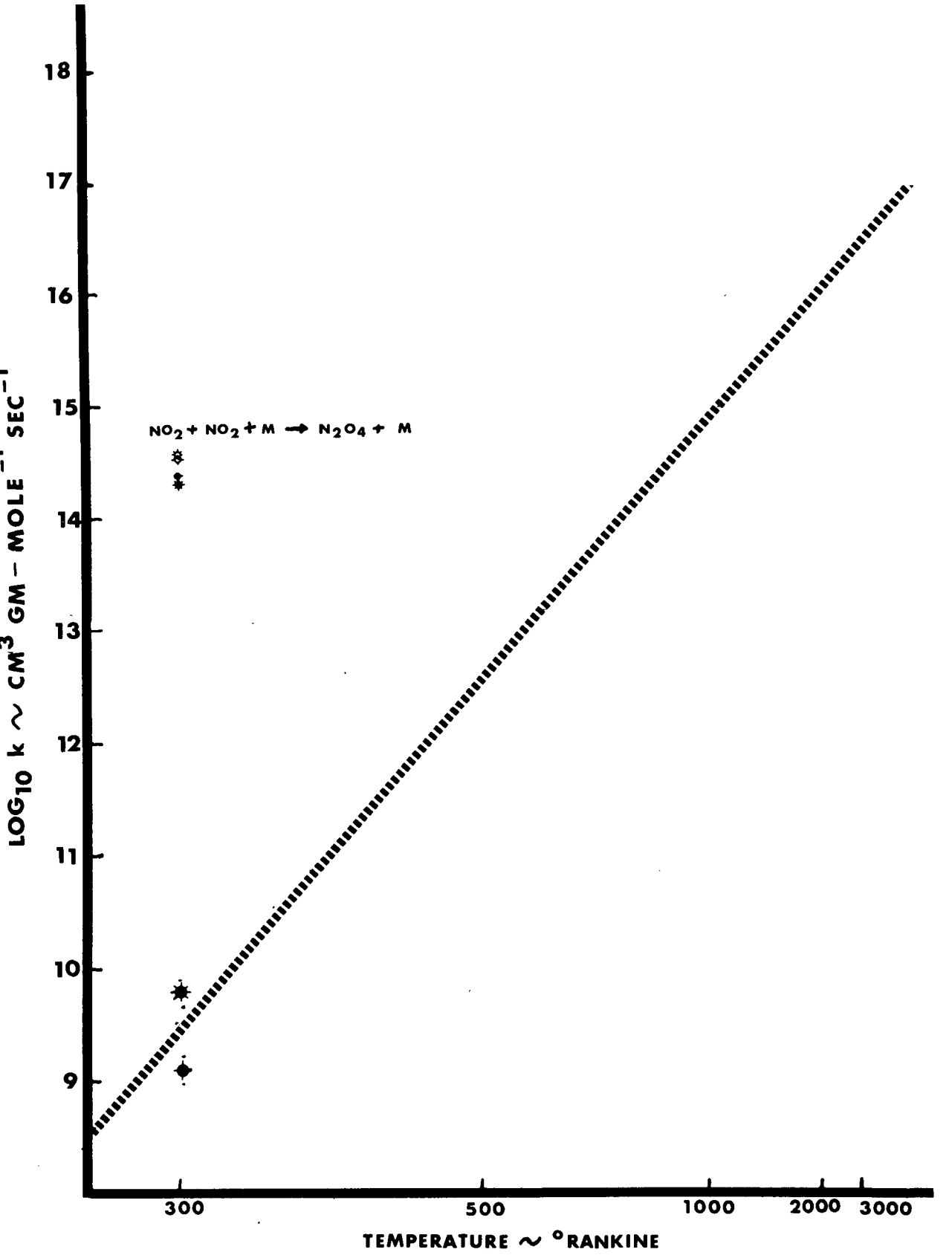

FIGURE 6 SPECIFIC RATE CONSTANT vs TEMPERATURE

$N_2O_4 + M \rightarrow NO_2 + NO_2 + M$

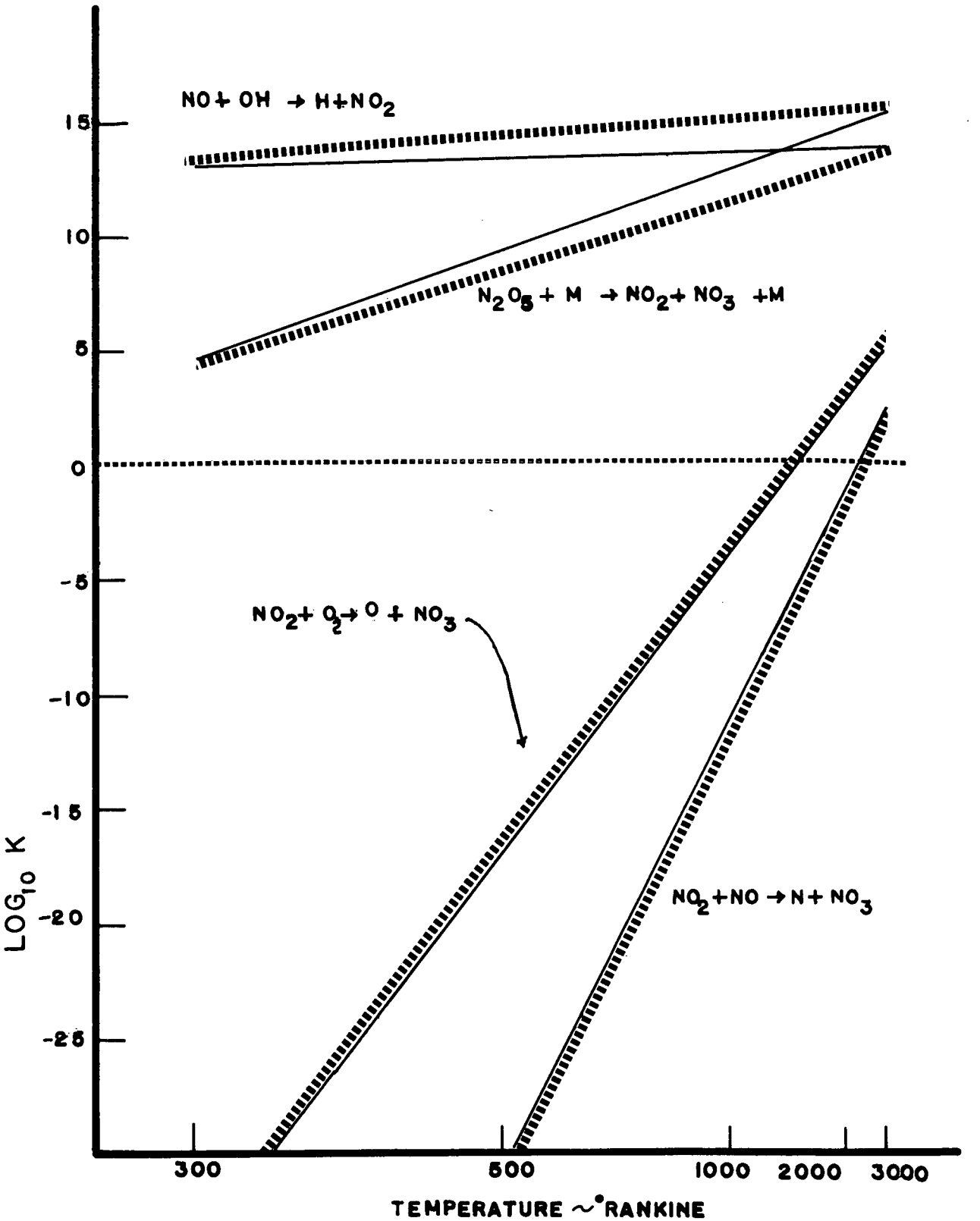

FIGURE 7 SPECIFIC RATE CONSTANT *vs* TEMPERATURE

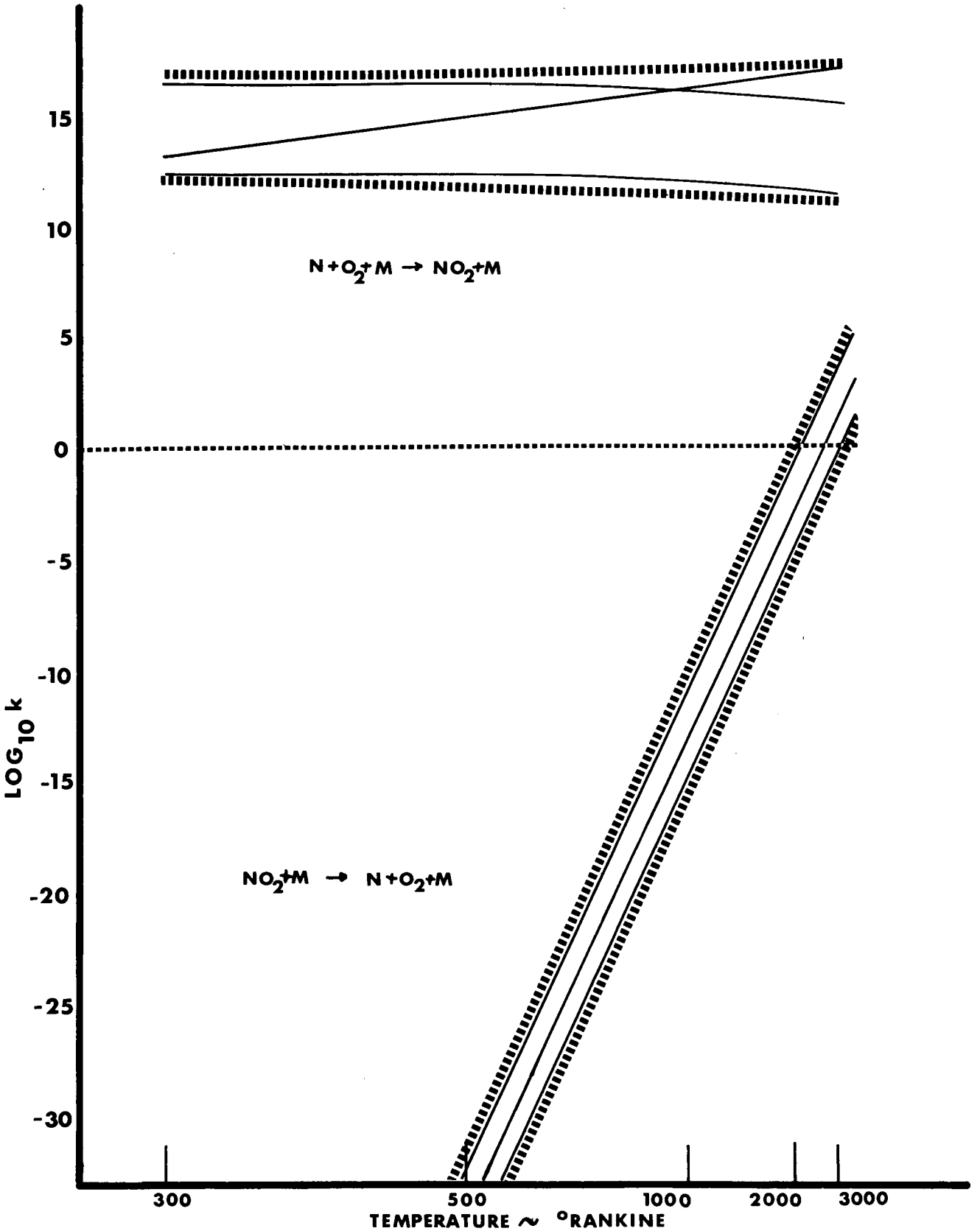

FIGURE 8 SPECIFIC RATE CONSTANT k vs TEMPERATURE
$NO_2+M \rightarrow N+O_2+M$ & $N+O_2+M \rightarrow NO_2+M$

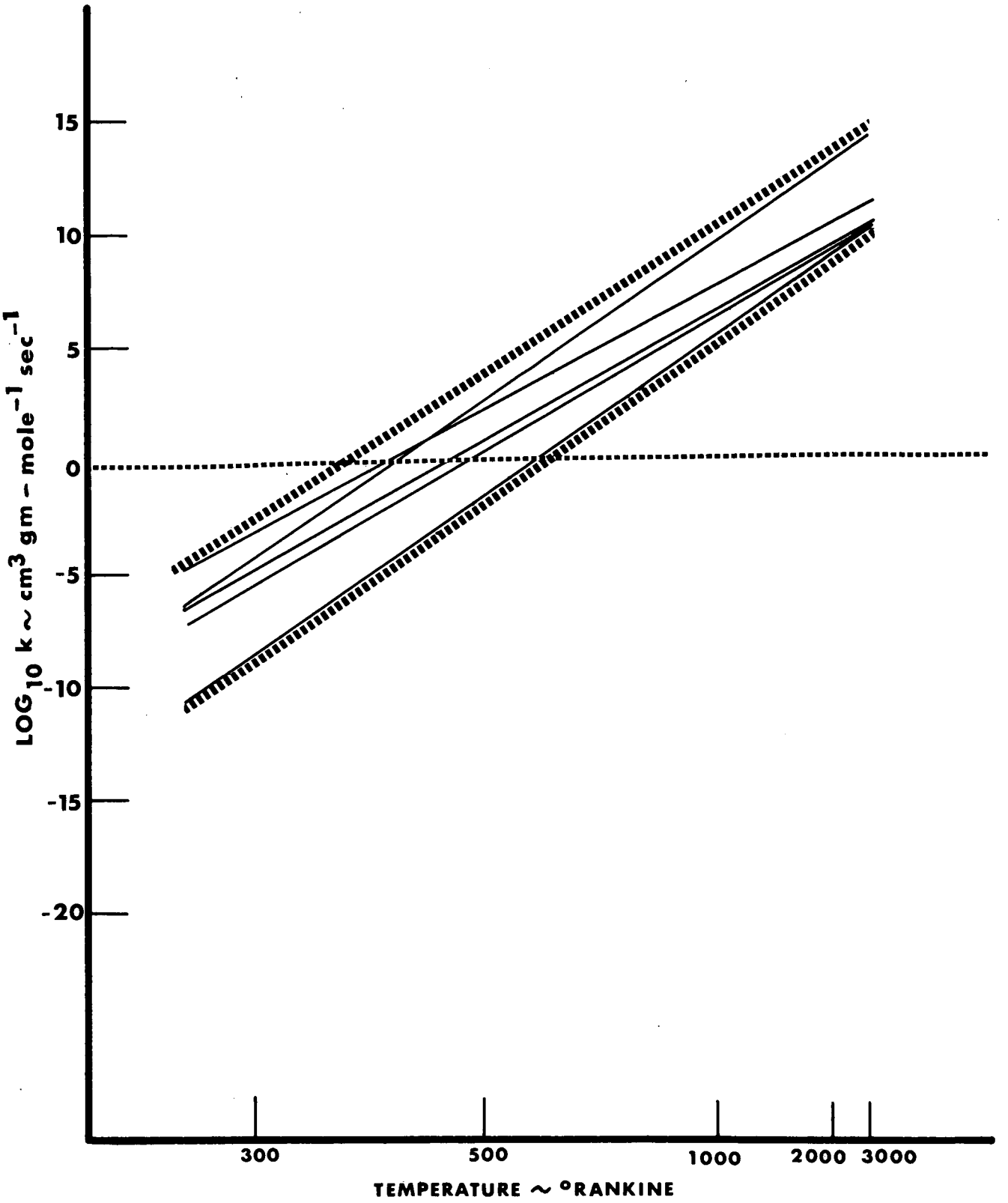

FIGURE 9 SPECIFIC RATE CONSTANT k vs TEMPERATURE

$NO_2 + NO_2 \rightarrow NO + NO + O_2$

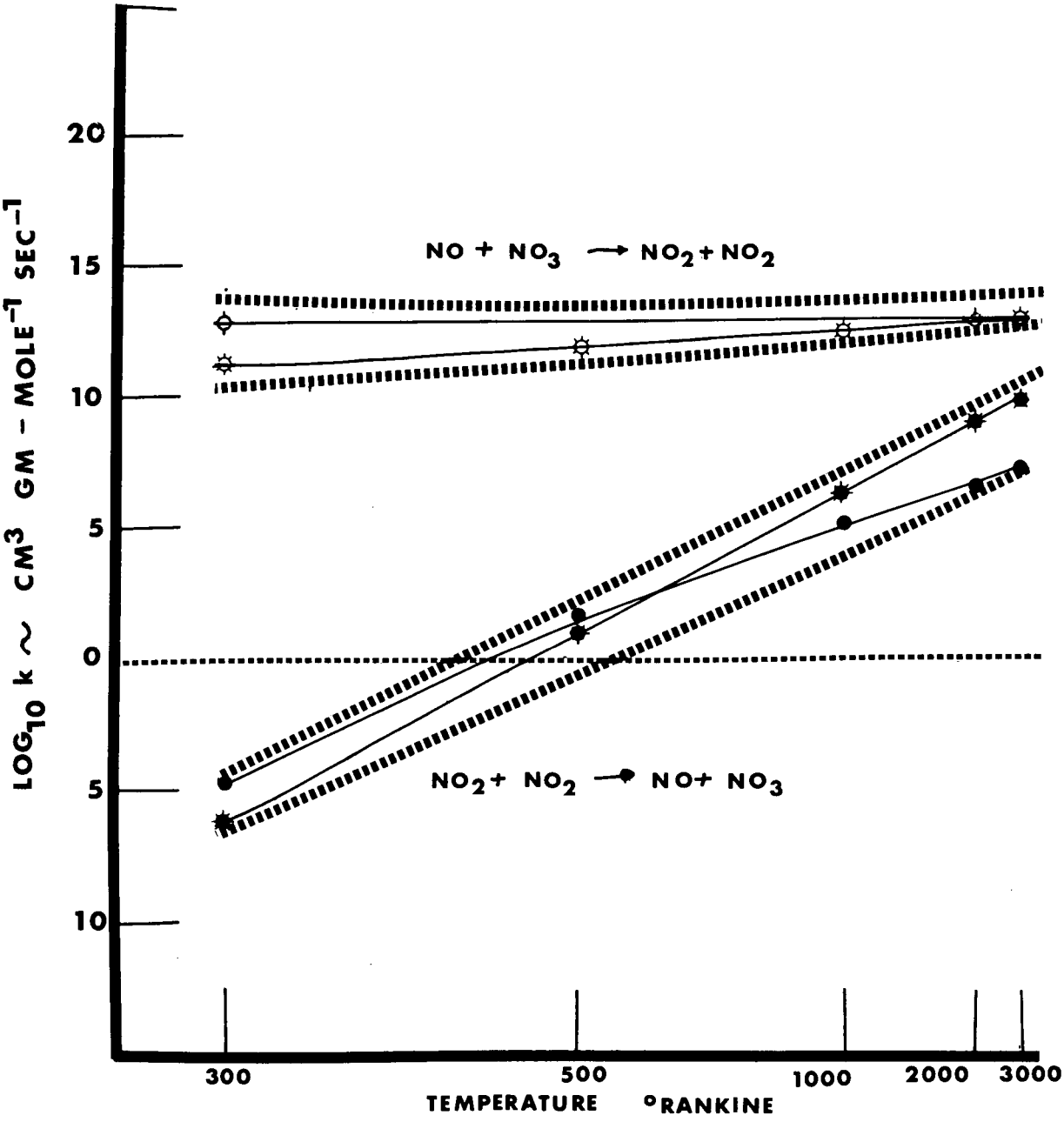

FIGURE 10: SPECIFIC RATE CONSTANT vs TEMPERATURE

$NO_2 + NO_2 \rightleftharpoons NO + NO_3$

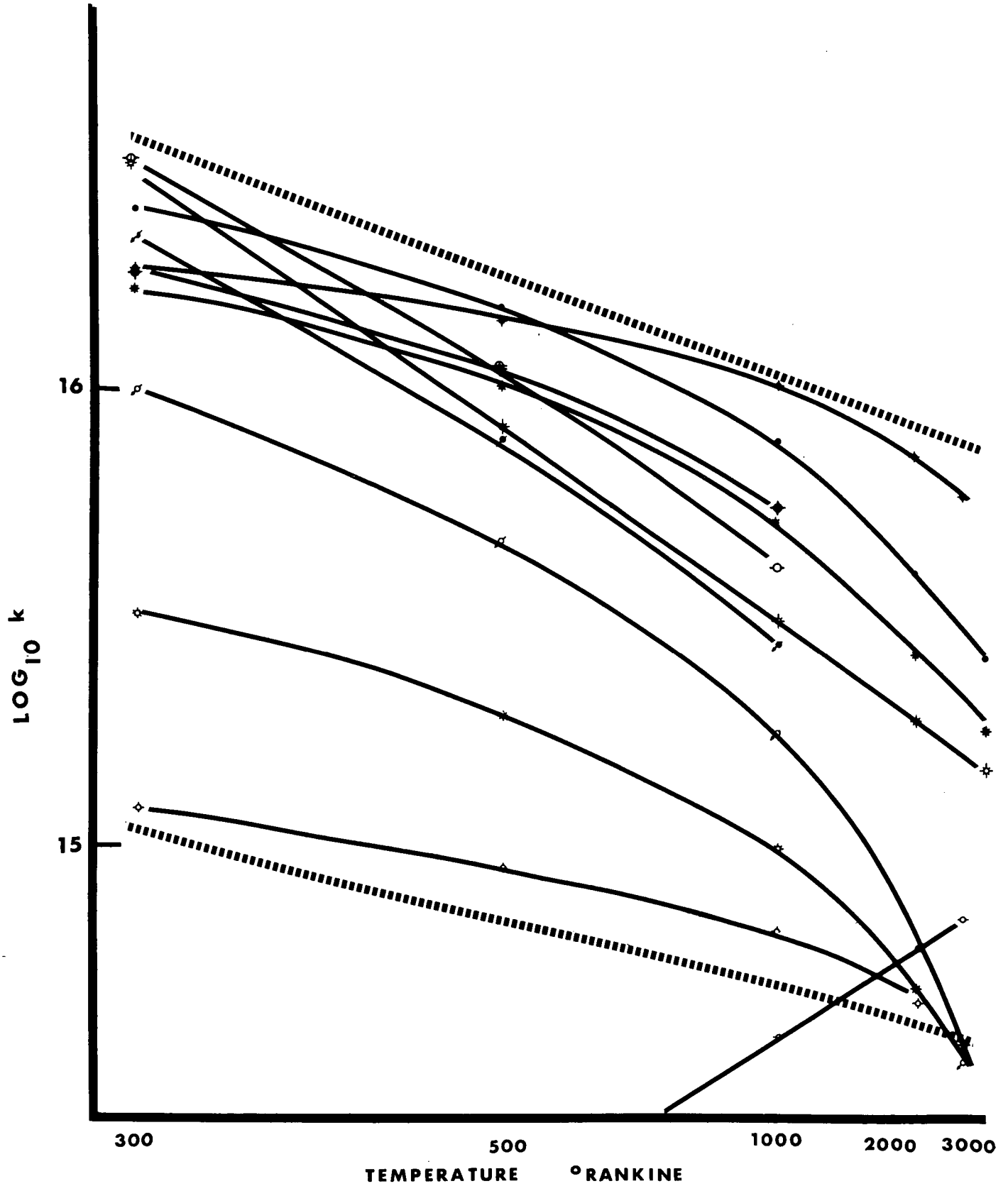

FIGURE 11 SPECIFIC RATE CONSTANT vs TEMPERATURE
$NO + O + M \longrightarrow NO_2 + M$

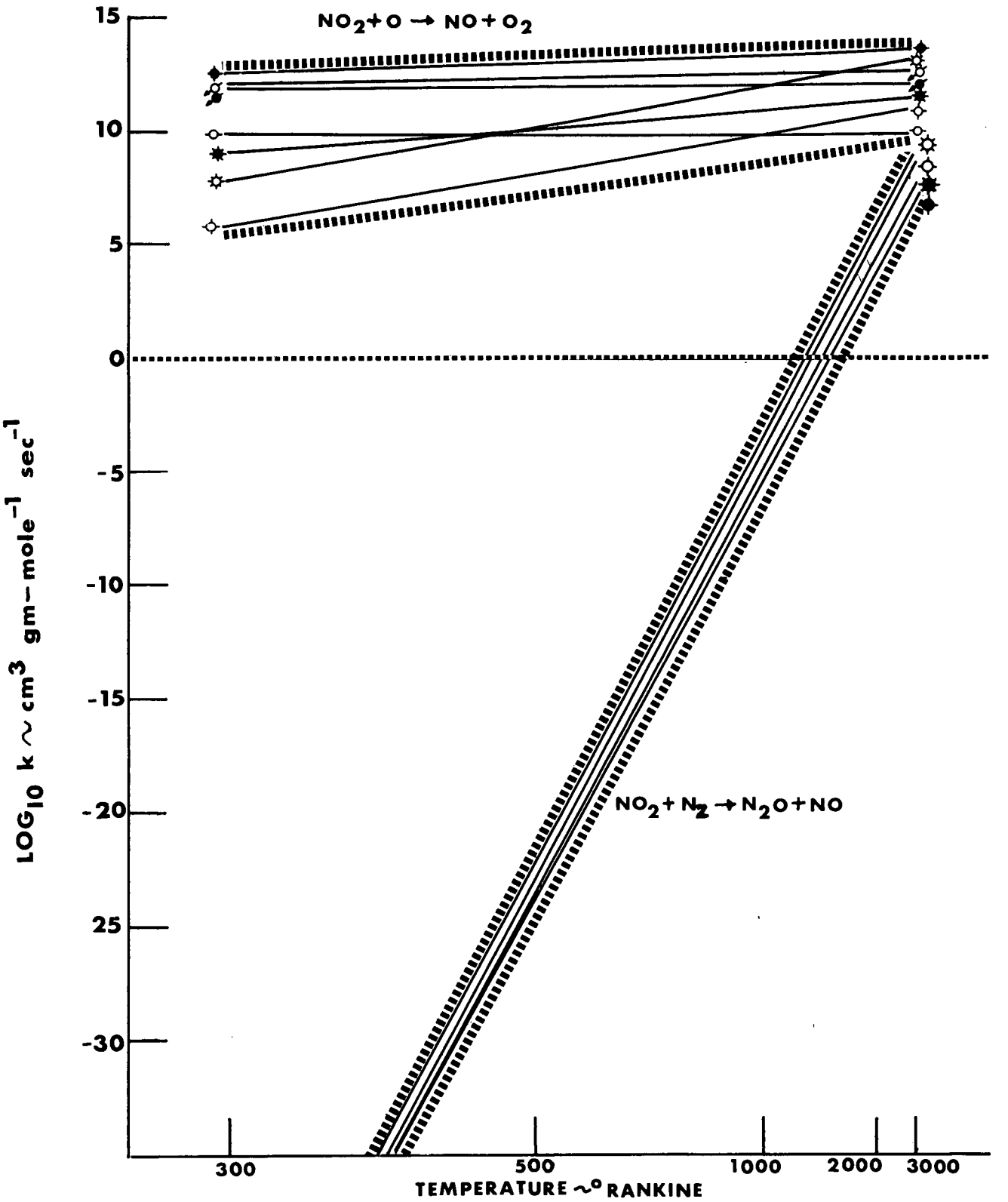

FIGURE 12 SPECIFIC RATE CONSTANT k vs TEMPERATURE

$NO_2+N_2 \rightarrow N_2O+NO$ & $NO_2+O \rightarrow NO+O_2$

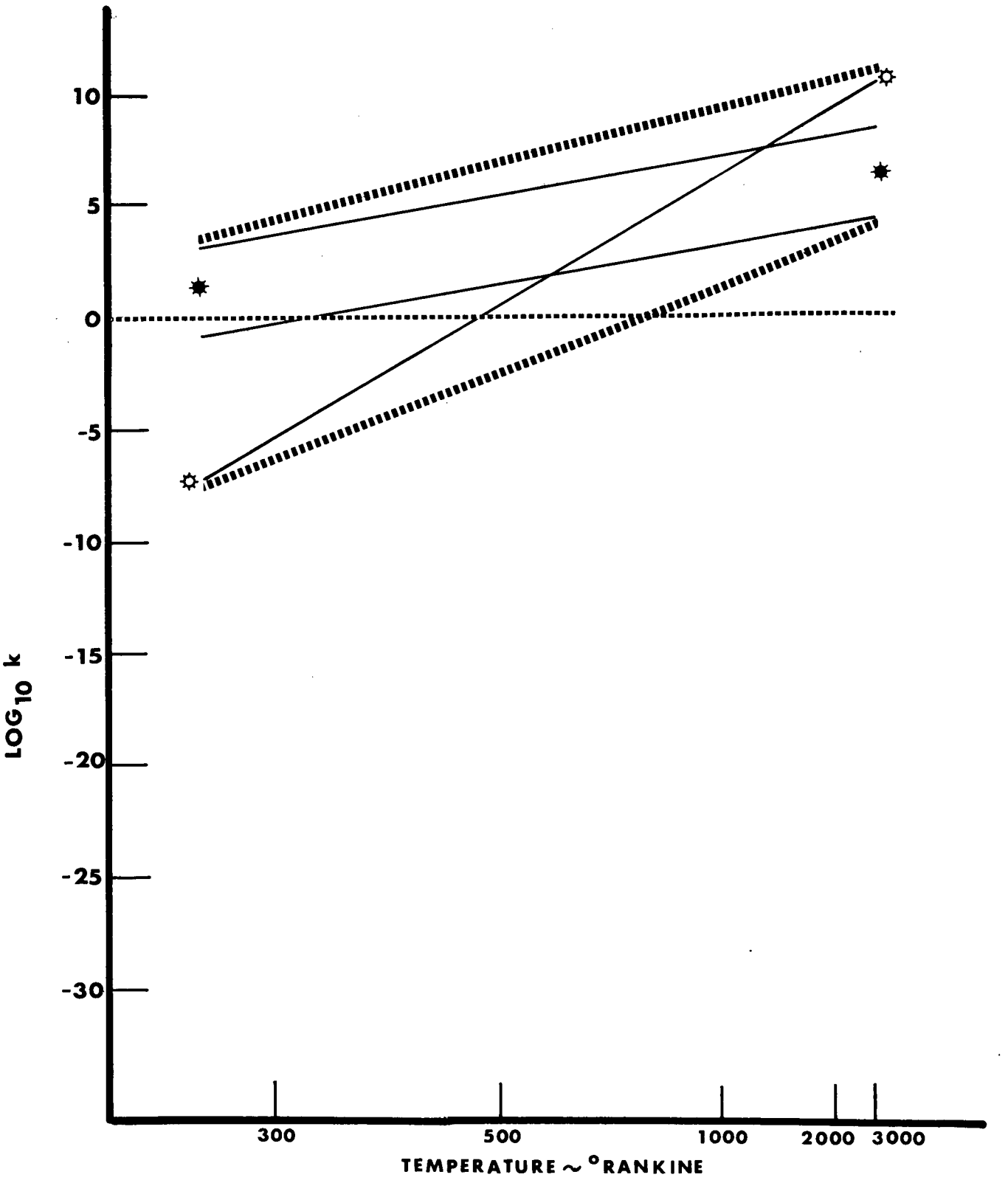

FIGURE 13 SPECIFIC RATE CONSTANT k vs TEMPERATURE

$NO + NO + O_2 \rightarrow NO_2 + NO_2$

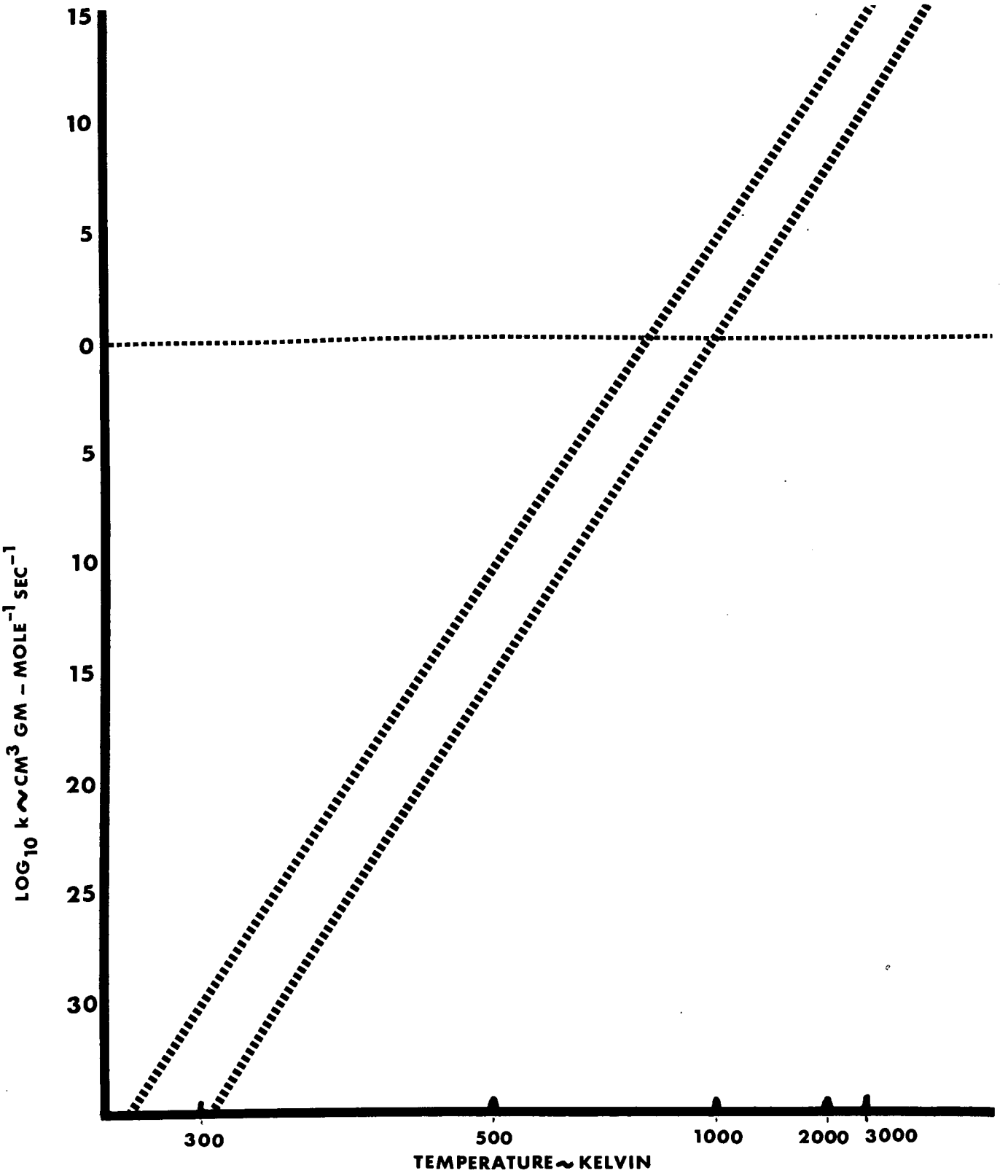

FIGURE 14 SPECIFIC RATE CONSTANT vs TEMPERATURE
$NO_2 + M \rightarrow O + NO + M$

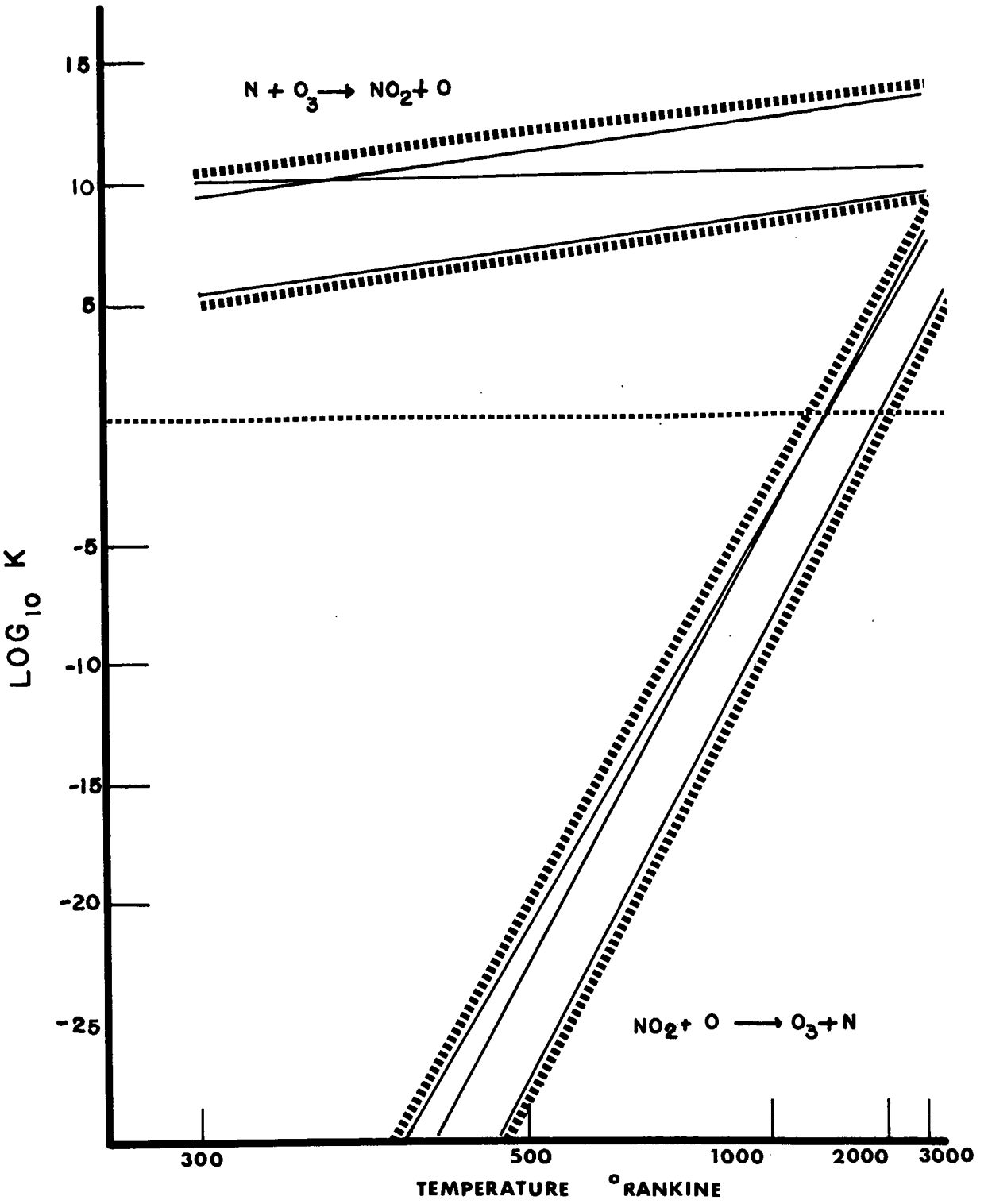

FIGURE 15 SPECIFIC RATE CONSTANT k vs TEMPERATURE

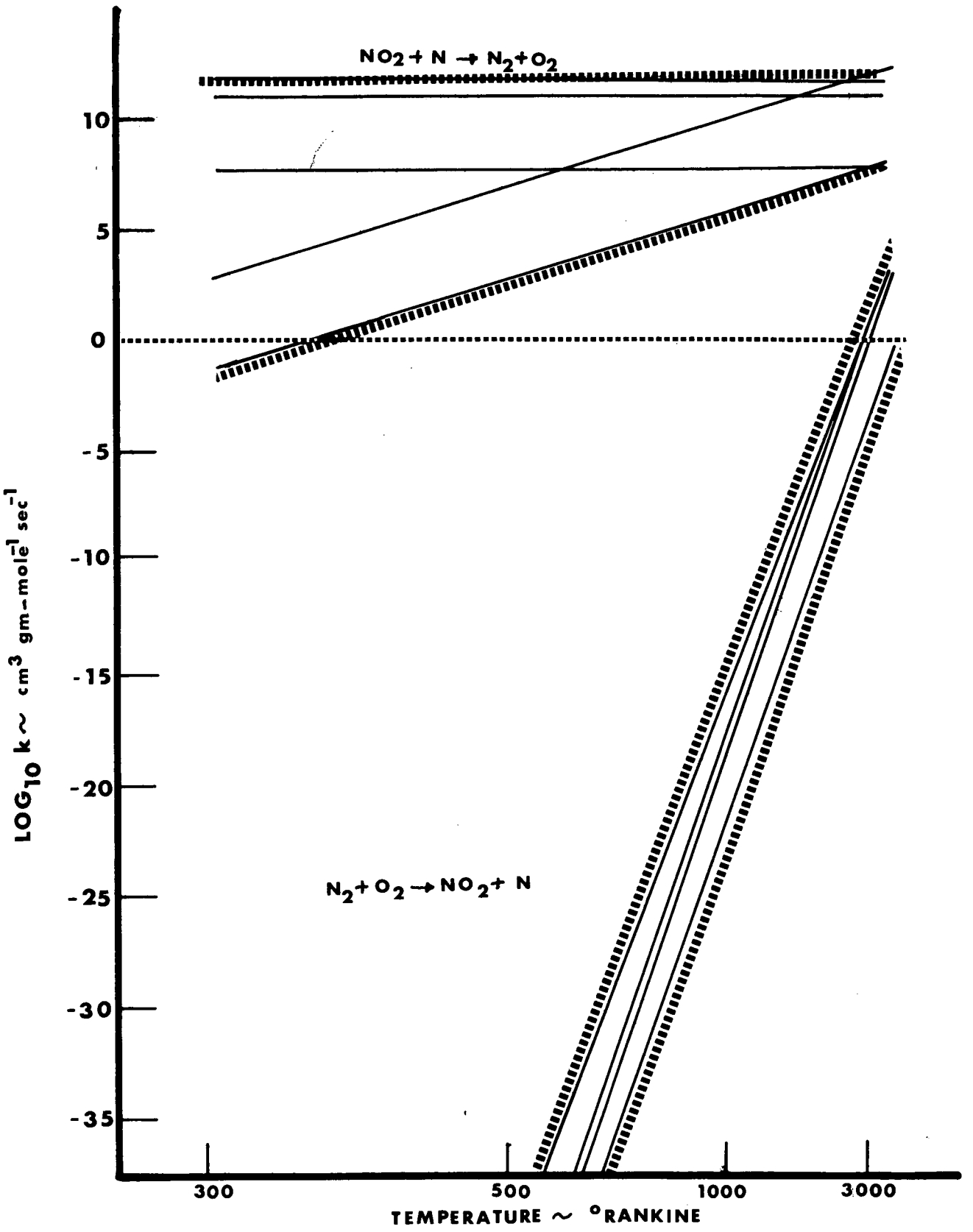

FIGURE 16 SPECIFIC RATE CONSTANT k vs TEMPERATURE
$NO_2 + N \rightleftharpoons N_2 + O_2$

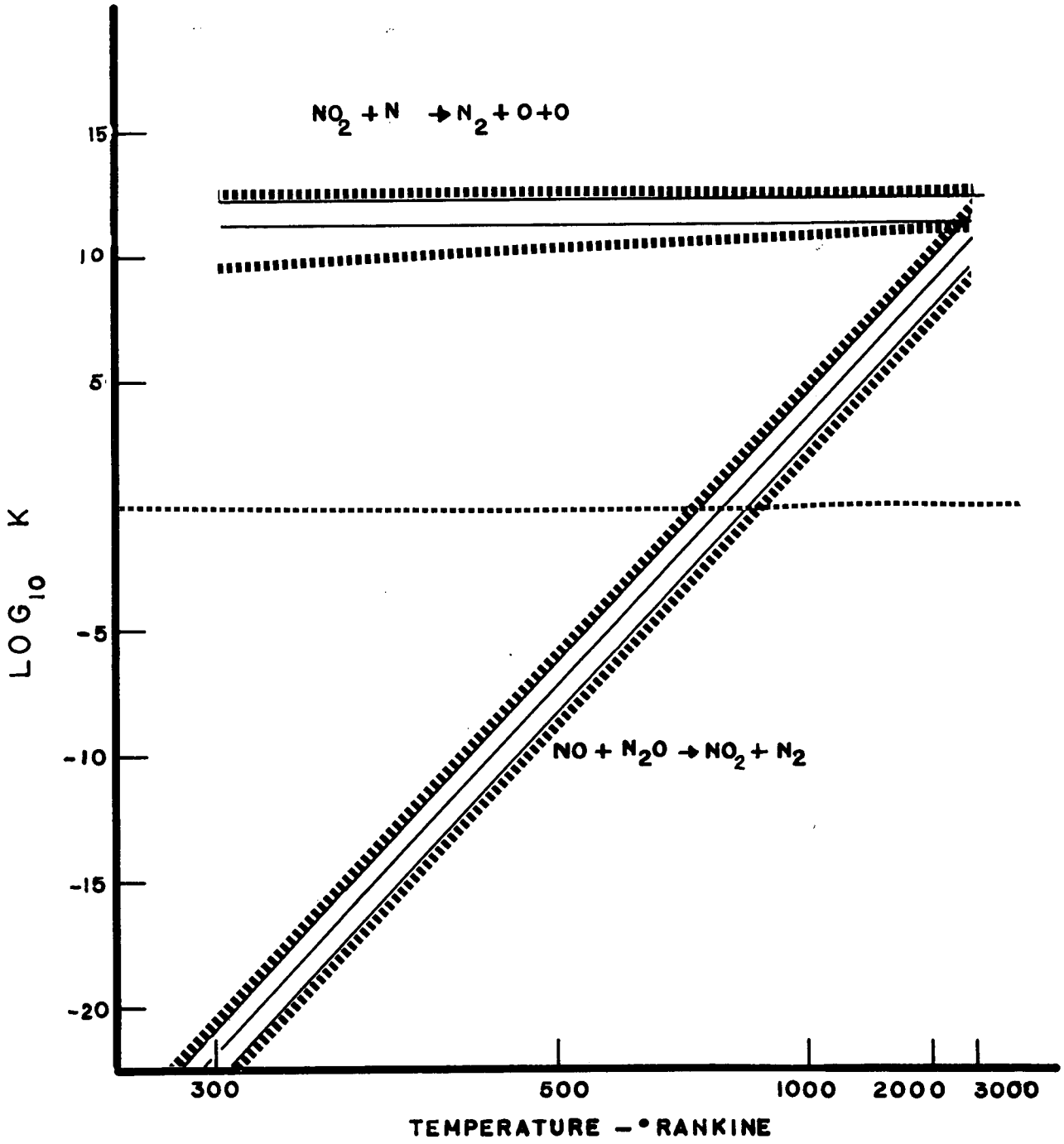

FIGURE 17 SPECIFIC RATE CONSTANT *vs* TEMPERATURE

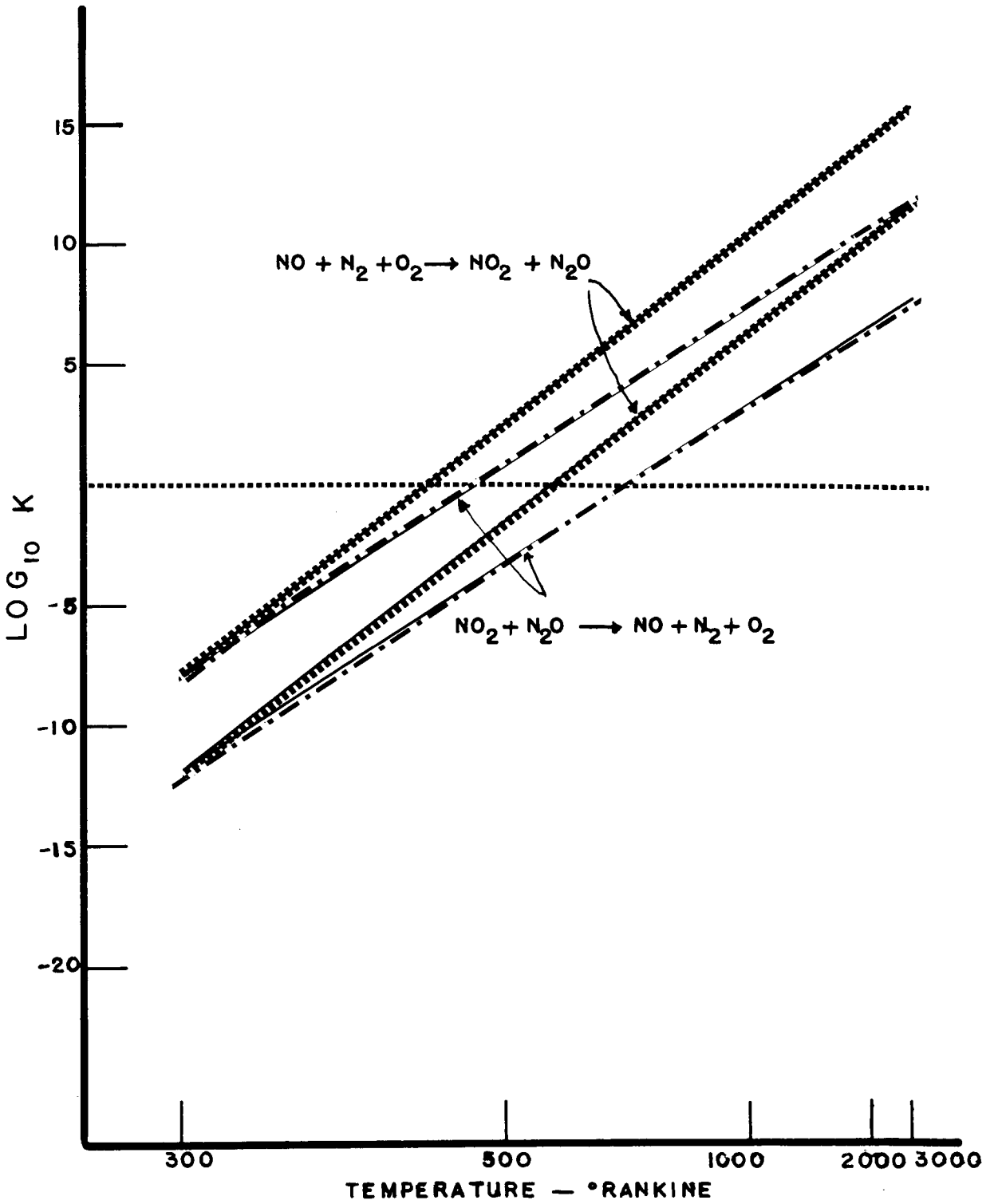

FIGURE 18 SPECIFIC RATE CONSTANT vs TEMPERATURE

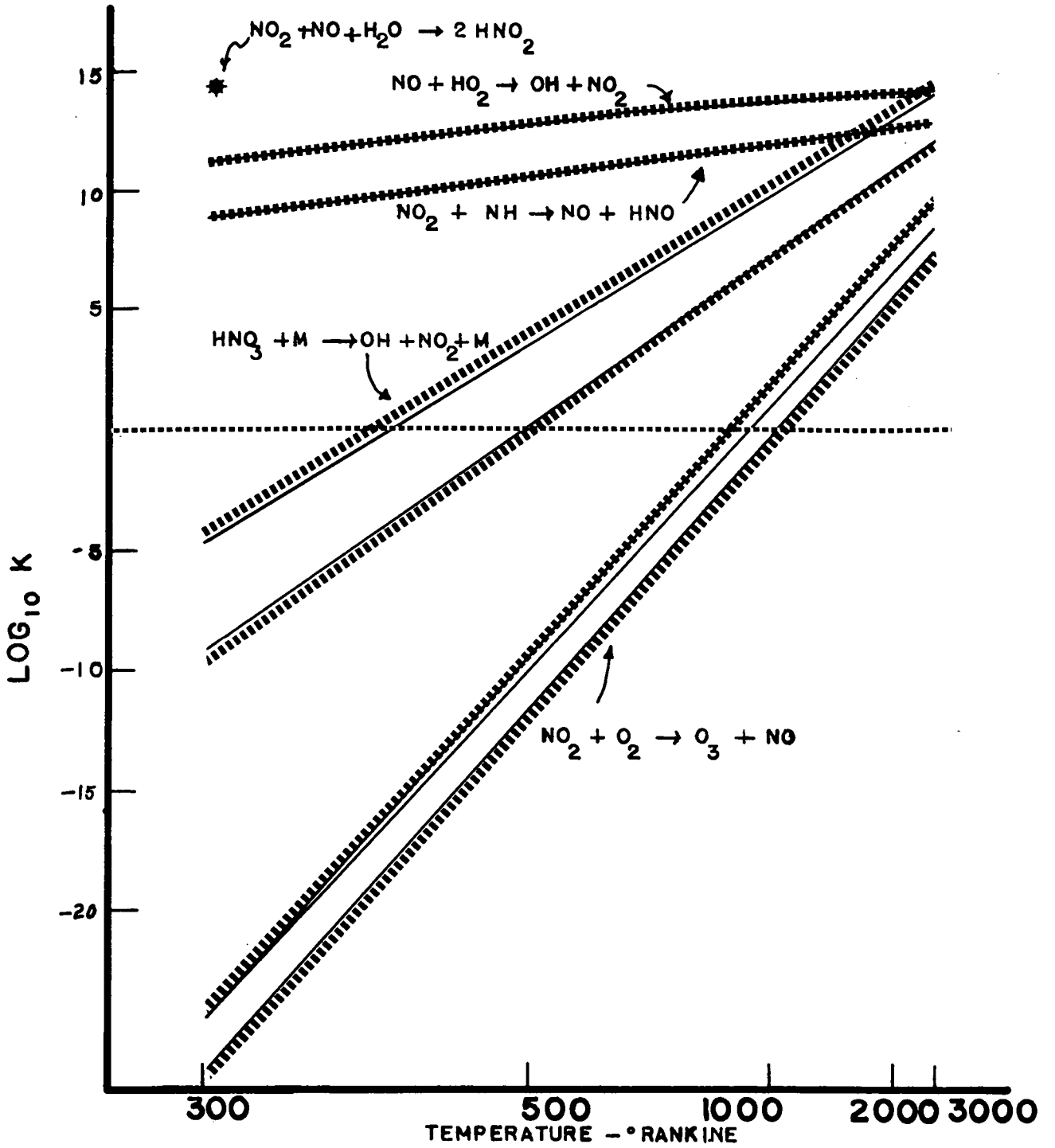

FIGURE 19 SPECIFIC RATE CONSTANT vs TEMPERATURE

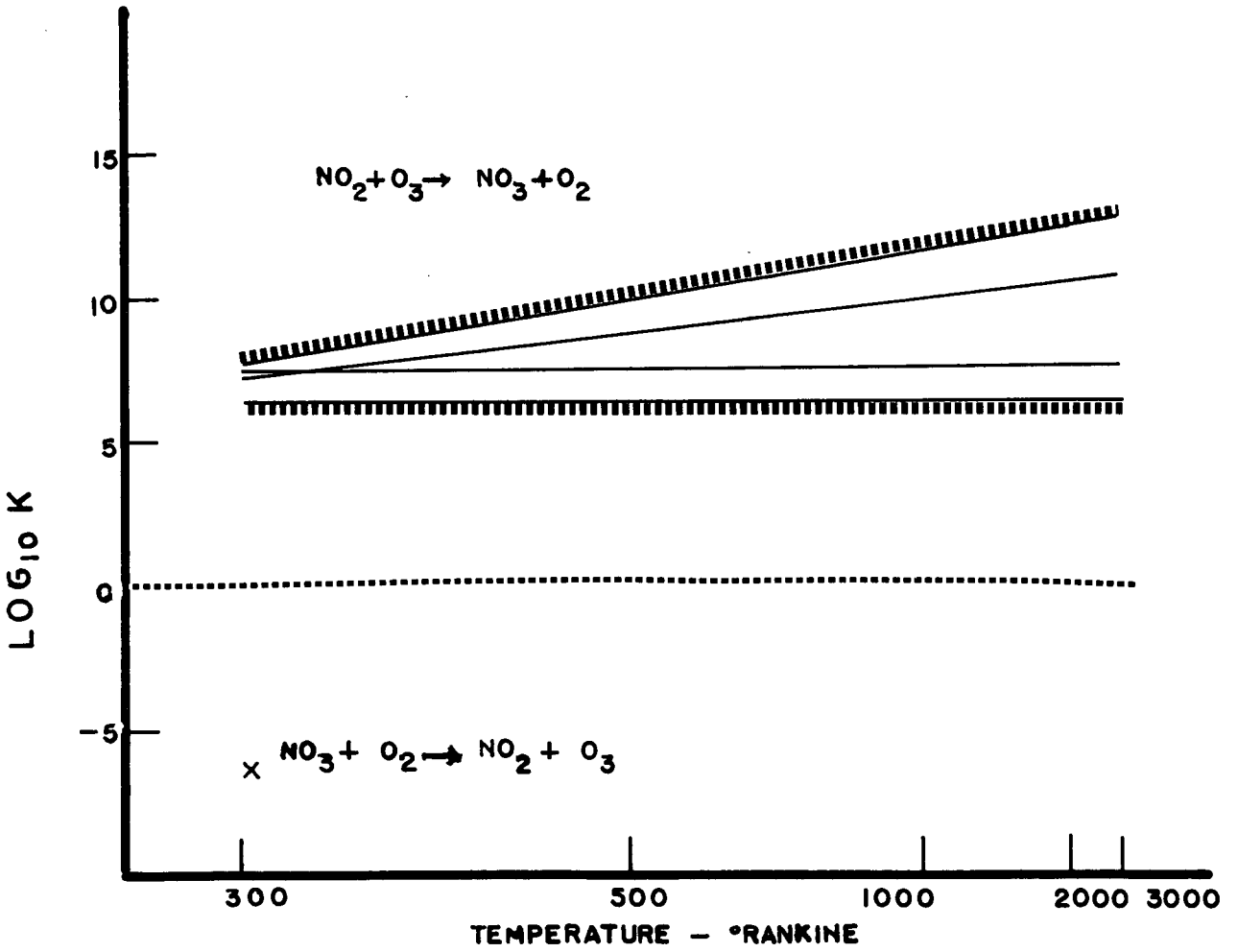

FIGURE 20 SPECIFIC RATE CONSTANT vs TEMPERATURE

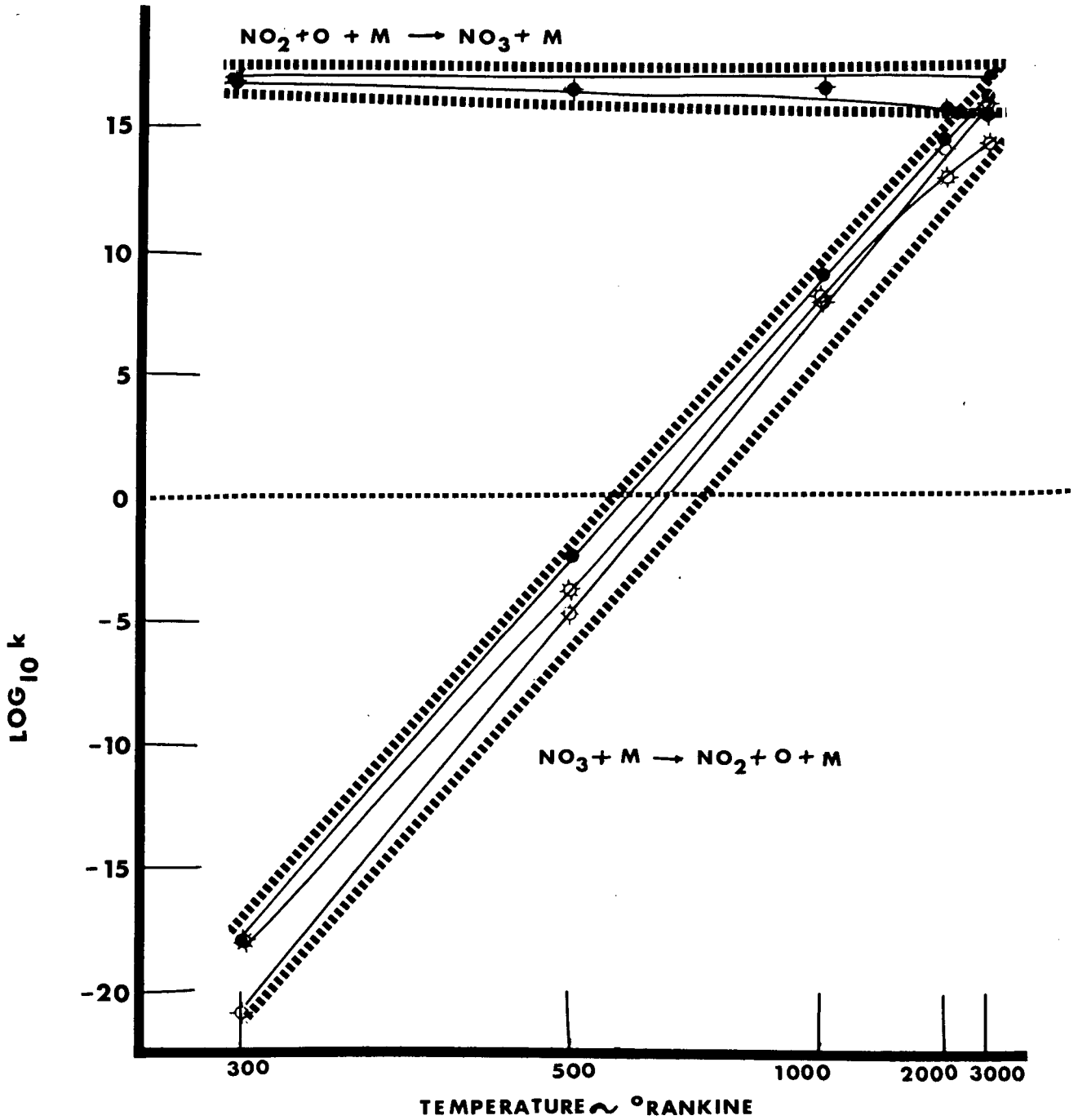

FIGURE 21 SPECIFIC RATE CONSTANT vs TEMPERATURE

$NO_2 + O + M \rightleftharpoons NO_3 + M$

C3

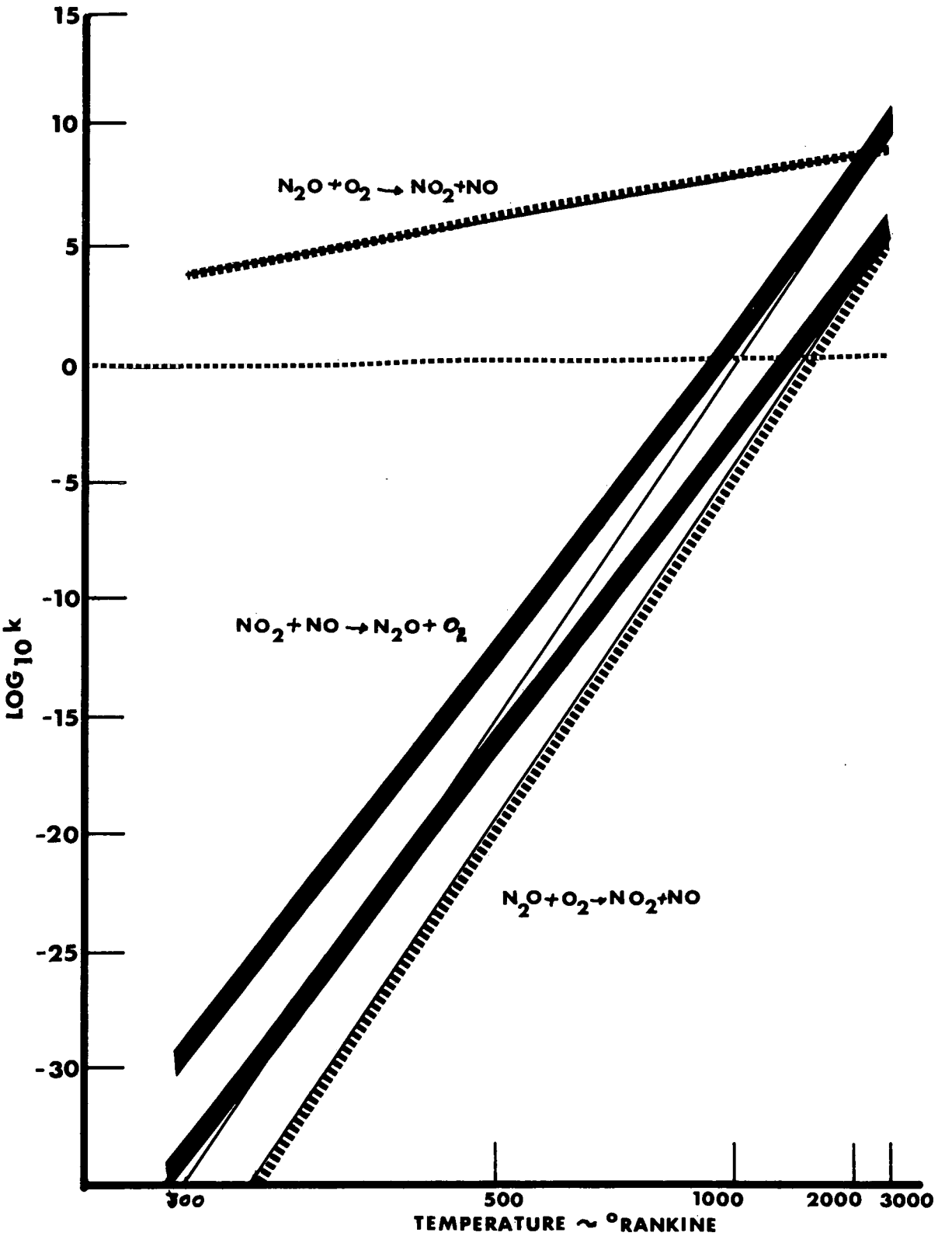

FIGURE 22 SPECIFIC RATE CONSTANT vs TEMPERATURE
$NO_2+NO \rightarrow N_2O+O_2$ & $N_2O+O_2 \rightarrow NO+NO_2$

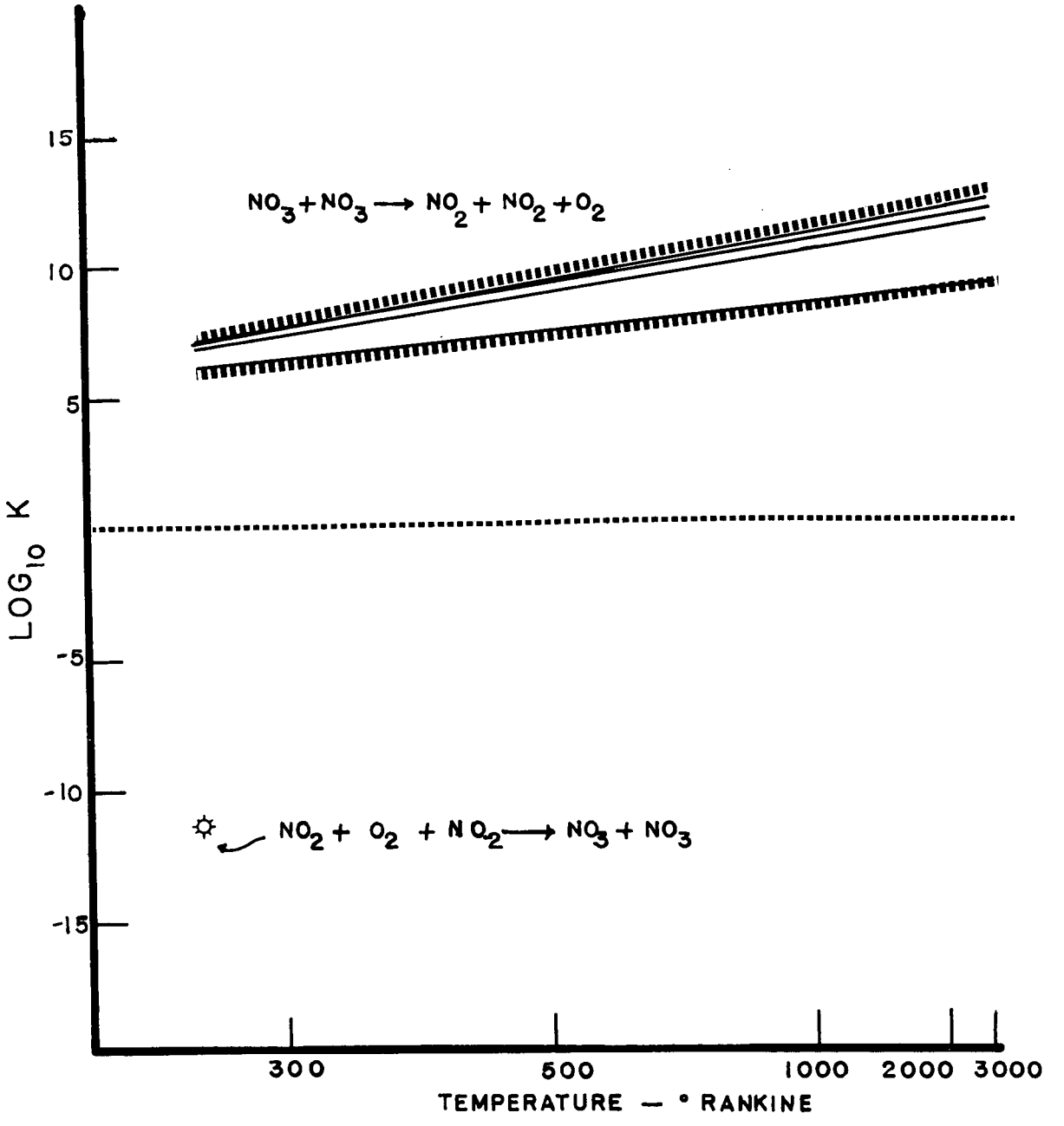

FIGURE 23 SPECIFIC RATE CONSTANT vs TEMPERATURE

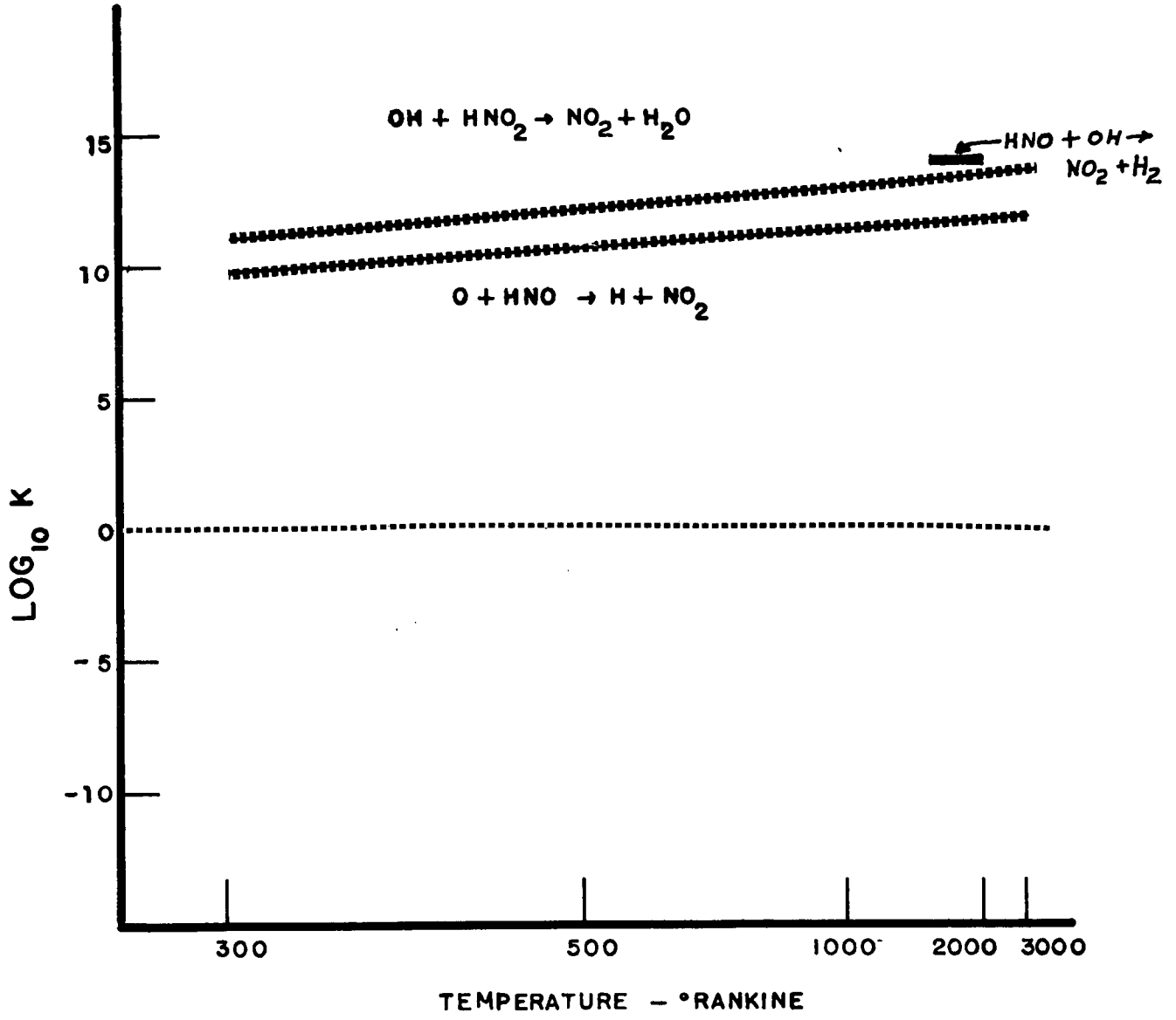

FIGURE 24 SPECIFIC RATE CONSTANT vs TEMPERATURE

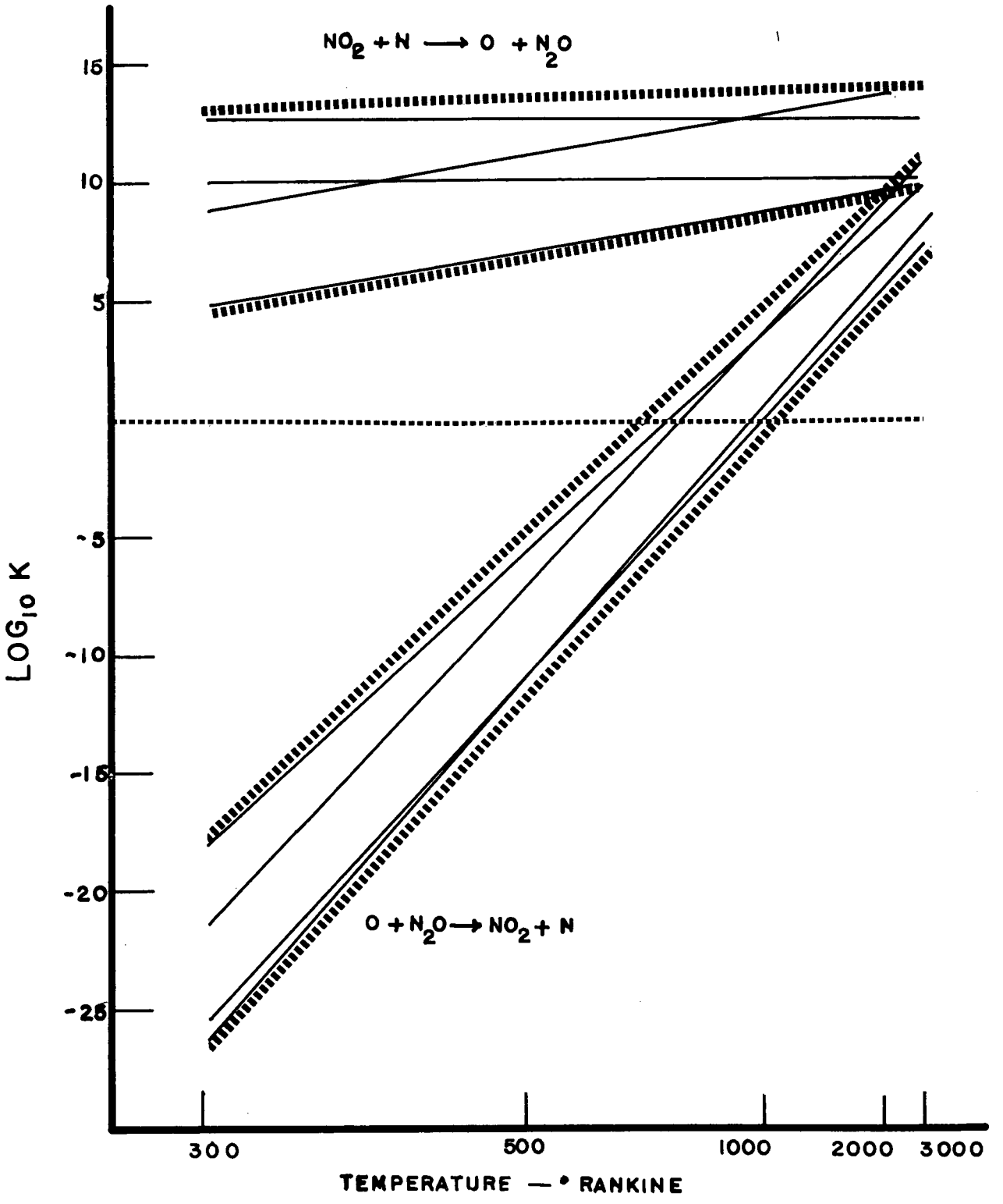

FIGURE 25 SPECIFIC RATE CONSTANT vs TEMPERATURE

REFERENCE

1. Ashmore, P. G. and Levitt, B. P., Res. Correspondence, 9(6), S25-S26 (1956). πρ 01314.

2. Baker, D. J. and Moore, W. M., Air Force Cambridge Res. Lab. Rept., AFCRL-64-897 (1 April 1964). πρ 05617.

3. Barnes, R. H., Jung, R. G., Kircher, J. F., Ritzman, R. L., Smith, J. C., and Steginsky, B., Battelle Memorial Inst. Repot. BMI-197-IO-2 (31 March 1964). πρ 05616.

4. Barth, C. A.,"Chemical Reactions in the Lower and Upper Atmosphere," pp. 303-326, Interscience, New York, 1961. πρ 00171.

5. Barth, C. A., Jet Propulsion Lab./ California Inst. Rept. 32-63 (14 April 1961). πρ 00198.

6. Benson, S. W., J. Chem. Phys., 38, 1251-1252 (1963). πρ 00664.

7. Benson, S. W., The Foundations of Chemical Kinetics, McGraw-Hill, New York, 1960. πρ 01219.

8. Blend, H., Univ. California, Los Angeles, Dept. Phys. Tech. Rept. 19 on Contract Nonr 233(48) (August 1962). πρ 01325.

9. Bortner, M. H. and Golden, J. A., General Electric Co., Missile Space Vehicle Dept. Rept. R61SD023 (February 1961). πρ 00188.

10. Bortner, M. H., General Electric Co., Missile Space Vehicle Dept. Rept. R61SD122 (June 1961). πρ 00192.

11. Bortner, M. H., General Electric Co., Missile Space D v. Dept. R63SD63 (August 1963). πρ 05567.

12. Bortner, M. H., General Electric Co., Missile Space Div. Rept. R63SD34 (September 1963). πρ 05569.

13. Bortner, M. H. and Povard, V. D., Air Force Cambridge Res. Lab. Rept. AFCRL-64-496 (March 1964). πρ 05612.

14. Bortner, M. H., Air Force Cambridge Res. Lab. Rept. AFCRL-65-392 (April 1965). πρ 05668.

15. Bortner, M. H. and Galbraith, H. J., General Electric Co., Missile Space Div. Final Rept. on Contract DA-49-146-XZ-325 (31 May 1965) πρ 05672.

16. Bradley, J. M., Shock Waves in Chemistry and Physics. Wiley, New York, 1962. πρ 00203.

17. Branscomb, L. M. and Lelevier, R. E., RAND Corp. Memo. RM-4364-PR (December 1964). πρ 05627.

18. Brass, P. D. and Toman, R. C., J. Amer. Chem. Soc., 54, 1003-1020 (1932). πρ 01308.

19. Broida, H. P., Schiff, H. I., and Sugden, T. M., Nature, 185, 759-760, (1960). πρ 01001.

20. Bulewicz, E. M. and Sugden, T. M., Proc. Roy. Soc., A277, 143-154 (1964). πρ 05603.

21. Carrington, T. and Davidson, N., J. Chem. Phys., 19, 1313 (1951). πρ 05501.

22. Carrington, T. and Davidson, N., J. Phys. Chem., 57, 418-427 (1953). πρ 01313.

23. Cher, M., J. Chem. Phys., 37, 2564-2570 (1962). πρ 01323.

24. Clyne, M. A. A. and Thrush, B. A., Proc. Roy. Soc., A269, 404-418 (1962). πρ 00661.

25. Clyne, M. A. A. and Thrush, B. A., Trans. Faraday Soc., 58, 511-515 (1962). πρ 01324.

26. Clyne, M. A. A. and Thrush, B. A., Proc. Roy. Soc., A275, 559-574 (1963). πρ 00668.

27. Davidson, N. and Schott, G. L., J. Chem. Phys., 27, 317-318 (1957). πρ 00636.

28. Davidson, N., Avco Mnfg. Corp., Avco Res. Lab. Res. Rept., 32 (June 1958). πρ 00137.

29. Eberstein, I. J. and Glassman, I., Tenth Symposium (International) on Combustion, pp. 365-374. The Combustion Institute, 1965. πρ 04477.

30. Faraday Society, Disc. Faraday Soc., 33, 273-299 (1962). πρ 00659.

31. Fenimore, C. P., J. Chem. Phys., 35, 3243 (1961). πρ 05531.

32. Fishburne, E. S., Bergbauer, D. M., and Edse, R., Air Force Aerospace Res. Lab. Rept. ARL-65-169 (August 1965). πρ 05676.

33. Fishburne, E. S. and Edse, R., J. Chem. Phys., 44, 515-520 (1966). πρ 05686.

34. Ford, H. W., Doyle, G. J., and Endow, N., J. Chem. Phys., 26, 1336 (1957). πρ 01316.

35. Ford, H. W., Doyle, G. J., and Endow, N., J. Chem. Phys., 26, 1337 (1957). πρ 00998.

36. Ford, H. W. and Endow, N., J. Chem. Phys., 27, 1277-1279 (1957). πρ 00638.

37. Ford, H. W. and Endow, N., J. Chem. Phys., 27, 1156-1160 (1957). πρ 00637.

38. Ford, H. W., Doyle, G. J., and Endow, N., J. Cgem. Phys., 32, 1256-1257 (1960). πρ 01002.

39. Ford, H. W., Can. J. Chem., 38, 1780-1794 (1960). πρ 05523.

40. Ford., H., Eighth Symposium (International) on Combustion, pp. 119-127. Williams and Wilkins, Baltimore, 1962. πρ 00657.

41. Fristrom, R. M., Ninth Symposium (International) on Combustion, pp. 560-575. Academic Press, New York, 1963. πρ 02941.

42. Gin, W., Univ. California, Los Angeles, M.S. Thesis (January 1959). πρ 01318.

43. Greene, E. F. and Toennies, J. P., Chemical Reactions in Shock Waves, Academic Press, New York, 1964. πρ 02307.

44. Haaland, C. M., Armour Res. Found./Illinois Inst. Tech. Phys. Div. Rept., ARFDA-28 (1960). πρ 00651.

45. Haaland, C. M., Armour Res. Found./Illinois Inst. Tech. Rept. ARF 1176-9 (December 1961). πρ 01003.

46. Harrison, H., Johnston, H. S., and Hardwick, E. R., J. Amer. Chem. Soc., 84, 2478-2482 (1962). πρ 05545.

47. Harteck, P. and Dondes, S., J. Chem. Phys., 27, 546-551 (1957). πρ 00114.

48. Harteck, P., Reeves, R. R., and Mannella, G. G., J. Chem. Phys., 29, 1333-1335 (1958). πρ 00642.

49. Harteck, P., and Dondes, S., J. Phys. Chem., 63, 956-961 (1959). πρ 00148.

50. Harteck, P. and Reeves, R. R., "Chemical Reactions in the Lower and Upper Atmosphere." pp. 219-238, Interscience, New York, 1961. πρ 00168.

51. Heicklen, J., AIAA, J., 5, 4-15 (1967). πρ 05726.

52. Hiraoka, H. and Hardwick, R., J. Chem. Phys., 39, 2361-2365 (1963). πρ 00666.

53. Huffman, R. E. and Davidson, N., J. Amer. Chem. Soc., 81, 2311-2316 (1959). πρ 00646.

54. Husain, D. and Norrish, R. G. W., Proc. Roy. Soc., A273, 165-179 (1963). πρ 01326.

55. Johnston, H. S. and Yost, D. M., J. Chem. Phys., 17, 386-392 (1949). πρ 01310.

56. Johnston, H. S., Foering, L., Tao, Y. S., and Messerling, G. H., J. Amer. Chem. Soc., 73, 2319-2321 (1951). πρ 01311.

57. Johnston, H. S., J. Amer. Chem. Soc., 73, 4542-4546 (1951). πρ 01312.

58. Johnston, H. S. and Crosby, H. J., J. Chem. Phys., 22, 689-692 (1954). πρ 00997.

59. Jonathan, N. and Doherty, G., Nat. Aeron. Space Admin. Contractor Rept. CR-67 (July 1964). πρ 05620.

60. Jost, A., Michel, K. W., Troc, J., and Wagner, H., Cg., Air Force Aerospace Res. Lab. Rept. ARL 63-157 (September 1963). πρ 04472.

61. Kaufman, F. and Kelso, J. R., J. Chem. Phys., 23, 602-603 (1955). πρ 05505.

62. Kaufman, F. and Kelso, J. R., J. Chem. Phys., 23, 1702-1707 (1955). πρ 00110.

63. Kaufman, F., Gerri, N. J., and Bowman, R. E., J. Chem. Phys., 25, 106-115 (1956). πρ 00634.

64. Kaufman, F., J. Chem. Phys., 28, 352-353 (1958). πρ 00641.

65. Kaufman, F., Proc. Roy. Soc., A247, 123-139 (1958). πρ 00644.

66. Kaufman, F. and Kelso, J. R., Seventh Symposium (International) on Combustion, pp. 53-56. Butterworths, London, 1959. πρ 00139.

67. Kaufman, F., Progress in Reaction Kinetics, Vol. 1, G. Porter and B. Stevens, eds., pp. 1-39. Pergamon Press, New York, 1961. πρ 00172.

68. Kaufman, F. and Kelso, J. R., Ballistic Res. Lab./Aberdeen Proving Ground preprint of paper for 1962 Army Science Conference (June 1962). πρ 00662.

69. Keneshea, T. J., Air Force Cambridge Res. Lab. Rept., AFCRL-63-711 (September 1963). πρ 05568.

70. Kistiakowsky, G. B. and Volpi, G. G., J. Chem. Phys., 27, 1141-1149 (1957). πρ 00116.

71. Kistiakowsky, G. B. and Kydd, P. H., J. Amer. Chem. Soc., 79, 4825-4830 (1957). πρ 00635.

72. Kistiakowsky, G. B. and Volpi, G. G., J. Chem. Phys., 28, 665-668 (1958). πρ 00120.

73. Klein, F. S. and Herron, J. T., J. Chem. Phys., 41, 1285-1290 (1964). πρ 05594.

74. Levitt, B. P., Trans. Faraday Soc., 59, 59-65 (1963). πρ 00669.

75. Ludwig, C. B. and Sulzmann, K. G. P., Convair Dir. General Dynamics Corp., Rept., ZPH-082 (February 1961). πρ 00187.

76. Mannella, G. G., Chem. Rev., 63, 1-20 (1963). πρ 00227.

77. McGee, J. J. and Heicklen, J., J. Chem. Phys., 41, 2974-2977 (1964). πρ 05598.

78. McHale, E. T., Knox, B. E., and Palmer, H. B., Tenth Symposium (International) on Combustion, pp. 341-351. The Combustion Institute, 1965. πρ 03978.

79. Moore, W. M., Kennealy, J. P., and Baker, D. J., Air Force Cambridge Res. Lab. Rept., AFCRL-65-291 (1 January 1965). πρ 05665.

80. Morrison, M. E., Rinker, R. G., and Corcoran, W. H., Ind. Eng. Chem. Fundamentals, 5, 175-181 (1966). πρ 05685.

81. Nawrocki, P. J. and Papa, R., Atmospheric Processes, Prentice-Hall, Englewood Cliffs, N. J., 1963. πρ 00222.

82. Nicolet, M., Air Force Cambridge Res. Lab. Rept., AFCRL-64-939 (10 December 1964). πρ 05628.

83. Ogryzlo, E. A. and Schiff, H. I., Can. J. Chem., 37, 1690-1695 (1959). πρ 00645.

84. Ogryzlo, E. A. and Schiff, H. I., J. Chem. Phys., 32, 628-629 (1960). πρ 00649.

85. Olschewski, H. A., Troe, J., and Wagner, H. Gg., Univ. Gottingen Final Sci. Rept. on Office of Aerospace Research Grant EOAR 65-75 (1 May 1966). πρ 05706.

86. Pergament, H. S., Air Force Rome Air Develop. Center Rept., RADC-TR-64-512, Sect. IV (December 1964). πρ 05625.

87. Phillips, L. F. and Schiff, H. I., J. Chem. Phys., 36, 1509-1517 (1962). πρ 00205.

88. Phillips, L. F. and Schiff, H. I., J. Chem. Phys., 42, 3171-3174 (1965). πρ 05652.

89. Reeves, R. R., Harteck, P., and Chace, W. H., J. Chem. Phys., 41, 764-768 (1964). πρ 05593.

90. Richards, W. T. and Reid, J. A., J. Chem. Phys., 1, 114-128 (1933). πρ 01309.

91. Rosser, W. A. and Wise, H., Jet Propulsion Lab./California Inst. Tech. Memorandum 20-111 (16 May 1955). πρ 05507.

92. Rosser, W. A., Jr. and Wise, H., J. Chem. Phys., 24, 493-494 (1956). πρ 00999.

93. Schiavello, M., and Volpi, G. G., J. Chem. Phys., 37, 1510-1513 (1962). πρ 03976.

94. Schiff, H. I., Ann. Geophys., 20, 115-127 (1964). πρ 05579.

95. Schott, G. L. and Davidson, N., J. Amer. Chem. Soc., 80, 1841-1853 (1958). πρ 00640.

96. Schuyler, F. S., IIT Res. Inst. Rept., IITRI-A6002 (July 1963). πρ 05565.

97. Sessler, G., Acustica, 10, 44-59 (1960). πρ 01320.

98. Tank. W., Geophysics Corp. of America Tech. Rept., 61-41-A (1 November 1961). πρ00656.

99. Thermochemistry Res. Dept., Aerospace Corp., Aerospace Corp. Rept. TR-100(9210-02)-1 (November 1966). πρ 05106.

100. Verbeke, G. J. and Winkler, C. A., J. Phys. Chem. 64, 319-323 (1960). πρ 05524.

101. Wayne, L. G. and Yost, D. M., J. Chem. Phys., 18, 767-768 (1950). πρ 05498.

102. Wegener, P. P., J. Chem. Phys., 28, 724-725 (1958). πρ 05514.

103. Wegener, P. P., Jet Propulsion Lab./California Inst. Tech. Progr. Rept. 20-370 (19 December 1958). πρ 01317.

104. Wegener, P. P., Combustion and Propulsion: Fourth AGARD Colloquium, Milan, April 4-8, 1960: High Mach Number Air-Breathing Engines, A. L. Jaumotte, A. H. Lefebvre, and A. M. Rothrock, eds., pp. 261-285. Pergamon Press, New York, 1961. πρ 01321.

105. Wegener, P. P., J. Chem. Phys., 41, 1512-1513 (1964). πρ 05595.

106. Westenberg, A. A., Private Communication: A. A. Westenberg, Applied Physics Laboratory, Johns Hopkins University, to H. S. Pergament, AeroChem Research Laboratories, Inc., 25 October 1963. πρ 05573.

107. Westenberg, A. A., Applied Physics Lab./Johns Hopkins Univ. Rept. SR 4-3 (31 December 1963). πρ 05574.

108. Westenberg, A. A. and De Haas, N., J. Chem. Phys., 40, 3087-3098 (1964). πρ 05592.

109. Zaslowsky, J. A., Private Communication: J. A. Zaslowsky, Olin-Mathieson Chemical Corporation, to B. G. Hunt, Australian Defense Scientific Service Weapons Research Establishment, 1962. πρ 05551.

Key to References: Figs. 1 through 25

Figure	Reaction	Reference
1	$N_2H_3 + N_2H_3 \rightarrow N_2 + NH_3 + NH_3$	29
1	$N_2H_3 + M \rightarrow NH + NH_2 + M$	29
1	$N_2H_4 + M \rightarrow NH_2 + NH_2 + M$	78
1	$N_2H_4 \rightarrow NH_2 + NH_2$	78
2	$H + N_2H_4 \rightarrow NH_2 + NH_3$	29
2	$N_2H_3 + M \rightarrow H + H_2 + N_2 + M$	29
3	$H + N_2H_3 \rightarrow H_2 + H_2 + N_2$	29
3	$H + N_2H_4 \rightarrow N_2H_3 + H_2$	93
3	$NH_2 + N_2H_4 \rightarrow N_2H_3 + NH_3$	29

Figure	Reaction	Reference
4	$NH_2 + N_2H_3 \rightarrow H_2 + N_2 + NH_3$	29
4	$NH + N_2H_4 \rightarrow NH_2 + N_2H_3$	29
4	$NH_2 + NH_2 \rightarrow N_2H_2 + H_2$	78
5	$N_2O_4 \rightarrow NO_2 + NO_2$	16,22,43: Line 8,18,21,22; 23: 90; 97: points
5	$NO_2 + NO_2 \rightarrow N_2O_4$	16
6	$N_2O_4 + M \rightarrow NO_2 + NO_2 + M$	16,22,43: Line; 23,8: points
6	$NO_2 + NO_2 + M \rightarrow N_2O_4 + M$	25,42,82,102 - 105
7	$NO + OH \rightarrow H + NO_2$	96
7	$N_2O_5 + M \rightarrow NO_3 + NO_2 + M$	16,43,95
7	$NO_2 + O_2 \rightarrow O + NO_3$	75
7	$NO_2 + NO \rightarrow N + NO_3$	75
8	$N + O_2 + M \rightarrow NO_2 + M$	79,11
8	$NO_2 + M \rightarrow N + O_2 + M$	75,11

Figure	Reaction	Reference
9	$NO_2 + NO_2 \rightarrow NO + NO + O_2$	11, 32, 53, 91, 92
10	$NO + NO_3 \rightarrow NO_2 + NO_2$	27, 40, 54, 56, 80, 82, 95
10	$NO_2 + NO_2 \rightarrow NO + NO_3$	1, 27, 32, 75, 92, 95
11	$NO + O + M \rightarrow NO_2 + M$	11, 13, 14, 15, 24, 28, 33, 37, 53, 63, 67, 75, 79, 81, 82, 85, 86, 106; 24, 26: positive slope
12	$NO_2 + O \rightarrow NO + O_2$	2, 4, 5, 6, 9, 10, 12-15, 28, 36, 37 39, 40, 41, 50, 59, 66, 67, 69-73, 75 79, 81, 82, 87, 98, 99: Upper band. 11, 47, 49, 82: lower band
12	$NO_2 + N_2 \rightarrow NO + N_2O$	9, 11, 28, 62, 75, 81, 99
13	$NO + NO + O_2 \rightarrow NO_2 + NO_2$	11: small slope band; 40, 53, 92, 79: steep slope line
14	$NO_2 + M \rightarrow O + NO + M$	9, 11, 16, 28, 33, 37, 43, 52, 53, 66, 74, 75
15	$N + O_3 \rightarrow NO_2 + O$	11: band; 19, 76: constant
	$NO_2 + O \rightarrow N + O_3$	75, 11

Figure	Reaction	Reference
16	$NO_2 + N \rightarrow N_2 + O_2$	10, 12, 47, 69, 81, 88, 99: const. band. 11, 13, 14, 15, 79: sloping band
16	$N_2 + O_2 \rightarrow NO_2 + N$	75, 11, 81, 99
17	$NO_2 + N \rightarrow N_2 + O + O$	47, 49, 50, 88
17	$NO + N_2O \rightarrow NO_2 + N_2$	9, 11, 28, 61, 62, 75
18	$NO_2 + N_2O \rightarrow NO + N_2 + O_2$	11
18	$NO + N_2 + O_2 \rightarrow NO_2 + N_2O$	11
19	$NO_2 + NO + H_2O \rightarrow HNO_2 + HNO_2$	101
19	$NO + HO_2 \rightarrow OH + NO_2$	82
19	$NO_2 + NH \rightarrow HNO + NO$	99
19	$HNO_3 + M \rightarrow OH + NO_2 + M$	43, 46
19	$NO_2 + O_2 \rightarrow O_3 + NO$	11, 28, 58, 75, 81
20	$NO_2 + O_3 \rightarrow NO_3 + O_2$	2, 34, 35, 38, 40, 50, 57, 55, 82, 94
20	$NO_3 + O_2 \rightarrow NO_2 + O_3$	95

Figure	Reaction	Reference
21	$NO_2 + \phi + M \rightarrow NO_3 + M$	6, 28, 37, 53, 67, 75, 81, 82.
21	$NO_3 + M \rightarrow NO_2 + O + M$	28, 36, 40, 53, 75, 81
22	$N_2O + O_2 \rightarrow NO_2 + NO$	75: upper line; 11, 99: lower band
22	$NO_2 + NO \rightarrow N_2O + O_2$	11: solid band
23	$NO_3 + NO_3 \rightarrow NO_2 + NO_2 + O_2$	7, 16, 40, 43, 82, 95
23	$NO_2 + O_2 + NO_2 \rightarrow NO_3 + NO_3$	95
24	$OH + HNO_2 \rightarrow NO_2 + H_2O$	96
24	$HNO + OH \rightarrow NO_2 + H_2$	20
24	$O + HNO \rightarrow H + NO_2$	99
25	$NO_2 + N \rightarrow O + N_2O$	2, 3, 10, 14, 47, 49, 50, 70, 72, 79, 81, 88, 100: constant band; 11: sloping band
25	$O + N_2O \rightarrow NO_2 + N$	75, 11, 81, 99

APPENDIX B

Calibration Spectra In Infrared And Visible Regions

B.i.(a)

Calibration Spectra In Infrared Region

1. 150 Watt Tungsten Lamp
2. Acetylene - Oxygen Flame
    a. Lean
    b. Rich
    c. Stoichiometric
3. Xenon Lamp

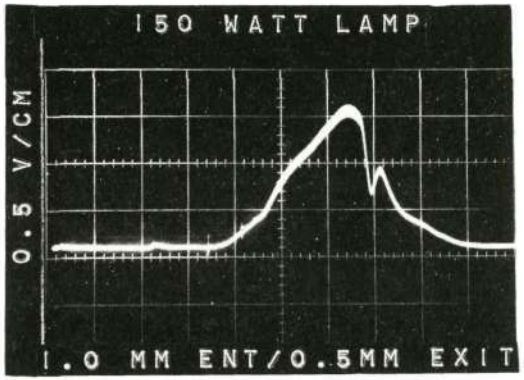

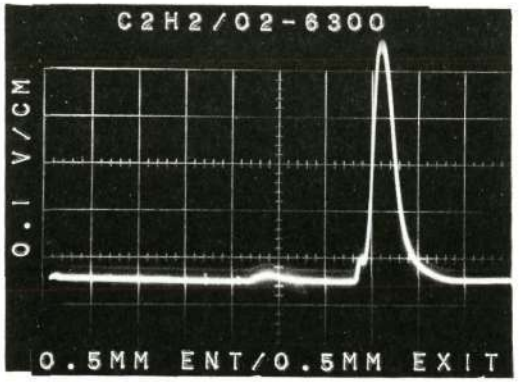

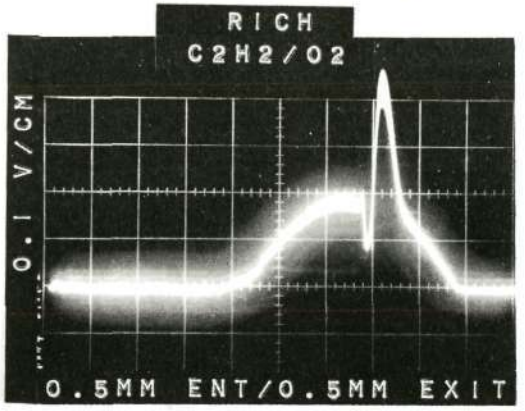

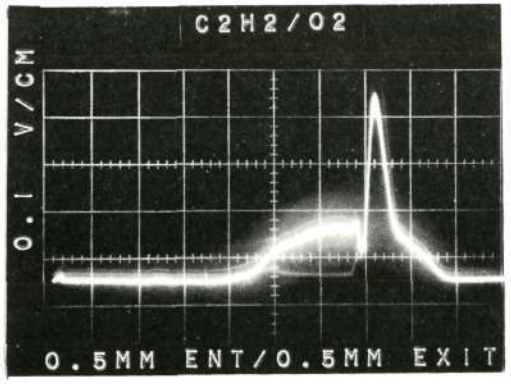

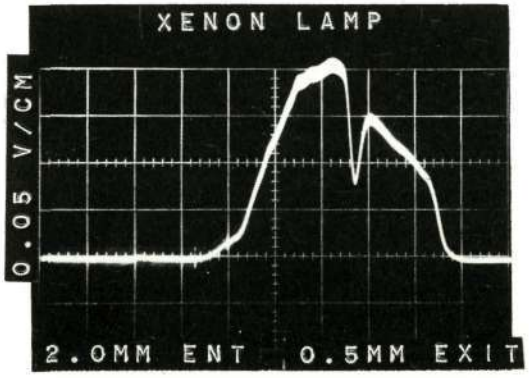

N_2H_4 / N_2O_4

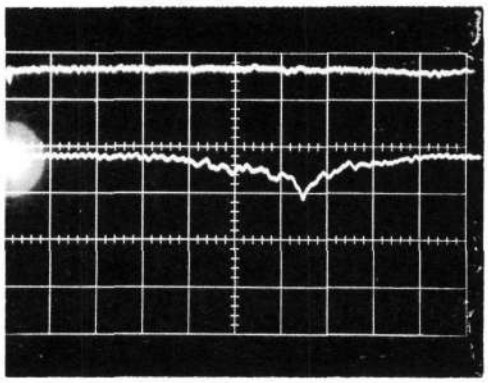

T + 161

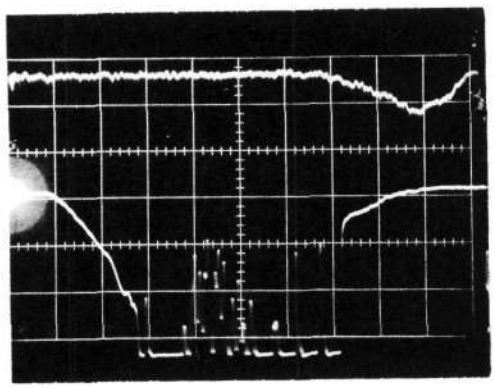

T + 162

Calibration Spectra In Visible Region

12. Argon Discharge Tube Spectra
13. Oxygen Discharge Tube Spectra
14. Nitrogen Discharge Tube Spectra
15. Mercury Discharge Tube Spectra
16. Propane Oxygen Flame

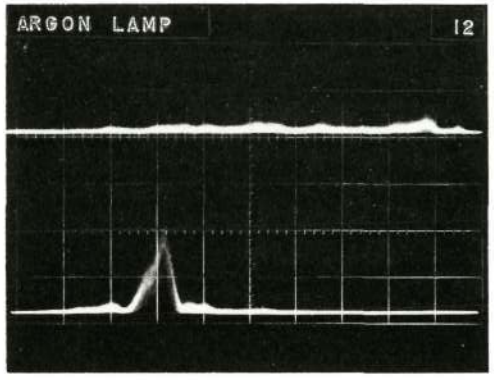

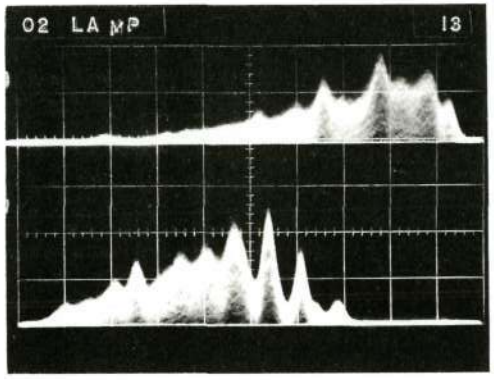

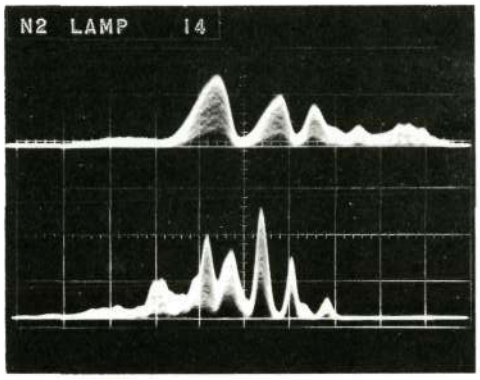

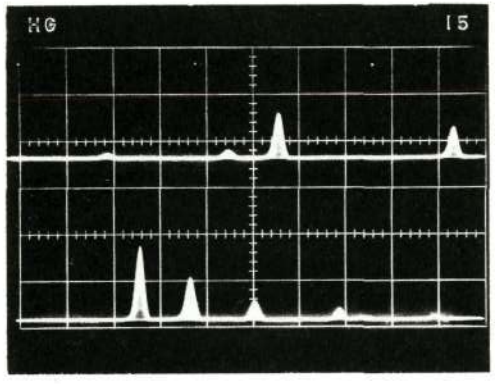

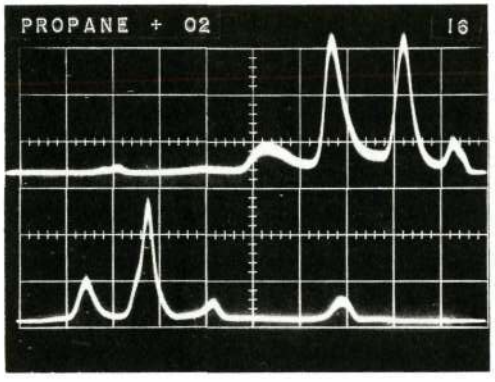

CALIBRATION SPECTRA IN VISIBLE REGION

APPENDIX C

Test Data

Test #13. Monomethyl Hydrazine/Nitrogen Tetroxide Simultaneous Flow of Both Fuel and Oxidizer.

a. Chamber Presure and long wave length (visible region) vs. time.

b. Chamber Pressure and short wave length (visible region) vs. time.

c. Short and long wave length visible emission spectra vs. time.

d. Short and long wave length visible emission spectra vs. time with 100 microsecond per cm time base (250 microsecond dead time between each oscilloscope tracing).

e. Pressure and emission spectra traces vs. time.

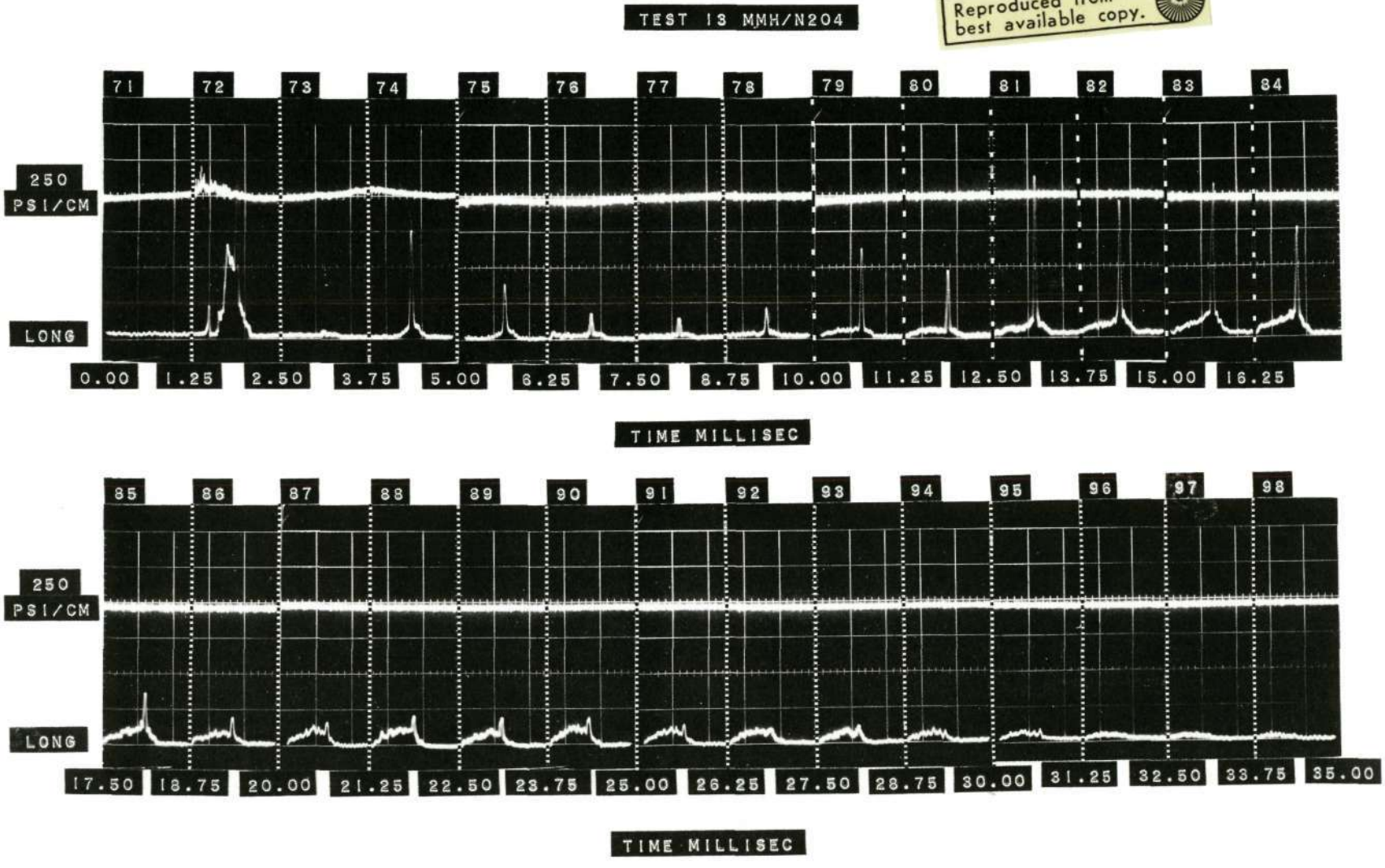

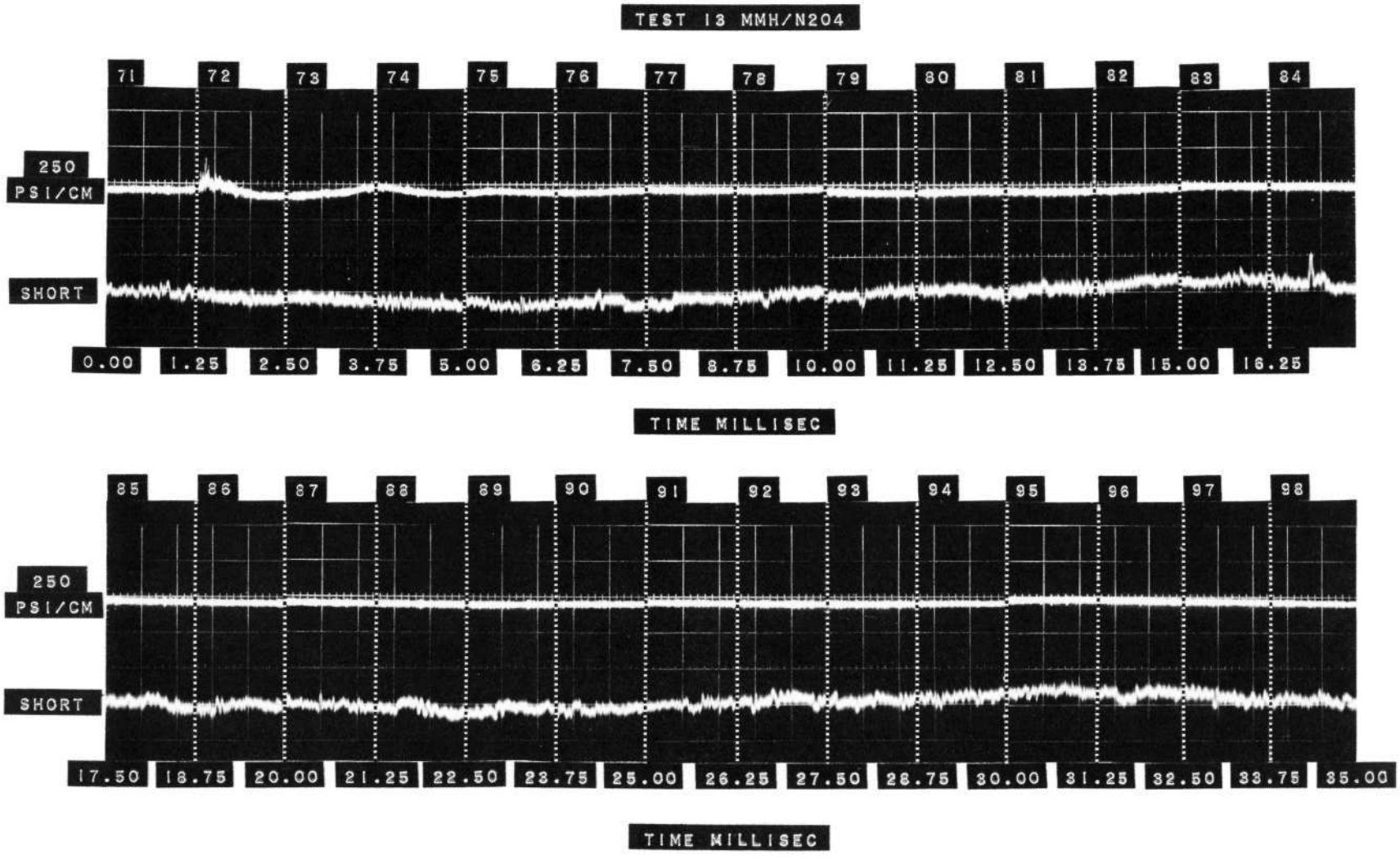
TEST 13 MMH/N204
71 72 73 74 75 76 77 78 79 80 81 82 83 84
250
PSI/CM
SHORT
0.00 1.25 2.50 3.75 5.00 6.25 7.50 8.75 10.00 11.25 12.50 13.75 15.00 16.25
TIME MILLISEC
85 86 87 88 89 90 91 92 93 94 95 96 97 98
250
PSI/CM
SHORT
17.50 18.75 20.00 21.25 22.50 23.75 25.00 26.25 27.50 28.75 30.00 31.25 32.50 33.75 35.00
TIME MILLISEC

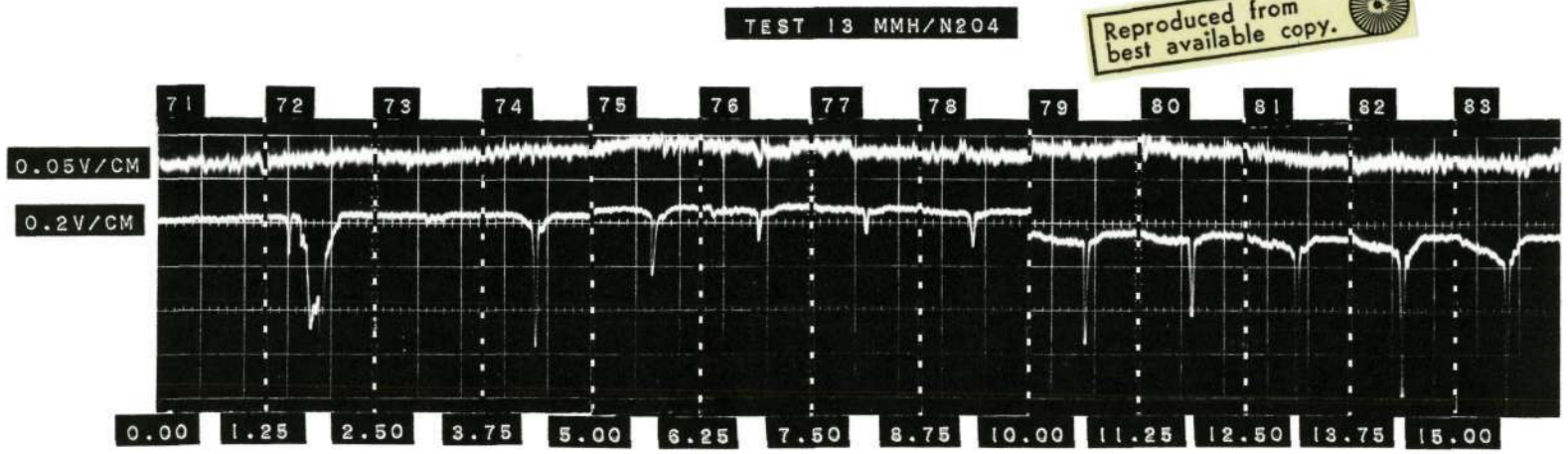

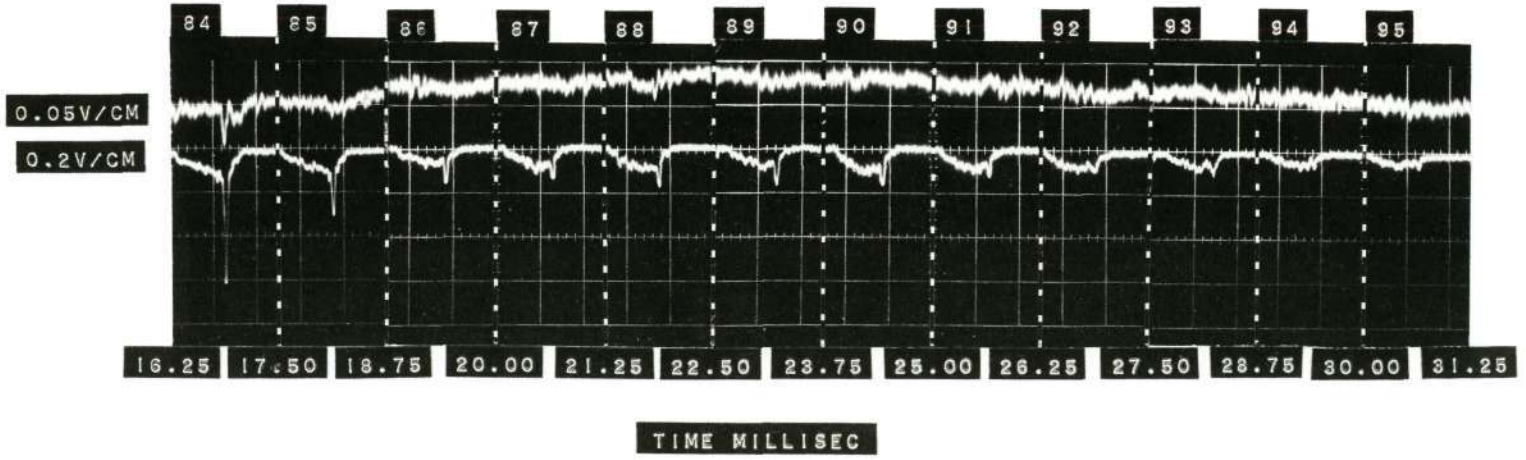

TEST 13 MMH/N204 d

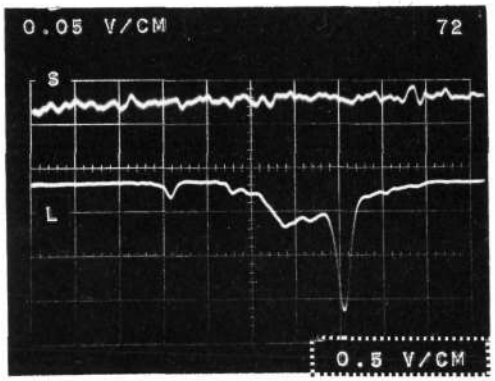

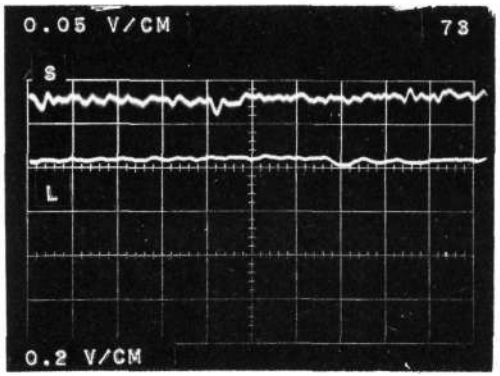

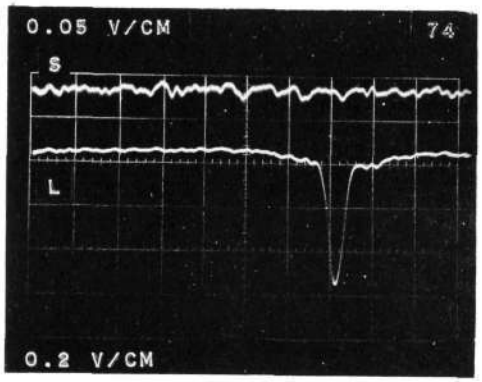

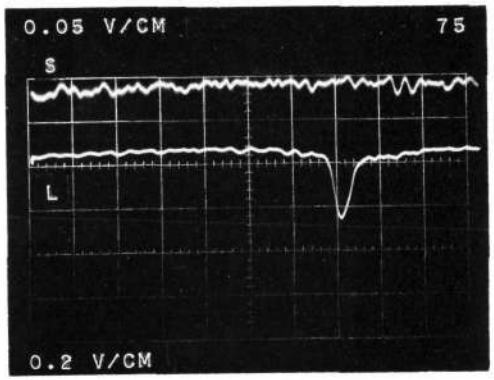

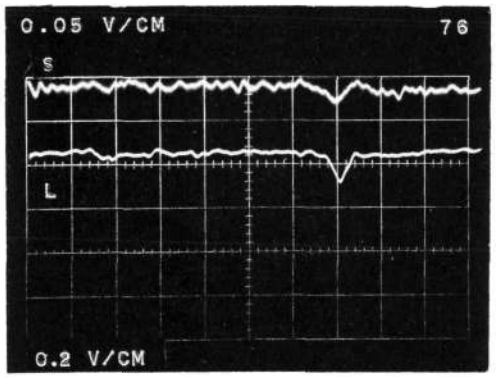

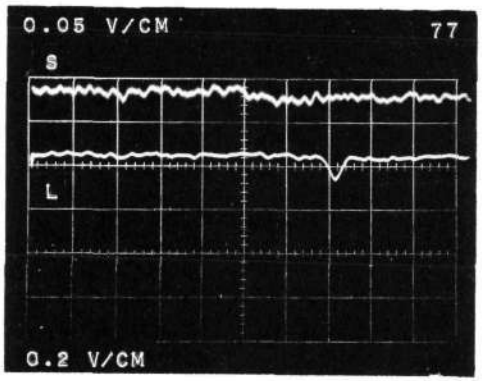

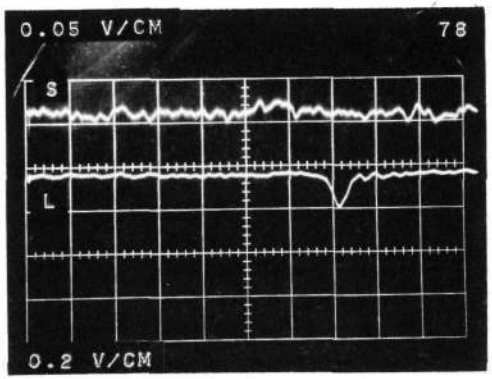

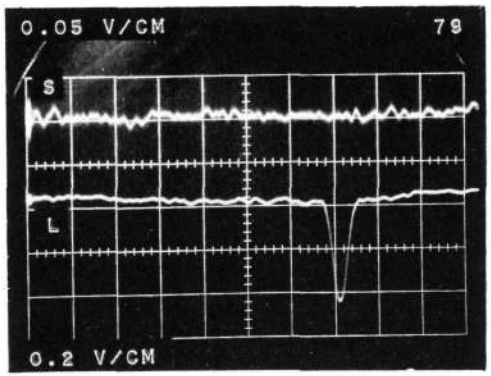

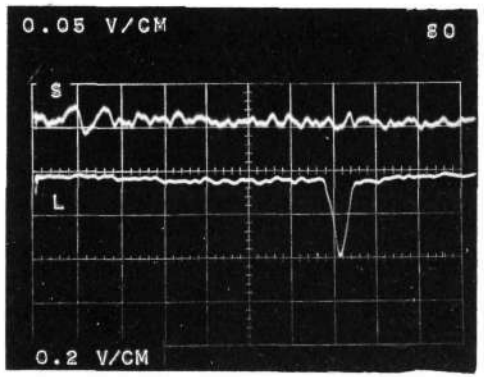

TEST 13 MMH/N204 d CONT.

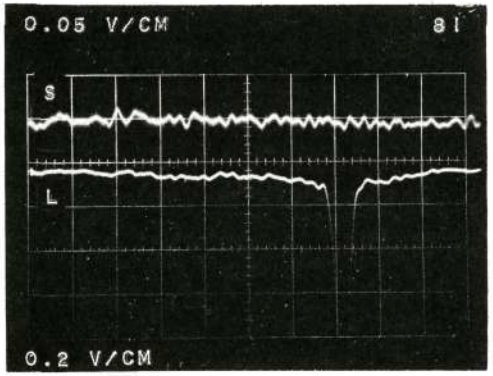

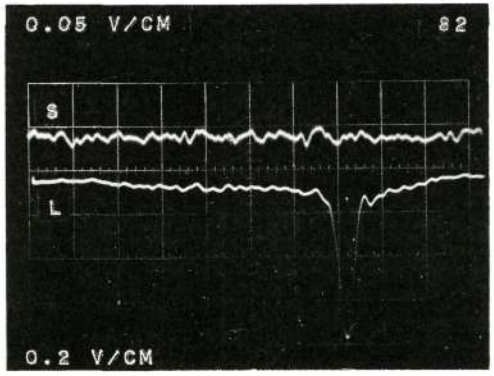

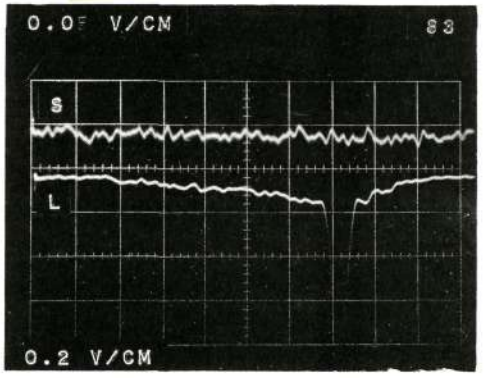

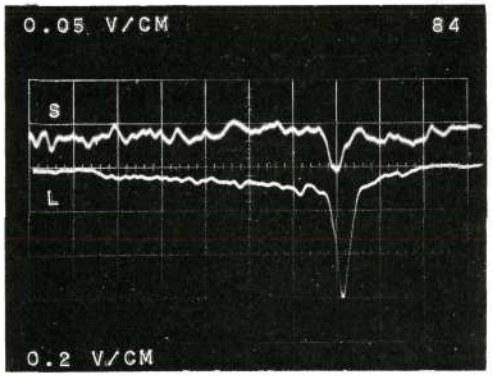

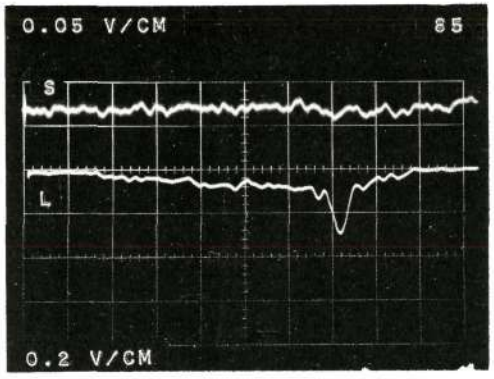

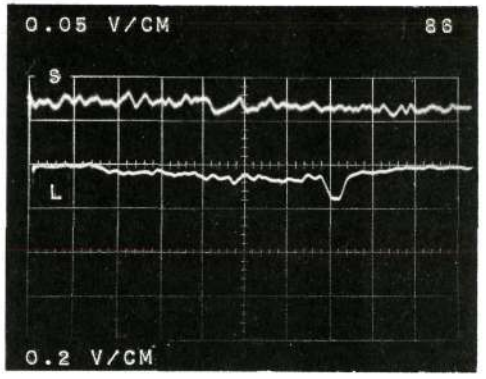

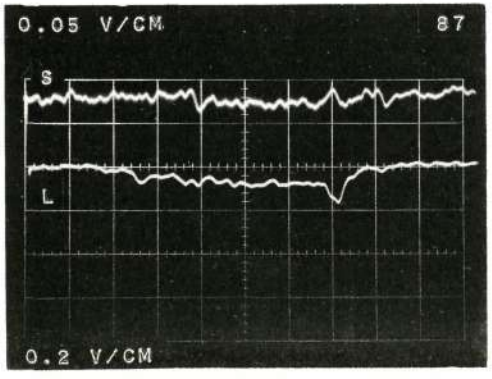

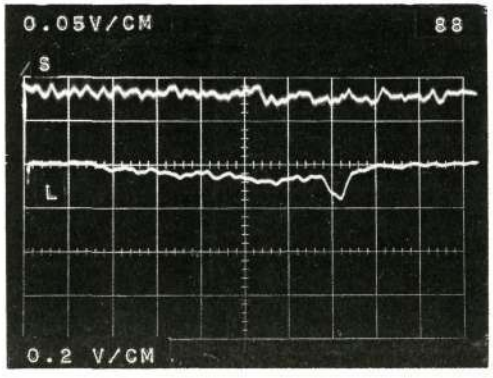

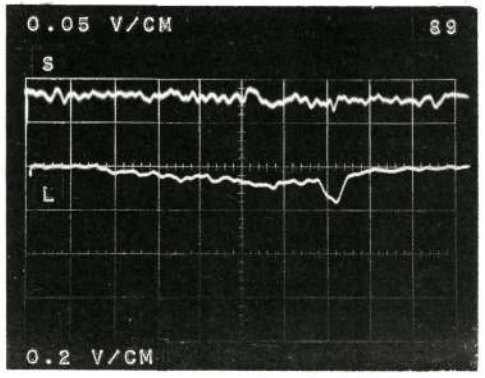

TEST 13 MMH/N204 d CONT.

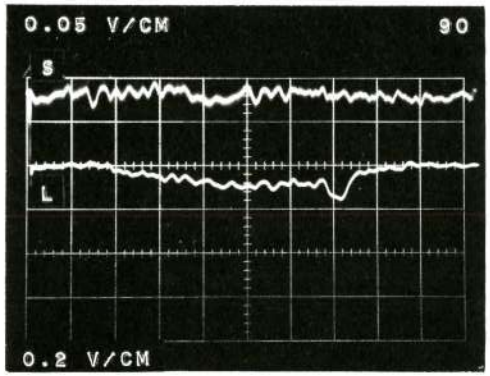

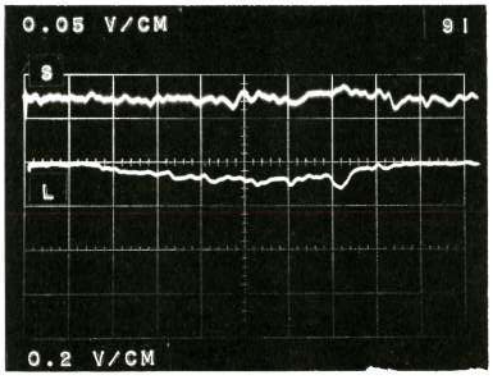

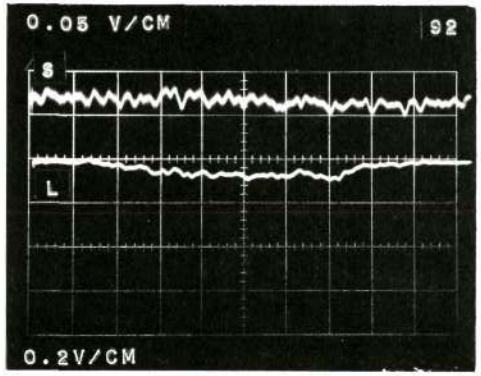

TEST 13 MMH/N204

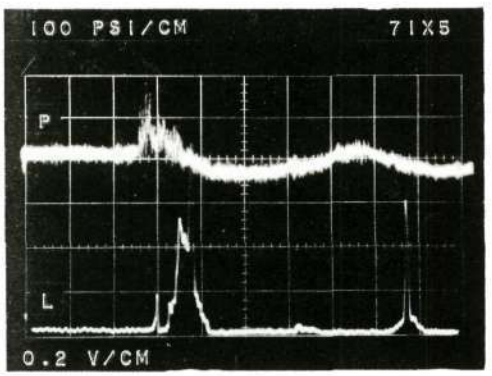

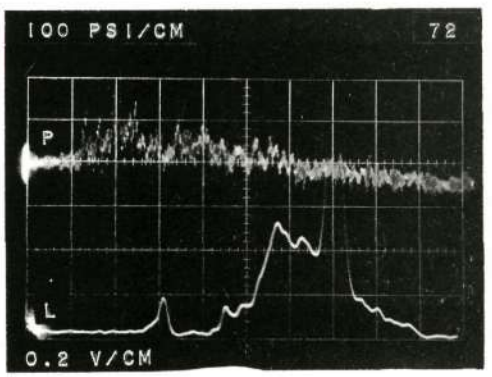

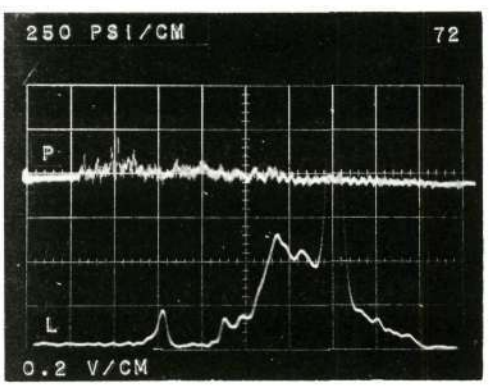

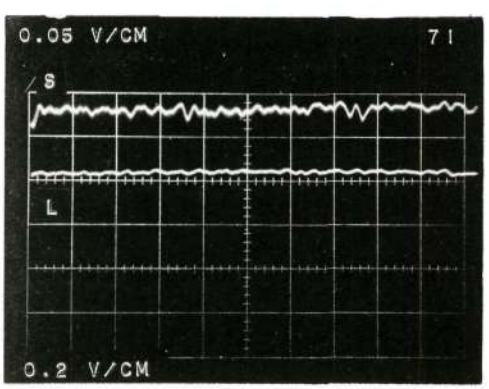

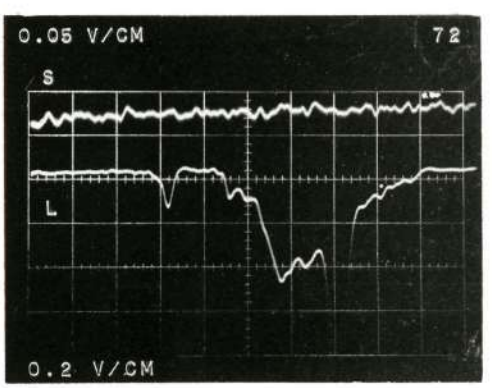

Test #14. Monomethyl Hydrazine/Nitrogen Tetroxide.

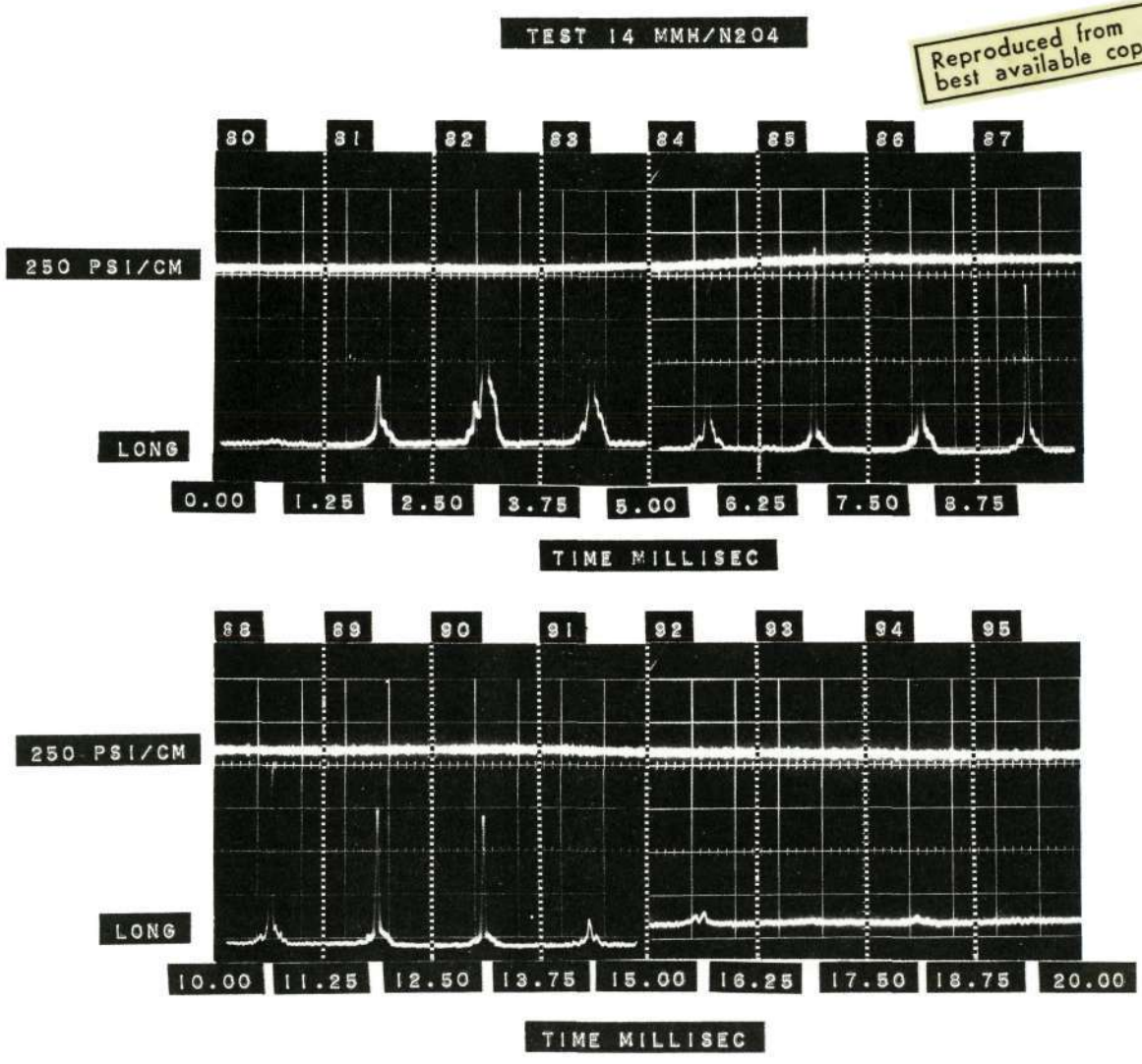

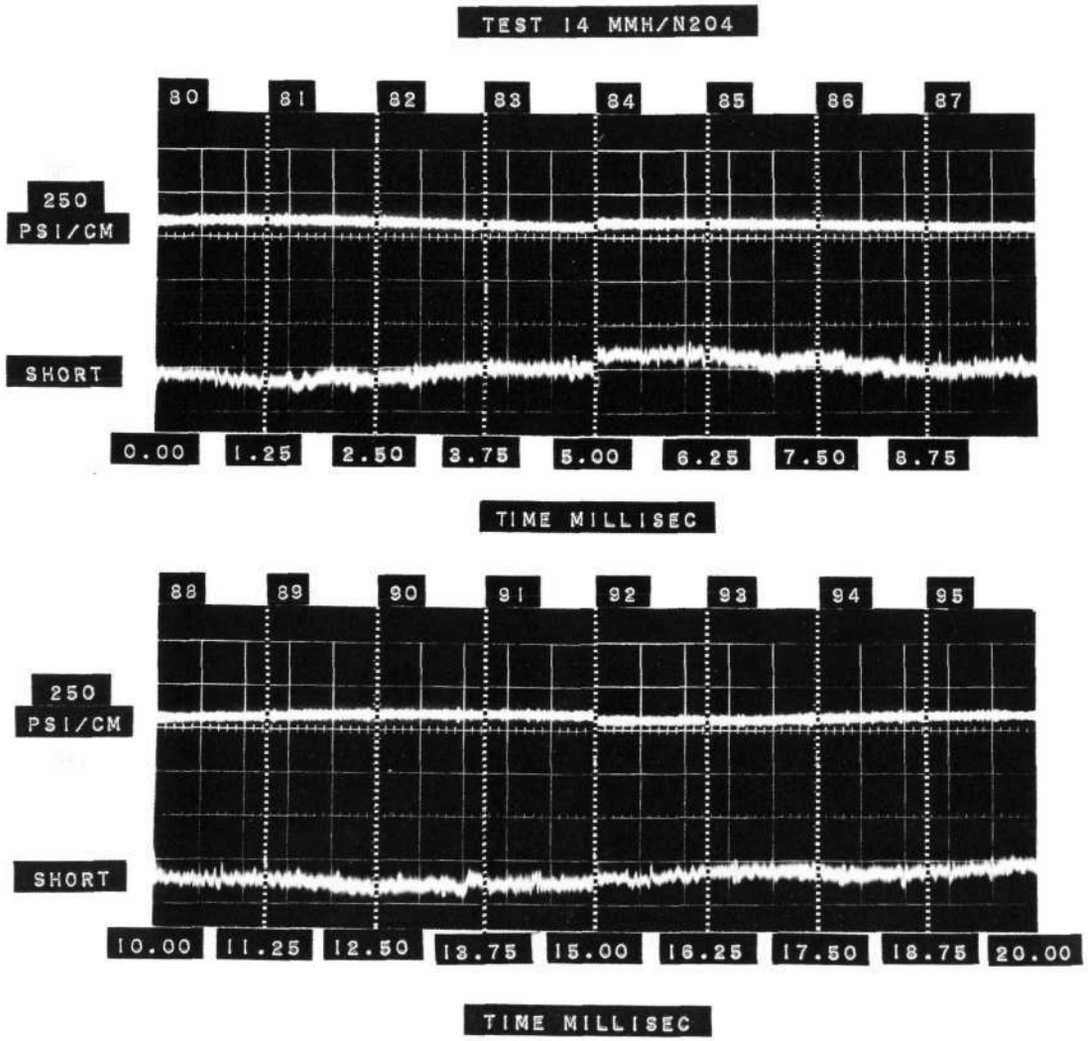
TEST 14 MMH/N204
80
81
82
83
84
85
86
87
250
PSI/CM
SHORT
0.00
1.25
2.50
3.75
5.00
6.25
7.50
8.75
TIME MILLISEC
88
89
90
91
92
93
94
95
250
PSI/CM
SHORT
10.00
11.25
12.50
13.75
15.00
16.25
17.50
18.75
20.00
TIME MILLISEC

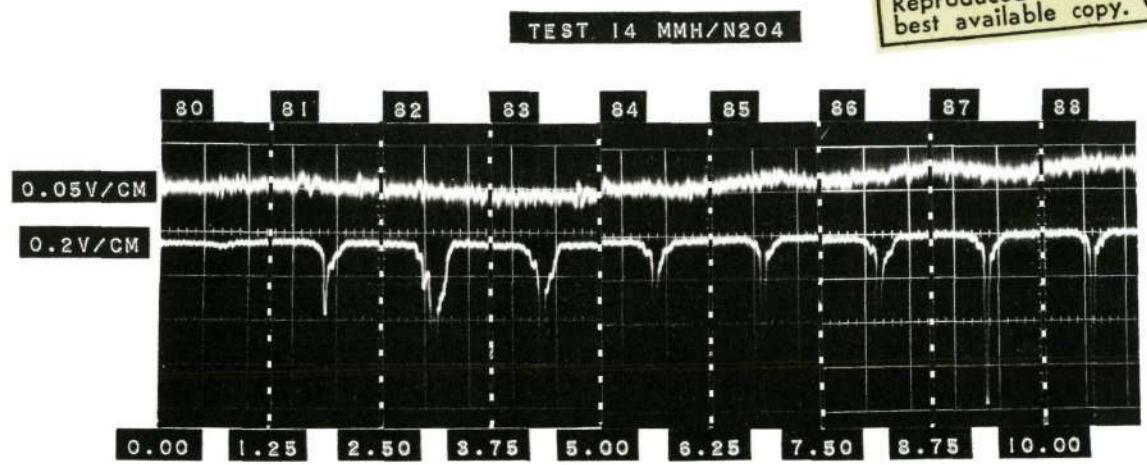

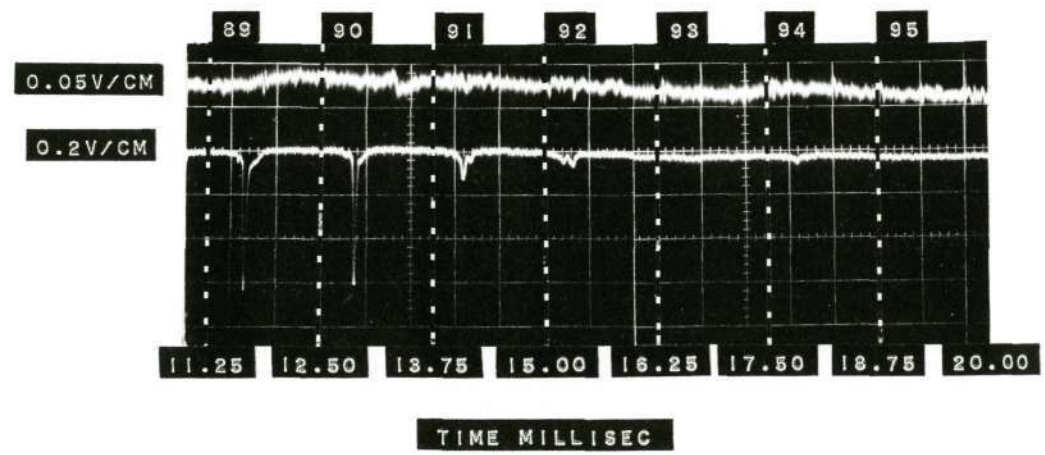

TEST 14 MMH/N204

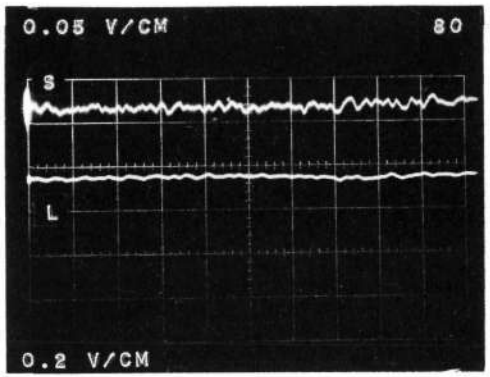

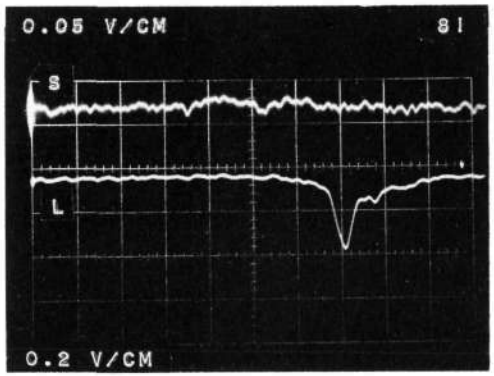

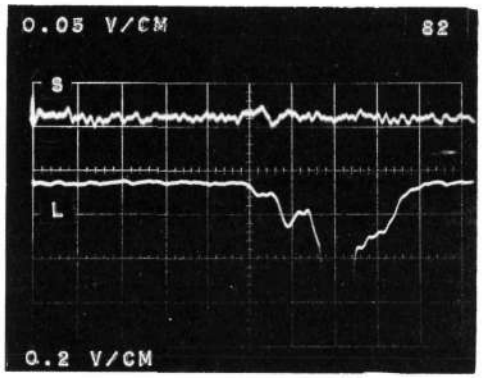

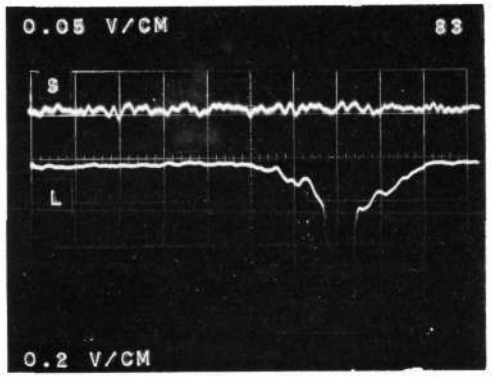

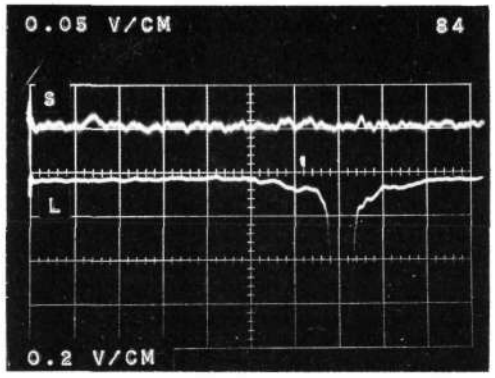

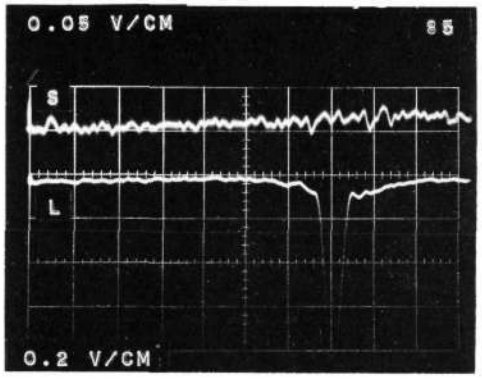

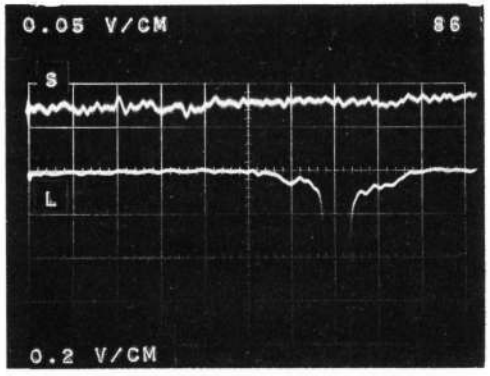

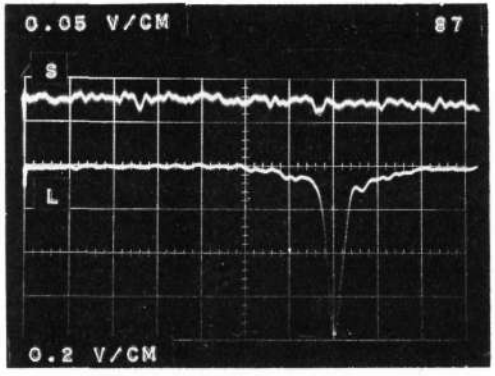

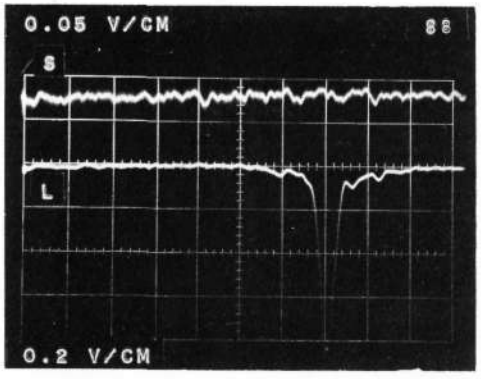

TEST 14 MMH/N2O4

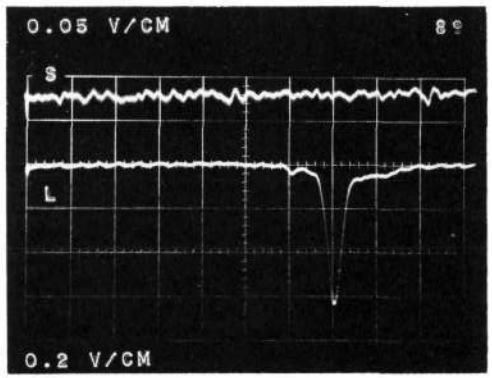

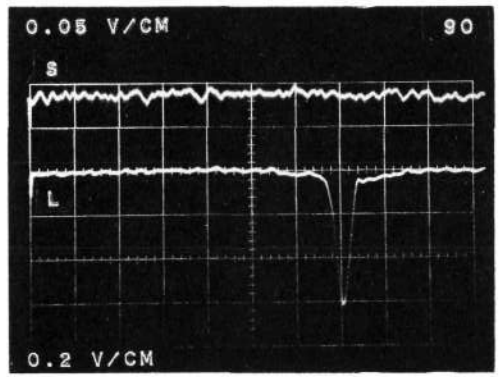

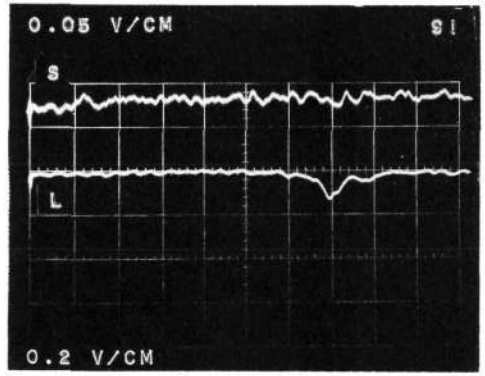

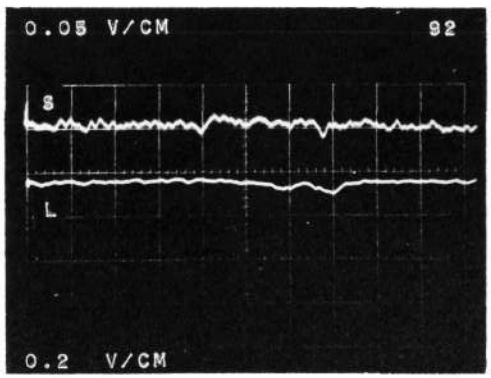

TEST 14 MMH/N204

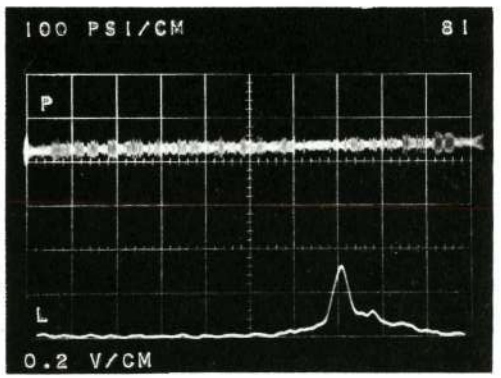

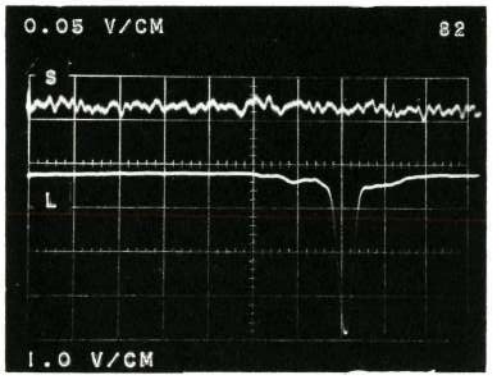

Test #15. Monomethyl-Hydrazine/Nitrogen Tetroxide - Short Oxider Lead.

a. Pressure and visible emission spectra vs. time. Time base 500 microsecond per cm. Long wave length visible emission spectra.

b. Pressure and visible emission spectra vs. time. Time base 500 microsecond per cm. Short wave length visible emission spectra.

c. Visible emission spectra vs. time. Time base 500 microsecond per cm. Upper trace short wave length visible emission. Lower trace long wave length visible emission.

d. Visible emission spectra vs. time. Time base 100 microseconds per cm. Upper trace short wave length visible emission spectra. Lower trace long wave length visible emission spectra.

e. Pressure and long wave length visible emission spectra vs. time.

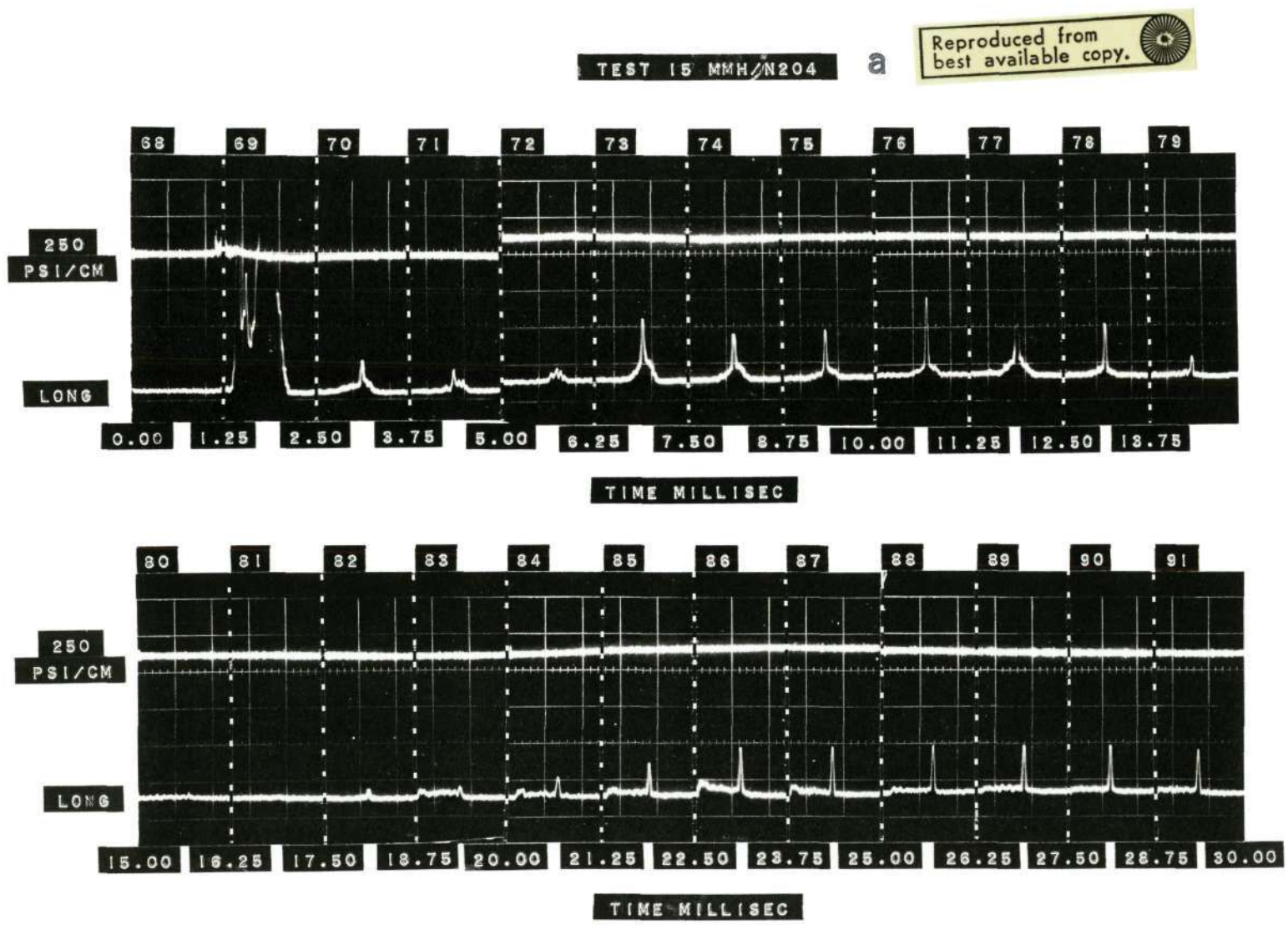

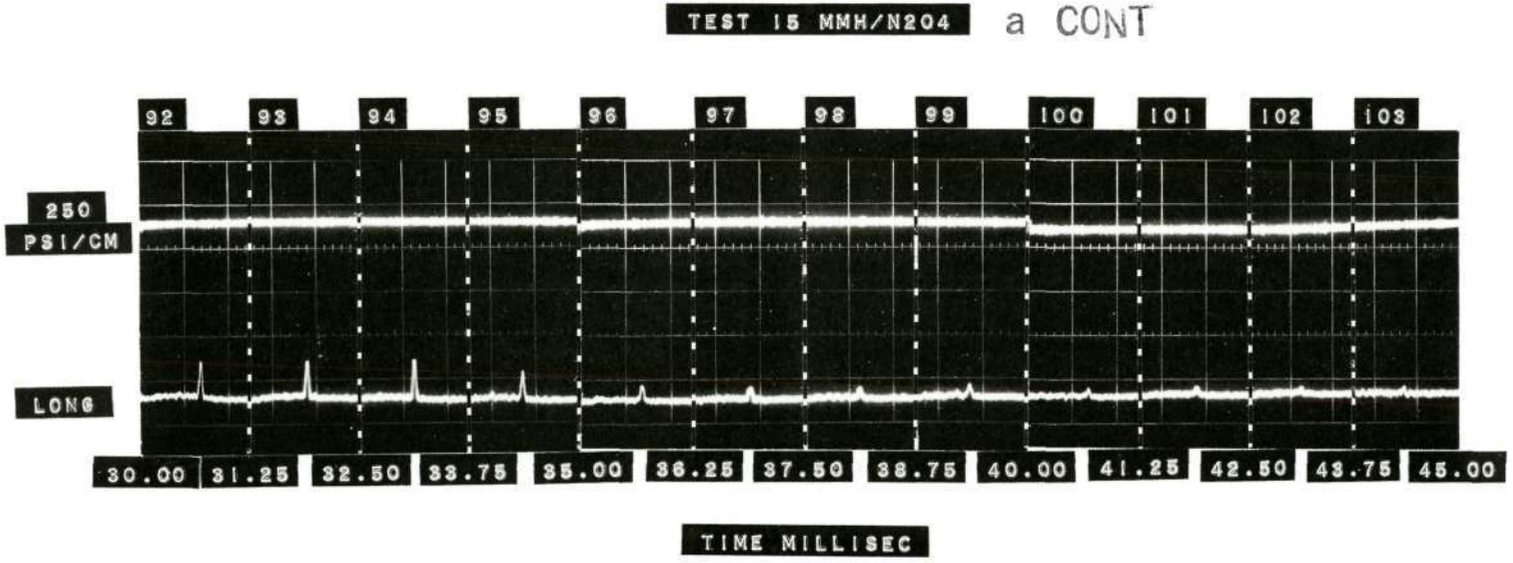
TEST 15 MMH/N204 a CONT
92
93
94
95
96
97
98
99
100
101
102
103
250
PSI/CM
LONG
30.00
31.25
32.50
33.75
35.00
36.25
37.50
38.75
40.00
41.25
42.50
43.75
45.00
TIME MILLISEC

TEST 15 MMH/N204 b

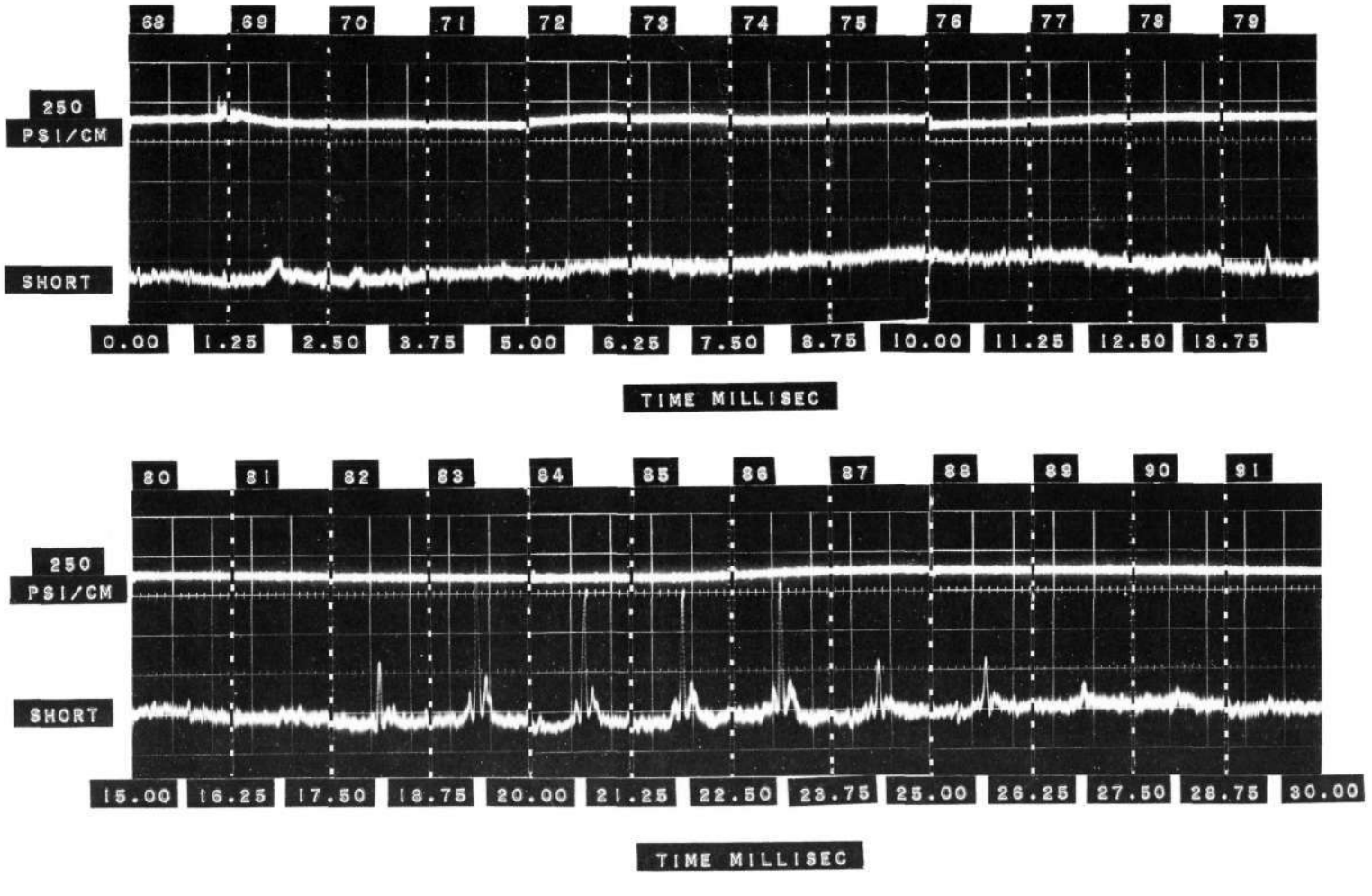

RUN 30 N2H4 c CONT

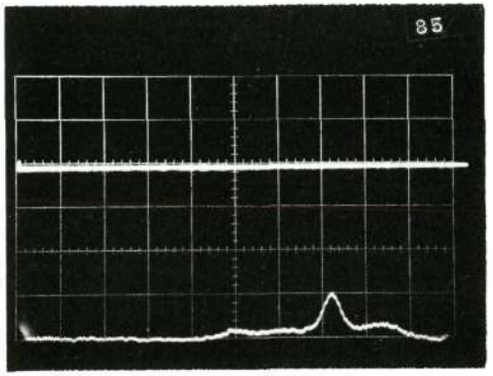

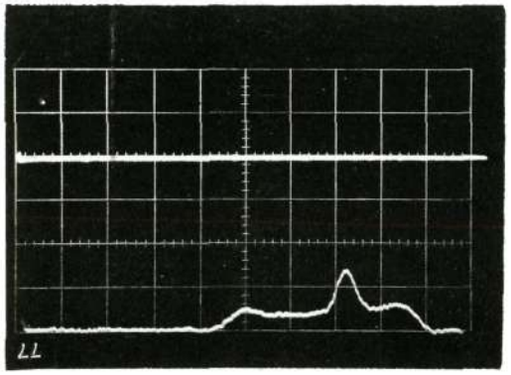

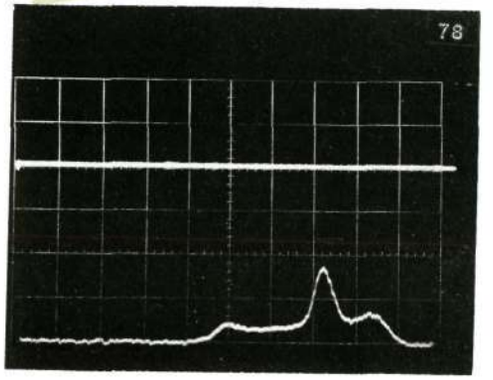

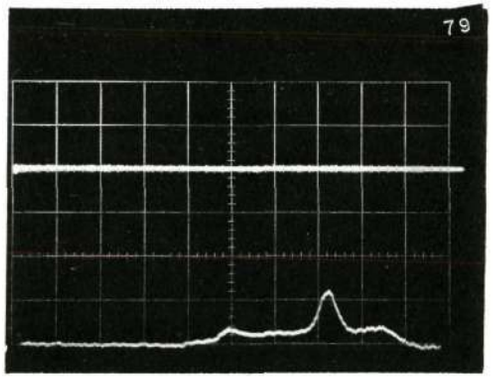

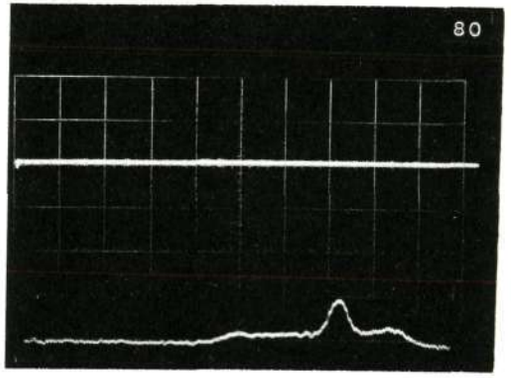

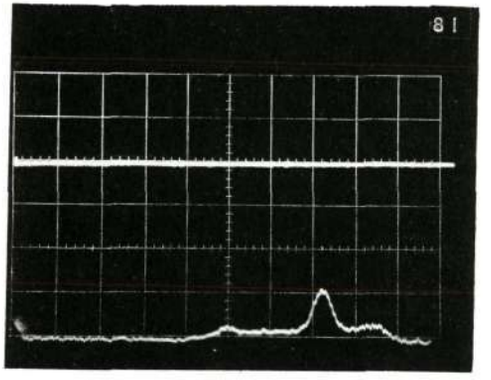

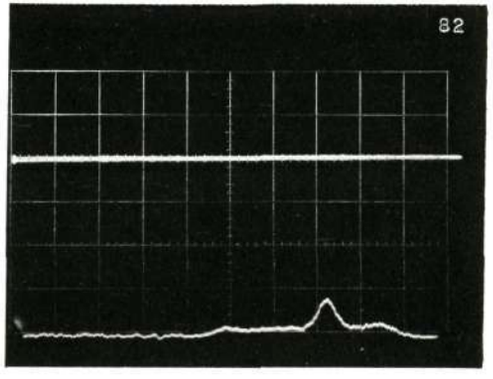

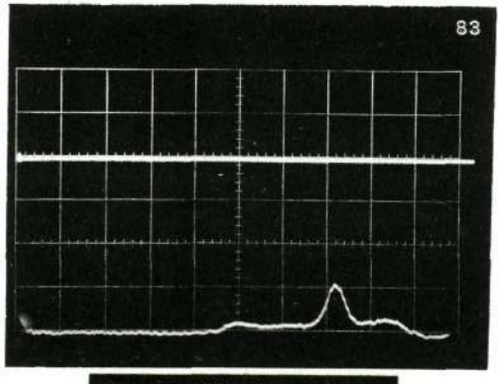

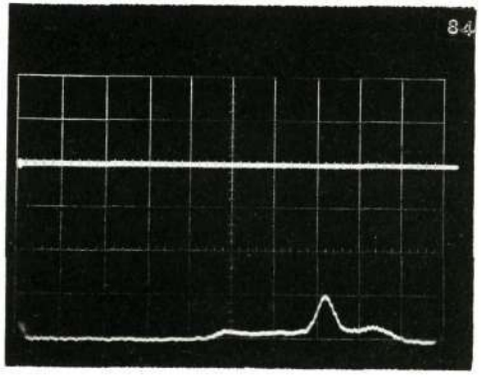

0.1 V/CM 500 LB/CM

C20

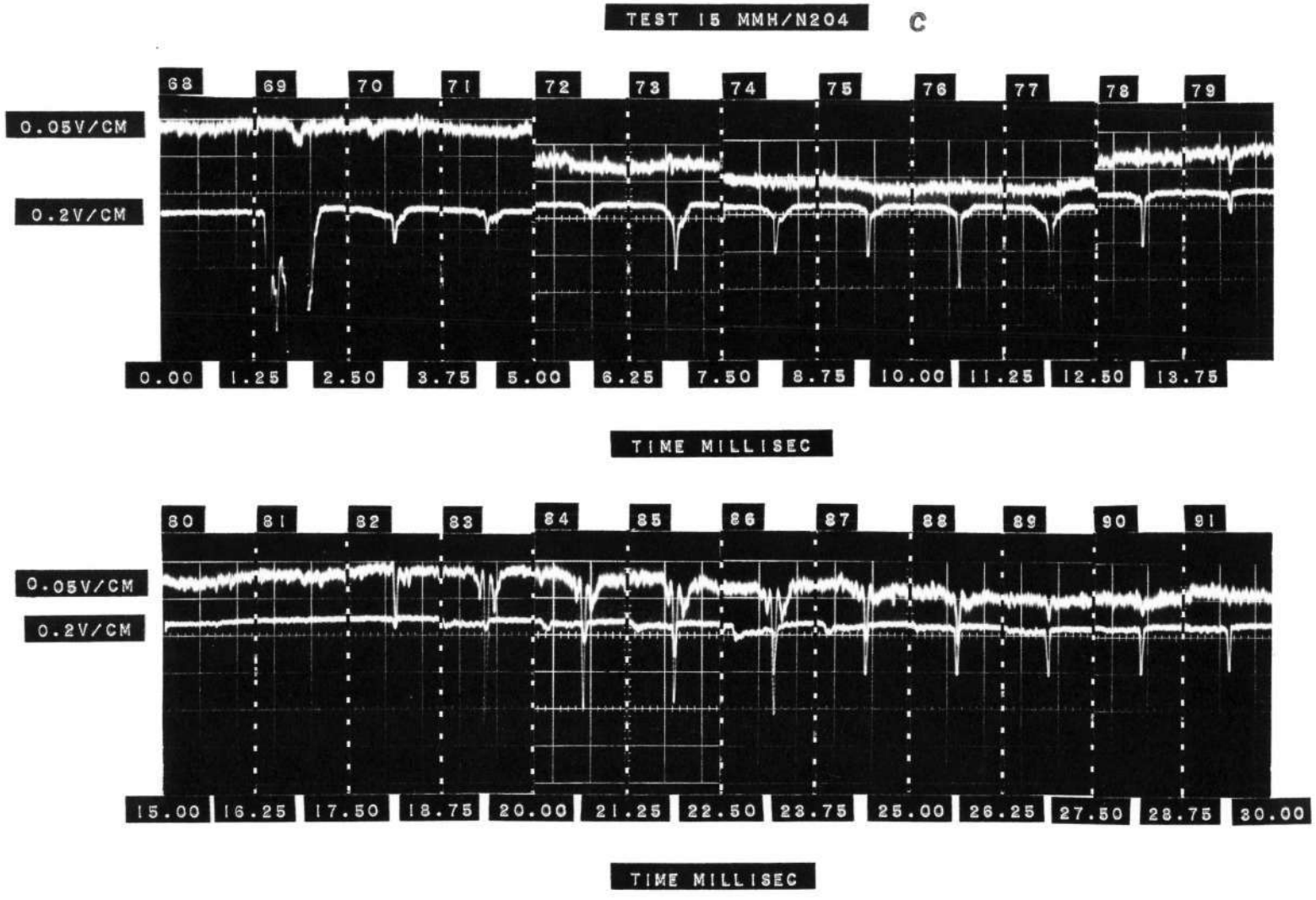
TEST 15 MMH/N204
C
68
69
70
71
72
73
74
75
76
77
78
79
0.05V/CM
0.2V/CM
0.00
1.25
2.50
3.75
5.00
6.25
7.50
8.75
10.00
11.25
12.50
13.75
TIME MILLISEC
80
81
82
83
84
85
86
87
88
89
90
91
0.05V/CM
0.2V/CM
15.00
16.25
17.50
18.75
20.00
21.25
22.50
23.75
25.00
26.25
27.50
28.75
30.00
TIME MILLISEC

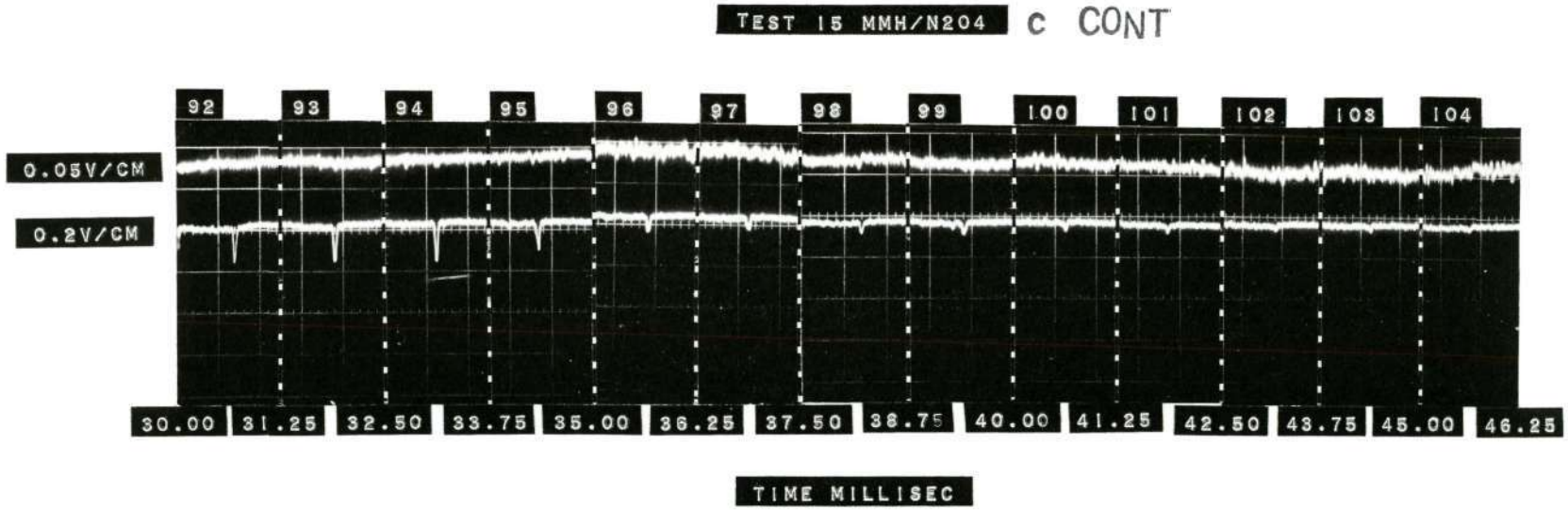

TEST 15 MMH/N204

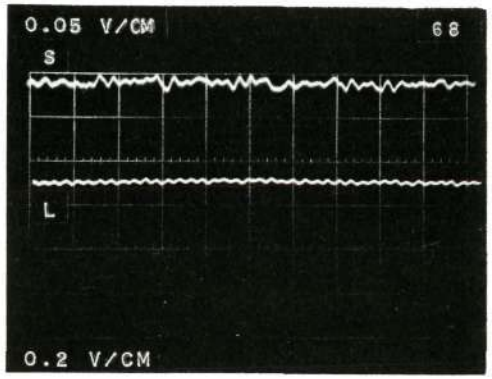

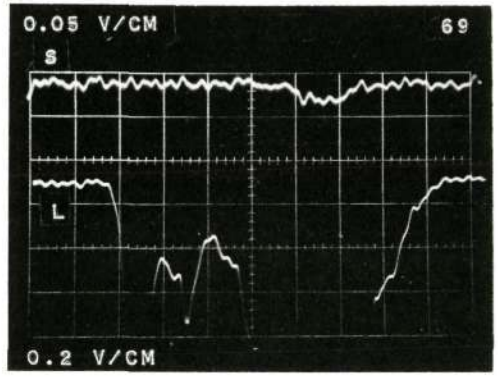

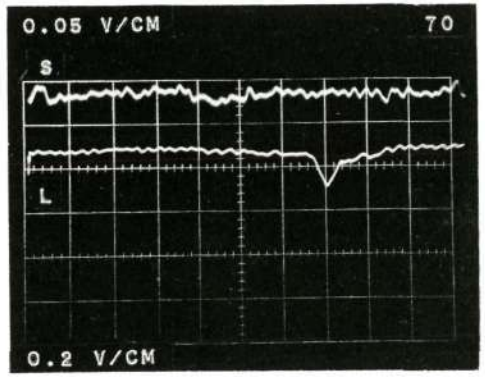

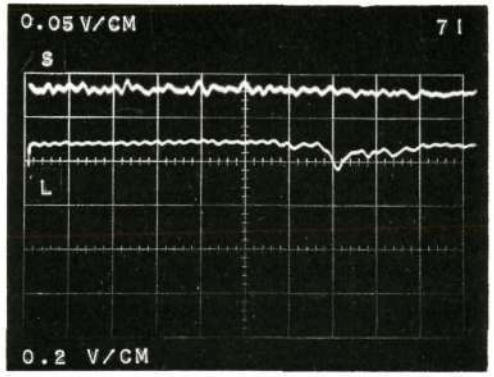

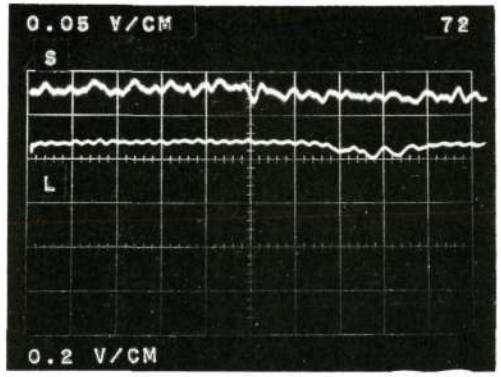

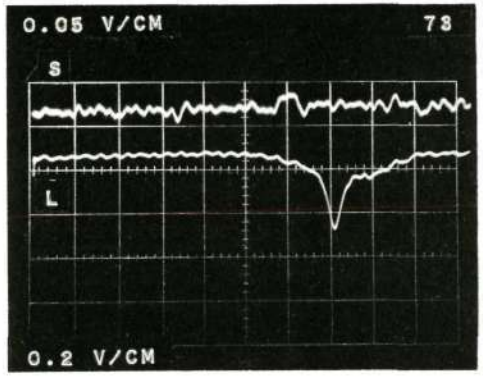

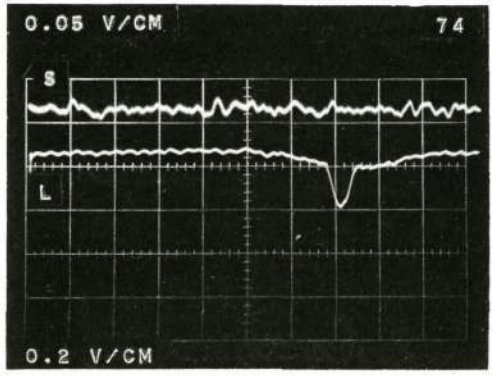

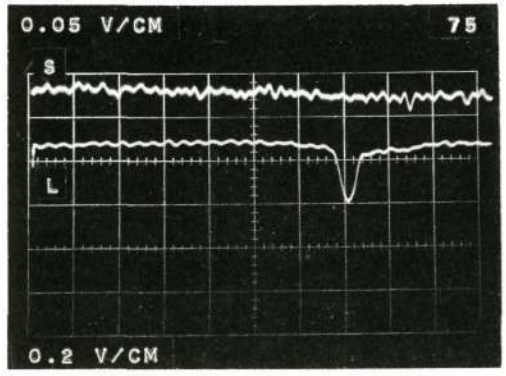

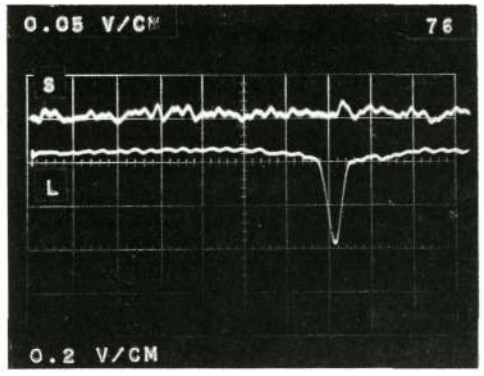

TEST 15 MMH/N204 d CONT.

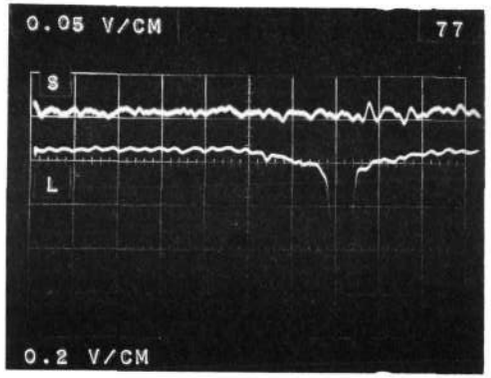

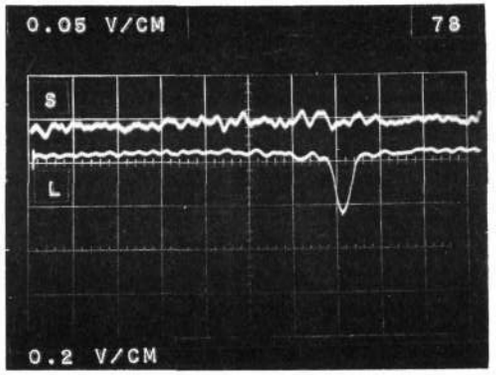

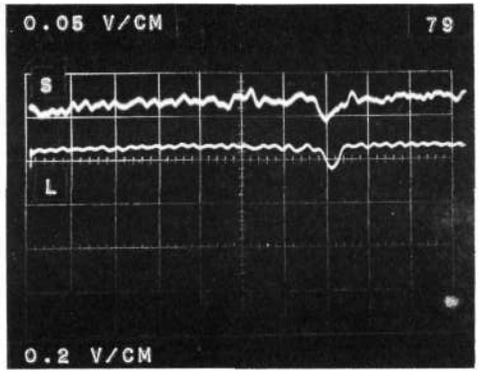

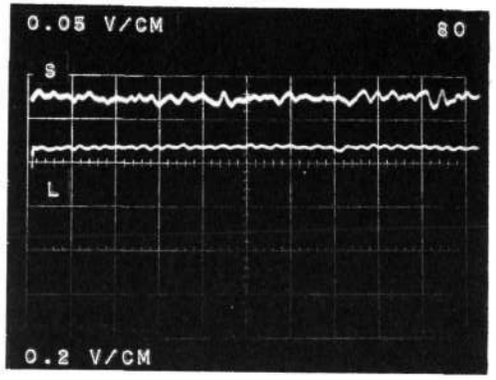

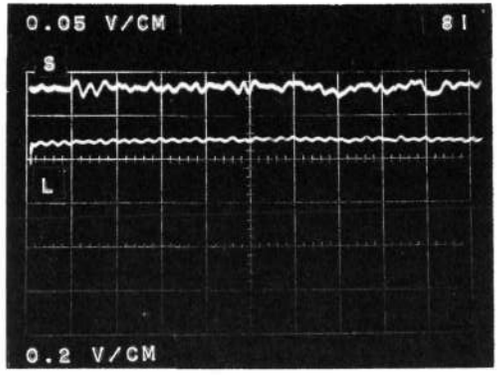

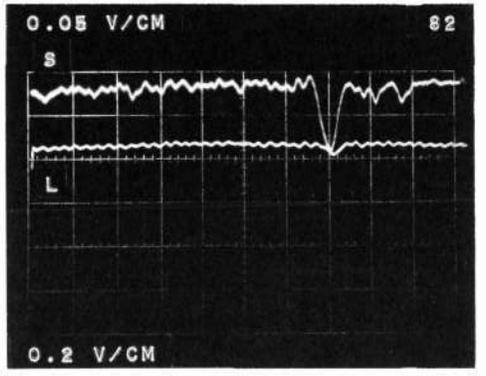

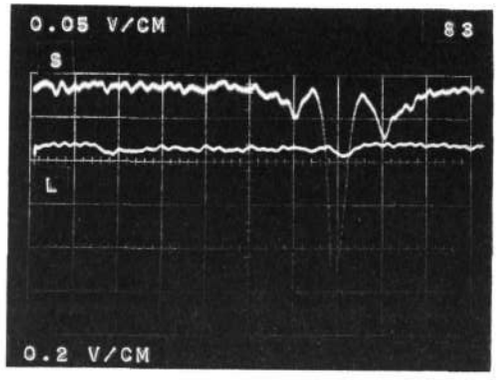

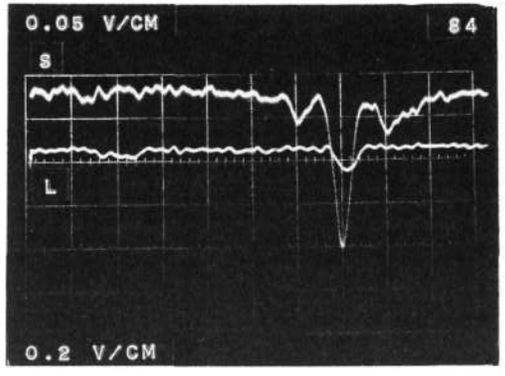

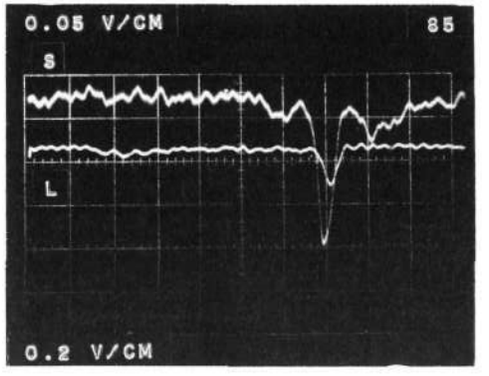

TEST 15 MMH/N204 d CONT.

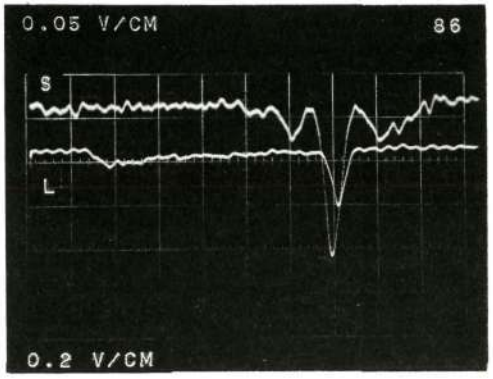

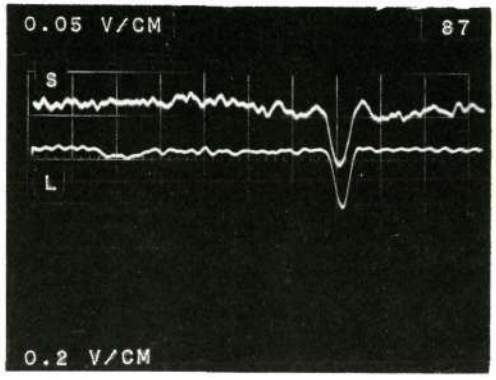

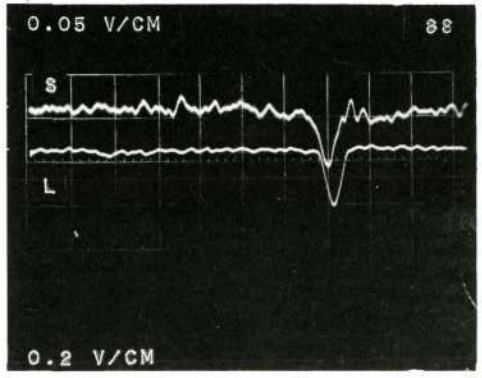

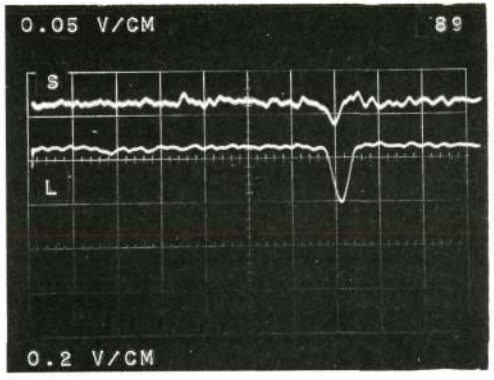

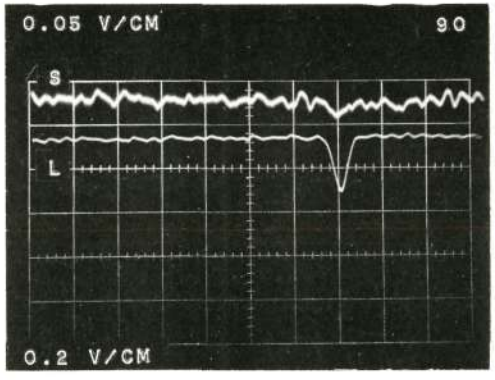

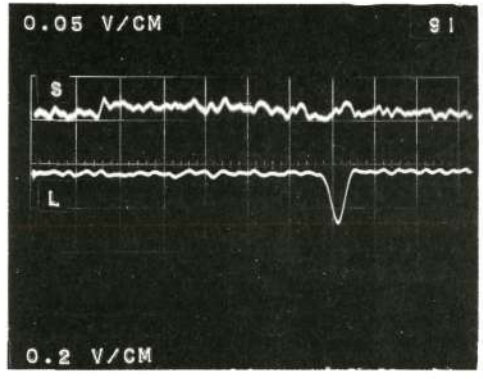

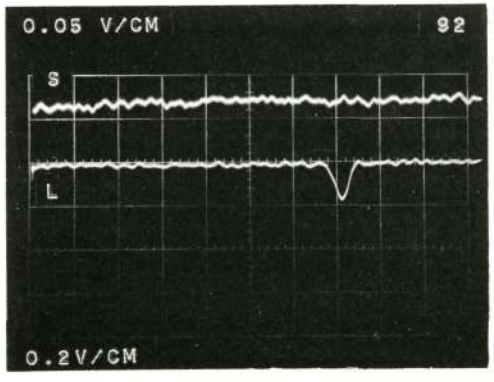

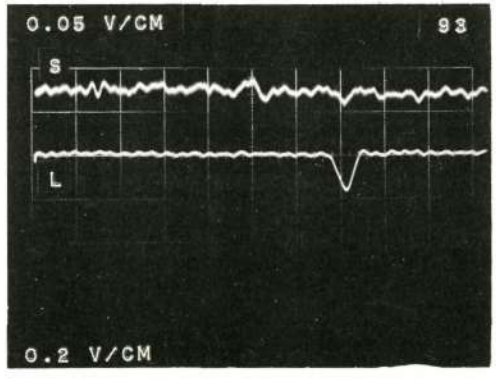

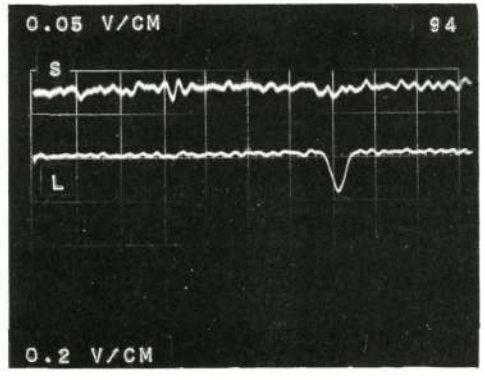

d CONT.

TEST 15 MMH/N204

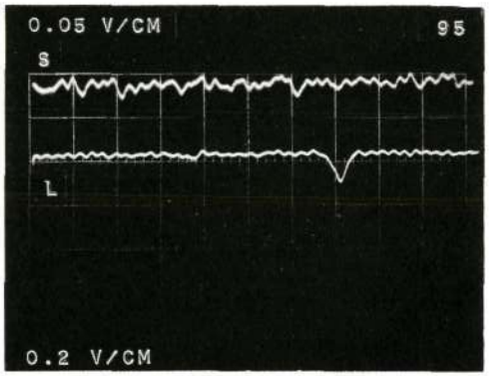

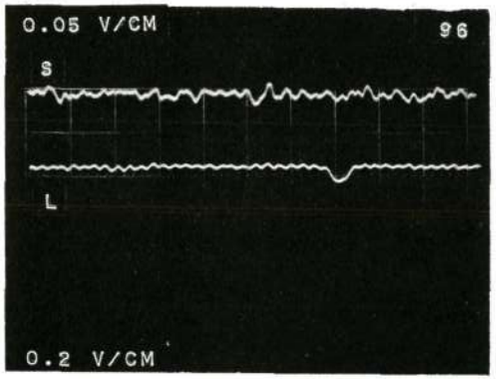

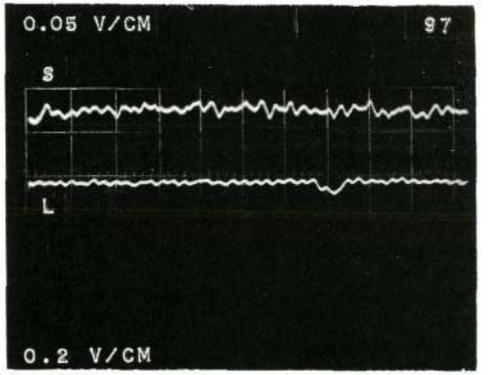

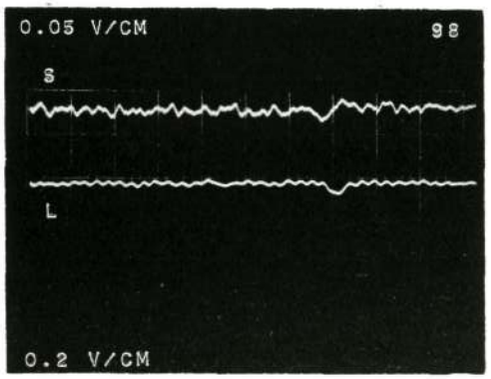

TEST 15 MMH/N2O4 e

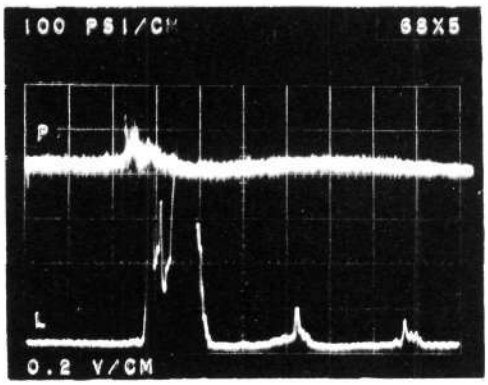

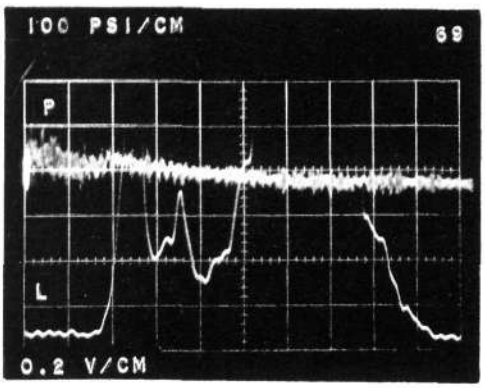

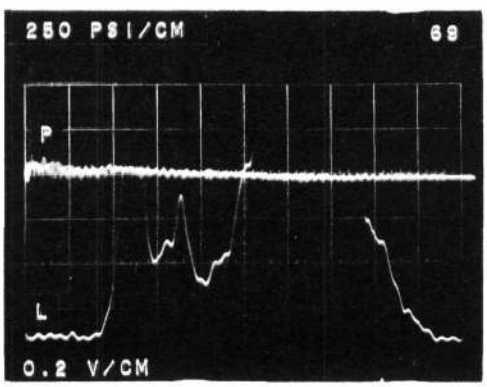

Test #16. Monomethyl Hydrazine/Nitrogen Tetroxide - Fuel Lead.

a. Pressure and short wave length visible emission spectra vs. time. Time base 500 microseconds per cm.

b. Visible emission spectra vs. time. Time base 500 microseconds per cm. Upper trace short wave length. Lower trace long wave length.

c. Pressure and visible emission spectra vs. time. Time base 500 microsecends per cm. Upper trace pressure. Lower trace long wave length visible emission spectra.

d. Visible emission spectra vs. time. Time base 100 microseconds per cm. Upper trace short wave length emission spectra. Lower trace long wave length emission spectra.

e. Pressure and visible emission spectra vs. time.

TEST 16 MMH/N204 a

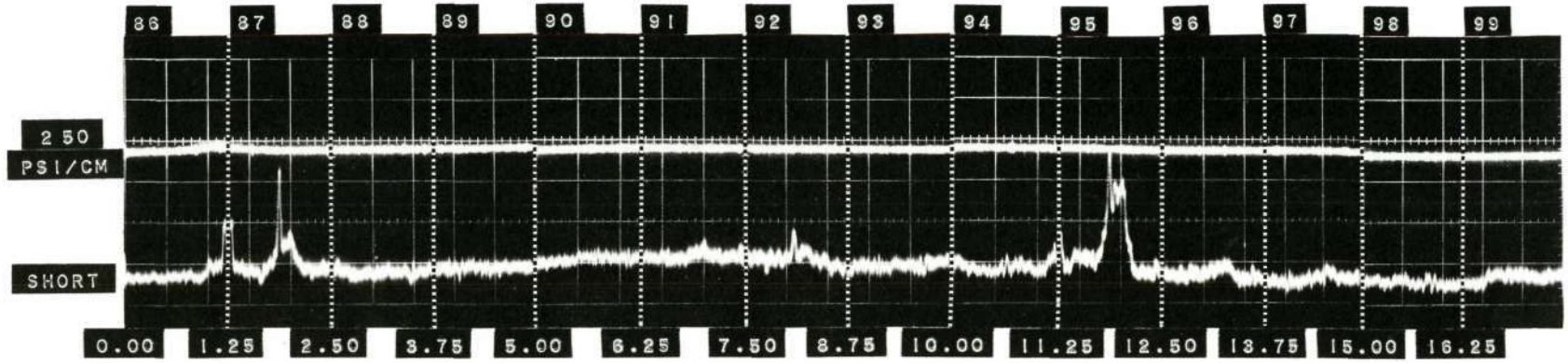

TIME MILLISECOND

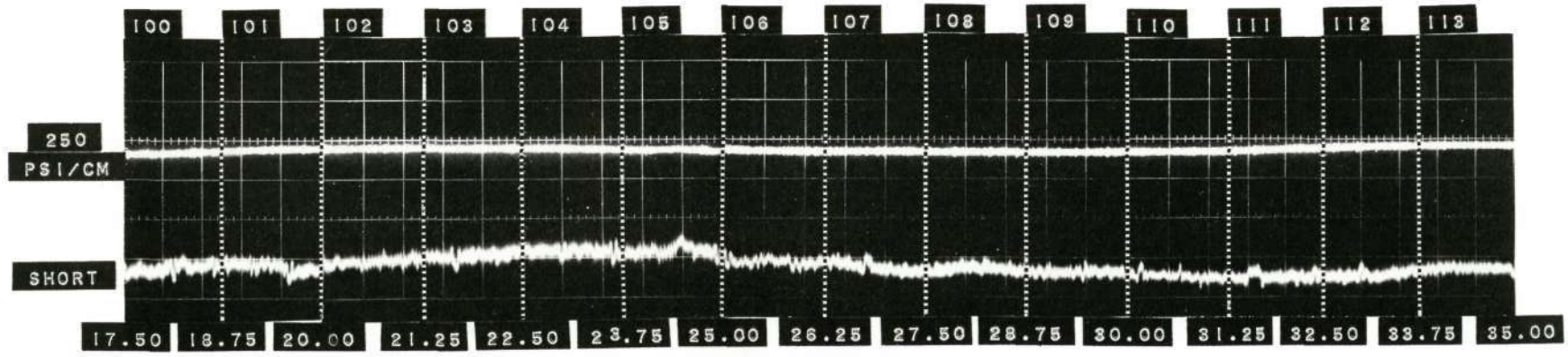

TIME MILLISECOND

TEST 16 MMH/N204 b

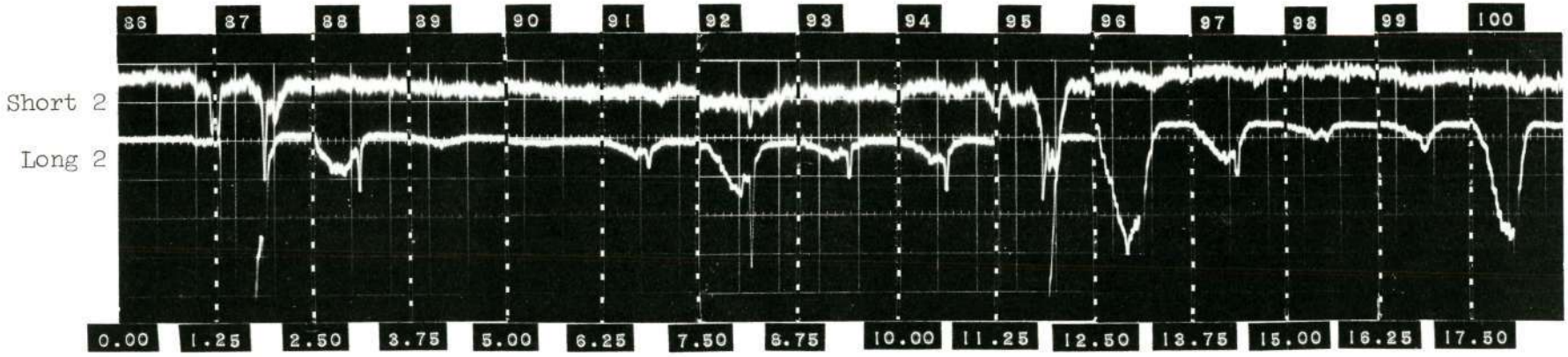

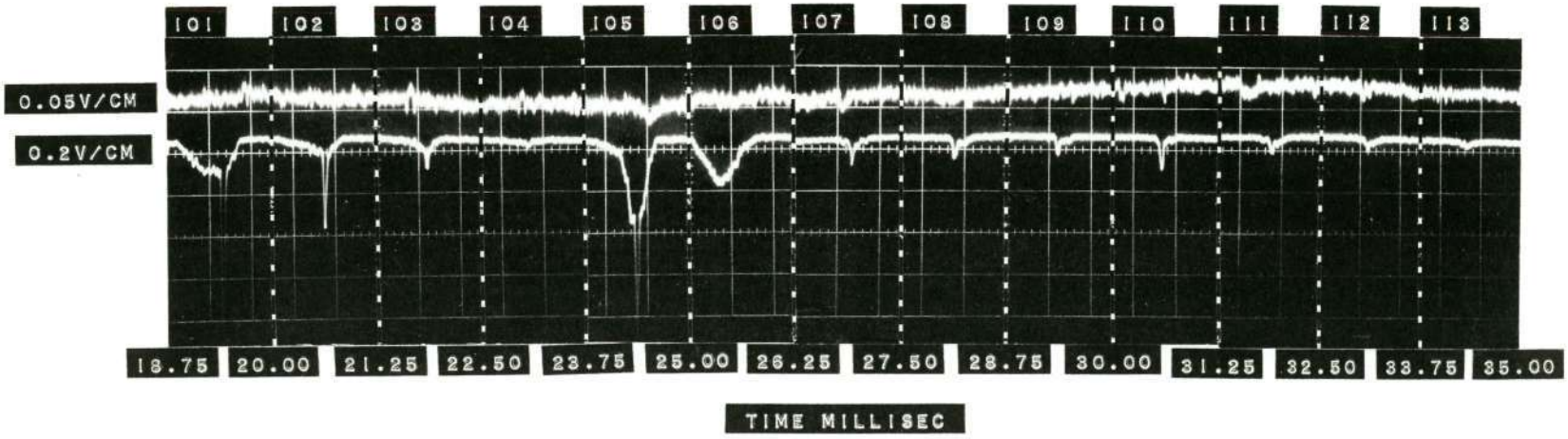

Page intentionally left blank

TEST 16 MMH/N204 *d*

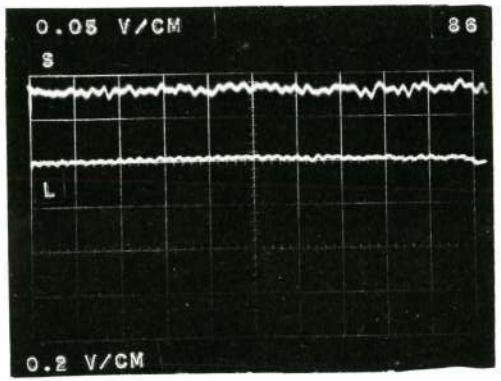

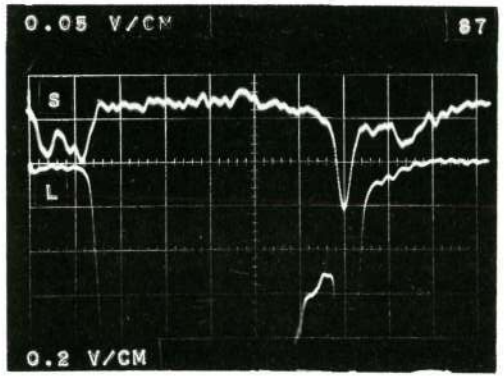

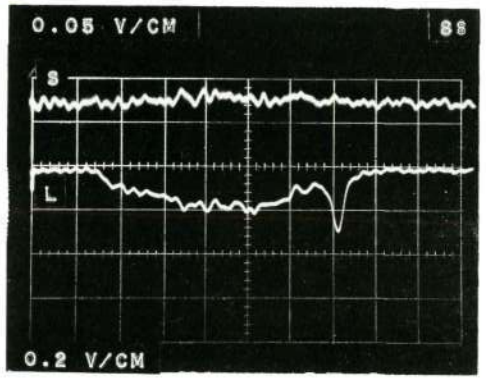

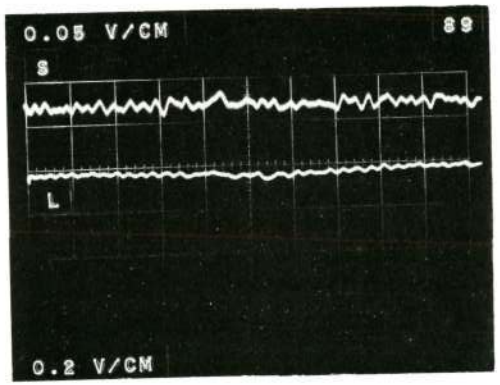

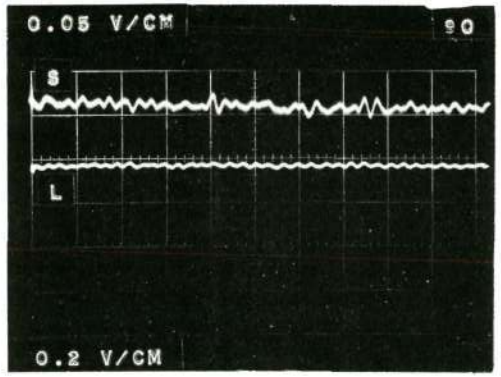

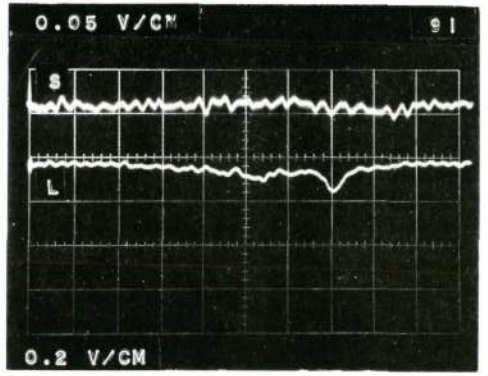

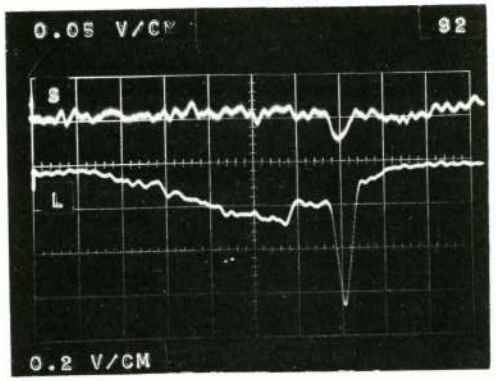

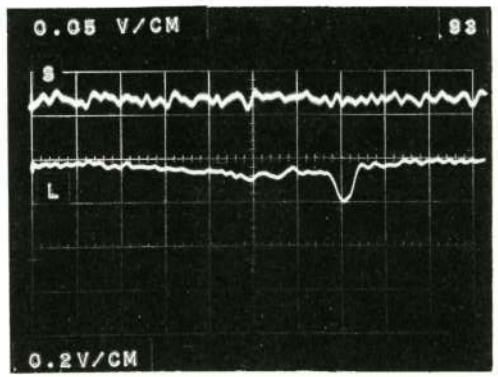

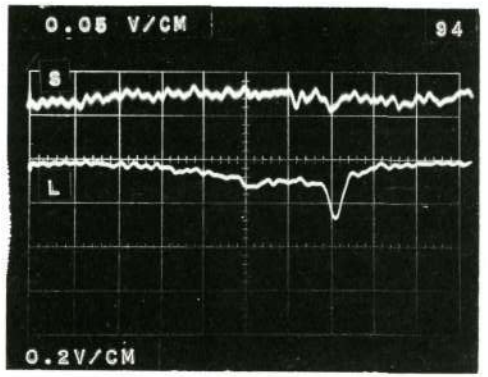

TEST 16 MMH/N204 d CONT.

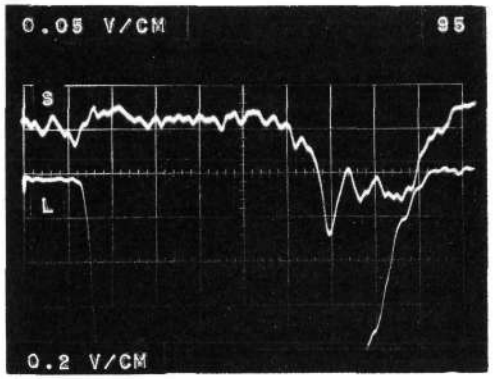

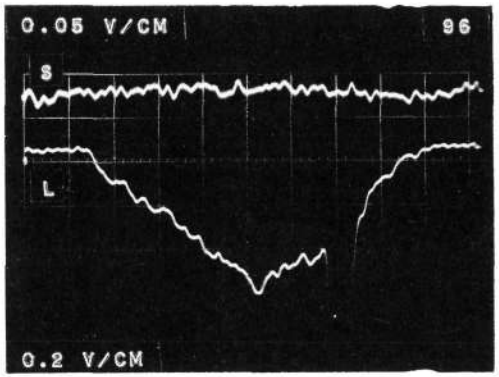

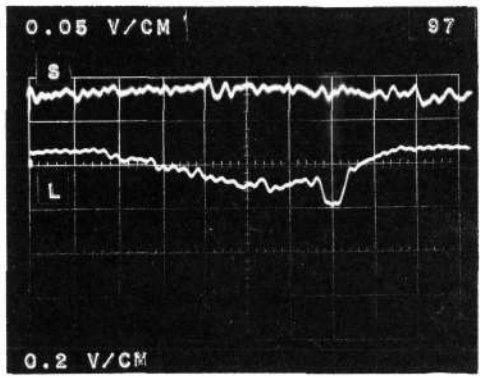

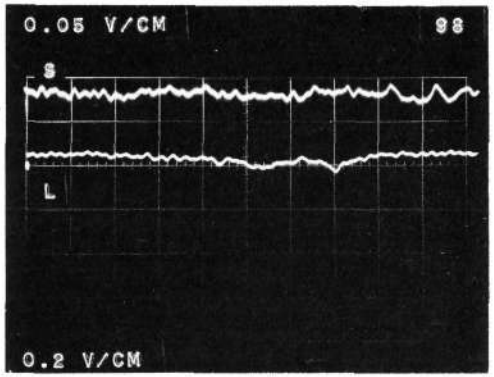

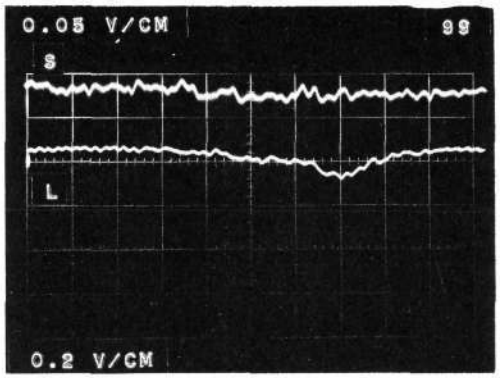

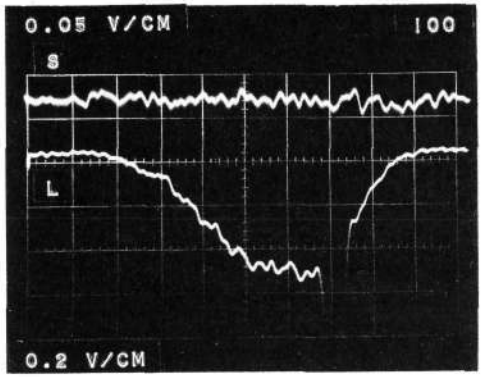

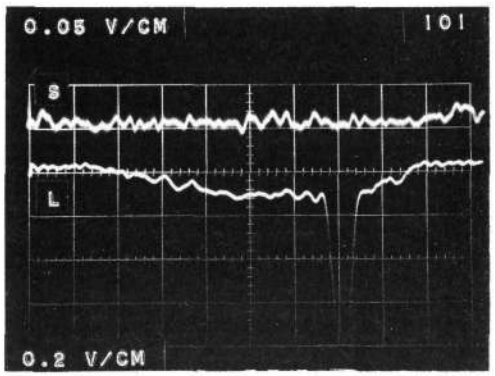

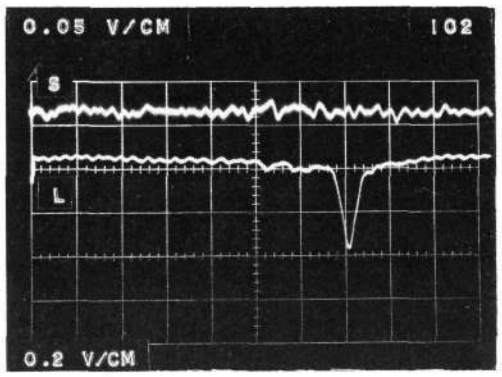

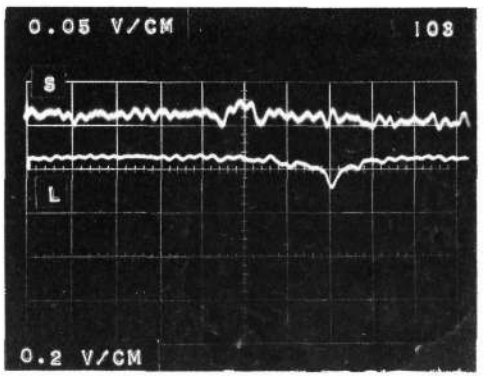

TEST 16 MMH/N204 d CONT.

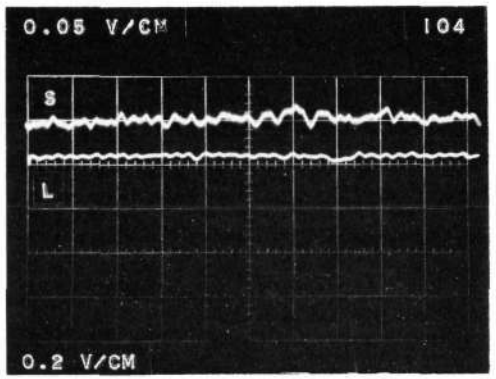

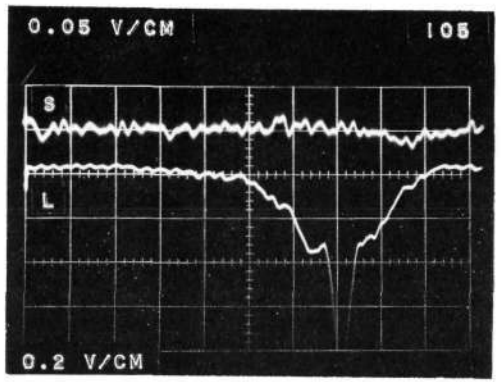

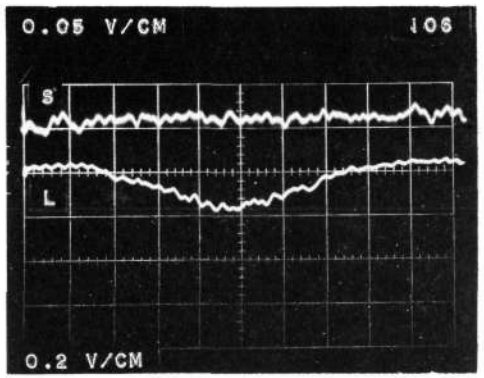

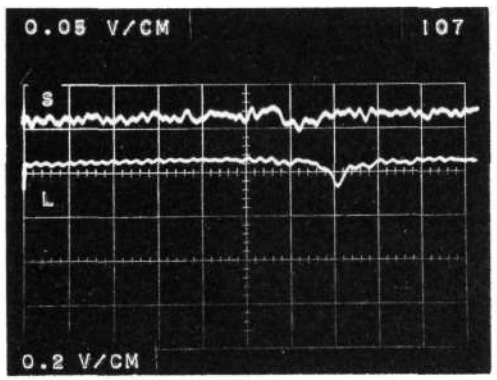

TEST 16 MMH/N204 e

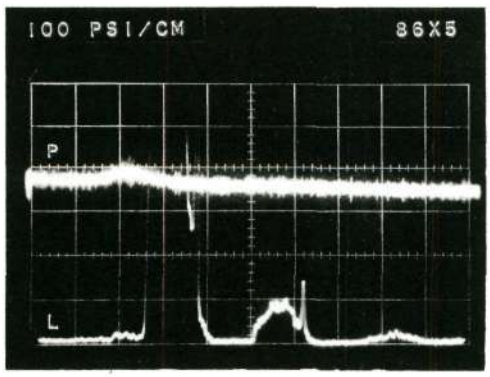

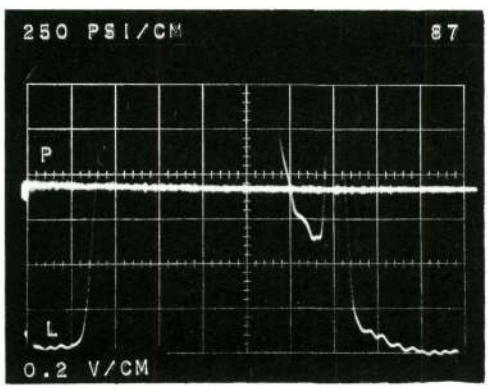

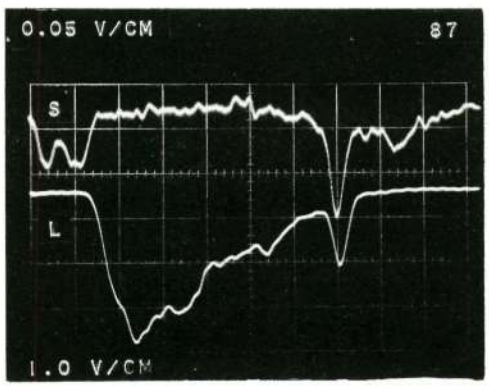

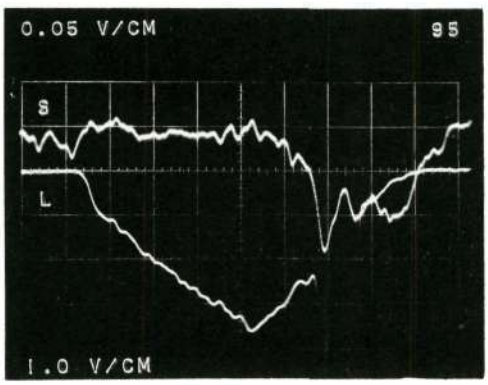

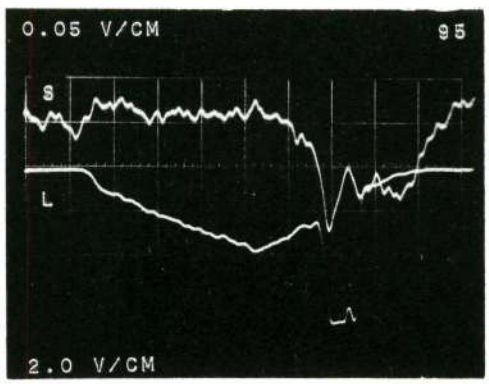

Test #18. Monomethyl Hydrazine/Nitrogen Tetroxide. Oxider Lead.

a. Chamber pressure and visible short wave length emission spectra vs. time - time base 100 microsecond per cm.

b. Chamber pressure and visible emission spectra (4000 - 6900Å) vs. time - time base 100 microsecond per cm. unless otherwise indicated.

c. Visible emission spectra vs. time - time base 500 microseconds per cm. Upper trace short wave length. Lower trace long wave length.

d. Visible emission spectra vs. time - time base 100 microseconds per cm. - Upper trace short wave length. Lower trace long wave length.

TEST 18 MMH/N204 a

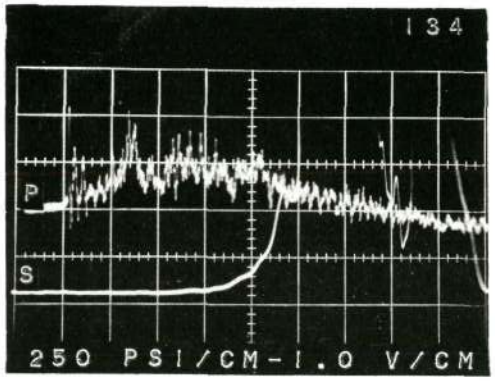

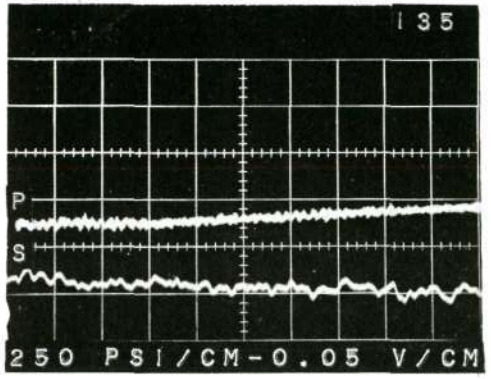

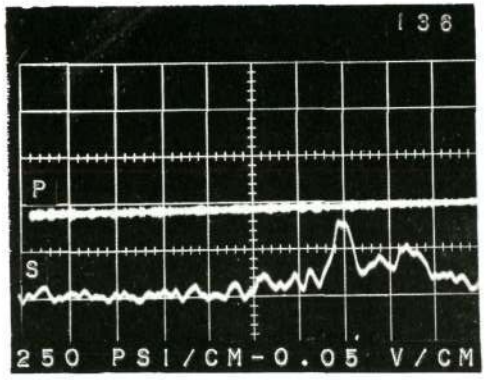

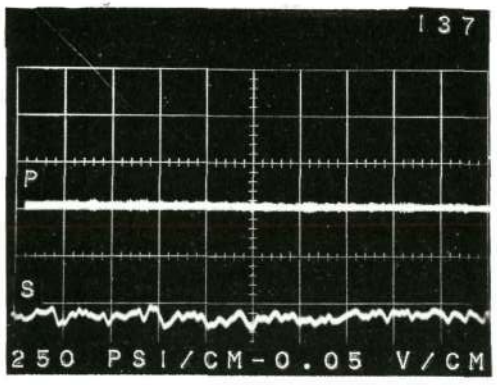

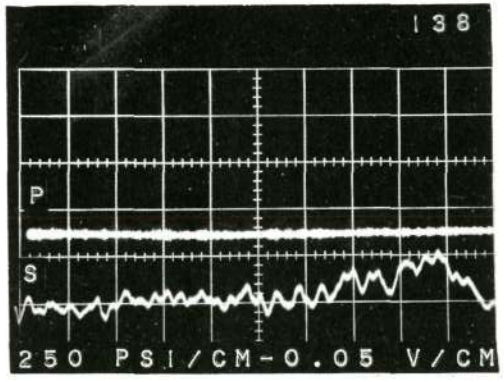

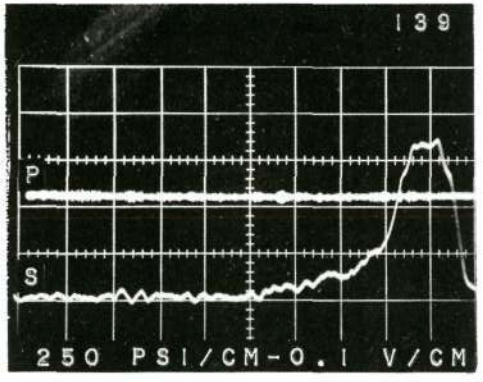

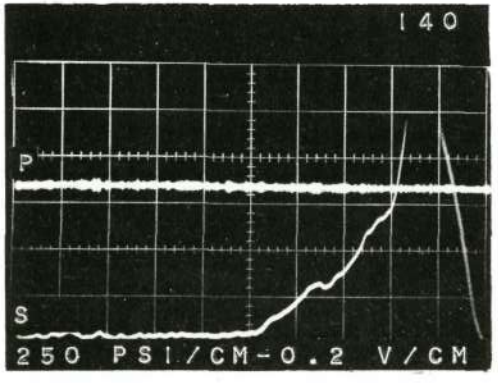

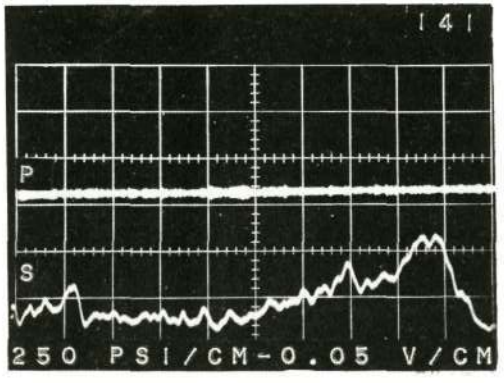

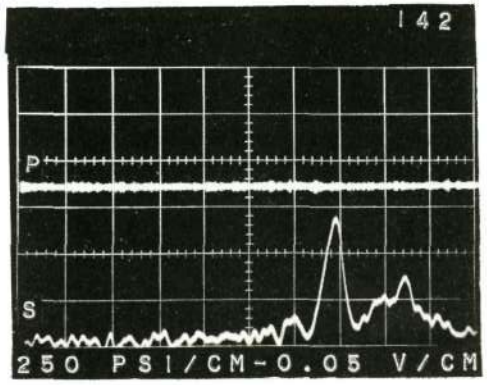

TEST 18 MMH/N204 a

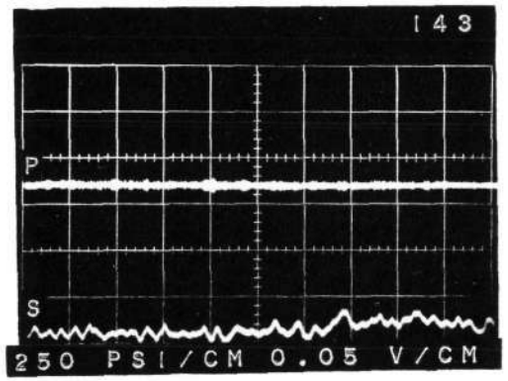

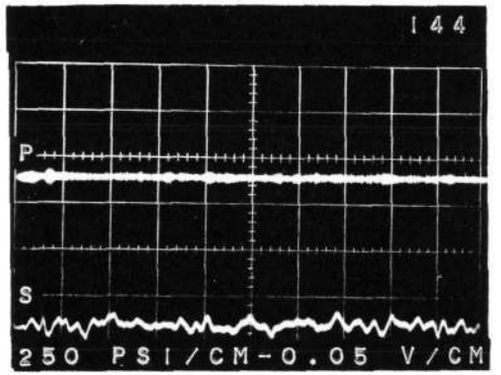

TEST 18 MMH/N204
4000-6900 ANGSTROMS

b

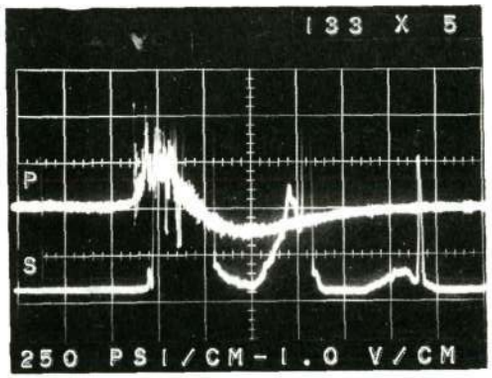

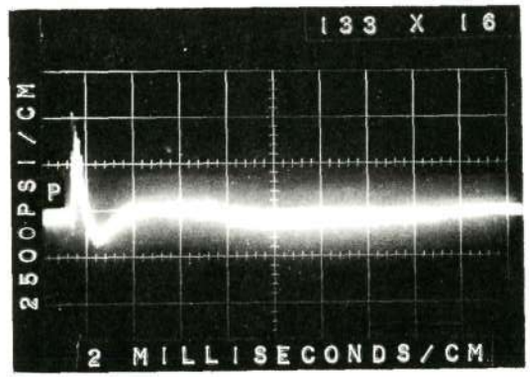

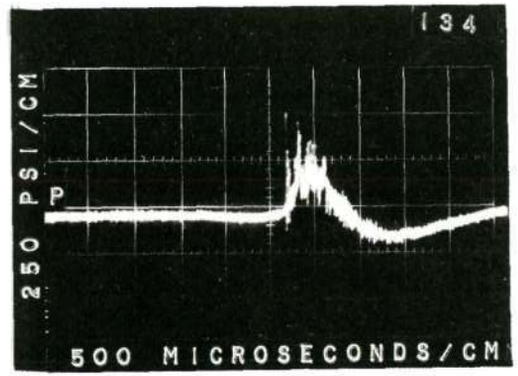

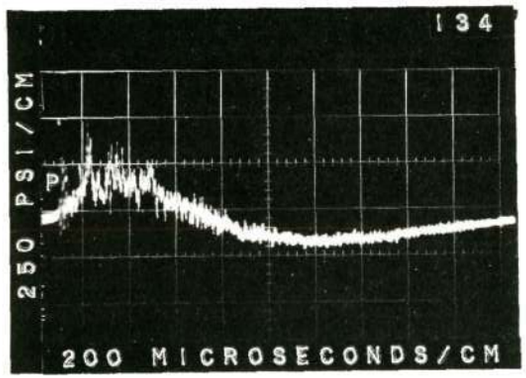

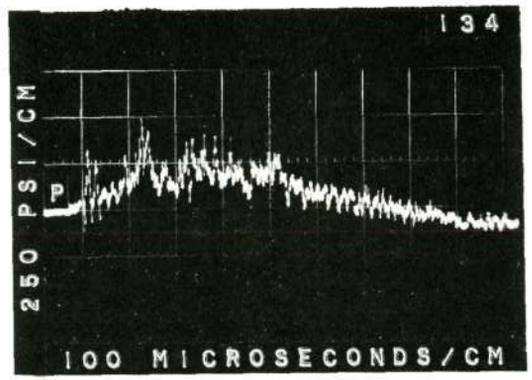

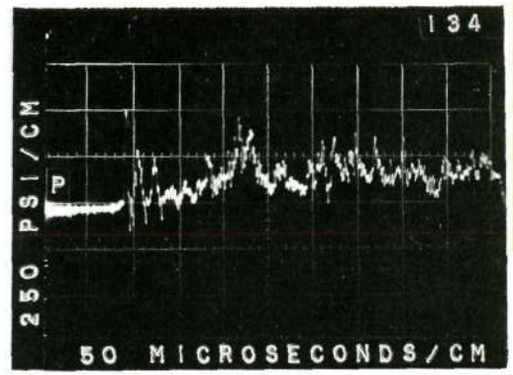

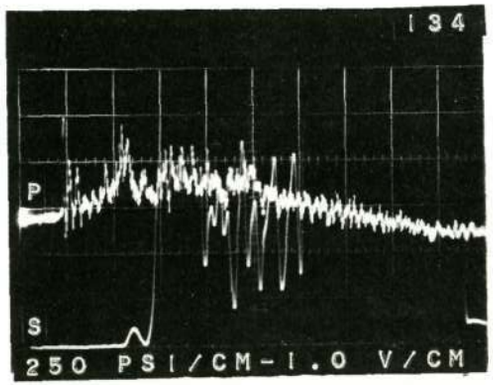

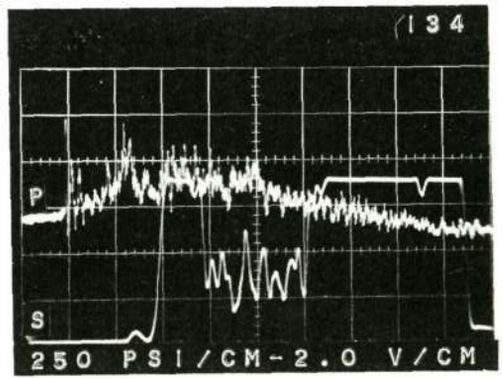

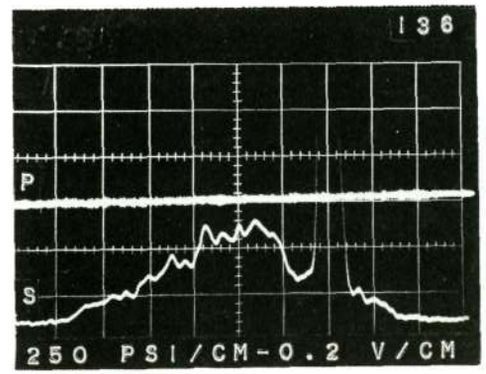

TEST 18 MMH/N204 b

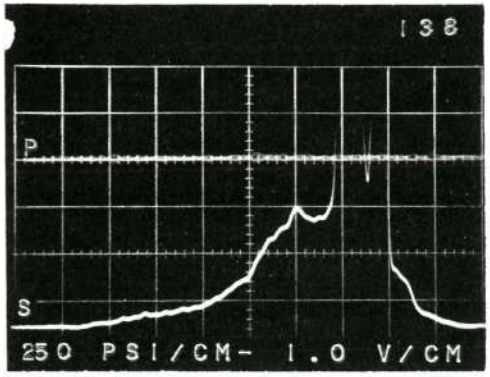

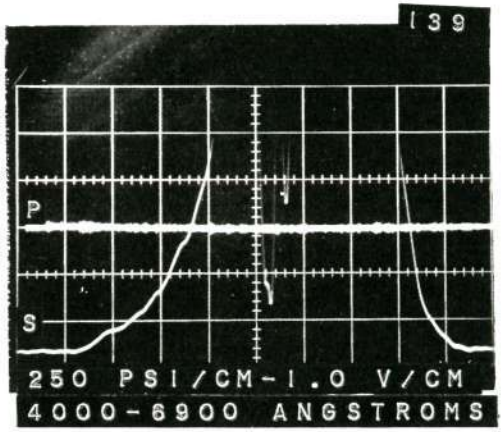

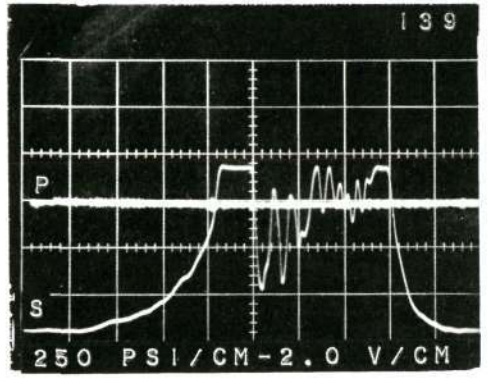

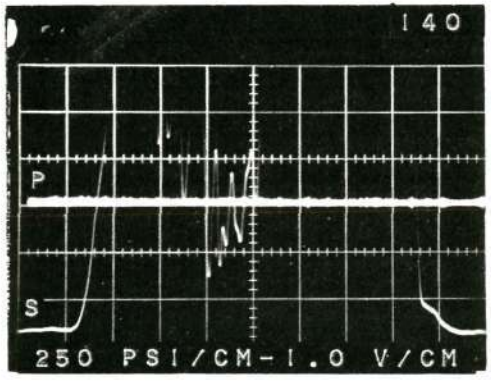

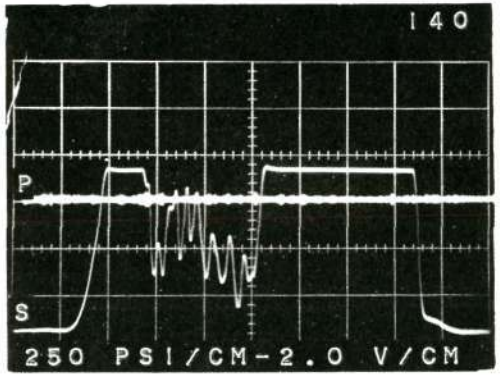

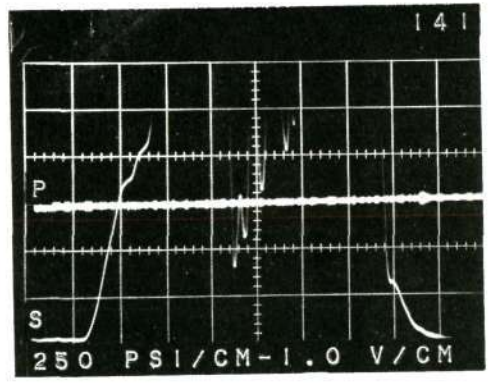

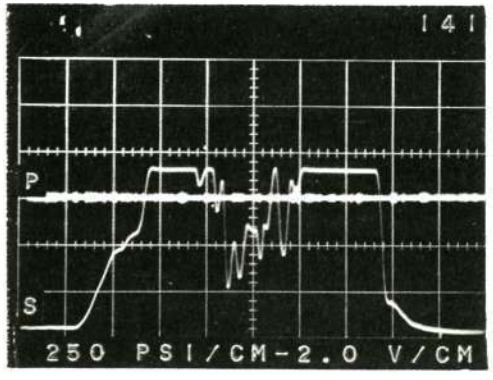

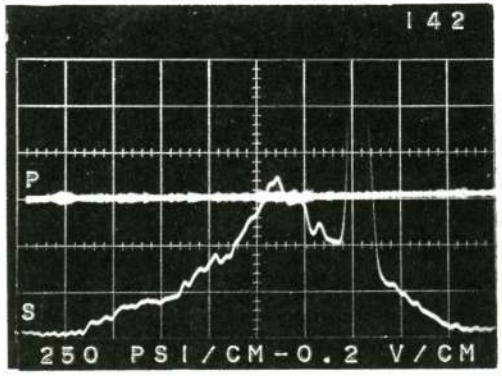

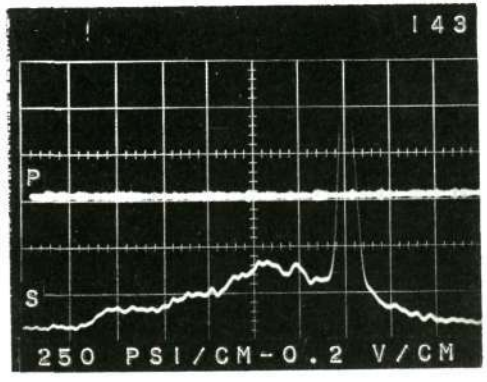

TEST 18 MMH/N204 b

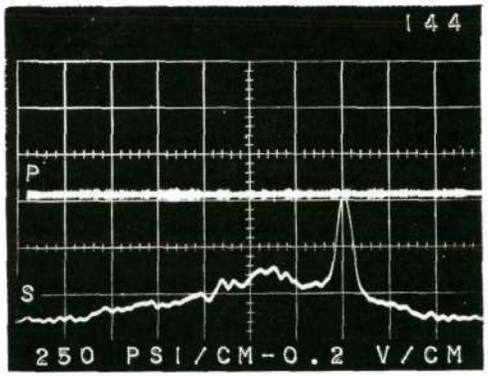

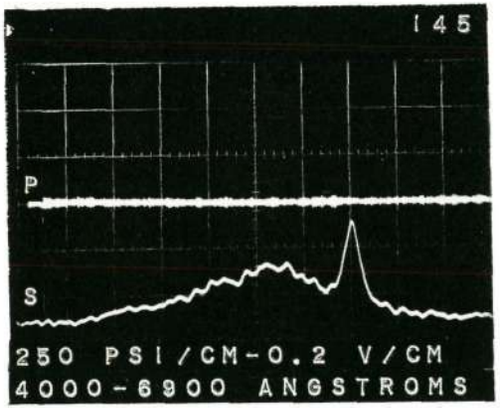

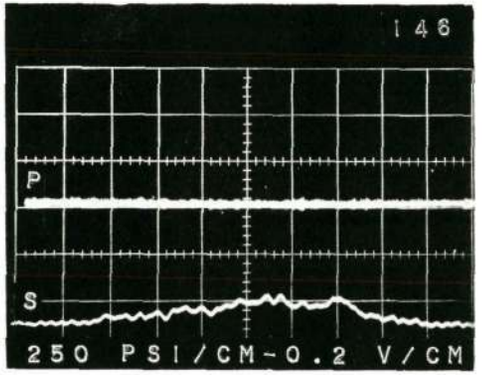

RUN 18 C

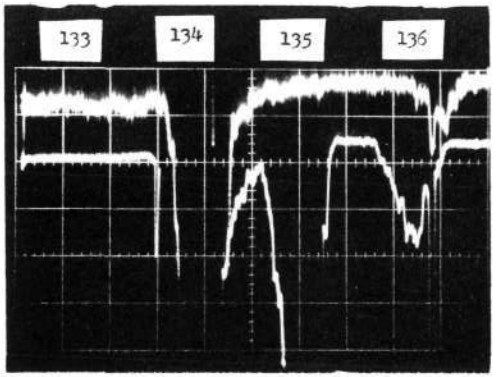

0.05 v/cm

0.2 v/cm

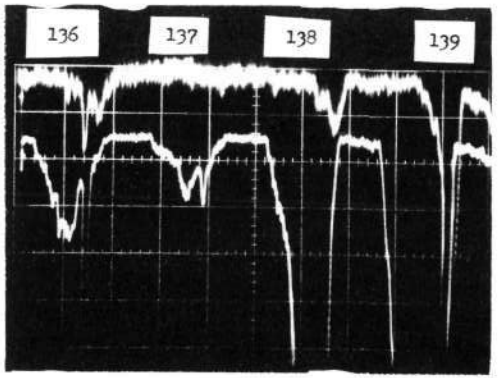

0.05 v/cm

0.2 v/cm

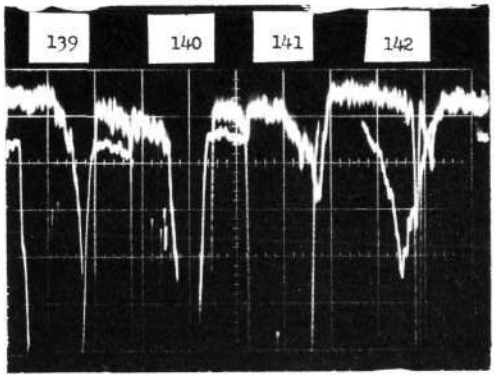

0.05 v/cm

0.2 v/cm

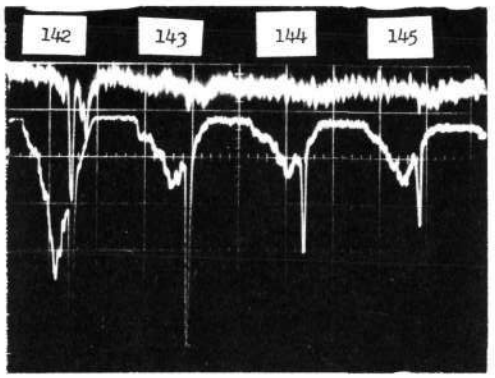

0.05 v/cm

0.2 v/cm

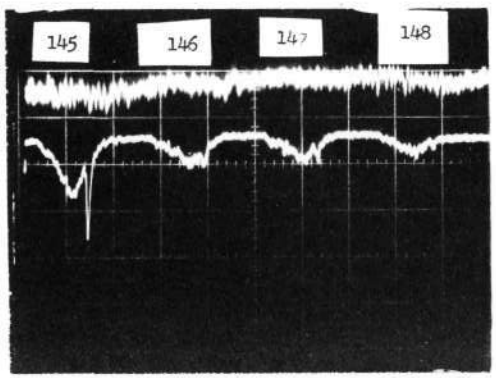

0.05 v/cm

0.2 v/cm

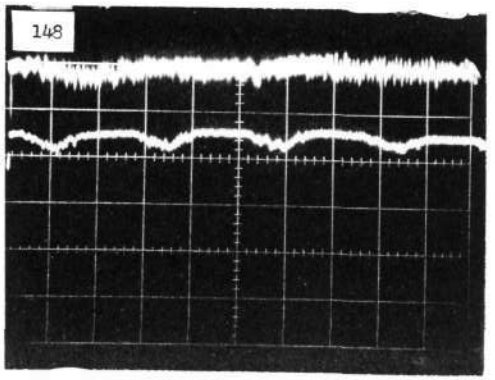

0.05 v/cm

0.2 v/cm

C42

RUN 18 d

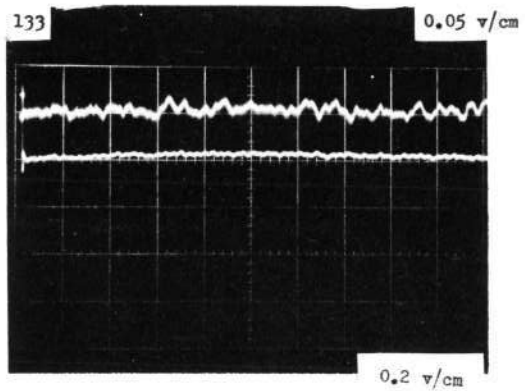
133
0.05 v/cm
0.2 v/cm

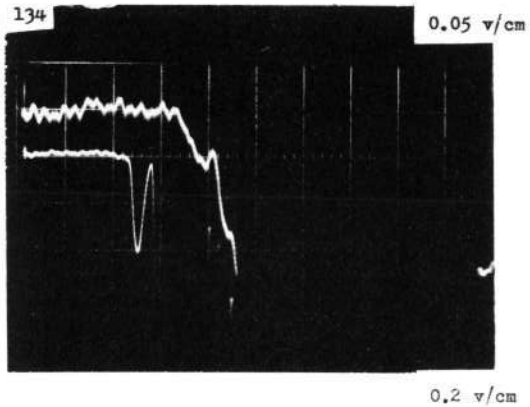
134
0.05 v/cm
0.2 v/cm

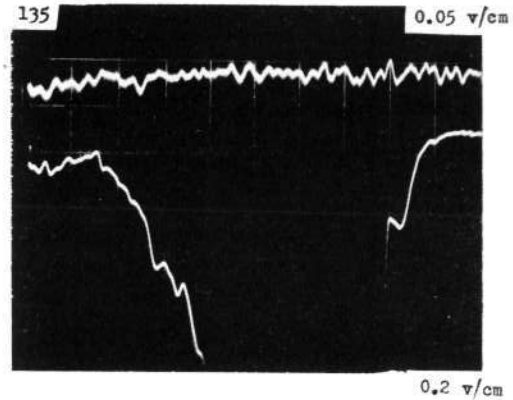
135
0.05 v/cm
0.2 v/cm

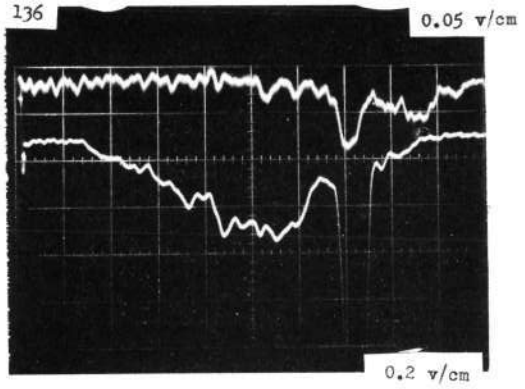
136
0.05 v/cm
0.2 v/cm

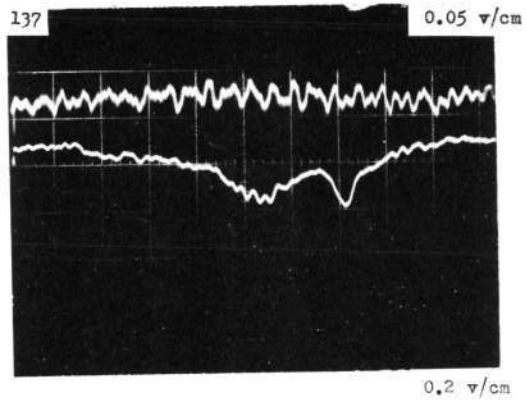
137
0.05 v/cm
0.2 v/cm

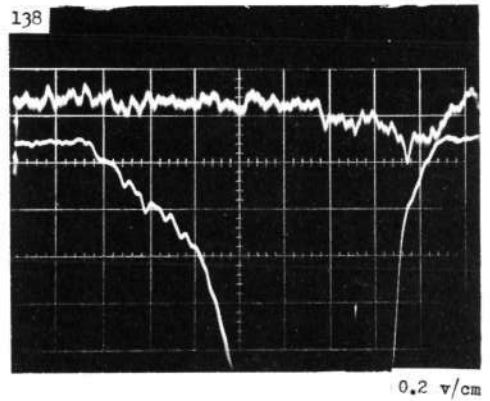
138
0.05 v/cm
0.2 v/cm

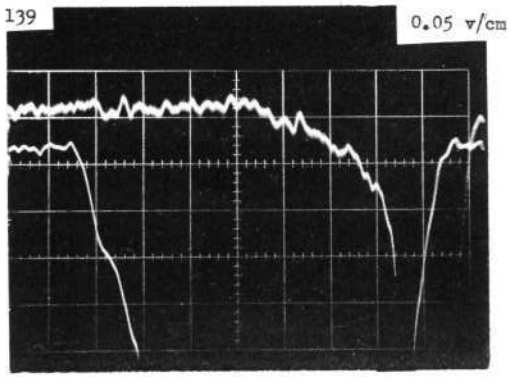
139
0.05 v/cm

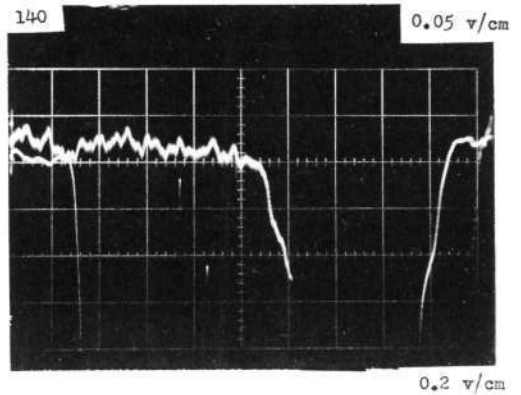
140
0.05 v/cm
0.2 v/cm

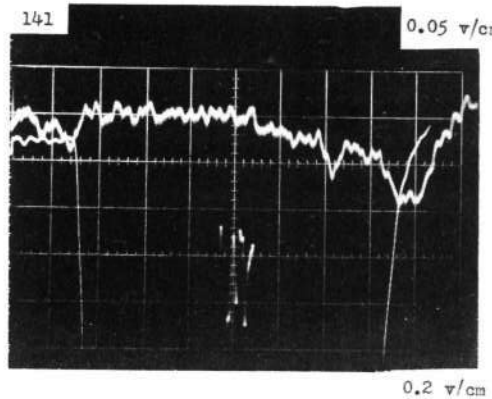
141
0.05 v/cm
0.2 v/cm

d CONT

RUN 18

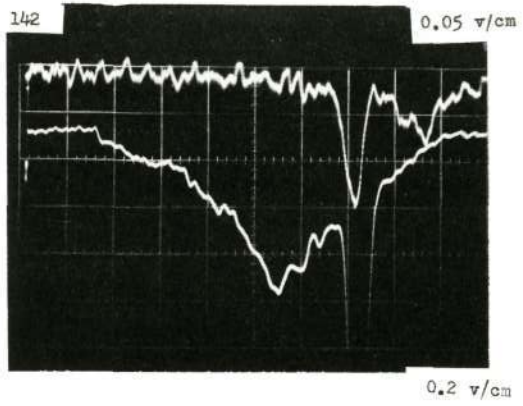

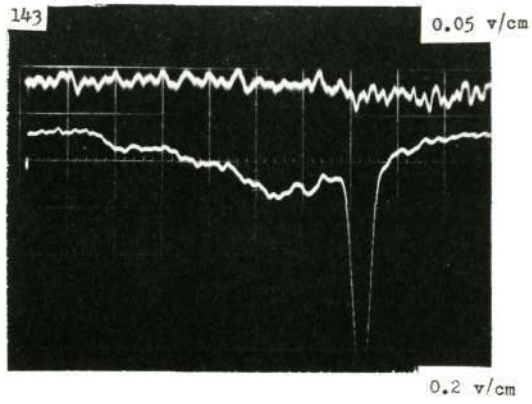

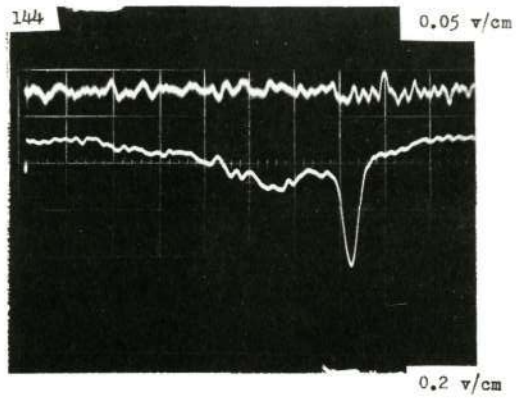

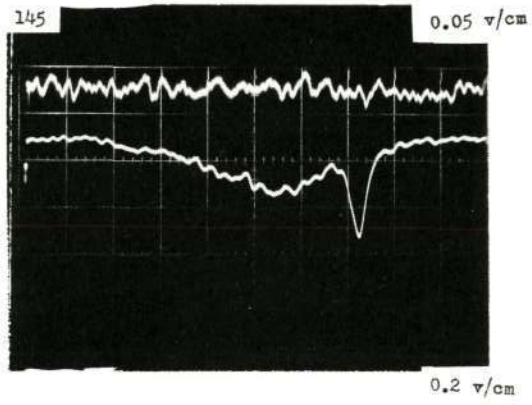

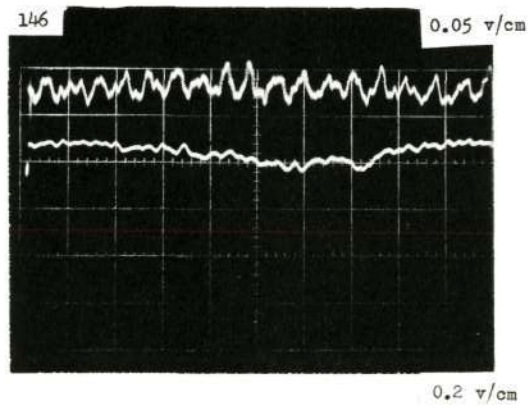

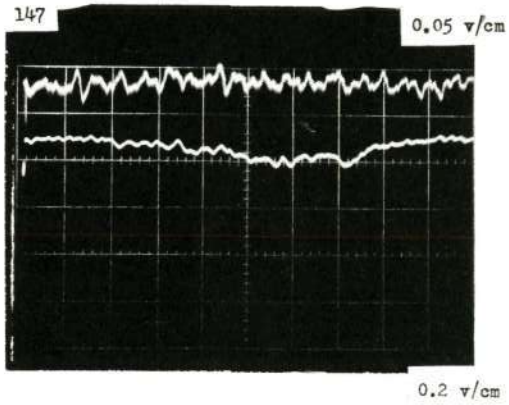

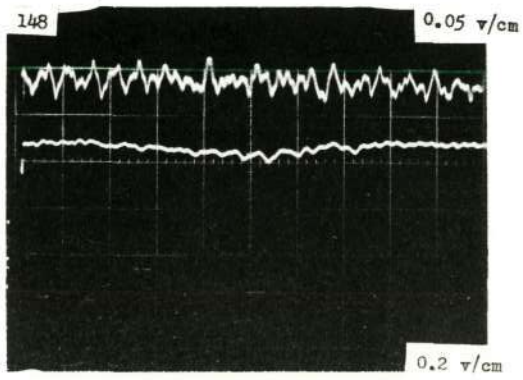

RUN 18 d CONT.

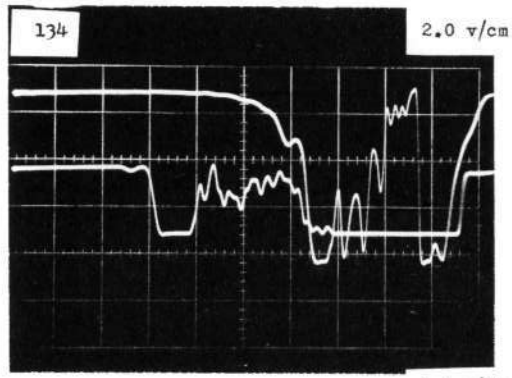

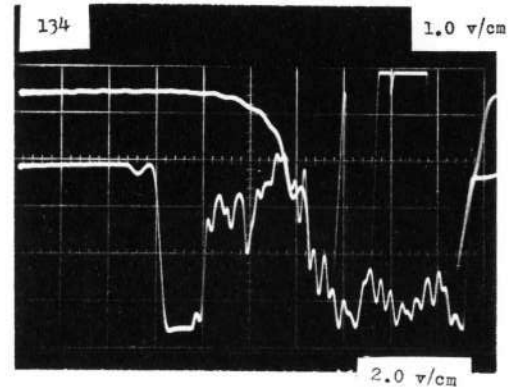

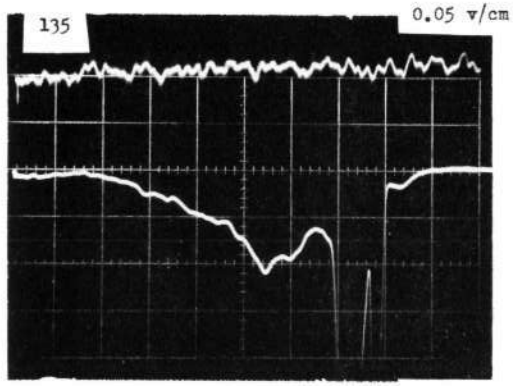

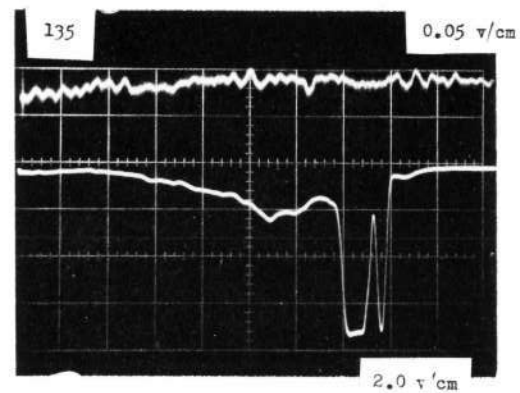

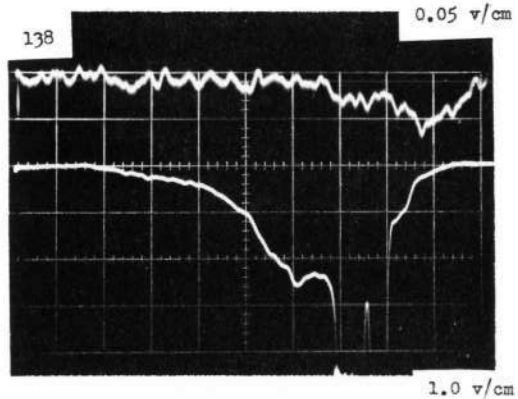

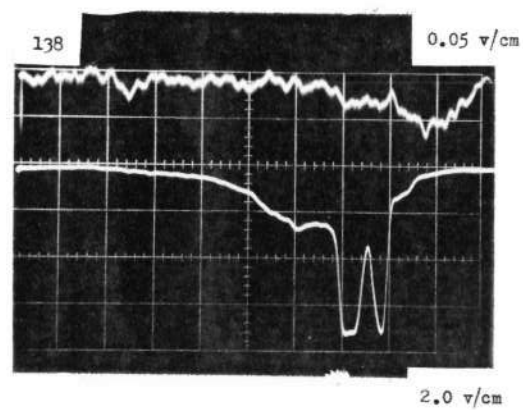

C 45

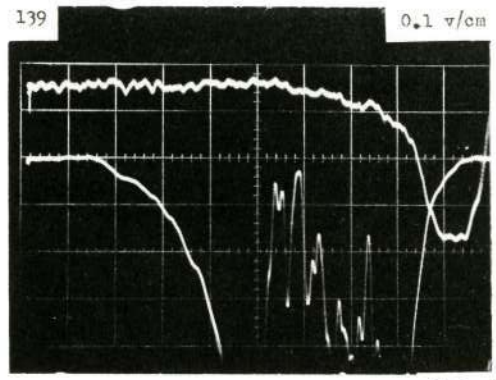

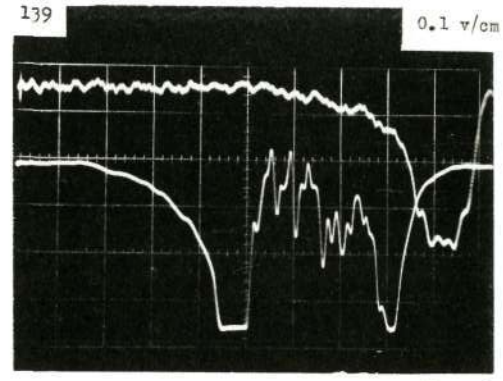

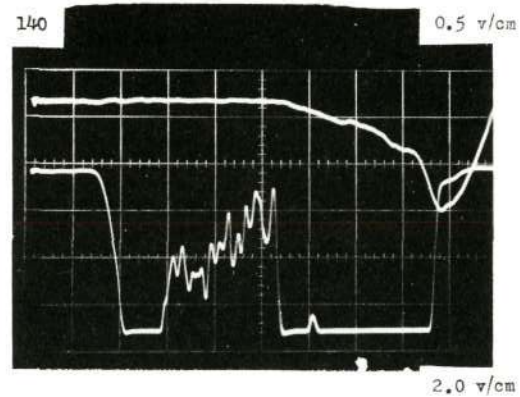

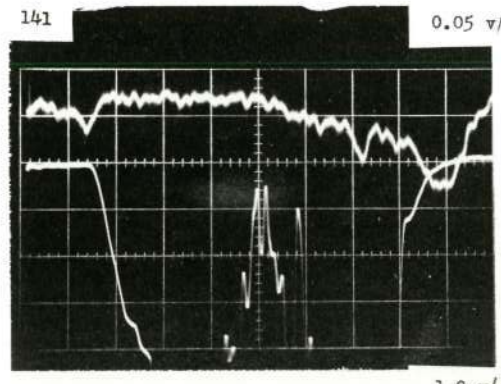

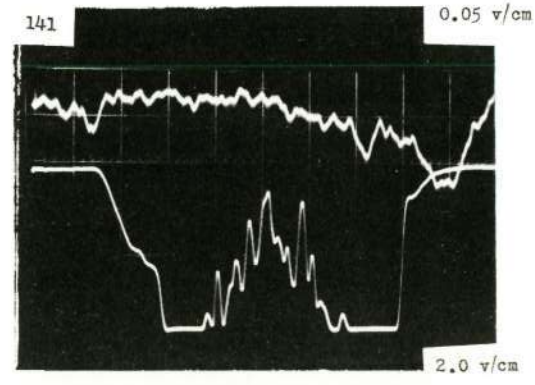

Test #23. Unsymmetrical Dimethylhydrazine / Nitrogen Tetroxide Fuel Lead.

a. Short and long wave length Emission Spectra in visible region - time base 500 microseconds per cm.

b. Short and long wave length Emission Spectra in visible region - time base 100 microsecond per cm - 250 microsecond dead time between oscillograph tractings.

TEST 23 UDMH/N204

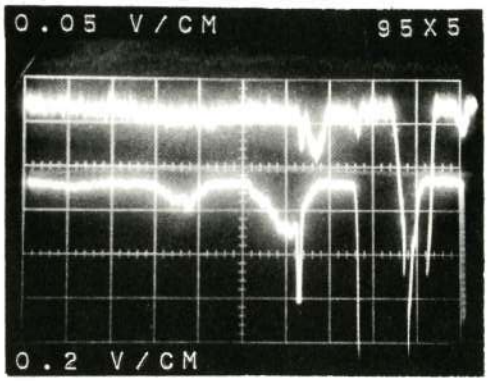

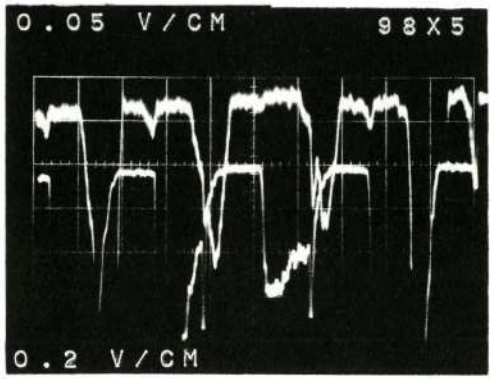

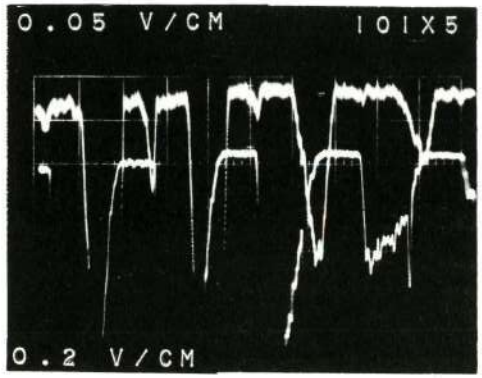

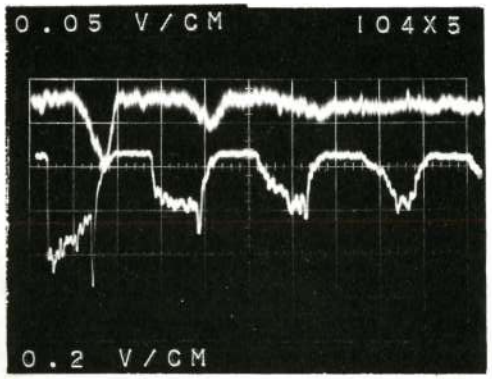

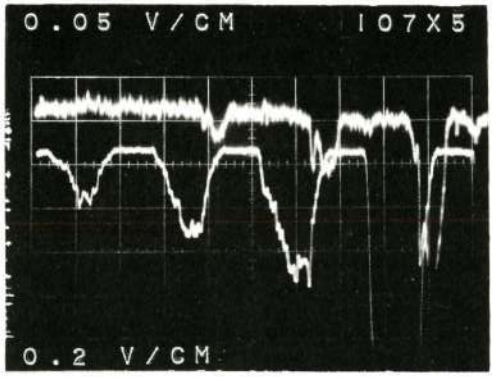

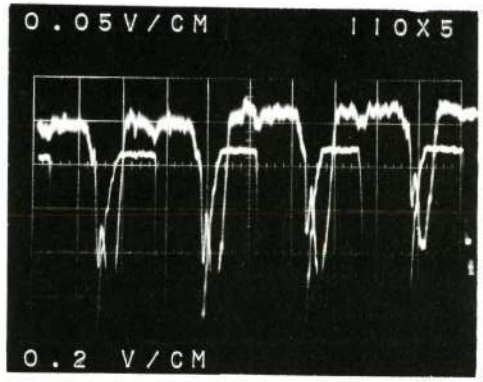

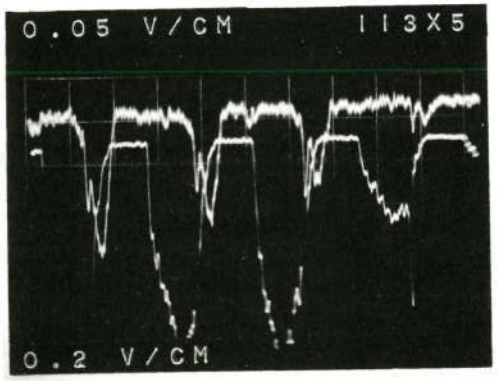

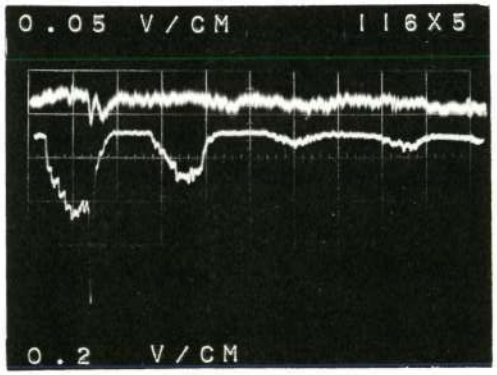

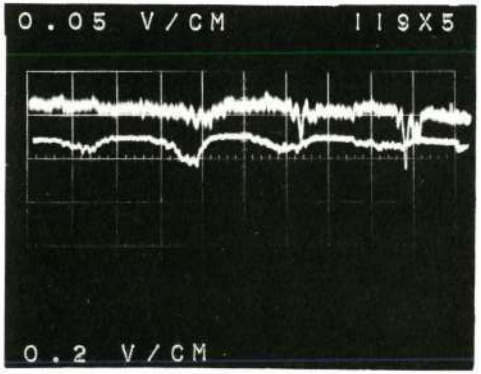

TEST 23 UDMH/N204 a CONT

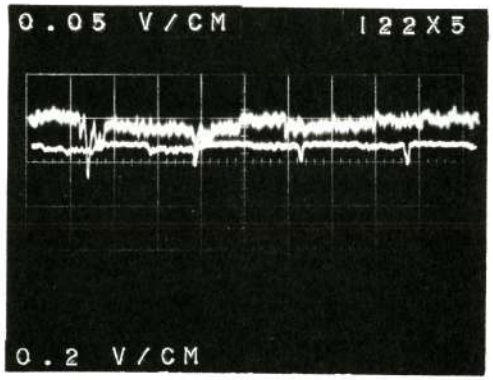

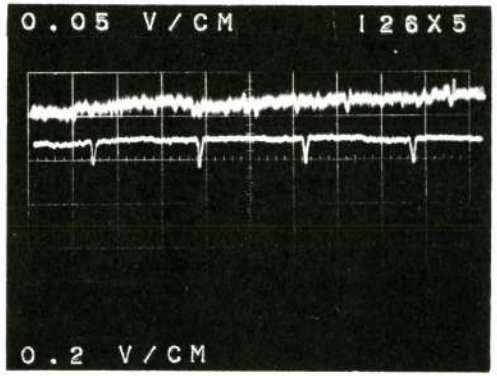

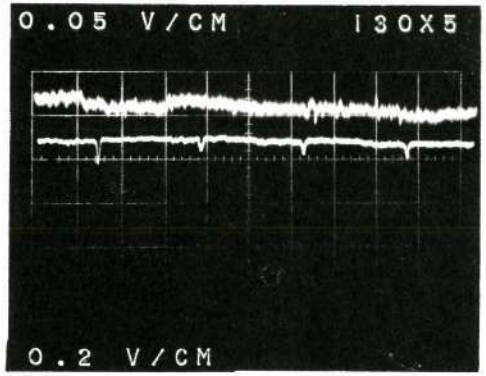

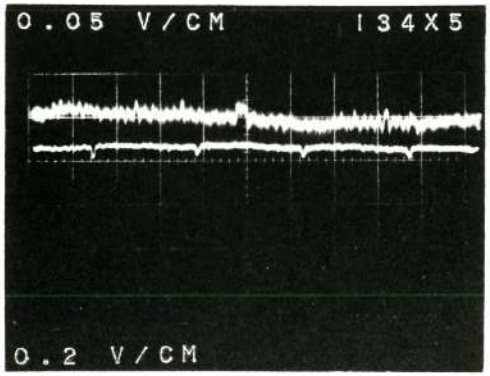

TEST 23 UDMH/N204 b

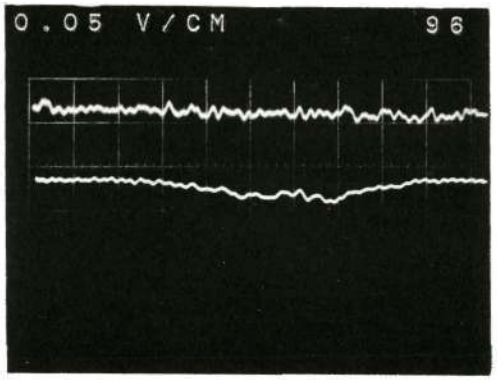

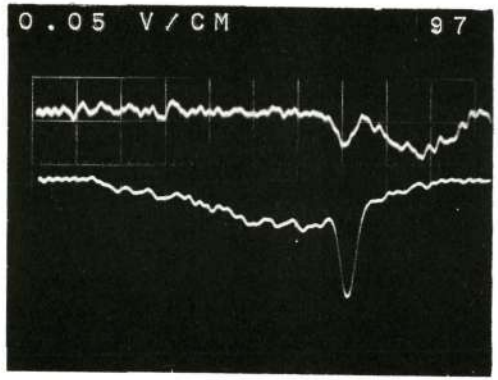

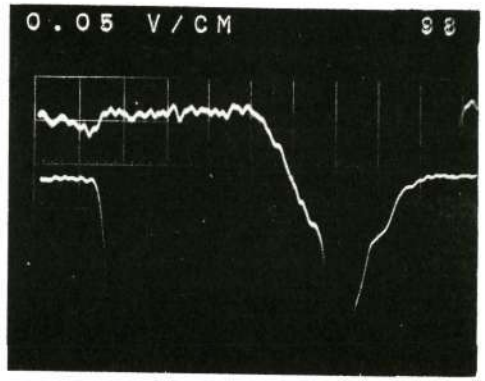

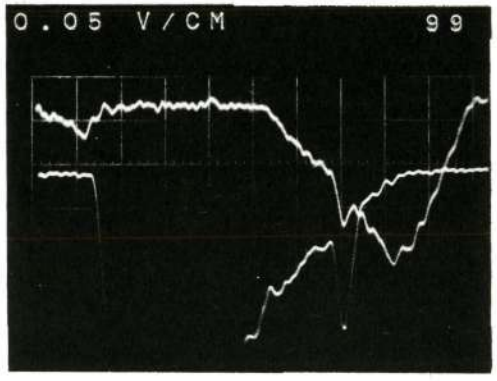

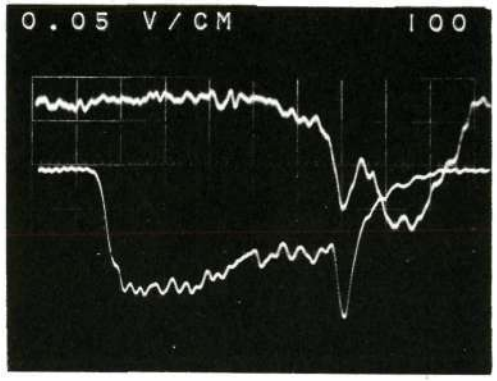

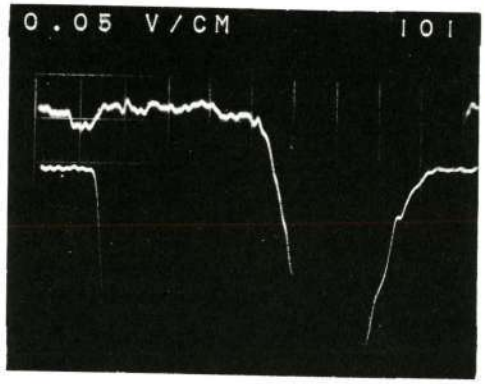

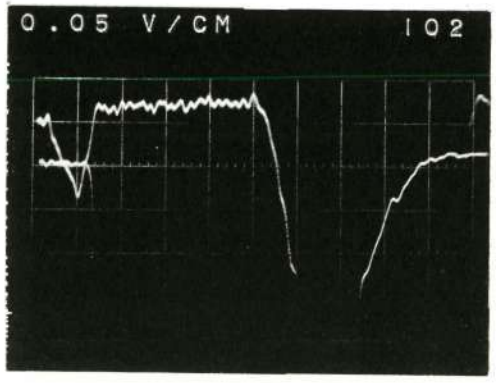

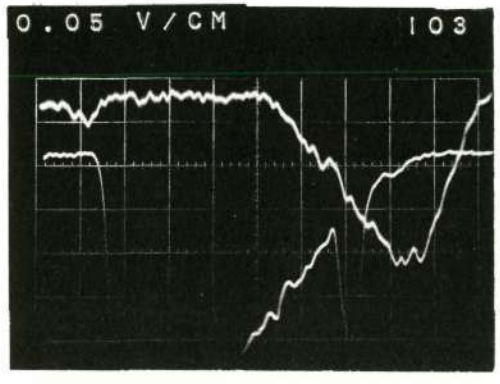

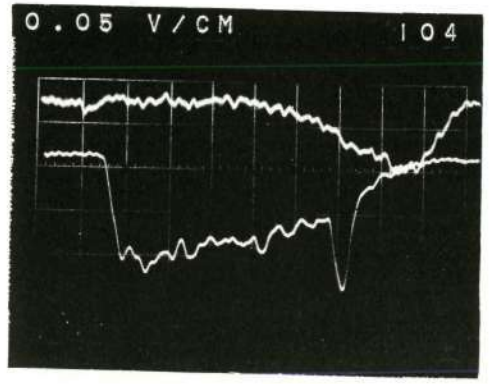

Test #30. Hydrazine/Nitrogen Tetroxide. Short Oxider Lead.

a. Chamber pressure and propellant flows vs. time.

Time base 20 milliseconds per cm.

b. Chamber pressure and IR emission spectra vs. time.

Time base 500 microseconds per cm.

c. Chamber pressure and IR emission spectra vs. time.

Time base 100 microseconds per cm. 250 microseconds dead time between oscilloscope records.

a

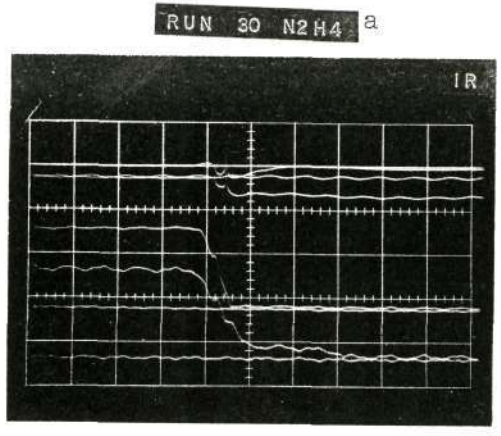

b

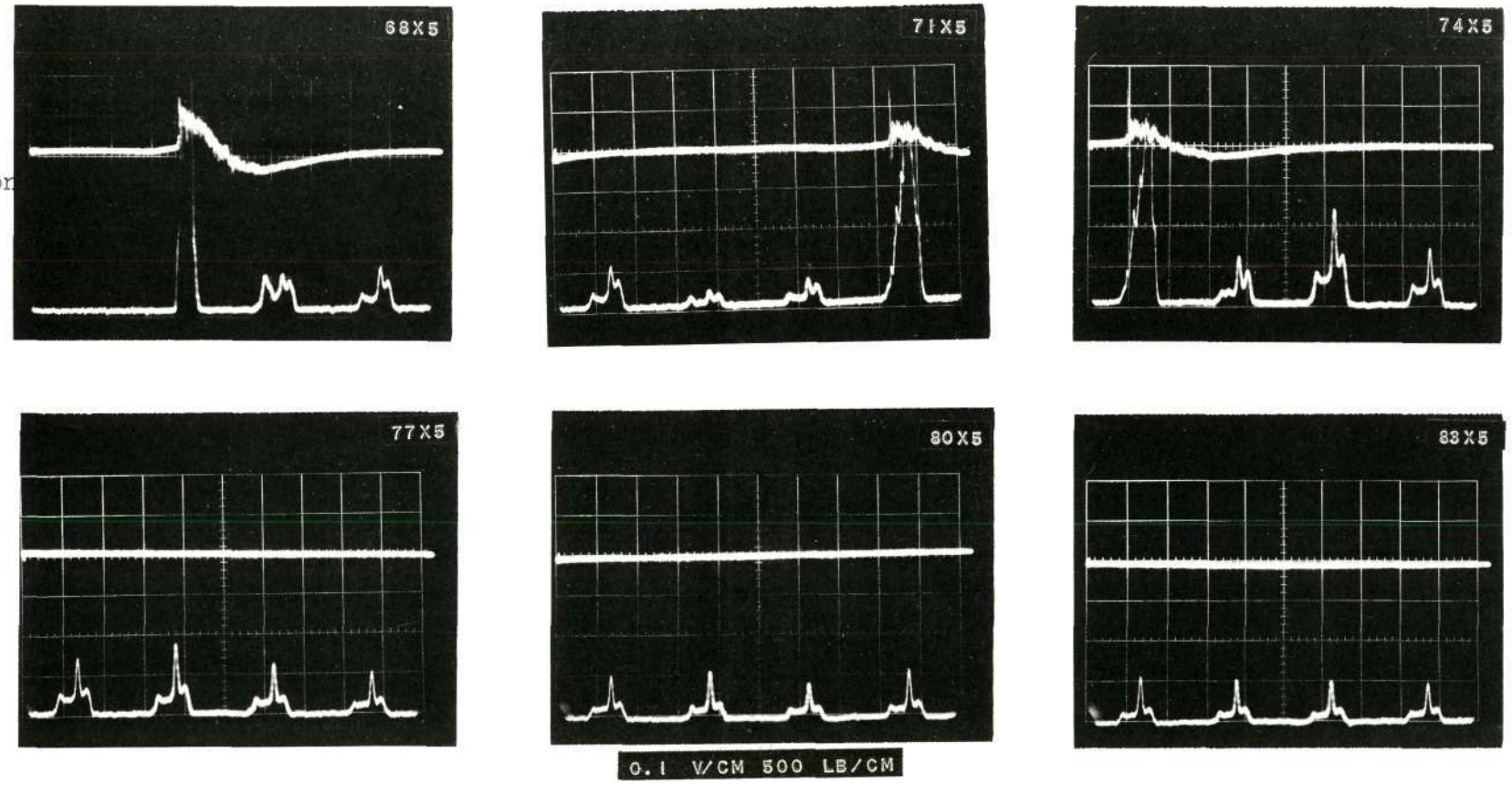

RUN 30 N_2H_4 b(cont.)

Pressure

IR Emission Spectra

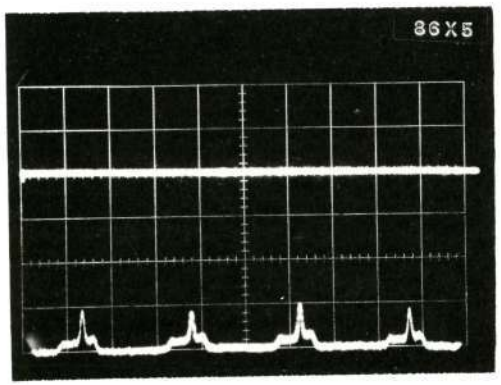

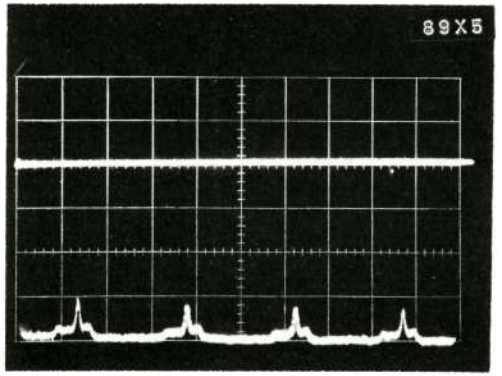

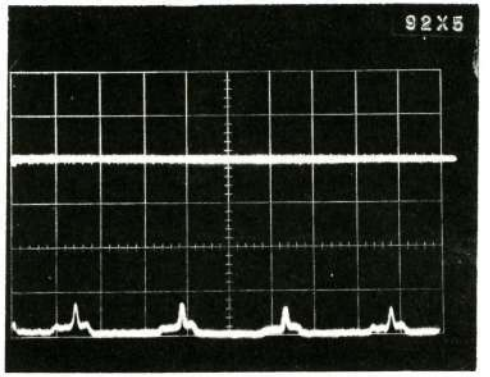

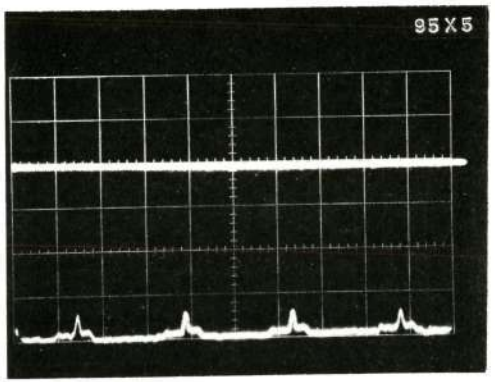

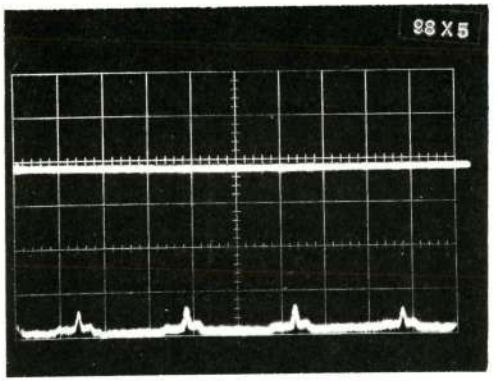

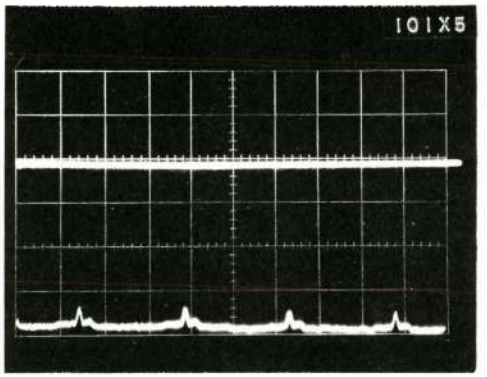

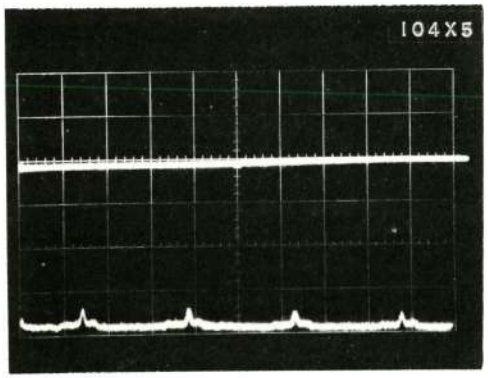

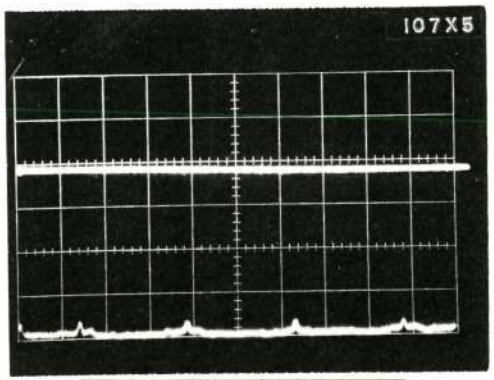

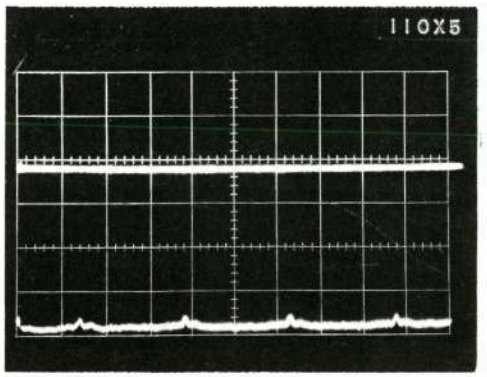

0.1 V/CM 500 LB/CM

Pressure

IR Emission

Spectra

RUN 30 N2H4 C

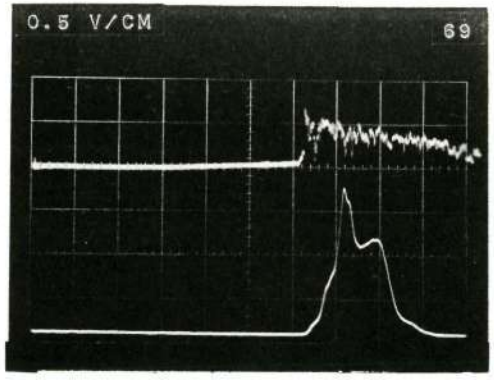

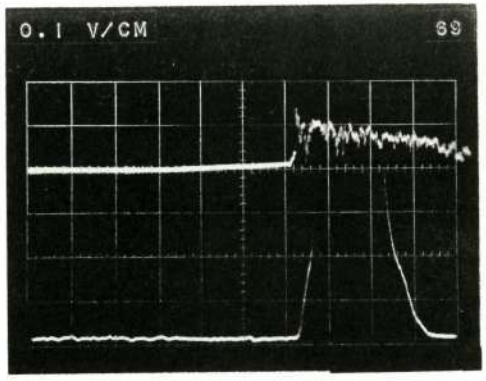

500 LB/CM

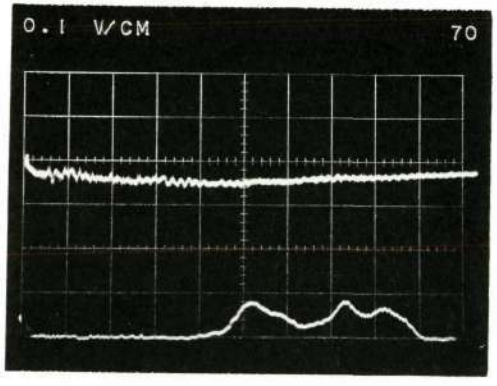

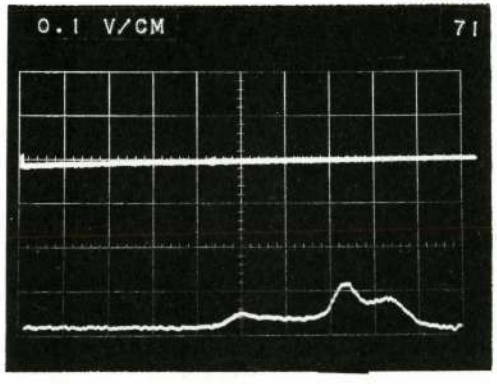

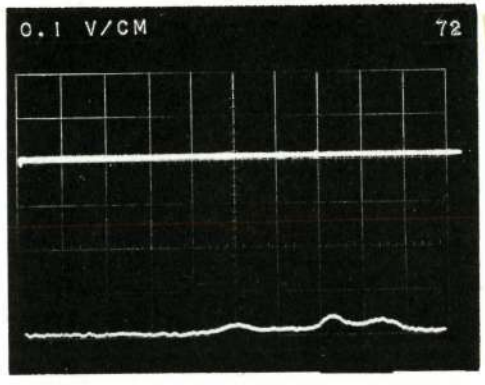

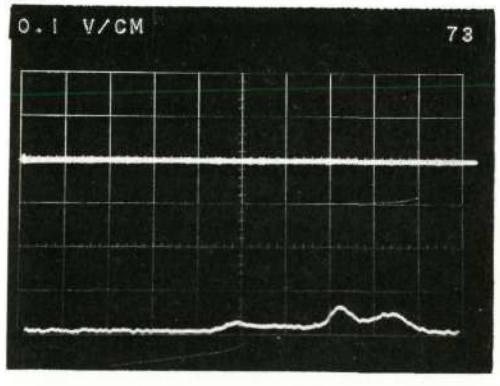

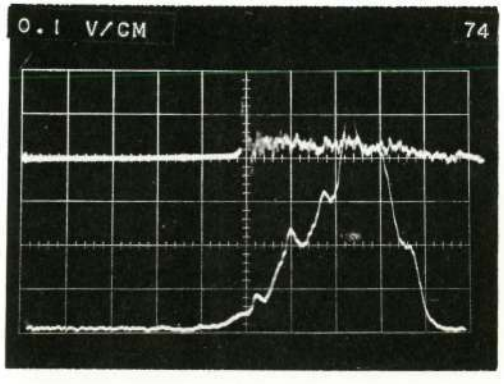

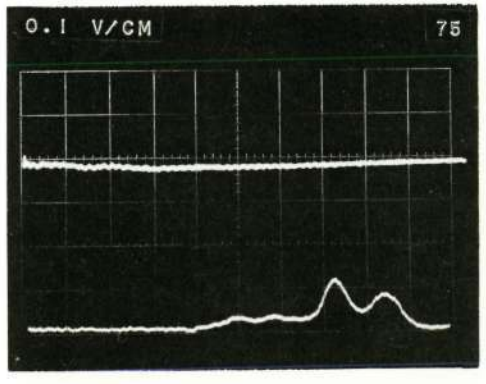

RUN 30 N_2H_4 c CONT

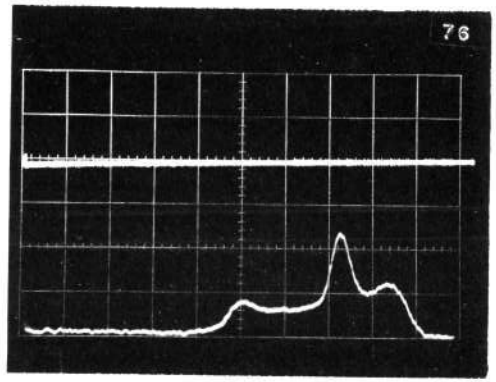

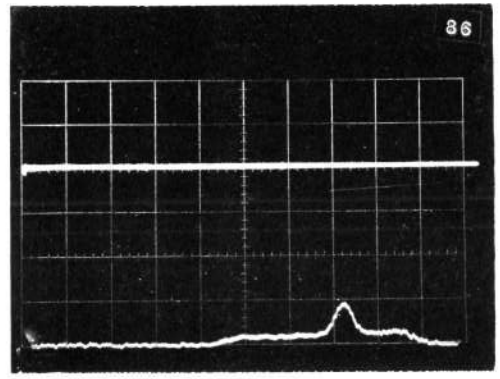

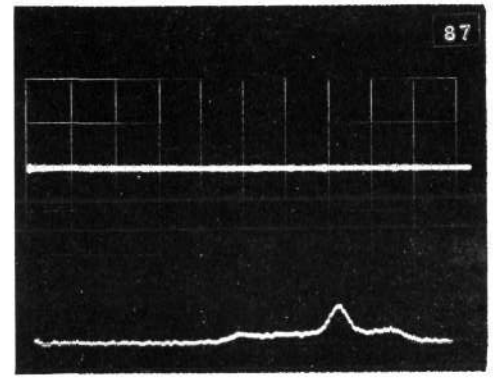

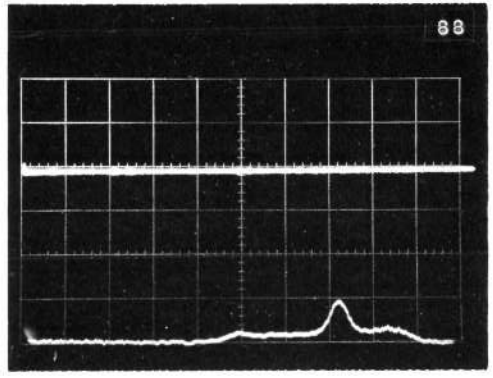

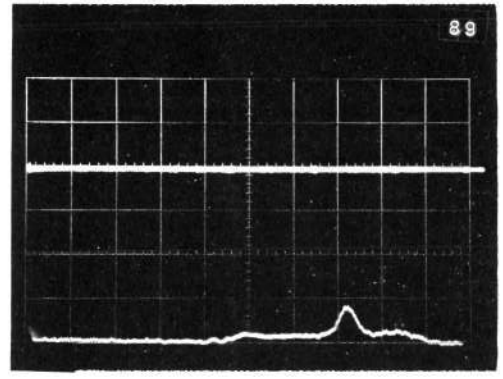

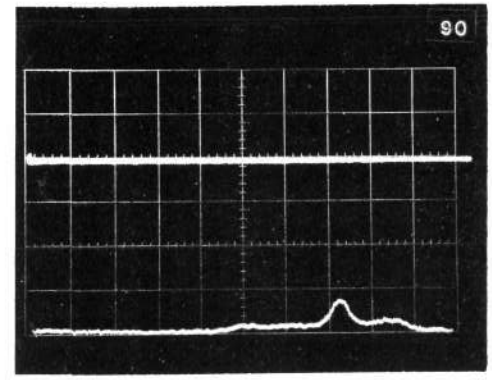

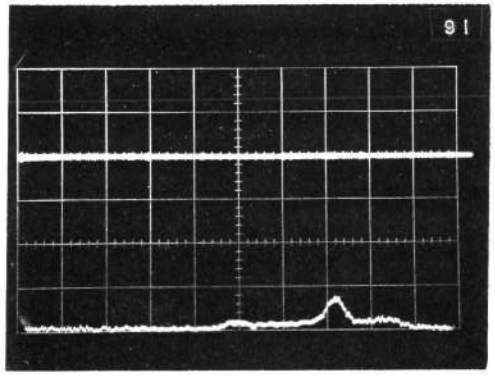

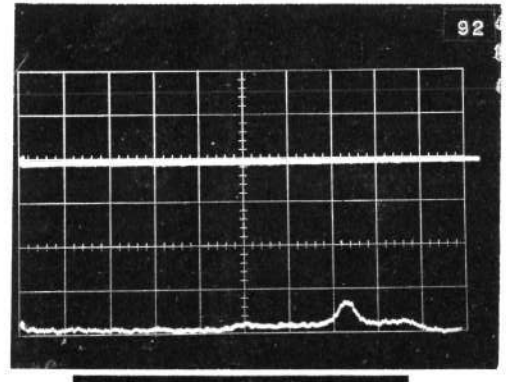

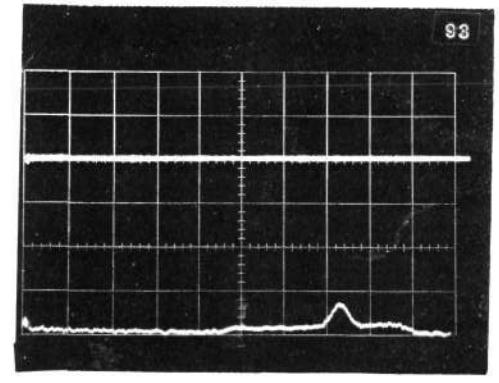

0.1 V/CM 500 LB/CM

TEST 15 MMH/N204 b CONT

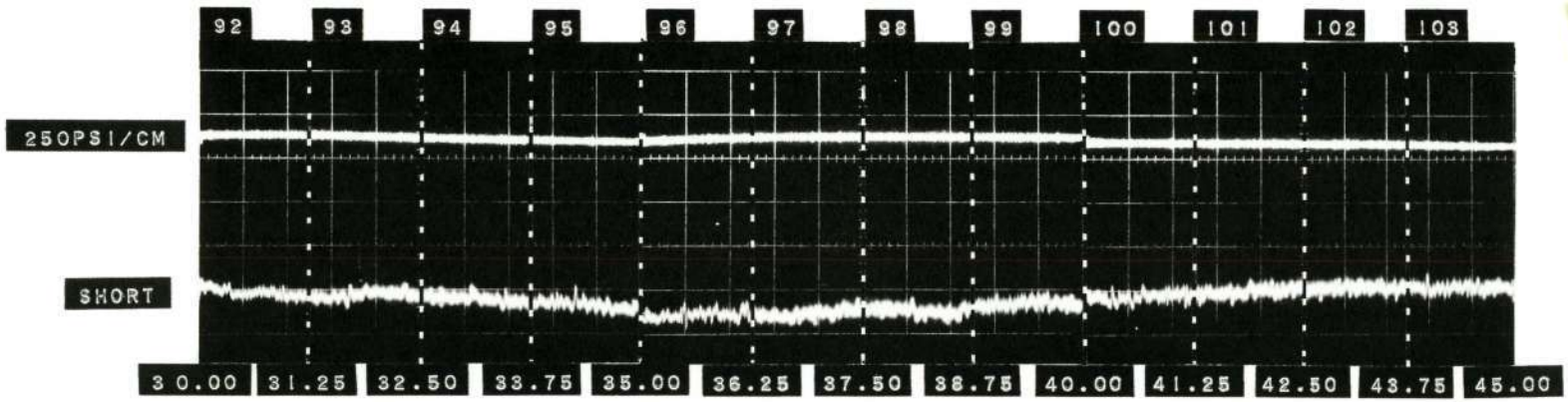

APPENDIX D

Spectral Characteristics of Selected Major Combustion Products

APPENDIX D. SPECTRAL CHARACTERISTICS OF SELECTED MAJOR COMBUSTION PRODUCTS

Species		Visible (Å)			IR (cm^{-1})	
CO		3911	4557	4932	2198	1596
		4154	4577	4981	2170	1576
		4260 max.	4654	5026	2134	1558
		4344	4659	5129	2133	1516
		4413	4769	5169	2112	1326
		4485	4798	5278	2082	1218
		4528	4896	5318	1739	1138
				5430	1620	1097
CO_2					4978	1343
					3715	667
					2349	
H_2O	weak absorption	5692 ↓ 8161	8227	9378		
		8162	8228	9381		
		8165	8274	9387		
		8170	8282	9427		
		8177	8288	9428		
		8189	8992	9438		
		8193	9000	9440		
		8198	9344	9460		
			9372	9461	5331 }	
				9522	3756 } gas	
				9545	3657 }	
					1595 }	
	emission	4216	7165		3445 }	
		4337	8097		3219 } liquid	
		4587	8916		1627 }	
		4731	9277			
		5126	9333			
		5480	9669			
OH		9500			3735	
					3181	
					2210	
					660	

APPENDIX D (Continued)

	Swan		Mulliken				
C_2	4698	5165	U.V.			1856	1641
	4715	5541				1830	1608
	4737	5586				1809	1107
	5129	5636				1788	
C	5794						
	7119						
C^+	3876	6578					
	3921	6583					
	4075	6784					
	4267	7231					
	5145	7236					
CH	4313Q					2816	
CN	Red	Main		Tail			
	6355Q	3584	3883	3405	3629	2164	
	6502Q	3586	4168	3433	3880	2069	
	7874R	3590	4181	3465	3910	1814	
	8067	3855	4197	3603	3945		
	9140R	3862	4216		3985		
	9393	3871					

APPENDIX D (Continued)

Species	Visible (Å)		IR (cm^{-1})	
CN^-			2250-2050	
C_2N_2	U. V.		2322 2149	
CO^+			2214 1734 1562	
H_3BO_3			3250 3150 1440 1185	1060 881 652 544
HCN	7880a 7912a		3311 2097 712	
HNCO			3531 2274 1327	797 670 572
HNO			3450	
			trans	cis
HNO_2	3417a 3539a 3545a 3680a		3426 1640 1292 856 637	3590 1696 1260 794 598 543
H_2O_2	3700a		3610 3417 2870	1262 890
	Flames	Chemiluminescence		
NH	3360Q 3370Q	3035R 3042Q 3240R 3253Q 3610R 3627Q	3300	

APPENDIX D (Continued)

Species	Visible (A)		IR (cm^{-1})	
NH_2	4723	5707		
	5166	5708		
	5525	6333		
	5705			
NH_3			N^{14}	N^{15}
			3448	3335
			3414	1625
			3337	961
			1627	926
			968	
			950	
			932	
N_3H			3336	1150
			2140	672
			1274	522
NO	3886		2374	1712
	3801		2371	1380
			2347	1300
			2327	1262
			1904	1170
			1876-N^{14}	1155
			1843-N^{15}	1038
			1748	1037
				1020
			stretch: 2400-900	
			monomer: 1883	
			cis-dimer: 1862, 1768	
			trans-dimer: 1740	
NO^+	6000		2220	

APPENDIX D (Continued)

Species	Visible (Å)	IR (cm^{-1})		
		N^{14}		N^{15}
NO_2	4350a	1618	485	1580
	4390a	1318	482	1306
	4448a	808	429	740
	4480a	750	381	
	4630a	672	370	
		O-N-O stretch:		900-400
NO_2^+		2360		
		1400		
		667		
N_2O	Continuous absorption through U.V. to 3065Å	$N^{14}N^{14}O$		$N^{15}N^{15}O$
		2224		2178
		1286		1281
		589		576
		$N^{15}N^{14}O$		$N^{15}N^{15}O$
		2203		2156
		1271		1266
		586		572

APPENDIX E

Visible Coincidence Table - Minor Species

APPENDIX E VISIBLE COINCIDENCE TABLE - MINOR SPECIES

Å

3035R - NH
3042Q - NH
3065a - N_2O

3240R - NH
3253Q - NH
3273 - B_2

3360Q - NH
3370Q - NH
3386 - NO
3405 - CN
3417a - HNO_2

3433 - CN
3465 - CN
3539a - HNO_2

3545a - HNO_2

3584 - NO,CN
3586 - CN
3590 - CN
3603 - CN
3610R - NH
3627Q - NH
3629 - CN
3680a - HNO_2

3700a - H_2O_2

3768R - BH^+

3792Q - BH^+
3801 - NO

3803R - BH^+
3855 - CN
3862 - CN
3871 - CN
3876 - C+
3880 - CN
3883 - CN

3910 - CN

3921 - C^+
3945 - CN
3985 - CN

4075 - C^+
4168 - CN
4181 - CN
4197 - CN
4216 - CN

4267 - C^+
4313Q - CH
4350 - NO_2

4390a - NO_2

4448a - NO_2

4480a - NO_2

4630a - NO_2

4698 - C_2

4715 - C_2

4723 - NH_2

4737 - C_2

5129 - C_2

5145 - C^+

5165 - C_2

5166 - NH_2

5525 - NH_2

5541 - C_2

5586 - C_2

5636 - C_2

5705 - NH_2

5707 - NH_2

5708 - NH_2

5794 - C

6000 - NO^+
6333 - NH_2

6355Q - CN
6502Q - CN

6578 - C^+

6583 - C^+

6784 - C^+
7119 - C

7231 - C^+

7236 - C^+
7874 - CN
7880a - HCN
7912a - HCN
8067 - CN
9140R - CN
9393 - CN

(a) - absorption
(Q) - Q branch
(R) - R branch

APPENDIX E (Continued)

INFRARED COINCIDENCE TABLE - MINOR SPECIES

cm^{-1}

3610 - H_2O_2

3590 - HNO_2

3531 - HNCO
3450 - HNO
3448 - NH_3

3426 - HNO_2

3417 - H_2O_2

3414 - NH_3

3337 - NH_3

3336 - N_3H

3335 - NH_3

3311 - HCN
3300 - NH
3250 - H_3BO_3

3150 - H_3BO_3

3000 - $B(OH)_2$

2976 - BH_3

2870 - H_2O_2

2816 - CH
2650 - BH_2

2500 - $B(OH)_2$

2430 - BH_2

2384 - BH_3

2374 - NO
2371 - NO

2360 - NO_2^+

2347 - NO
2327 - NO

2322 - C_2N_2

2274 - HNCO

2270 - $B^{10}H_4$

2264 - $B^{11}H_4$

2250 - $B^{10}H_4$

2244 - $B^{11}H_4$

2224 - N_2O

2214 - CO^+
2203 - N_2O

2178 - N_2O

2164 - CN
2156 - N_2O

2149 - C_2N_2

2140 - N_3H

2097 - HCN
2069 - CN
1904 - NO
1876 - NO
1856 - C_2

1843 - NO
1830 - C_2

1814 - CN
1809 - C_2

1788 - C_2

1765 - BH_3

1748 - NO

1734 - CO^+
1712 - NO
1696 - HNO_2

1640 - HNO_2

1627 - NH_3

1625 - NH_3

1618 - NO_2

1608 - C_2

1580 - NO_2

1562 - CO^+
1440 - H_3BO_3

1400 - NO_2^+

1380 - NO
1327 - HNCO
1322 - BO_2

1318 - NO_2

1306 - NO_2

1300 - NO, BO_3^{-3}, $B(OH)_2$

1292 - HNO_2

1286 - N_2O

1281 - N_2O

1274 - N_3H

1271 - N_2O

1262 - H_2O_2, NO

1260 - HNO_2, N_2O

1210 - $B^{11}H_4$

1208 - $B^{10}H_4$

1185 - H_3BO_3

1170 - NO
1155 - NO
1150 - N_3H, $B(OH)_2$

1107 - C_2

1100 - $B(OH)_2$

1093 - $B^{10}H_4$

1080 - $B^{11}H_4$

1070 - BO_2

1061 - B_2

1060 - H_3BO_3

1038 - NO
1037 - NO
1020 - NO
1000 - $B(OH)_2$

968 - NH_3

961 - NH_3

950 - $B(OH)_4NH_3$

947 - $B(OH)_4$

932 - NH_3

926 - NH_3

890 - H_2O_2

881 - H_3BO_3

856 - HNO_2

840 - BH_3

808 - NO_2

802 - BH_3

797 - HNCO
794 - HNO_2

754 - $B(OH)_4$

750 - NO_2, BO_3^{-3}, $B(OH)_2$

749 - $B(OH)_4$

747 - $B(OH)_4^-$

740 - NO_2

712 - HCN
672 - N_3H, NO_2

670 - HNCO

667 - NO_2^+

652 - H_3BO_3

650 - BO_3^{-3}

637 - HNO_2

598 - HNO_2

589 - N_2O

586 - N_2O

576 - N_2O

576 - N_2O

572 - HNCO, N_2O

544 - H_3BO_3

543 - HNO_2

533 - $B(OH)_4$

522 - N_3H

485 - NO_2

482 - NO_2

464 - BO_2

460 - $B(OH)_2$

450 - $B(OH)_2$

429 - NO_2

381 - NO_2

379 - $B(OH)_4$

370 - NO_2